

New Methods for the Investigation of Organic Thin-Film Devices

Dissertation

for the award of the academic degree of

Doctor of Natural Science

– Dr. rer. nat. –

from the faculty of Biology, Chemistry and Geosciences

University of Bayreuth

submitted by

Helmut Hänsel

born in Konstanz

Bayreuth, 2004

New Methods for the Investigation of Organic Thin-Film Devices

Dissertation

zur Erlangung des akademischen Grades eines
Doktors der Naturwissenschaften
– Dr. rer. nat. –

der Fakultät für Biologie, Chemie und Geowissenschaften
der Universität Bayreuth

vorgelegt von

Helmut Hänsel

aus Konstanz

Bayreuth, 2004

Die vorliegende Arbeit wurde in der Zeit von Oktober 1996 bis September 1998 am Institut für Physikalische Chemie der Ludwig-Maximilian Universität in München und von September 1998 bis Januar 2004 am Lehrstuhl für Physikalische Chemie der Universität Bayreuth jeweils in der Arbeitsgruppe von Herrn Prof. Dr. Georg Krausch angefertigt.

Vollständiger Abdruck der von der Fakultät für Biologie, Chemie und Geowissenschaften der Universität Bayreuth genehmigten Dissertation zur Erlangung des akademischen Grades eines Doktors der Naturwissenschaften (Dr. rer. nat.).

Datum der Einreichung: 26. Januar 2004

Datum des wissenschaftlichen Kolloquiums: 3. Juni 2004

Prüfungsausschuss:

Prof. Dr. Carlo Unverzagt (Vorsitzender)

Prof. Dr. Georg Krausch (Erstgutachter)

Prof. Dr. Hans-Werner Schmidt (Zweitgutachter)

Prof. Dr. Matthias Ballauff

Prof. Dr. Josef Breu

Meinen Eltern

Contents

1	Introduction	1
2	Scanning Probe Techniques	3
2.1	AFM on Composite-Based OLEDs	3
2.1.1	Abstract	3
2.1.2	Introduction	3
2.1.3	Experimental Methods	4
2.1.4	Results and Discussion	5
2.1.5	Conclusion	10
2.2	SNOM on Composite-Based OLEDs	11
2.2.1	Introduction	11
2.2.2	Experimental	11
2.2.3	Results	13
2.2.4	Conclusion	14
2.3	Near-field Detection of the Electroluminescence of OLEDs	16
2.3.1	Introduction	16
2.3.2	Experimental	16
2.3.3	Results	16
2.3.4	Conclusion	20
2.4	Scanning Electroluminescence Microscopy (SELM)	21
2.4.1	Abstract	21
2.4.2	Introduction	21
2.4.3	Experimental	22
2.4.4	Results	23
2.4.5	Conclusion	26
3	Combinatorial Techniques	27
3.1	Introduction	27
3.2	Overview	28
3.3	Optical-Wave Propagation in Thin Films	30

3.3.1	Transfer Matrix Formalism	30
3.3.2	Substrate Correction	34
3.3.3	Absorption, Exciton Generation and Photo Current	36
3.4	Ellipsometry	38
3.4.1	Introduction	38
3.4.2	Theory	38
3.4.3	Experimental	38
3.4.4	Determination of Optical Constants	39
3.4.5	Determination of Film Thickness	50
3.5	UV/Vis Spectrometry	55
3.6	Combinatorial Setup	58
3.6.1	Mechanical Details	58
3.6.2	Electrical Details	59
3.6.3	Optical Details	62
3.7	Solar-Cell Performance and Long-Term Stability I	69
3.7.1	Abstract	69
3.7.2	Introduction	69
3.7.3	Experimental	69
3.7.4	Results and Discussion	71
3.7.5	Conclusion	72
3.8	Solar-Cell Performance and Long-Term Stability II	74
3.8.1	Abstract	74
3.8.2	Experimental	74
3.8.3	Results	75
3.8.4	Conclusion	80
3.9	Optical and Electronic Contributions in Solar Cells	82
3.9.1	Abstract	82
3.9.2	Introduction	82
3.9.3	Experimental Setup	83
3.9.4	Theory	83
3.9.5	Results and Discussion	85
3.9.6	Summary and Conclusion	96
3.9.7	Experimental Details	98

3.10 Influence of inert gas on the Degradation of OLEDs	100
3.10.1 Abstract	100
3.10.2 Introduction	100
3.10.3 Experimental	101
3.10.4 Results and Discussion	101
3.10.5 Conclusion	106
3.11 Phosphorescent Emitter OLEDs	109
3.11.1 Introduction	109
3.11.2 Experimental	109
3.11.3 Results and Discussion	110
3.11.4 Conclusion	112
3.12 Materials	116
Summary	119
Zusammenfassung	121
List of Publications	123
Bibliography	125
Danksagung	135

1 Introduction

The discovery of conductivity in hydrocarbon polyacetylene in 1977 by Heeger, MacDiarmid, and Shirakawa [Shi77] was the starting point for a completely new field of physics: Organic Semiconductors. Already eight years before, electrically stimulated luminescence on anthracene single crystals had been observed [Hel65]. And five years later, in 1982, electroluminescence was reported from amorphous anthracene films [Vin82]. However, the poor stability of these devices made them a purely academic setup unsuitable for practical application. This situation changed drastically when a stable photovoltaic cell and a stable organic electroluminescent device were reported by Tang *et al.* [Tan86, Tan87]. Since that time, the field of organic semiconductors has experienced enormous progress, as the advantages of organic devices over their inorganic analogues seem evident: the devices are very thin, they can be produced on flexible substrates, large-area processing is comparatively simple, and a wide range of colours is accessible, which makes the materials interesting for flat-panel displays as well as for colour-sensitive photodetectors. Still the most difficult problem with the organic devices is long-term stability. Their sensitivity to moisture and oxygen creates the need for efficient encapsulation of the devices. During the last few years, this issue has been successfully addressed and first applications of organic light-emitting devices (OLEDs) can be found in car hifi radios (Pioneer) or cellular phones (Samsung).

Despite the recent progress towards commercial application there are, however, still unsolved fundamental questions concerning structural order, charge transport, interface physics, and, particularly with the usage of heavy-metal dopants, the physics of excited states.

In this work scanning-probe techniques and combinatorial techniques have been applied to organic thin-film devices to address some of these questions. The work is therefore organised in two parts, each devoted to one field of experimental techniques, one focussing on the electro-optical properties on a molecular scale, the other dealing with macroscopic properties and device physics.

In the first part, four scanning probe techniques are presented and structural aspects of devices and their influence on device performance are investigated. Two different types of single-layer OLEDs are studied. "Atomic force microscopy (AFM) on composite-based OLEDs" is used to investigate the morphological changes of a polymer/monomer blend system due to heat and their implications on light-emitting devices of this type. In the section "Scanning near-field optical microscopy (SNOM) on composite-based OLEDs" the optical properties of phase-separated films are studied. "Near-field Detection of the Electroluminescence of OLEDs" reveals information on the spatial homogeneity of electroluminescence emission and on the growth of dark-spot defects. Finally, "Scanning Electroluminescence Microscopy (SELM)" is presented as a new probe technique that uses locally excited electroluminescence to study the spatial variation of electro-optical properties of OLED materials.

The focus of the second part is on the influence of material combinations and of layer

thickness on the performance and on the degradation of organic thin-film devices. A theoretical description of the propagation of optical waves in thin films forms the basis of the chapter. This part is an essential ingredient for the understanding of the combinatorial experiments with photovoltaic cells presented later in this chapter. Ellipsometry is used to characterise the optical properties of organic materials. Both combinatorial ellipsometry and UV/Vis spectrometry are used to map out the layer structure of single and double layer libraries. Performance and degradation of photovoltaic cells are discussed as a function of layer thickness and as a function of materials. Most prominently, the observed performance enhancement by an additional layer of TiO_2 is shown to have an electrical and an optical component. Finally, results on OLEDs are presented. The heat transport capability of inert gas is shown to play an essential role in preventing the degradation of OLEDs. Furthermore, the degradation processes in vacuum and in inert gas atmosphere are found to differ significantly. The role of current anomalies is discussed in this context. At the end of this part, an overview of the organic materials employed is given.

All the experimental techniques presented here, including the theoretical description and the combinatorial data evaluation, have been either newly developed within the framework of this thesis or they are improvements on previously existing techniques.

2 Scanning Probe Techniques

2.1 Atomic Force Microscopy on Composite-Based Organic Light-Emitting Diodes

2.1.1 Abstract

Thermal annealing of organic light-emitting diodes based on polymer composites prior to the metal deposition is found to substantially improve the devices' luminescence efficiency. Phase separation between the matrix polymer and the hole conducting low-molecular-weight component is shown to be the origin of this behavior. We use atomic force microscopy along with selective dissolution of one of the components to establish the domain morphology of the devices. The presence of the metal electrode is shown to significantly influence the phase-separation process. Finally, a correlation between the domain morphology and the electro-optical properties is established¹.

2.1.2 Introduction

The behaviour of polymer blends confined to thin films has been studied extensively throughout the last decade both experimentally [Jon91, Bru92, Kra95, Bud99] and theoretically [Bin99, Mül01, Pur97]. Meanwhile comprehensive knowledge has been accumulated regarding how external interfaces can influence the phase behaviour and the morphology formed during phase separation. While most of this knowledge is the result of studies of model polymer blends, practical implications of what is often referred to as surface-directed phase separation have only rarely been discussed [Ari02, Mor01, Ari01, Gre99a]. This is partly due to the fact that technologically relevant blend systems tend to be more complex and less well-defined than model systems, thereby rendering systematic studies difficult if not impossible. However, polymer-blend surfaces and thin films are indeed important in a variety of technological applications. Therefore, the transfer of the concepts from model systems to applications is an important and challenging task. The field of organic light-emitting devices (OLEDs) is a good candidate for such transfer. The field has rapidly grown in the past few years [Fri99, Hee98] and first applications have entered the market. Different functionalities such as charge injection, charge transport or colour and polarisation tuning are typically provided by different materials that are either used in layered structures or as composites, or in combinations of both [Par94, Wu97, Sai00, Mit01, Bal98, Lee00, Gre99b]. Especially the composite systems are often thermodynamically unstable. There are studies on polymer-blend systems by Adachi *et al.* [Ada97], where it is shown that PMMA and PC-TPD phase-separate already during spin-coating to form submicrometer-sized emission sites in the final device. Neher

¹The results of this chapter are published in [Hän03a]

et al. used doped polyimide alignment layers to achieve polarised emission which also phase-separate during preparation. The mechanical rubbing of the alignment layer gave detailed insight into the phase morphology [Mei02]. Little is known, though, about the morphological influence on device performance and even less about the thermal stability of the morphologies and subsequent degradation of the devices. Composite systems consisting of a polymer and a low-molecular-weight species are expected to show a weaker tendency towards phase separation than polymer blends, as the incompatibility increases with the molecular weight of the components. Spin-coated films therefore do not necessarily phase-separate during preparation. Furthermore, the low-molecular-weight component can act as a plasticiser and influence the phase-separation kinetics. In the present contribution, we study the phase morphology of a thin-film organic light-emitting diode based on a low-molecular-weight hole conducting material blended with an inert polymer material. We have exposed a series of devices with varying dopant concentrations to elevated temperatures for different periods of time and we have compared films with a free surface with films covered with a metal electrode. We demonstrate that this treatment increases the device efficiency. We also show that this effect is related to structural changes within the composite matrix.

2.1.3 Experimental Methods

Single-layer OLEDs were fabricated by spincoating the active luminescent layer (EML) from a chloroform solution (≈ 2000 rpm, 20 mg/ml) onto ITO-coated substrates (resistivity $< 20 \Omega/\text{sq.}$). The thickness was typically 100 nm. The EML consisted of varying amounts of N,N'-diphenyl-N,N'-(3-methylphenyl)-1,1'-biphenyl-4,4'-diamine (TPD (Syntec GmbH) varied between 10 %wt and 40 %wt), 0.5 %wt perylene as the luminescent molecule, and poly(methylmetacrylate) (PMMA; $M_w=15000$ g/mol) as electrically inert polymer matrix. The devices were then subjected to vacuum in order to remove residual solvent. Calcium (100 nm) was evaporated to serve as a low work function cathode. The diode area defined by the cathode was 0.09 cm^2 . The different OLED devices were then characterised by monitoring the I - V characteristics and the electroluminescence intensity. The complete preparation and the characterisation were performed under an inert gas atmosphere. The heat treatment was carried out under vacuum conditions as well as under ambient conditions. No influence of the surrounding atmosphere on the phase morphologies has been observed. The phase structure of the samples was investigated by scanning force microscopy (AFM). All AFM images were taken on commercial scanning force microscopes ('Multimode' and 'Dimension 3100', Digital Instruments) operated in Tapping Mode[®]. In some cases the samples were washed in cyclohexane to selectively remove the TPD domains from the sample. AFM images were taken at the same spot of the samples prior to and after thermal annealing or cyclohexane washing.

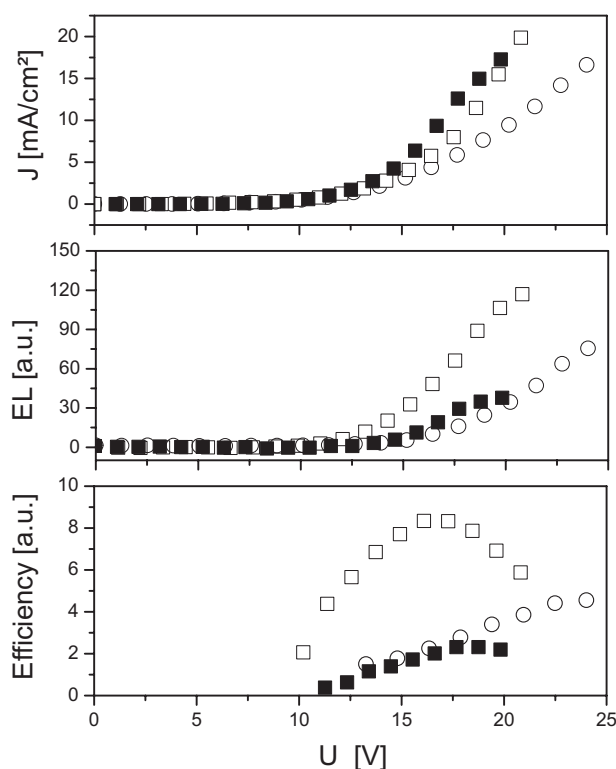


Figure 2.1: Characterisation of devices of the general structure $ITO / TPD(40\%wt):PMMA 100\text{ nm} / Ca$. Voltage dependence of the current density (a), the electrochrominance output (b), and the efficiency (c) of a “regular” device (open circles), a “pre-heated” device (open squares), and a “post-heated” device (solid squares).

2.1.4 Results and Discussion

Optoelectronic Properties

Figure 2.1 shows the optoelectronic properties of OLEDs containing 40 %wt of TPD after exposure to different heating protocols. If the device is subjected to heat (100 °C, 5 min) prior to the deposition of the top electrode (open squares), the conductivity increases, as is evident from the reduced current onset; the onset voltage for electrochrominance (EL) is lowered and the efficiency is raised by up to a factor of 4 compared with the non-treated reference device (open circles). By contrast, if the thermal treatment is done after deposition of the electrode (solid squares), the conductivity also increases, but there is only a slight reduction in the EL onset voltage. The efficiency, however, remains more or less unchanged. Similar observations were obtained at lower TPD content, the main difference being an increase in both EL and current onset voltage with decreasing TPD content (not shown here), as has been reported before [Blo98]. This effect can be attributed to the improved hole conductivity at higher TPD content.

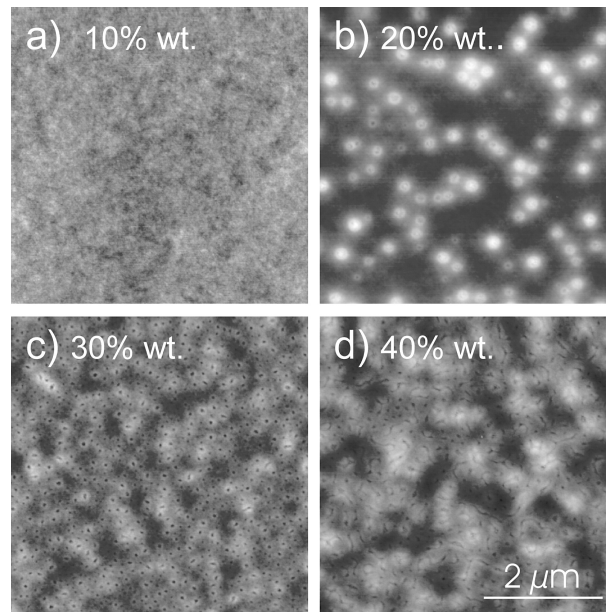


Figure 2.2: *Topographic surface scans (5×5 mm) of samples containing various amounts of TPD dispersed in PMMA after a 5-minute heat treatment at 100°C : 10 %wt, 20 %wt, 30 %wt, and 40 %wt (height scales are 5, 20, 10 and 20 nm, respectively).*

Morphology

We investigated the surface structure of the PMMA/TPD blend layers for different TPD concentrations. Due to the low thickness of the layers, these investigations can to some extent yield information about the morphology in the bulk of the films. After spin-casting, the films exhibit an average roughness of about 1 nm, regardless of TPD content. In order to simulate the aging process in OLEDs under operational conditions, the samples were heated to 100°C for 5 minutes (akin to the OLEDs; see above). The heating was performed on a hotplate under ambient conditions.

The results of this procedure are shown in Figure 2.2 for TPD concentrations ranging between 10 %wt and 40 %wt. While the film surface remains relatively smooth for the lowest TPD concentration, characteristic changes of the film morphology are induced by the heat treatment at higher TPD content. For 20 %wt TPD, the film surface develops isolated protrusions, which are quite uniform in size (diameter: some 100 nm; height: some 10 nm). In addition, a few holes are observed in the film surface, surrounded by a protruding rim. At higher TPD concentrations, the density of these protrusions increases, leading to a percolating elevated structure with small holes. In order to understand the underlying process, we have studied the temporal evolution of the surface morphology for a TPD concentration of 24 %wt on a silicon substrate. Figure 2.3 shows a series of cross sections through AFM images taken at the identical location of the sample after successive heating steps. The curves are shifted along the vertical axis for clarity. We find that the originally flat surface develops protrusions, which first tend to grow in height to about 10 nm and then expand laterally. At later stages of annealing, characteristic crater-like depressions are formed in the centres of the protrusions, which correspond to what was

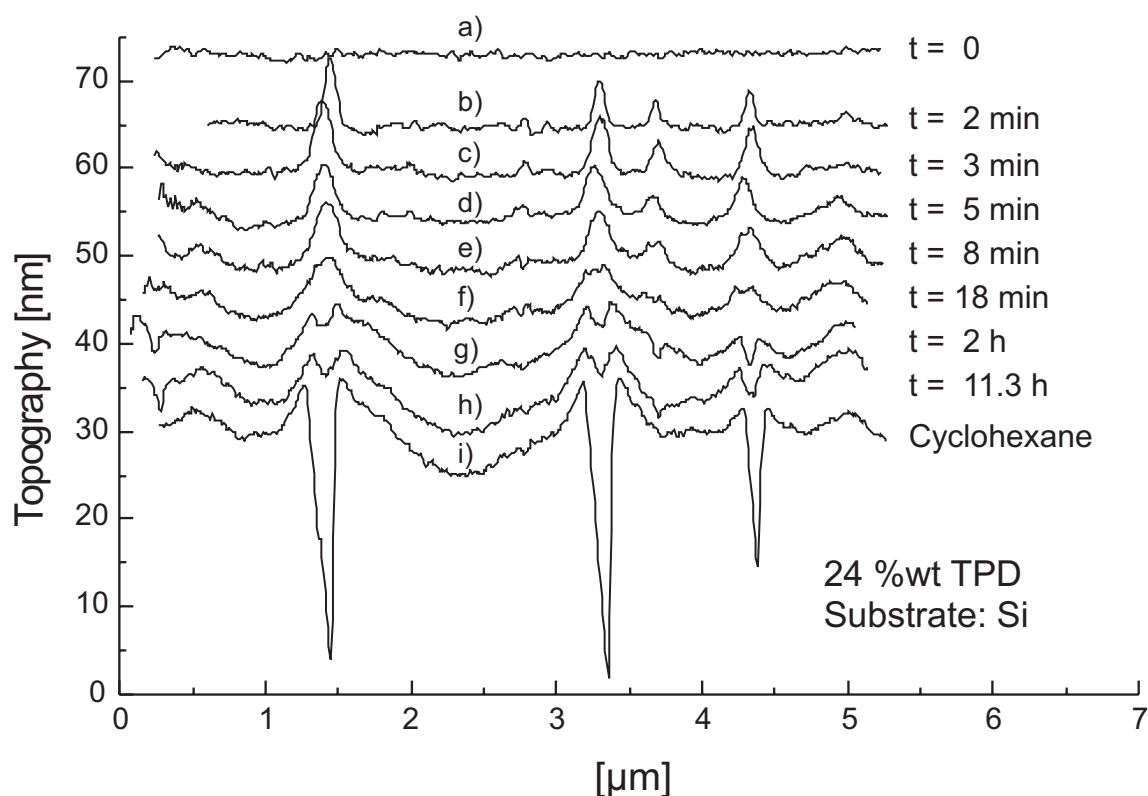


Figure 2.3: *Cluster formation: Morphological change of a sample containing 24 %wt of TPD dispersed in PMMA on a silicon substrate during heating. The cross section of AFM images taken at (a) $t = 0$ min, (b) $t = 2$ min, (c) $t = 3$ min, (d) $t = 5$ min, (e) $t = 8$ min, (f) $t = 18$ min, (g) $t = 120$ min, and (h) $t = 680$ min are displayed. The individual curves are offset for clarity. The bottommost curve shows the topography after treatment with cyclohexane.*

referred to as “holes” above. These depressions are only a few nanometres deep and do not deepen further on prolonged annealing. After the final heating step, the sample was immersed in cyclohexane. Being a selective solvent for TPD, cyclohexane is expected to remove potential TPD agglomerations located close to the surface. This treatment results in the formation of 30 nm deep craters around the centre of each protrusion while the surface area in between the protrusions remains largely unaffected (the bottom curve in Figure 2.3). This finding indicates that the protrusions formed on annealing can be attributed to TPD agglomerations located in the vicinity of the sample surface. Such agglomerations may result from phase separation between PMMA and TPD. At higher TPD concentration, the AFM images indicate that an underlying bi-continuous domain morphology has formed on top of which we find the same type of holes.

We now turn to a detailed discussion of the formation of these holes. The holes form during the early stages of annealing and do not grow in depth for longer annealing times. In order to understand the origin of these features, it proves helpful to consider in some detail the shape of the cross sections through the TPD agglomerations after TPD removal in cyclohexane. The remaining PMMA surface is not flat but has formed wide rims around the TPD clusters (the bottom curve in Figure 2.3). This is in agreement with studies of

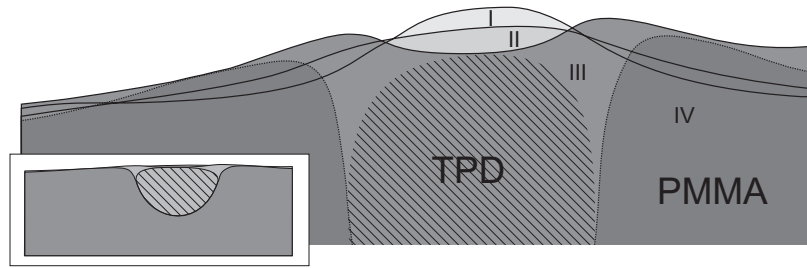


Figure 2.4: *Sketch of the phase-separation process for an uncovered composite film. I) phase separation leads to TPD clusters that locally deform the film surface, II) the surface deformation spreads further out, III) dewetting of the PMMA from the TPD clusters, IV) film morphology after selective dissolution of the TPD clusters. The inset shows the whole layer with the natural aspect ratio.*

thin polymer-blend films where phase segregation leads to similar surface patterning upon annealing [Kar98, Ade99]. Karim *et al.* were able to show by secondary ion mass spectroscopy that the droplet-forming component was covered with a thin layer of the matrix material [Kar98]. In our case, the formation of the holes indicates a different situation: we assume that the clusters are originally completely covered with a thin PMMA layer which then ruptures and dewets from the TPD clusters as they grow in size and come closer to the surface. Obviously, these holes will not grow in depth beyond the thickness of the PMMA layer. A sketch of the morphology development is given in Figure 2.4. We note that such experiments were performed for different temperatures between 60 °C and 120 °C (not shown here). These results indicate that the morphological changes are similar for all temperatures, while the kinetics of structure formation is naturally faster at higher temperatures. For further investigation, experiments were performed on real OLED devices where the polymer film was partially covered with calcium as cathode layer. No changes in the surface morphology of the calcium layer could be detected upon annealing. This finding is reasonable considering the small height of the protrusions observed on the free polymer surfaces (10 nm), the electrode thickness (100 nm), and the mechanical stiffness of the metal layer. After annealing, we removed the Ca electrode by immersing the samples into a hydrogen peroxide solution and investigated the surfaces (i.e. the original Ca/polymer interface) by AFM. The result of this procedure is shown in Figure 2.5a-c together with images taken at a location that was not covered with calcium (Figure 2.5d-f) for comparison. While protrusions and craters similar to the ones shown in Figure 2.3 have formed on the free polymer surface (Figure 2.5d), hardly any surface features are formed underneath the metal electrode upon annealing (Figure 2.5a). Even after cyclohexane treatment no changes of the film surface were observed (not shown here). More interestingly, however, a second annealing step performed after electrode removal leaves the surface rather smooth (Figure 2.5b), but leads to similar hole formation as in Figure 2.5d, though on a smaller length scale and less pronounced. Immersion in cyclohexane then reveals a large number of small holes in the polymer surface, confirming the existence of numerous small TPD clusters (≈ 20 nm) in close proximity to the polymer surface (Figure 2.5c). These results indicate differences in the phase-separation process between the uncovered and the metal-covered polymer film. In the originally uncovered area (Figure 2.5d-f), the second annealing step does not significantly alter the surface mor-

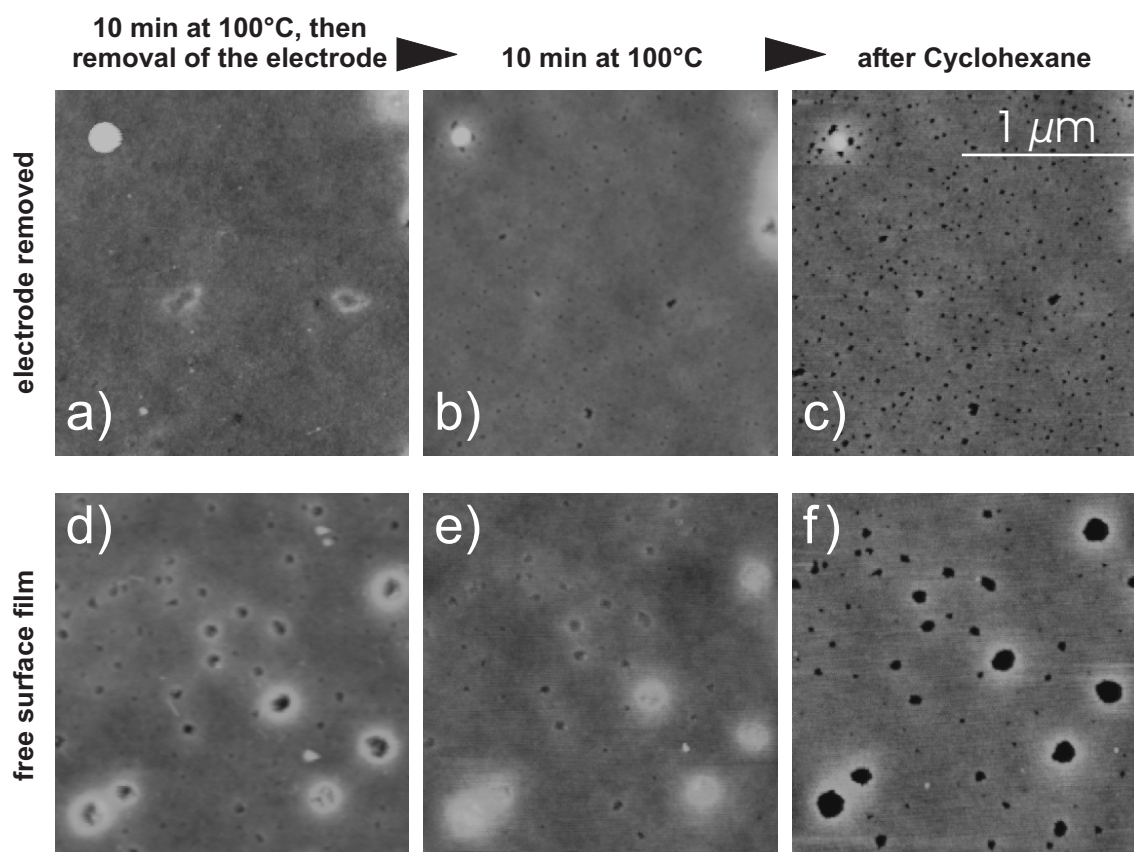


Figure 2.5: Comparison of the annealing process underneath a calcium electrode (top) and in the close proximity of the electrode (bottom) for a sample containing 20 %wt of TPD dispersed in PMMA. Temporal evolution of the surface relief after $t=10$ min (left, electrode was removed by immersing of the device in water), $t=20$ min (middle), and after cyclohexane treatment (right). The height range is 20 nm for all images.

phology, and immersion in cyclohexane results in the dissolution of large TPD clusters in agreement with the experiments discussed above.

If we assume that the presence of the metal electrode would suppress the phase separation between PMMA and TPD, the second annealing step (after electrode removal) should result in a surface morphology similar to the one formed after the first annealing step for the free polymer surface. A comparison of Figures 2.5b and 2.5e clearly demonstrates that this is not the case. Therefore, we are led to assume that phase separation has indeed taken place even underneath the electrode, however in a distinctly different way compared with the uncovered polymer film. Obviously, the presence of the metal electrode suppressed the formation of large domains in the early stage of phase separation. Ade *et al.* have shown that for thin films phase separation can be separated into three stages: initial phase separation, rapid coarsening, and coalescence. The understanding of the coarsening is that phase-separated domains rearrange in shape and lead to mass flow on a short time scale. Once separate domains have formed, coalescence happens on a larger time scale, as it can only happen due to diffusion and coalescence. Thus, even the late stage of an annealed film still exhibits complex three-dimensional polymer/polymer interfaces. This

leads us to the following interpretation of our results for the metal-covered films. The confinement of the film due to the electrode decreases the mobility of the domains and prevents the formation of larger TPD-rich domains. Nevertheless, stable domains form on a similar time scale as observed for uncoated films, but they are smaller in size. However, the metal coating prevents them from reaching the free surface. The second annealing step (after removal of the top metal layer) leads to a dewetting from the TPD clusters so that the subsequent cyclohexane treatment can selectively dissolve the TPD out of the film. The coalescence of domains, as described in Refs. [Kar98, Ade99], has not been observed in our experiments, as we have not performed experiments on very long time scales. (Annealing for 6 days at 100°C did not produce any change). Another reason for not observing coalescence could be the fact that TPD acts as a plasticiser for PMMA, thus slowing down the coalescence process with progressing phase segregation.

In summary, the annealing process leads to the formation of TPD clusters separated by PMMA domains with a reduced TPD content. The diameter of the clusters is larger than the film thickness for uncoated films and smaller than the film thickness for metal-coated films. With this knowledge, we can interpret the electro-optical properties presented in Section 2.1.4: The phase separation of PMMA and TDP leads to coherent current paths and thus increases the overall conductivity of the device. This is true for either heating protocol. However, only the preheated devices show a change in luminescence efficiency. We assume that this is due to the changed surface morphology of the film. We may speculate that the surface roughness leads to field inhomogeneities and that there is better mechanical contact between the cathode and the TPD phase due to prior dewetting. Both mechanisms would facilitate electron injection, which is an essential limiting factor for this kind of device, especially at low voltages. This is in agreement with the findings of Carter *et al.* when mixing insulating oxide nanoparticles with the luminescent material [Car97].

2.1.5 Conclusion

We have investigated the effect of thermal annealing on the morphology and performance of organic light-emitting diodes based on polymeric composites. We find clear evidence of phase separation between the polymer matrix and the hole conductor. The phase-separation process is strongly influenced by the presence of the top metal electrode. Both pre-heated and post-heated devices show an increase in conductivity whereas only pre-heating of the films leads to an increase in efficiency. This is correlated to the change in surface morphology.

2.2 Scanning Near-Field Optical Microscopy on Composite-Based Organic Light-Emitting Diodes

2.2.1 Introduction

The investigation of polymer/monomer blend systems for organic light-emitting devices (OLEDs) by atomic force microscopy (AFM) has shown that phase separation is an important issue for device performance. Having understood certain topological aspects, we are led to the question whether further information on the systems could be found by optical means. As the scales involved are in the sub- μm range, spatially resolved optical information is only accessible by confocal microscopy or by optical near-field techniques. Scanning optical near-field microscopy (SNOM) seems an adequate tool, particularly as topographical and optical information can be detected simultaneously. L.M.Do and coworkers have investigated the growth of dark spots in MEH-PPV OLEDs by confocal laser-scanning microscopy [Do96] and the group of M.Fujihira has applied local fluorescence spectroscopy to prove the interdiffusion of TPD and Alq₃ in dark spots of multi-layer OLEDs [Do96, Fuj96] and to investigate the energy transfer from TPD to Alq₃ [Yam01]. With regard to our phase-separated polymer/monomer system two questions come to mind: first, is it possible to detect the phase separation by local fluorescence microscopy, particularly at an early stage of phase separation or inside a metal-covered film where the limits of AFM are exceeded?² Second, if there is any phase separation in a functional OLED and if the dopant-enriched phases build current paths, do these paths lead to higher fluorescence? These two questions involve the use of the two fundamental modes of SNOM, namely the use of a local light source (*emission mode*) and local light detection (*collection mode*). We address both questions with a prototype SNOM which was supplied to us by *Carl Zeiss Jena* and *Digital Instruments* for a beta test.

2.2.2 Experimental

The system of interest is a single-layer OLED with a blend of poly(methylmetacrylate) (PMMA; $M_w=15000$ g/mol) and N,N'-diphenyl-N,N'-(3-methylphenyl)-1,1'-biphenyl-4,4'-diamine (TPD) as the emitter layer. Small concentrations (< 1%wt) of perylene are added as a lumophore. Heating of the uncovered blend film leads to strong phase segregation and topological changes of the surface (see 2.1 for details). To be able to detect the phase separation the different phases have to be distinguishable by one of their optical properties. In the case of TPD and PMMA this is the strong fluorescence of TPD in the near UV. For first experiments the PMMA/TPD samples are prepared on glass substrates without ITO and calcium electrodes and their UV/Vis absorption spectrum is measured (Lambda 5, Perkin Elmer) to find the optimum wavelength for fluorescence excitation. We find that the right-hand shoulder of the short-wavelength absorption peak at 353 nm is mainly responsible for the fluorescence with a maximum fluorescence intensity around 400 nm (see Figure 2.7).

²Such a sample would be perfect for determining the resolution of the SNOM, as no topologically induced artefacts enter into the optical signal.

This makes an argon-ion laser with its emission lines at 351.1 nm and 363.8 nm an ideal excitation source. We have therefore used a high-power argon-ion laser (Stabilite 2017, Spectra Physics), emitting in dual-line mode at the wavelengths given above. The laser light is coupled into a single-mode glass fibre optimised for a wavelength of 633 nm. The residual light from the discharge plasma is cut off by a short-pass filter. The light from the sample is divided by a beam-splitter (FT 395, Zeiss Filterset 01) into a $\lambda < 395$ nm and $\lambda > 395$ nm beam to separate the fluorescence from the transmitted excitation beam. Additionally, the long-wavelength spectrum is filtered by a long-pass filter (LP 397, Zeiss Filterset 01, see Figure 2.7).

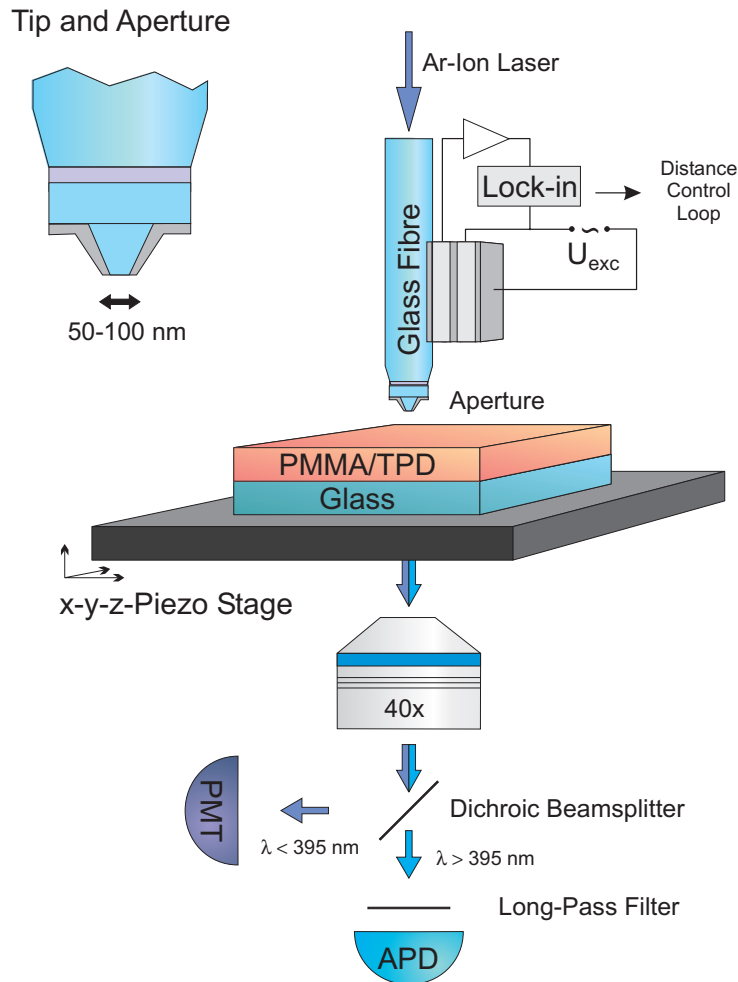


Figure 2.6: Sketch of SNOM setup for fluorescence microscopy. In order to locally excite fluorescence, the glass fibre with its microfabricated aperture has to be brought into the optical near-field of the emitter layer. Shear-force detection is used to control the distance between tip and sample. An argon-ion laser is used for fluorescence excitation and a dichroic beamsplitter with a centre wavelength of 395 nm and a long-pass filter split the beam into a transmission and a fluorescence component.

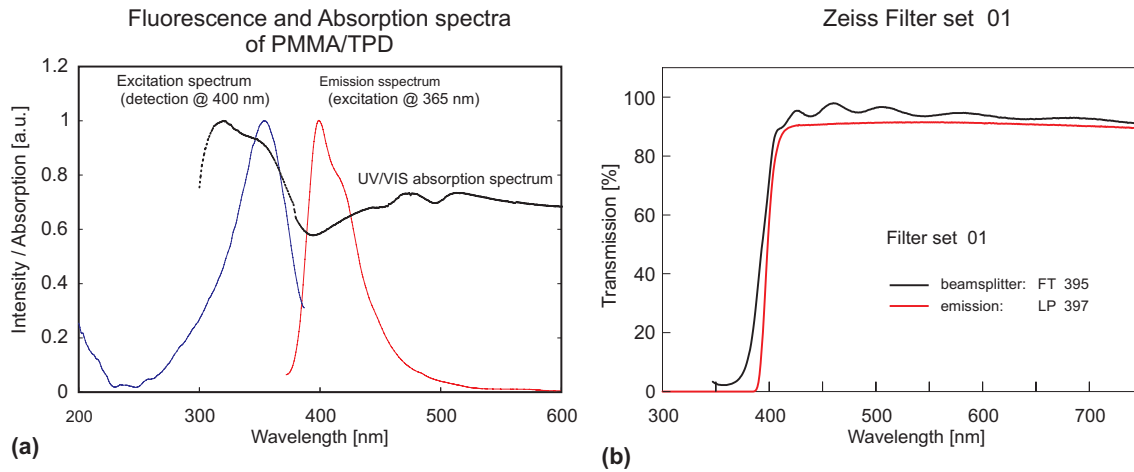


Figure 2.7: (a) Excitation, emission and absorption spectra of TPD/PMMA sample. The excitation spectrum exhibits a peak at 353 nm, the fluorescence maximum is found around 400 nm. (b) Transmission spectra of the dichroic beam-splitter and the long-pass of the Zeiss Filterset 01 used in the detection path.

2.2.3 Results

In a first experiment we tested whether fluorescence can be detected with this setup. For this purpose, we recorded the spectral intensity of the total light emerging from the sample and compared it to the raw signal from the fibre (Figure 2.8). Apart from the laser peak, we realise a broad fluorescence around 420 nm, which obviously results from the fluorescence of optical components in the setup, as it is insensitive to the presence of the sample. The use of a 40 \times slide-corrected objective “Neofluar”, which is optimised for UV, reduces the fluorescence in the detection path, but the remaining fluorescence of the fibre makes any detection of the sample fluorescence impossible. It should be said that there are, of course, less fluorescent glass fibres available on the market. With the micro-fabricated aperture directly glued to the 633 nm fibre we were, unfortunately, restricted to the use of that very fibre. Nevertheless, we were able to record SNOM images of the phase-separated sample. But we have to bear in mind that both the lower and the higher wavelength signals have to be understood as transmission signals, which makes the interpretation of the optical contrast less conclusive, as we will see.

Figure 2.9 shows two successive scans of a phase-separated PMMA/TPD sample with a TPD concentration of 20 %wt at low and high laser power. We present the topography and the signals of a photomultiplier and an avalanche photodiode (Single Photon Counting Module, EG&G) in the detection paths for $\lambda < 395$ nm and a $\lambda > 395$ nm respectively. The topography of the sample shows the expected elevations of TPD-rich domains (see 2.2). The dip in the middle of the protrusions indicates a later stage in the phase-separation process (compare 2.3). Both the higher and the lower wavelength transmission show a very clear correlation with the topographic signal. (Both transmission images have been flattened along the slow scan axis to compensate for fluctuations in the laser intensity.) The contrast behaves as one would expect from absorption. TPD-rich phases appear darker, PMMA appears lighter. This argument is valid for both detection paths as the

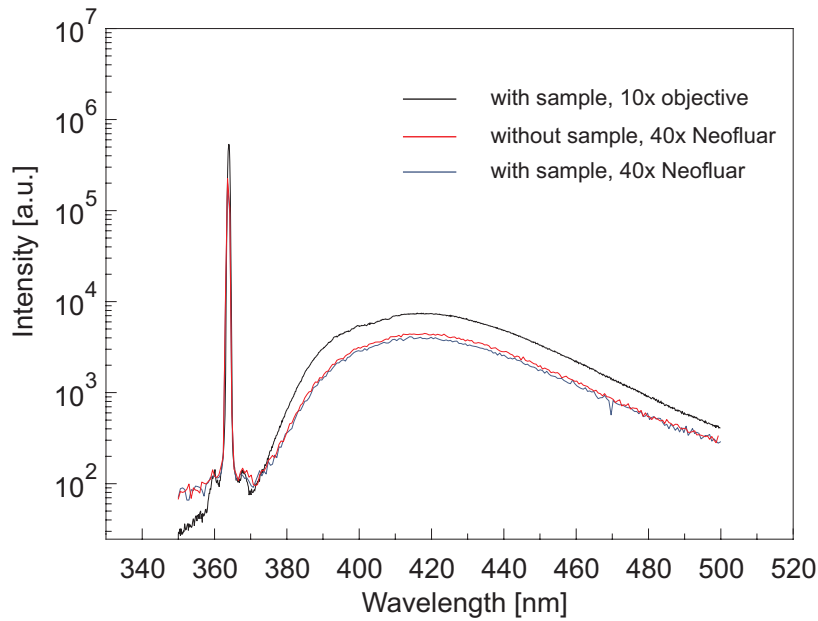


Figure 2.8: *Spectral intensity of the total light passing through the objective with and without a sample inserted and measured with two different objectives. The broad fluorescence peak around 420 nm, which dominates the spectra, results from the fibre fluorescence and makes any detection of the sample fluorescence impossible. The fact that the fluorescence peak observed with the 10× objective is larger than the one observed with the Neofluar objective is attributed to the additional fluorescence of the 10× objective itself.*

UV/Vis absorption of TPD is rather broad. However, we observe a correlation between topography and intensity also at places where TPD is not the origin of the topographic contrast. This effect is particularly clear when we look at the artefact near the scale bar in the first image and compare it with the second scan. Nevertheless, there are spots where the optical contrast exceeds what would be expected from a topographical artefact. The arrows indicate a spot where, following an absorption argument, we would expect a TPD-rich phase. In the topographical image, however, we only see the very border of a protrusion. We therefore assume that at this spot the observed optical contrast is due to absorption and that, in general, the signal is composed of a topographical and an absorption component. The contrast inversion of the $\lambda < 395$ nm signal at high laser intensity is an artefact due to the saturation of the APD.

2.2.4 Conclusion

We have studied a phase-separated PMMA/TPD sample by scanning near-field optical microscopy (SNOM). Unfortunately, detection of the sample fluorescence was not possible due to the strong fluorescence of the glass fibre. Restricting ourselves to the resulting transmission signals, we found a strong correlation between topography and transmission signal. However, the observed contrast is the superposition of absorption and a topographical artefact, which makes the interpretation of the pictures difficult. Future investigation of this system should be carried out with UV-compatible glass fibres or with fibreless

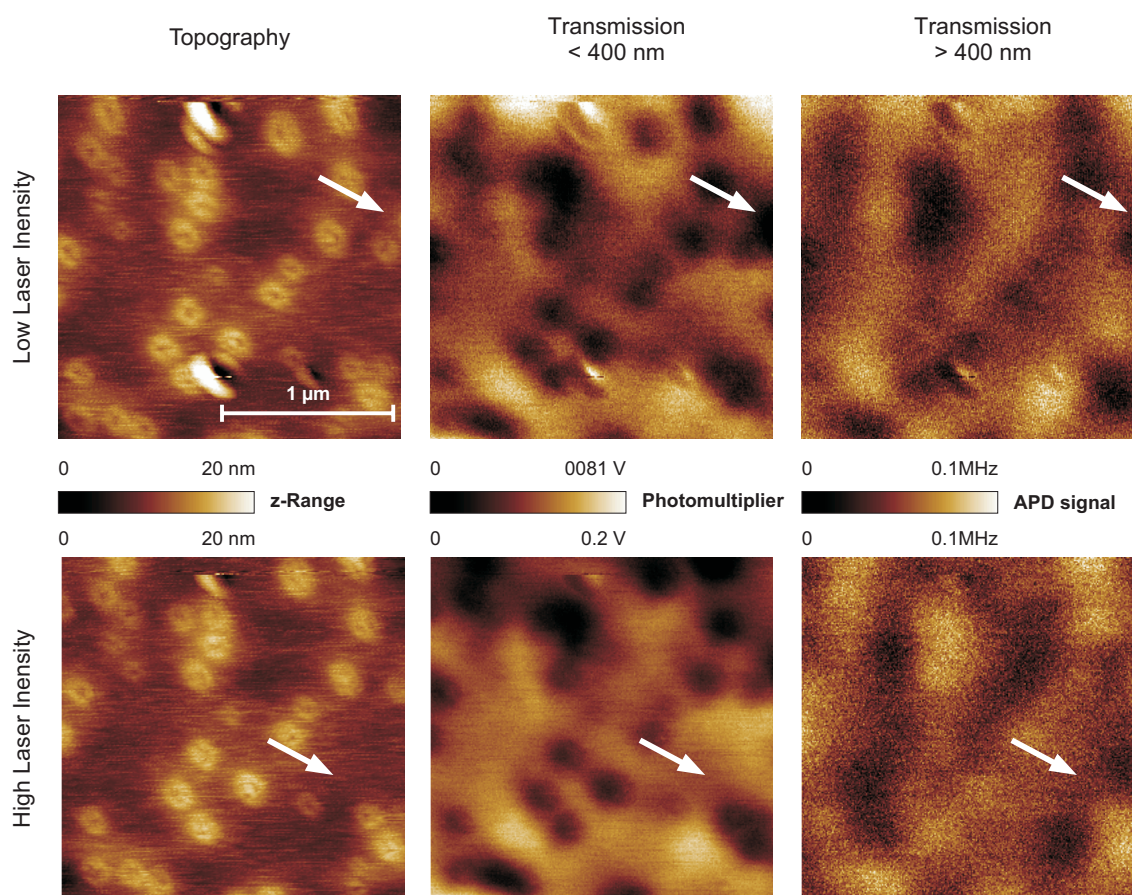


Figure 2.9: *Topography, transmission < 395 nm, and transmission > 395 nm of a phase-separated PMMA/TPD sample with a TPD concentration of 20 %wt. The pictures in the first row are recorded at low, the pictures in the second row at high laser intensity. The arrow indicates positions of high optical contrast, although the topography is rather flat. The contrast inversion of the bottom right-hand graph is an artefact due to saturation of the detector.*

apertures. Our efforts to locally detect the electroluminescence of this system were unsuccessful. We have therefore chosen a different system for this kind of investigation and report the results in the following chapter.

We note that today's most promising OLEDs are doped with organic heavy-metal complexes, which may also phase-separate upon heating. Since the absorption of some of these complexes is in the visible range, the fluorescence of the glass fibre and the other optical components should not be a problem other than in the reported case. Particularly, polymer OLEDs with phosphorescent emitter doping, e. g. poly(vinylcarbazole) (PVK) and tris(2-phenylpyridine) iridium $\text{Ir}(\text{ppy})_3$ as presented by Lee *et al.* [Lee00], are candidates for strong phase segregation. Scanning near-field fluorescence microscopy might therefore be an interesting tool if ever phase separation appears to be an important issue in this type of device.

2.3 Near-field Detection of the Electroluminescence of Organic Light-Emitting Diodes

2.3.1 Introduction

In the introduction to the previous chapter, we have raised the question whether the formation of local current paths in composite-based OLEDs could be observed by scanning near-field optical microscopy. In contrast to the fluorescence microscopy described above, such an experiment involves the collection mode of SNOM and has to be performed *in situ*, i. e. with the OLED in operation. In consequence, there are two essential requirements to be fulfilled. First, the aperture of the SNOM has to be brought into the near-field of the emitter layer of functional OLED. The glass substrate being 1 mm thick makes the detection through the cathode layer the only possible solution. Second, the electroluminescence has to be strong enough to supply a signal through the cathode layer which is detectable in an area of about $100 \times 100 \text{ nm}^2$ or less. The OLEDs built from a PMMA/TPD blend did not fulfil this requirement. Instead, we have focussed on a different system, in collaboration with the group of M. Schwoerer, Universität Bayreuth, EPII. The single layer Alq₃ devices prepared by this group proved to possess the required intensity for the experiment to work.

2.3.2 Experimental

A single-layer device was prepared by vapour deposition of Alq₃ and a 15 nm thin, semi-transparent Al/Ca film on an ITO glass substrate. Measurements of such devices under ambient conditions have to be performed very quickly, as both cathode materials are very sensitive to oxidation and as the cathode layer is very thin. Figure 2.10 shows the Alq₃ device together with the detection setup. Simultaneous to the recording of the SNOM images optical micrographs can be taken, as the sample is self-luminescent and no illumination is necessary, which would disturb the SNOM measurement.

2.3.3 Results

Figure 2.11 shows two optical micrographs of an early and a late stage of degradation, which document the expected instability of the OLED in air. In the early stage we perceive numerous dark spots of different sizes distributed homogeneously over the device. The spots are all of a round shape and exhibit a protrusion in their centre. At a later stage the dark spots have grown and covered a large part of the device by coalescing. The centre protrusion has grown and a dark rim has formed around the protrusion. This is in agreement with the results found by other groups [Sat94, Bur94, McE96, Fuj96, Do97, Azi98a, Azi98b, Lie00, Ke01, Kol01, Lim01, Ke02] and is ascribed to oxygen and humidity-induced degradation of the cathode.

After taking the first image, we focussed on one of the defects that was at the limit of visibility and performed collection-mode scans at that position (Figure 2.12). The dark

spot manifests itself very clearly in the EL signal by an inner part of constant count rate and a rim of increasing EL. Around the defect the EL intensity is nearly constant. A closer look, however, reveals a slight spatial variation which could originate from local current

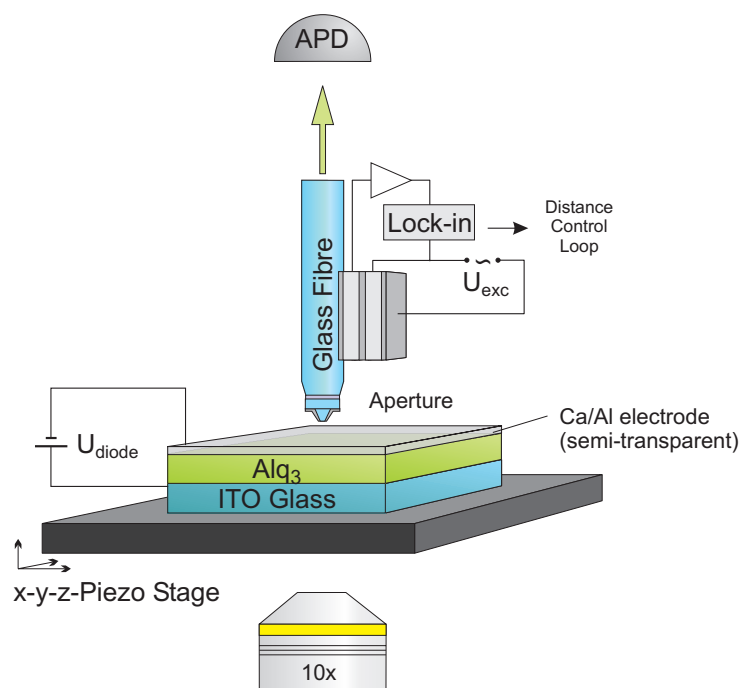


Figure 2.10: *SNOM setup for local EL detection. The near-field condition is achieved by the use of a semi-transparent electrode. Shear-force detection is used to control the distance between tip and sample and the EL is detected by an avalanche photodiode (APD). Bottom view optical micrographs can simultaneously be taken through a 10× or 40× objective.*

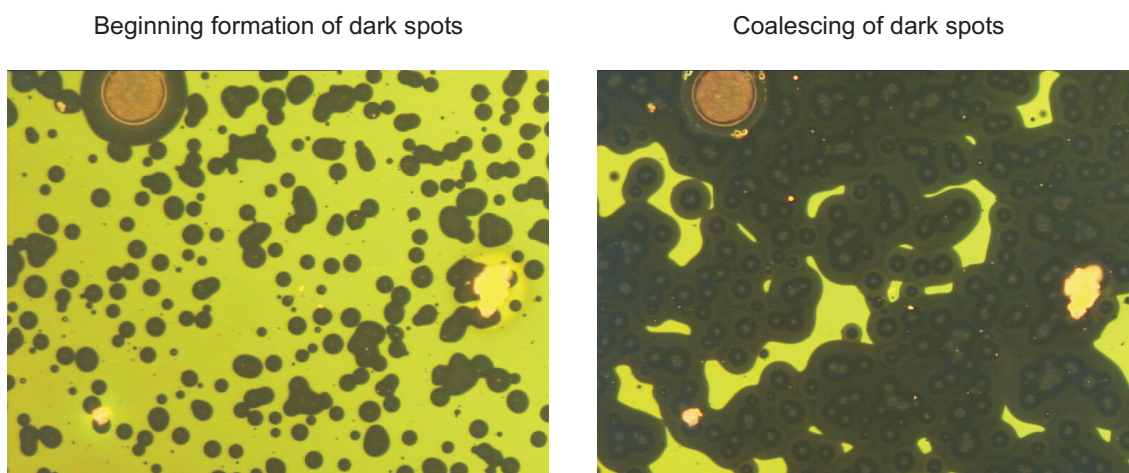


Figure 2.11: *In situ micrographs of the dark-spot formation. The pictures were taken with a weak darkfield illumination. The main contrast—and the green colour—results from the electroluminescence of the device. Left: Early stage of degradation; many different sizes of dark spots can be found. Right: Late stage of degradation; most of the dark spots have coalesced, restricting the electroluminescent area to very small regions.*

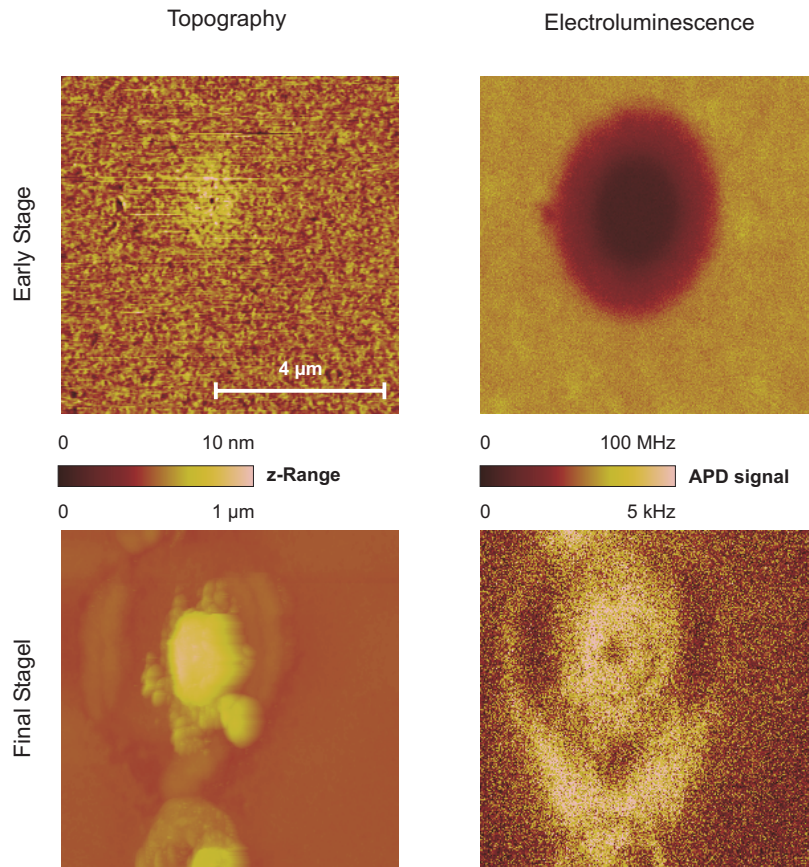


Figure 2.12: *Topographic and electroluminescence signal of an evolving dark spot. The upper graphs show the very early state of degradation: only a slight elevation is seen in the topographic image whereas the EL shows a clear defect the middle of the image. After 20 min of operation, the electrode is completely torn off and a huge protrusion has formed in the centre of the dark spot.*

paths. The topographic image shows a shallow elevation in the middle of the defect which is probably the early stage of electrode delamination, sometimes also referred to as bubble formation [Ke02]. The second image was recorded 20 minutes later after the EL had completely vanished. The topographic image proves that the defect had exploded and torn off the electrode, while in the middle, a μm high protrusion had formed. The remaining EL signal is due to scattered light from different parts of the device.

At this point we want to draw attention to a remarkable fact: in the first scan there is no correlation at all between the EL signal and the topography; the sample is still flat at the border of the defect. We can use this fact to estimate the bare optical resolution of the SNOM without any topographical artefacts involved. For this purpose, we have made a cross section through the EL signal of the defect structure and focussed on the intensity profile at the inner border of the defect. The shape of the profile suggests that the EL intensity increases linearly with the distance from the inner border of the defect. In the

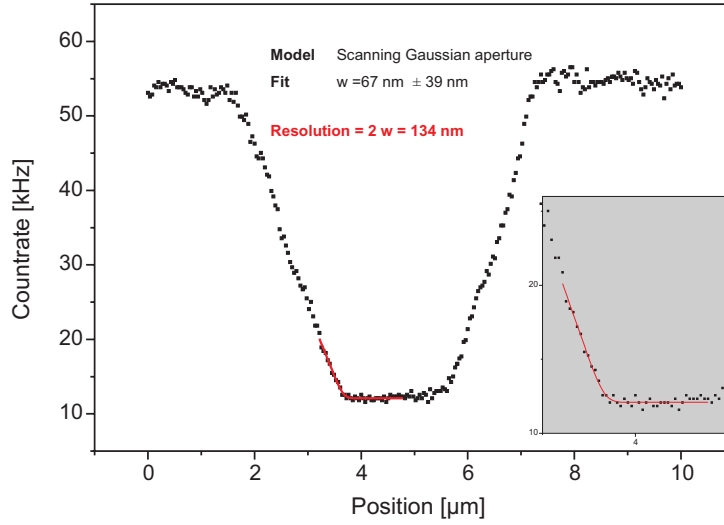


Figure 2.13: *EL intensity along a cross section through the defect. The shape of the EL at the inner border of the defect is modelled by a linear increase which has to be convoluted with the aperture function to give the detection signal of the APD. The fit leads to an effective optical resolution of $2w=134$ nm.*

inner part the intensity is assumed constant:

$$I(x) = \begin{cases} 0 & : x \leq 0 \\ \frac{x}{x_I} I_0 & : 0 < x \leq x_I \\ I_0 & : x > x_I \end{cases} \quad (2.1)$$

The transmission of the aperture is modelled by a Gaussian aperture function $A(x, y)$ of width w :

$$A(x, y) = \frac{2}{\pi w^2} e^{-\frac{2(x^2+y^2)}{w^2}} \quad (2.2)$$

The intensity I_{APD} that is coupled into the glass fibre is then given by the convolution of the emitted intensity and the aperture function. With the above assumptions we are led to an analytically solvable integral that can serve as a fit function for the data:

$$\begin{aligned} I_{\text{APD}}(x) &= \iint_{-\infty}^{\infty} A(x - x', y) I(x) dy' dx' \\ &= I_0 \left(1 + \sqrt{\frac{2}{\pi}} \frac{w}{x_I} \left(e^{-\frac{x^2}{2w^2}} - e^{-\frac{(x-x_I)^2}{2w^2}} \right) \right. \\ &\quad \left. + \frac{x}{x_I} \operatorname{erf} \left(\frac{x}{\sqrt{2}w} \right) + \left(1 - \frac{x}{x_I} \right) \operatorname{erf} \left(\frac{x-x_I}{\sqrt{2}w} \right) \right) \end{aligned} \quad (2.3)$$

The fit results in an aperture width of 67 nm, corresponding to an optical resolution of $2w=134$ nm. Note that this value is a very conservative estimate since the emission intensity profile was modelled with a perfectly sharp edge. But already with this conservative value we have overcome the classical diffraction limit of $\lambda/2$.

2.3.4 Conclusion

In summary, scanning near-field optical microscopy is capable of simultaneously detecting the topography and the electroluminescence of OLEDs. The EL intensity was found to be largely homogeneous over areas without dark spots. Very small variations in EL intensity, not resulting from dark spots, have been observed but could not be intensively studied since the experimental time was restricted by the fast degradation in air (≈ 30 min). The growth of dark spots has been monitored *in situ*. In the early stage, the EL vanishes in a circular area, while only slight topographical changes are observed. As a side-effect, this finding allowed us to estimate the SNOM's resolution to be better than 134 nm. At a later stage, the centre of the dark spot has grown eruptively and the electrode is torn off. We speculate that such micro-explosions are responsible for the self-insulating character of the dark spots. This is the more interesting as recent studies of OLEDs have shown that the degradation in vacuum leads to conducting defects which become insulating upon further operation in inert gas atmosphere (3.10). We are therefore currently planning comparative AFM investigations of devices that degrade in vacuum and in inert gas atmosphere.

2.4 Scanning Electroluminescence Microscopy (SELM)

2.4.1 Abstract

We have developed a scanning microscopy technique that is able to simultaneously record the topography, the conductivity, and the locally induced electroluminescence of organic light-emitting devices (OLEDs). The setup involves a scanning near-field optical microscope (SNOM) in which the fibre probe has been replaced by a PtIr tip. Contrary to classical STM, the distance is controlled by a shear-force detection which is essential to distinguish between conductivity and topography. Sub- μm resolution has been achieved on a single layer Alq₃ device. Because of its ability to locally induce and measure electroluminescence we have named this technique scanning electroluminescence microscopy (SELM).

2.4.2 Introduction

In the previous section we have dealt with the question whether inhomogeneities in the layers of OLEDs would affect the local electroluminescence efficiency. *In situ* experiments on a single layer Alq₃ device revealed a largely homogeneous emission down to the sub- μm scale. Nevertheless, small variations in the EL have been observed. But due to the fast degradation of the cathode material in air a profound study of these variations was not possible. One way of eliminating or at least reducing the degradation issue is to only locally inject charge carriers by an STM and to detect the resulting electroluminescence. Similar experiments have already been carried out on inorganic quantum-well structures [Ren91] and on PPV-based OLEDs [Alv97, Lid97, Alv98]. The experiments cited were performed in vacuum and allowed the additional measurement of cathodoluminescence spectra at selected spots. In two of the papers, the correlation between topography and EL is discussed. However, what is referred to as *topography* is the iso-current surface, which does not necessarily coincide with the topography. This has been shown on an atomic scale very impressively for planar aromatic molecules, where depending on the choice of the substrate and the bias voltage the HOMO or the LUMO levels of the molecules are imaged [Str98]. But the difference can be very important, also on mesoscopic scales, particularly in the case of organic semiconducting materials: since the charge transport in amorphous organic materials is accomplished by a hopping process, the iso-current surface will reflect the locations of hopping centres rather than the *true surface*. Very similar arguments have led to a discussion on the *topography signal* of TappingModeTM AFM. In that case the *true surface* was identified by a careful analysis of force–distance curves at each pixel [Kno01]. In our case, we proceeded very similarly. We used shear-force detection for the independent measurement of the topography and we recorded shear force, current, and EL as a function of the distance.

2.4.3 Experimental

We replaced the glass-fibre probe of a commercial SNOM (TwinSNOM, Omicron) by an etched PtIr tip [Zet00], through which charge carriers can be injected directly into the organic layer of an OLED where the top electrode has been omitted. The resulting electroluminescence can be detected through the glass substrate in the far-field via a $40\times$ slide-corrected objective and through a high numerical aperture objective on the scanning side, which we did not use in experiments shown below. The tip is glued to a pair of piezo crystals, which are used to vibrate the tip at a resonance frequency around $\approx 52\text{kHz}$ and to detect the vibrational response, as schematically shown in Figure 2.14. The phase difference between the exciting and the detected signal (we will refer to it as *phase*) is used for the distance feedback loop. Figure 2.15 shows a photograph of the instrument and two detailed photos of the tip holder and the scanning unit. Since the intensities of locally excited EL are very low, we use an avalanche photo diode (Single Photon Counting

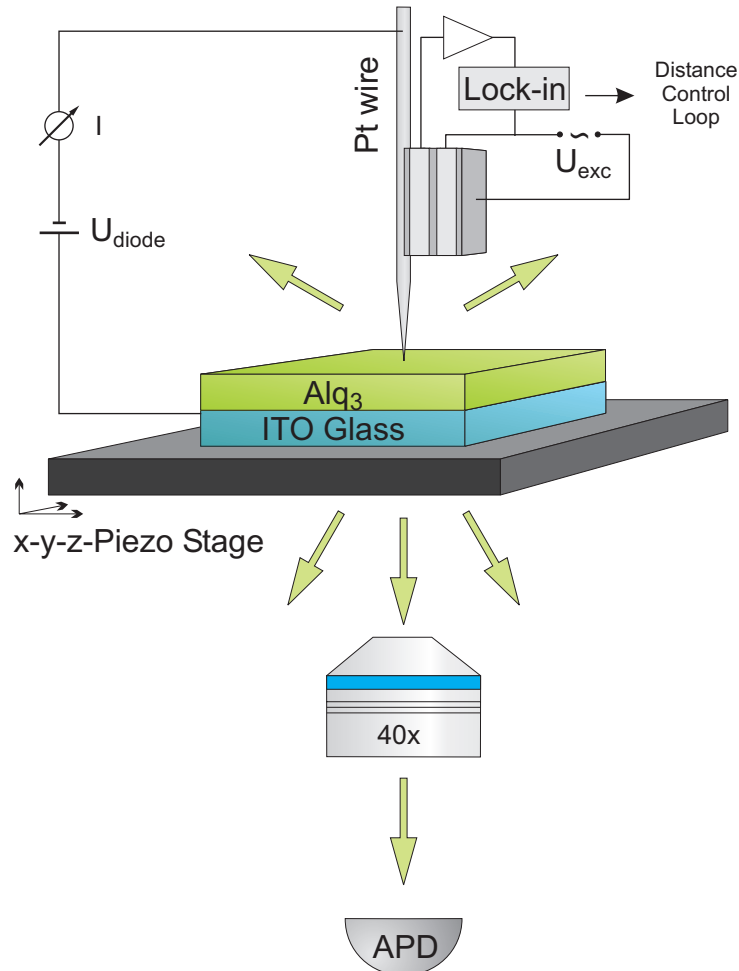


Figure 2.14: *Setup of the Scanning Electroluminescence Microscope (SELM). Shear-force detection is used to control the distance between the Pt tip and the sample. Current and EL are measured simultaneously during scanning. Bottom view micrographs can be taken through a $40\times$ slide-corrected objective.*

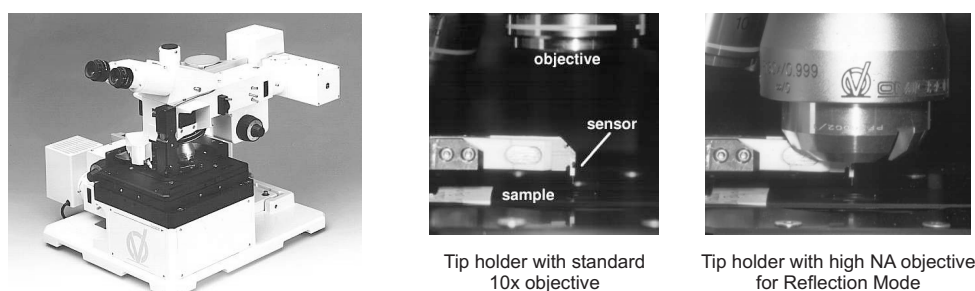


Figure 2.15: Photograph of the scanning near-field optical microscope “TwinSNOM” (Omicron) and two close-ups of the tip holder, the scanning unit and the objectives.

Module, EG&G) and an external multi-channel counter board (MCD, FastTec) for EL detection. The counter board is controlled by a Labview program and synchronised with the SNOM via trigger pulses sent from the SNOM control unit. The current is recorded after amplification by a home-built preamplifier of gain 2×10^8 . Externally acquired data are joined with the Omicron data files with the help of a Labview program to accommodate further evaluation.

2.4.4 Results

In a first experiment we investigated whether the EL of a 50 nm Alq_3 layer on an ITO-coated glass substrate can be detected. For this purpose, the tip was placed on the sample with the feedback loop enabled. A bias voltage of 10 V was applied. In this situation, the tip is not yet in contact with the surface, since the shear force is due to air movement close

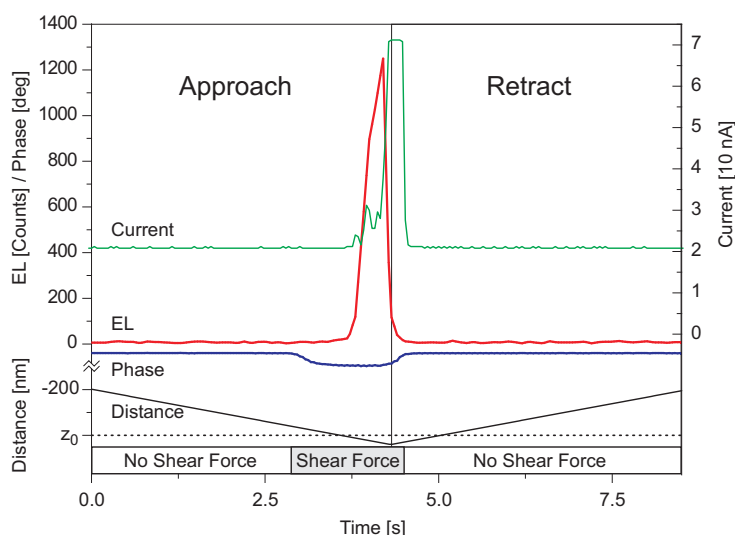


Figure 2.16: Phase, current, and EL during an approach–retract cycle with an applied bias voltage of 10 V. The current and EL set in simultaneously around position z_0 and vanish upon retraction of the tip. The early change in the phase signal is probably due to the water layer on the substrate.

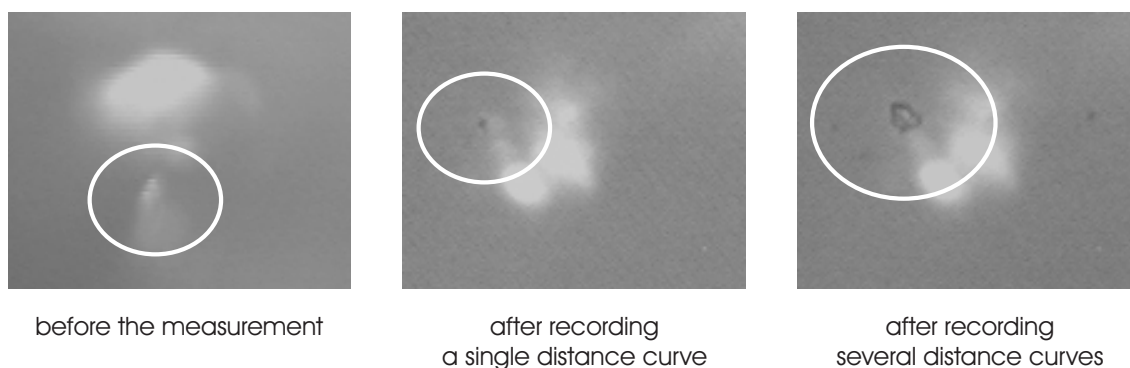


Figure 2.17: *The damage that occurs during measurements in air can be detected by optical microscopy. The damage grows as a function of the injected charge.*

to the surface and due to the water film that is always present under ambient conditions. Consistently, no current flow was observed. Then the feedback was interrupted and the tip was retracted 200 nm from the surface. During the following approach and retract cycle the phase, the current, and the EL were recorded. The result is displayed in Figure 2.16. The bottom curve shows the position of the tip relative to position z_0 , which the tip was retracted from. The phase signal is a measure of the shear force between tip and sample. It is initially constant and starts to deviate before z_0 is reached. We attribute this to the water layer on the substrate. Close to position z_0 both current flow and EL are observed. Upon retraction of the tip the EL and the current vanish, as expected. The measurement could be repeated and led to similar results. However, after several measurements, we found severe damage to the organic layer, which could also be resolved optically with the inverted microscope from below as shown in Figure 2.17. We attribute the damage to electrochemical reactions with oxygen and water together with the strong mechanical stress exerted in this particular measurement. This problem was solved by performing the measurement in a droplet of silicon or paraffin oil. The oil not only excludes air from the measurement but also reduces the difficulties that arise from the water film on the surface. We were able to take several similar curves at a single location and no damage was observed.

In a second experiment, we tried to set the parameters so that the tip is closer to the surface and to record a scan image under these conditions. However, the sample was completely destroyed after the measurement. Obviously, the softness of the organic material does not permit scanning during stable electrical contact.

The way out of this dilemma is to perform an approach–retract cycle at each pixel of a scan while detecting shear force, current, and electroluminescence. In Figure 2.18 we present the result of a measurement where 20×20 distance scans were performed in an area of $2 \times 2 \mu\text{m}^2$ with applied bias voltage of 10 V. The parameters of the approach–retract cycle were chosen more conservatively in order not to damage the sample. The tip position was varied between 30 nm and -20 nm. Graph (a) shows the topography which has been determined by the shear-force measurement. Graphs (b) and (c) show the EL recorded 1 nm and 15 nm below the setpoint of the feedback control loop. The colours are interpolated between pixels for better visibility.

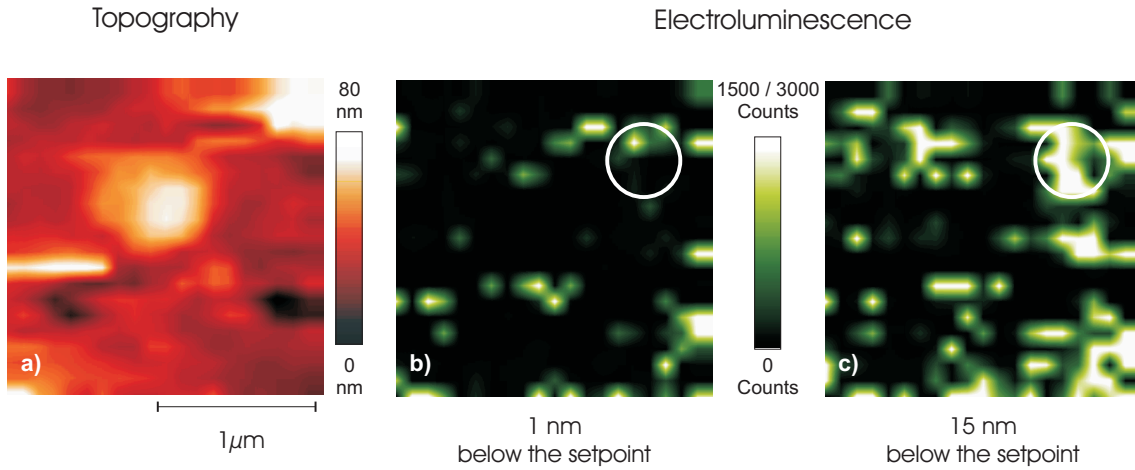


Figure 2.18: 20×20 SELM image: (a) Topography, (b) EL 1 nm below z_0 , (c) EL 15 nm below z_0 . In (b) only little EL is observed at isolated spots, in (c) EL is found in coherent areas (e. g. white circle).

The figure shows that 1 nm below the setpoint only a few, mostly isolated spots exhibit EL. 15 nm below the setpoint, however, EL is found in larger coherent areas, for example in the region marked by the white circle. On the other hand, there are regions which do not show EL at all for the chosen parameters of the distance sweep. Hence, the electro-optical properties of the Alq₃ layer seem to vary on a 100 nm scale. A clear correlation between topography and EL was not observed. This result is consistent with the findings of Alvarado *et al.* [Alv97] and Lidzey *et al.* [Lid97], who also find spatial variation of locally excited EL.

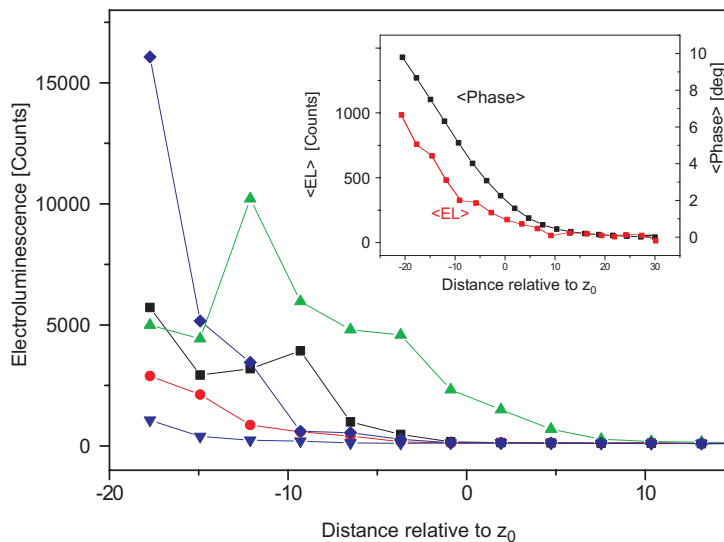


Figure 2.19: EL-distance curves from five different locations taken during the SELM measurement described above. The EL increases with decreasing distance, the onset and the intensity of the EL however shows strong variation. The inset displays the EL-distance curve and the phase-distance curve averaged over all 400 pixels.

We now take a look at the EL–distance curves that were recorded during the measurement presented. Figure 2.19 shows the EL–distance dependence at five different locations. In agreement with the results presented above (2.16) we find that the EL typically starts when the tip is lowered several nanometres beyond z_0 and increases upon further lowering. The onset and the intensity of the EL, however, show strong local variation. It is interesting to note that averaging over all pixels leads to a fairly smooth EL–distance curve (inset), although the fluctuations within one curve are large. Remarkably, the average EL sets in before the setpoint. Additionally, we display the averaged phase–distance curve to demonstrate the sensitivity of the distance control. The phase starts to deviate from its initially constant value shortly before EL sets in.

2.4.5 Conclusion

We have developed a scanning probe technique (SELM) that is able to simultaneously measure topography, current and locally excited EL. The degradation that can occur when the measurement is performed in air is eliminated by the use of a droplet of silicon oil or paraffin oil. This proves that the previously observed damage was due to electrochemical reactions rather than mechanical stress. (We note here that this protection from degradation might also be applicable to the local EL detection with SNOM presented in the previous chapter.) The application of SELM to a single-layer Alq₃ device has revealed that there are strong local variations in the electro-optical properties of the Alq₃ layer, which is consistent with the findings of other groups on polymer-based devices. The nature of these variations, however, has not been clarified and their understanding needs further investigation. The averaging of locally acquired distance curves leads to an average characteristic property of the device, which in future experiments might be linked up with macroscopic properties.

3 Combinatorial Techniques

3.1 Introduction

During the last few years, *combinatorial chemistry* has been established as an efficient method to screen in parallel a huge variety of materials for a certain property or functionality. The naming originates from the way in which *combinations* of educt materials are used to give a diversity of new materials that vary in their chemical composition and in consequence in their respective properties, such as solubility, fluorescence, etc. Such sets of materials are also called *a library*.

Mathematically speaking, combinatorics, or combinatorial mathematics, deals with the number of ways there are to bring about a certain event or with the number of elements in a set with a certain property. These sets are always finite and hence the parameters describing these sets are necessarily discrete. Combinatorial methods in chemistry and biology, however, not only include variation of discrete parameters such as substituents, solvents or catalysts, but also variation of continuous reaction parameters, such as pressure, concentration, temperature, etc. In most experiments though, these parameters are not continuously varied. Instead, experimentalists discretise the parameter space artificially by taking samples at certain points of the parameter space, i. e. at a finite set of concentrations, pressures, temperatures, etc.¹. Therefore, the term combinatorial chemistry is applied also to this kind of experiments.

Combinatorial methods have, during the last decade, become a highly efficient tool in the biotechnology and pharmaceutical industries that is responsible for many advances in modern drug development, particularly as the combinatorial approach is meanwhile extended also to the synthesis of materials. Despite this obvious success, combinatorial approaches are found to meet some skepticism in the academic community [Ami02]. This may partly be due to the fact that the industries' attention is often turned to the efficient screening of a diversity of materials rather than to the understanding of the underlying principles that make a material outstanding for a certain application. This is sometimes felt to be an inherent problem of the combinatorial approach itself rather than of what the approach is used for. This perception of combinatorial methods may also result from low publishing activities of the departments of research and development.

Concerning the variation of materials, it is particularly difficult to provide a theoretical description of the experiment. The structure-property relation is often complex, involving different fundamental material properties that cannot always be systematically varied. The more parameters enter, the more difficult the task becomes. Nevertheless, there have been advances during the last few years in revealing such relations by analysing correlations between, for example, topological information indices and the property in

¹In some experiments, e. g. in thickness dependent measurements of organic thin-film devices, a certain parameter can even be varied quasi-continuously. This, however, is only reasonable, if the only response of the device can be locally resolved, as in the case of electroluminescence.

question [Wie96, Ben97]. Needless to say, this type of research has only been possible due to recent developments in computer technology. In any case, combinatorial experiments are the only way of mapping out the huge parameter space necessary to provide reliable data that a theory can be tested against or that a correlation analysis can rely on.

The situation is slightly different when a continuous parameter is varied. In this case, the influence of the variation can be studied much more easily, as the range of the parameter can be adapted to the response of the system. Moreover, continuous variations are often easier to model.

In the *Makromolekulare Chemie I* department of the University of Bayreuth, an efficient evaporation technique for the combinatorial fabrication of organic and hybrid organic/inorganic thin-film devices has been developed [Sch99a, Sch99b]. Up to 64 organic light-emitting devices or solar cells with varying layers and layer thicknesses can be evaporated onto a single substrate. In this way, the influence of secondary parameters such as plasma etching of the anode layer, partial pressure of oxygen during TiO₂ evaporation or temperature variation during evaporation of the metal electrode is minimised, as these parameters are identical for all devices on the substrate. The use of such an approach seems very promising for any kind of low-molecular organic-compound devices and has been successfully applied to the optimisation of OLEDs [Sch99a, Sch99b, Sch00, The02]. In the recent past, the group of W. Riess at IBM R schlikon together with K. Neyts at the University of Ghent has adopted this experimental design for both experimental [Bei02, Rie03] and theoretical investigations [Ney98, Ney00] of OLEDs.

In this work, we are offering a number of improvements on the Bayreuth combinatorial approach: we have developed both hardware and software for a simultaneous and comparative analysis of OLEDs and thin-film solar cells in a controlled environment. In the case of organic solar cells, we have performed theoretical calculations for the thickness dependence of the photocurrent and we can claim to understand the processes involved in single and dual heterojunction devices both qualitatively and quantitatively.

3.2 Overview

In this section we will briefly set out the structure of this chapter; it is meant as a guide through the ensuing sections.

The propagation of optical waves plays an important role in the development of thin-film devices. First, it is essential for the functioning of the devices themselves, second, it is a necessary tool for the determination of the optical constants of newly synthesised materials. Therefore, the beginning of the chapter is devoted to the theory of optical-wave propagation in homogeneous media. In the subsequent section we apply this theory to the ellipsometric determination of refractive indices and extinction coefficients of different layer materials.

With this knowledge we turn to the combinatorial experiments that we have established for the combinatorial analysis of the thin-film devices. Exact knowledge of the film thickness in multi-layer systems is essential not only for the reliable fabrication of combinatorial device arrays but also for the quantitative analysis of the data. Scanning Force Microscopy

(AFM) is able to provide this information for single-layer devices and has been used for the calibration of the optical methods. But as it cannot, in a simple way, vertically resolve the difference between two materials and as it can be automated only with difficulty, we have decided to use two optical methods that are able to retrieve this information also for multi-layer systems. Spectroscopic ellipsometry is a reliable method if the substrates are highly reflective, e. g. silicon. Complementarily, UV/Vis spectrometry is the method of choice for transparent substrates.

Section 3.6 is dedicated to the description of the experimental setup that has been developed for the combinatorial short- and long-term study of multi-device arrays. Finally, we present experimental data together with a detailed analysis of solar cells and OLEDs. This part is divided into five subtopics: two performance and degradation studies of thin-film solar-cell arrays, a detailed analysis of the processes involved in double-heterojunction solar cells and two performance and degradation studies of OLEDs in vacuum and in inert gas atmosphere.

3.3 Optical-Wave Propagation in Thin Films

3.3.1 Transfer Matrix Formalism

The most efficient way of calculating the propagation of optical waves in thin films where multiple reflection occurs is the transfer matrix formalism. There are, of course, different textbooks on this subject, for instance [Hea65], and the topic has been discussed in various papers [Pet99, Peu03]. But as mistakes can be found even in very prominent literature, we will give a short summary here. Furthermore, this section can be understood as a theoretical guide to the Mathematica[®] code that has been developed in order to flexibly implement the theory in different applications and to visualise data and theory.

In contrast to recently published articles, we allow for a tilt angle of the beam to the surface normal. The reason for this is three-fold. First, we use the formalism for the evaluation of ellipsometry measurements, where the tilt angle is essential. Second, in this way we are able to calculate the influence of non-perpendicular irradiance and thus to better approximate natural conditions for solar cells. Last but not least, it is numerically sensible to calculate the field distribution starting from the electrical field at the illuminated surface, and not, as mostly done, from the back of the device: when investigating the influence of the electrode thickness, the results will be erroneous as soon as the transmission tends to zero. Numerical errors will propagate to the calculated field at the surface. The inverse case, i. e. the reflection vanishing completely, is highly improbable for glass-covered devices.

Depending on the ratio of the film thickness to the longitudinal coherence length of the light, the matrix transfer formalism can be used to calculate either the electric field or the intensity at an arbitrary position within the film. As the layer thickness in low-molecular organic-compound devices is mostly ≤ 200 nm and as the optical wavelengths and with them the coherence lengths are longer, we can safely assume coherent superposition of the reflected waves within the multi-layer system. We will therefore write the theory for electric fields and only once, when we come to propagation through the substrate, apply it to intensities. We always assume homogeneous media and hence optical coefficients that are independent of the direction of propagation. All solutions then have to be composed from plane waves or attenuated plane waves of the form

$$E(\mathbf{x}, t) = E_0 e^{i(n \mathbf{kx} - \omega t)} \quad (3.1)$$

with E_0 the amplitude of the electric field (mostly chosen to be real), n the (complex) refractive index, $\mathbf{k} = \frac{2\pi}{\lambda} \mathbf{e}$ the wave vector of the incident wave with \mathbf{e} the propagation direction, \mathbf{x} the position in the film and ω the frequency of the light. We note that later we will use $\mathbf{kx} = |\mathbf{k}| z \cos \alpha$ with z the vertical position in the film and α the tilt of the wave vector to the film normal. We further note that attenuation can be included by using a complex index of refraction as will be explained in more detail later in this chapter.

The basis of the matrix transfer formalism is that in planar multi-layer systems with homogeneous media Snellius' Law ensures that the angle at which light travels through the substrate only depends on the refractive index of the material and on the tilt angle of the incident beam to the surface normal. It is completely independent of the number of

reflections the beam has undergone and of the paths it has taken.

$$n_0 \sin \alpha_0 = n_i \sin \alpha_i \quad (3.2)$$

In the view of wave-particle duality, this law can be understood as the conservation of the momentum parallel to the film surface, which is a direct consequence of the translational invariance of the film geometry.

$$\hbar \mathbf{k}_{0\parallel} = \hbar \mathbf{k}_{i\parallel}, \quad (3.3)$$

because $|\mathbf{k}_{i\parallel}| = n_i |\mathbf{k}_0| \sin \alpha_i$. In a reflection experiment, we can therefore, at each vertical position in the film, decompose the amplitude of the electric field in a downwards and an upwards-travelling component (see Figure 3.1). This decomposition can be written as a two-element vector, which we will call the *field vector* or simply the *field*

$$\mathbf{E}_i = \begin{pmatrix} E_i^\downarrow \\ E_i^\uparrow \end{pmatrix}. \quad (3.4)$$

Note that \mathbf{E}_i is not a regular vector but a component vector, each element of which has an associated electrical field vector that depends on the tilt angle and on the polarisation via

$$\mathbf{E}^\downarrow = \begin{pmatrix} E_{i\parallel}^\downarrow \sin \alpha \\ -E_{i\parallel}^\downarrow \cos \alpha \\ E_{i\perp}^\downarrow \end{pmatrix} \quad \mathbf{E}^\uparrow = \begin{pmatrix} E_{i\parallel}^\uparrow \sin \alpha \\ E_{i\parallel}^\uparrow \cos \alpha \\ E_{i\perp}^\uparrow \end{pmatrix}, \quad (3.5)$$

where we denote the s- and p-polarisation with \perp and \parallel respectively.

It turns out that if the field-component vector is known at a single location of the film, the field at any other location can be calculated by the action of so-called *transfer matrices* upon the field vector.

$$\begin{pmatrix} E_j^\downarrow \\ E_j^\uparrow \end{pmatrix} = M_{ij} \cdot \begin{pmatrix} E_i^\downarrow \\ E_i^\uparrow \end{pmatrix} \quad \text{or} \quad \mathbf{E}_j = \mathbf{T}_{ij} \cdot \mathbf{E}_i \quad (3.6)$$

The two relevant processes are propagation and refraction at interfaces; hence, we need two types of matrices. The propagator matrix \mathbf{P}_i is nothing but a diagonal matrix with the time-independent part of the plane wave in the diagonal elements. The interface matrix \mathbf{T}_i follows from the interference of reflected and transmitted beams, as illustrated in Figure 3.1

$$\mathbf{P}_i = \begin{pmatrix} e^{i d_i n_i \cos(\alpha_i)} & 0 \\ 0 & e^{i d_i n_i \cos(\alpha_i)} \end{pmatrix} \quad (3.7)$$

$$\mathbf{T}_{ij} = \frac{1}{t_{ji}} \begin{pmatrix} t_{ij} t_{ji} - r_{ij} r_{ji} & r_{ij} \\ -r_{ji} & 1 \end{pmatrix}. \quad (3.8)$$

In the latter case, we have to take into account the polarisation of the beam. We do this by treating the \perp - and \parallel -polarisations separately, any other polarisation being a composition

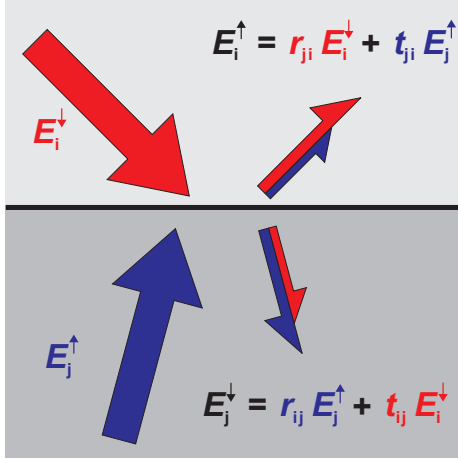


Figure 3.1: *Interface Matrix.* The direction of the arrows indicates the beam path, the size of the arrows indicates the amplitude of the electrical field. If the amplitudes of the incoming beams E_i^\downarrow and E_j^\uparrow are known, the amplitudes of the outgoing beams can be calculated as the sum of the reflected and transmitted beams. In matrix form, the two equations for the interfering beams yield:

$$\begin{pmatrix} E_j^\downarrow \\ E_i^\uparrow \end{pmatrix} = \frac{1}{t_{ji}} \begin{pmatrix} t_{ij} t_{ji} - r_{ij} r_{ji} & r_{ij} \\ -r_{ji} & 1 \end{pmatrix} \cdot \begin{pmatrix} E_i^\downarrow \\ E_j^\uparrow \end{pmatrix}$$

of these two. The reflectivities and transmissibilities for the fields are then given by the *Fresnel formulae*

$$\begin{aligned} t_{ij\perp}(n_i, n_j, \alpha_i) &= \frac{2 n_i \cos(\alpha_i)}{n_i \cos(\alpha_i) + \frac{\mu_i}{\mu_j} \sqrt{n_j^2 - n_i^2 \sin^2(\alpha_i)}} \\ r_{ij\perp}(n_i, n_j, \alpha_i) &= \frac{n_i \cos(\alpha_i) - \frac{\mu_i}{\mu_j} \sqrt{n_j^2 - n_i^2 \sin^2(\alpha_i)}}{n_i \cos(\alpha_i) + \frac{\mu_i}{\mu_j} \sqrt{n_j^2 - n_i^2 \sin^2(\alpha_i)}} \\ t_{ij\parallel}(n_i, n_j, \alpha_i) &= \frac{2 n_i n_j \cos(\alpha_i)}{\frac{\mu_i}{\mu_j} n_j^2 \cos(\alpha_i) + n_i \sqrt{n_j^2 - n_i^2 \sin^2(\alpha_i)}} \\ r_{ij\parallel}(n_i, n_j, \alpha_i) &= \frac{\frac{\mu_i}{\mu_j} n_j^2 \cos(\alpha_i) - n_i \sqrt{n_j^2 - n_i^2 \sin^2(\alpha_i)}}{\frac{\mu_i}{\mu_j} n_j^2 \cos(\alpha_i) + n_i \sqrt{n_j^2 - n_i^2 \sin^2(\alpha_i)}} \end{aligned} \quad (3.9)$$

for two successive layers, i and $j = i + 1$. n_i is the refractive index of the medium i and μ_i is the relative magnetic permeability, which can be assumed to be 1 for organic materials and optical frequencies. α_i is the tilt angle of the beam to the surface normal in the respective medium and follows from Snellius' Law (see Equation 3.2).

$$\alpha_i = \arcsin\left(\frac{n_0}{n_i} \sin(\alpha)\right) \quad (3.10)$$

Using the general properties of the Fresnel coefficients $r_{ij} = -r_{ji}$ and $t_{ij} t_{ji} - r_{ij} r_{ji} = 1$, Equation 3.8 can be simplified to give

$$\mathbf{T}_{ij} = \frac{1}{t_{ji}} \begin{pmatrix} 1 & r_{ji} \\ r_{ji} & 1 \end{pmatrix}. \quad (3.11)$$

With this result, we can calculate the electric field after traversing a stack of layers with n interfaces by applying the respective transmission and propagator matrices on the initial

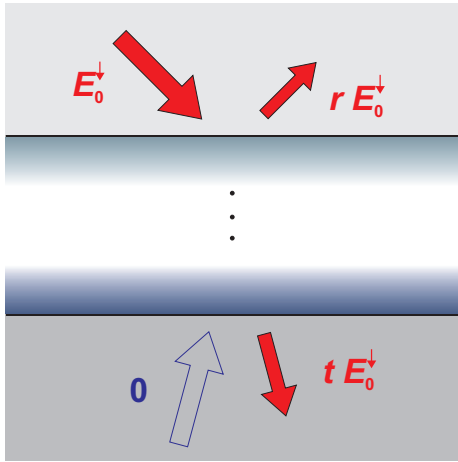


Figure 3.2: *Total Transfer Matrix.* In a classic reflection experiment we can exclude any contribution to the upwards-travelling component from the bottom layer. We can therefore write the following equation for the total reflectivity and transmissibility

$$\begin{pmatrix} t E_0^\downarrow \\ 0 \end{pmatrix} = \mathbf{T}_{\text{tot}} \cdot \begin{pmatrix} E_0^\downarrow \\ r E_0^\uparrow \end{pmatrix} \quad \mathbf{T}_{\text{tot}} = \begin{pmatrix} T_{11} & T_{12} \\ T_{21} & T_{22} \end{pmatrix} \quad (3.14)$$

field vector \mathbf{E}_0

$$\mathbf{E}_n = \mathbf{T}_{\text{tot}} \cdot \mathbf{E}_0 \quad (3.12)$$

$$\mathbf{T}_{\text{tot}} = \mathbf{T}_{(n-1)n} \cdot \mathbf{P}_{n-1} \cdots \mathbf{T}_{12} \cdot \mathbf{P}_1 \cdot \mathbf{T}_{01}. \quad (3.13)$$

Exploiting the fact that there is no upwards-travelling component in the bottommost layer (Figure 3.2), we can derive the total reflectivity and transmissibility by solving the linear equation 3.14.

$$r = -\frac{T_{21}}{T_{22}} \quad t = T_{11} - \frac{T_{12} T_{21}}{T_{22}} \quad (3.15)$$

with the total reflectivity r and transmissibility t .

Absorbing media can be included in this formalism by passing to a complex index of refraction, as the underlying equations (3.9 and 3.2) all hold [Jac75] for complex refractive indices²

$$n \rightarrow \tilde{n} = n + i k \quad (3.16)$$

n classic refractive index
 k extinction coefficient.

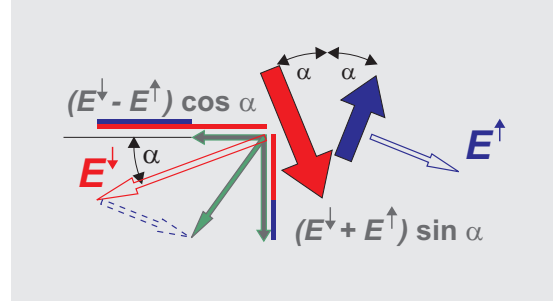
Note that we distinguish between the extinction coefficient k and the absolute value of the wave vector $|\mathbf{k}|$.

Now that we know the field strength E_0 of the incident beam, we are able to calculate the field vector \mathbf{E} at the first interface

$$\mathbf{E}_0 = E_0^\downarrow \begin{pmatrix} 1 \\ r \end{pmatrix}, \quad (3.17)$$

²Depending on the sign convention chosen for the plane wave the complex refractive index is defined as $n + i k$ or $n - i k$. We prefer to write the plane wave as $E = E_0 \exp(i(kx - \omega t))$ in formal analogy to the free-particle wave. With this convention the sign in the exponential function of the propagator matrix will be opposite to what can be found in some textbooks.

Figure 3.3: *Electrical-field decomposition for a p-polarised beam. The electrical-field vectors (empty arrows) lie in the plane of incidence, perpendicular to the direction of propagation (filled arrows). The green arrows indicate the projections of the total electrical field onto the surface normal and onto the film surface.*



and thus the field at an arbitrary position in layer j

$$\mathbf{E}(z) = \mathbf{T}(z) \cdot \mathbf{E}_0 \quad (3.18)$$

$$\mathbf{T}(z) = \mathbf{P}_j(z - \sum_{i=1}^{j-1} d_i) \cdot \mathbf{T}_{(j-1)j} \cdot \mathbf{P}_{n-1} \cdots \mathbf{T}_{12} \cdot \mathbf{P}_1 \cdot \mathbf{T}_{01} . \quad (3.19)$$

Finally, we calculate the absolute square $|E(z)|^2$ of \mathbf{E} , as this term will finally enter into the exciton generation rate. We have to bear in mind that \mathbf{E} is not a regular vector and that the geometry of the field components depends on the polarisation. For the \perp -polarised beam, the vector of the electric field lies in the plane of the film; hence, the two fields of upwards- and downwards-travelling waves simply add. For \parallel -polarised beams, we first calculate the projections of the electric field onto the surface normal and onto the film surface and then add their absolute squares. This can be seen geometrically from Figure 3.3, or numerically from Equation 3.5.

$$|\mathbf{E}(z)|_{\uparrow\downarrow}^2 = |E(z)|^2 = \begin{cases} \perp & : |E^\downarrow + E^\uparrow|^2 \\ \parallel & : |(E^\downarrow - E^\uparrow) \cos \alpha|^2 + |(E^\downarrow + E^\uparrow) \sin \alpha|^2 \end{cases} \quad (3.20)$$

Note that we have introduced the notation $|\cdot|_{\uparrow\downarrow}$ to distinguish the absolute value of component vectors from that of regular vectors.

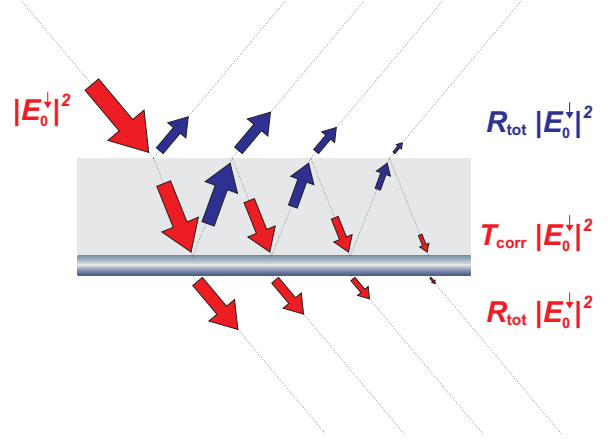
3.3.2 Substrate Correction

Until now, we have neglected any reflection from the back of the substrate, which can occur if the substrate is transparent or semi-transparent. To include the substrate layer we cannot use the matrix formalism in the form presented, as the coherence length of the illumination lamp or the sunlight is shorter than the thickness of the substrate. The fact that the substrate surfaces are neither exactly parallel nor planar further decreases the coherence. For incoherent beams, however, the squares of the electric field add instead of the fields themselves. It is therefore reasonable to define reflectivities and transmissibilities for $|E|^2$, which follow straight-forwardly from the Fresnel coefficients.

$$R = |r|^2 \text{ and } T = |t|^2 . \quad (3.21)$$

We could now use the matrix formalism by substituting $r \rightarrow R, t \rightarrow T$ in Equation 3.1 using the general properties $R_{ij} = R_{ji}$ and $T_{ij} T_{ji} = |1 - r_{ij}^2|^2$ and $P \rightarrow |P|^2$. We tend,

Figure 3.4: *Substrate Correction.* There are three cases of interest where $|E^2|$ can be comfortably obtained by a superposition argument: (a) total reflection R_{tot} , (b) transmission up to the interface between substrate and film T_{corr} , and (c) total transmission T_{tot} . In all cases, the geometric series helps to determine the total field.



however, to derive the required correction directly from a superposition argument, as the matrix formalism is a little bulky for a two-interface problem.

Figure 3.4 shows that the downwards-travelling wave at the substrate/film interface is a superposition of multiply reflected waves

$$|E_0^{\text{corr}}|^2 = |E_0|^2 T_{\text{as}} \beta (1 + R R_{\text{as}} \beta^2 + (R R_{\text{as}} \beta^2)^2 + (R R_{\text{as}} \beta^2)^3 + \dots). \quad (3.22)$$

with the absorption along a single pass through the substrate layer given by

$$\beta = e^{-2|\mathbf{k}|d_s \text{Im}(\tilde{n}_s \cos \alpha)} \quad \text{or} \quad \beta = e^{-2k_s |\mathbf{k}|d_s} \quad \text{for } \alpha = 0. \quad (3.23)$$

Exploiting the geometric series

$$\sum_{i=0}^{\infty} x^i = \frac{1}{1-x}, \quad (3.24)$$

we find

$$|E_0^{\text{corr}}|^2 = |E_0|^2 \frac{T_{\text{as}} \beta}{1 - R R_{\text{as}} \beta^2}, \quad (3.25)$$

where the indices ‘a’ and ‘s’ denote ‘air’ and ‘substrate’. The matrices of the thin-film structure and the corresponding coefficients r , R , and T have now to be calculated with the substrate material as the top layer.

Putting equations 3.17, 3.18, and 3.25 together, we can write the field \mathbf{E} as a function of the position z

$$\mathbf{E}(z) = \mathbf{T}(z) \cdot \begin{pmatrix} 1 \\ r \end{pmatrix} \cdot E_0 \sqrt{\frac{T_{\text{as}} \beta}{1 - R R_{\text{as}} \beta^2}} \quad (3.26)$$

In complete analogy, the total reflection and total transmission evaluate to

$$R_{\text{tot}} = R_{\text{as}} + \frac{T_{\text{as}} R T_{\text{sa}} \beta^2}{1 - R R_{\text{as}} \beta^2} \quad (3.27)$$

$$T_{\text{tot}} = \frac{T_{\text{as}} T \beta}{1 - R R_{\text{as}} \beta^2}. \quad (3.28)$$

3.3.3 Absorption, Exciton Generation and Photo Current

In Chapter 3.9 we will need an expression for the exciton generation probability. We will therefore briefly deduce the required expressions.

With the knowledge of the previous chapter, we have all the instruments to describe $|E(\mathbf{x})|$ at any location in the film. We can therefore easily determine the associated energy flux, called *irradiance* or *intensity*

$$I(z) = \frac{n \epsilon_0 c}{2} |E(z)|^2 \quad (3.29)$$

with ϵ_0 the dielectric constant, c the speed of light and n the real part of the refractive index $n = \text{Re}(\tilde{n})$.

The local absorption rate is expected to be proportional to the photon flux and hence to the intensity. To derive the proportionality constant, we consider a plane wave travelling through an absorbing medium, i. e. a medium with a non-vanishing imaginary part of the refractive index $k = \text{Im}(\tilde{n})$. The intensity distribution follows directly from 3.1 and 3.29

$$I(z) = \frac{n \epsilon_0 c}{2} |E(z_0)|^2 e^{-2 k |\mathbf{k}| (z-z_0)} = I(z_0) e^{-2 k |\mathbf{k}| (z-z_0)}. \quad (3.30)$$

We note that by comparing this equation with the Lambert-Beer Law

$$I(z) = I(z_0) e^{-\alpha (z-z_0)} \quad (3.31)$$

with α the absorption coefficient, we obtain the following relation:

$$\alpha = 2 k |\mathbf{k}| = \frac{4\pi}{\lambda} k. \quad (3.32)$$

Due to this close connection the words *extinction coefficient* and *absorption coefficient* are often used interchangeably.

The power absorption in the medium $Q(z)$ is then given by the derivative of the energy flux

$$Q(z) = \left| \frac{\partial}{\partial z} I(z) \right| = n k |\mathbf{k}| \epsilon_0 c |E(z)|^2. \quad (3.33)$$

Dividing $Q(z)$ by the photon energy leads to the photon absorption rate. For excitonic absorption, this quantity can be identified with the exciton generation rate $G(z)$

$$G(z) = \frac{Q(z)}{\hbar \omega}, \quad (3.34)$$

which can be further evaluated to

$$G(z) = n k \frac{\epsilon_0}{\hbar} |E(z)|^2 \text{ or} \quad (3.35)$$

$$G(z) = k \frac{2}{\hbar c} I(z). \quad (3.36)$$

Often it proves useful to normalise the exciton generation rate to the incident photon flux $\Phi = \frac{I_0}{\hbar\omega}$, which is then called *exciton generation efficiency* or sometimes *absorption efficiency*

$$\eta_{EG}(z) \equiv \eta_A = \frac{G(z)}{\Phi} = 2k|\mathbf{k}| \frac{I(z)}{I_0} = 2nk|\mathbf{k}| \frac{|E(z)|^2}{|E_0|^2}, \quad (3.37)$$

which can be further evaluated to

$$\eta_{EG}(z) = 2nk|\mathbf{k}| \frac{T_{as}\beta}{1 - RR_{as}\beta^2} \left| \mathbf{T}(z) \cdot \begin{pmatrix} 1 \\ r \end{pmatrix} \right|_{\uparrow\downarrow}^2. \quad (3.38)$$

The total exciton generation rate can now be calculated by integrating η_{EG} over all wavelengths weighed with the spectral photon flux density $\phi(\lambda)$, which can be obtained from the spectral power distribution $S(\lambda)$ by division by $\hbar\omega$.

$$G_{EG}^{tot}(z) = \int_0^\infty \eta_{EG}(z) \phi(\lambda) d\lambda = \int_0^\infty \eta_{EG}(z) \frac{S(\lambda)}{\hbar\omega} d\lambda \quad (3.39)$$

With 3.38, this equation yields

$$G_{EG}^{tot}(z) = \int_0^\infty 2nk \frac{S(\lambda)}{\hbar c} \frac{T_{as}\beta}{1 - RR_{as}\beta^2} \left| \mathbf{T}(z) \cdot \begin{pmatrix} 1 \\ r \end{pmatrix} \right|_{\uparrow\downarrow}^2 d\lambda. \quad (3.40)$$

Finally, we have to pay attention to the course of the excitons after their generation, as the excitons need to be separated in order to contribute to the current. In a very general way we may write the short-circuit current as

$$I_{SC}(\lambda, z) = qA G(\lambda, z) \eta_{ED}(z) \eta_{CT} \eta_{CC}, \quad (3.41)$$

with q the elementary charge, A the device surface, η_{ED} the efficiency for exciton diffusion to a charge-separating surface, η_{CT} the charge transfer efficiency, and η_{CC} the charge-collection efficiency. In the last equation we have written $G(\lambda, z)$ rather than $G(z)$ to emphasise the wavelength dependency.

With the last two equations we have the prerequisites necessary to discuss the film thickness dependency of the short-circuit current. This will be done in Chapter 3.9.

3.4 Ellipsometry

3.4.1 Introduction

Ellipsometry is the study of the reflectivity of thin films. It takes advantage of the difference in reflection for the s(\perp)- and p(\parallel)-polarised beam when light is reflected by a stack of coplanar layers. With such reflectivity measurements it is possible not only to retrieve the optical properties of materials but also to determine the individual thickness of layers in a multi-layer system.

In this chapter we present ellipsometry measurements for the materials used in our solar cells. We determine the optical constants of the glass substrate, TiO₂, CuPc, and of DMPTI. Furthermore, we use the optical constants to determine the layer thickness of two perpendicular gradients of CuPc and DMPTI on glass. For this purpose, we have automated the ellipsometer to take spectra at a rectangular array of points.

3.4.2 Theory

In ellipsometry the reflectivity is typically characterised by two angles Ψ and Δ that are a measure of the transmission ratio and relative phase difference for the s- and p-polarised beam. In the previous chapter, we have established the theory for the calculation of the reflection and transmission coefficients for electrical fields $r_{\perp}, r_{\parallel}, t_{\perp}, t_{\parallel}$ (Equation 3.15). These coefficients can be complex, meaning that the reflected and transmitted waves are not only attenuated by $|r|$ or $|t|$ but also undergo a phase shift $\arg(r)$ or $\arg(t)$. With these definitions, the characteristic angles of ellipsometry read as follows:

$$\Psi = \arctan \left(\left| \frac{r_{\parallel}}{r_{\perp}} \right| \right) \quad (3.42)$$

$$\Delta = \arg \left(\frac{r_{\parallel}}{r_{\perp}} \right). \quad (3.43)$$

Both angles vary with the incident angle and, of course, with the wavelength as the refractive index is dependent on the wavelength. For the evaluation of the ellipsometric data, a theoretical prediction for Ψ and Δ is made on the basis of the optical parameters and the film thickness and the result is then compared with the measurement.

3.4.3 Experimental

For all of our measurements, we have used a variable-angle spectroscopic ellipsometer *Sentech 850* which is able to determine Ψ and Δ for the whole visible range simultaneously. The accessible angle ranges from 40 to 70 degrees. The measurements are typically performed in the range between 350 and 850 nm and at angles of 40, 50, 60, and 70 degrees. The sample position can be electronically controlled. In order to adapt the operation mode

of the ellipsometer to the combinatorial arrays, we have developed a macro-package on the basis of the accompanying script language that allows the automated measurement at a definable rectangular grid. As the spectra have to be taken at locations without electrode (see Figure 3.21), the positioning of the sample is a tedious task. With the automated measurement, this positioning needs to be done only for two diagonally opposite spots, which saves a lot of time. Furthermore, the integration times can be set to higher values to improve the signal-to-noise ratio. In this way, the experimenter's time is reduced from one working day to less than an hour. With the same macro-language, we have automated the evaluation of the spectra, using the built-in algorithms of the ellipsometer software. Alternatively, we have used our Mathematica[®] package for an evaluation at single wavelengths.

3.4.4 Determination of Optical Constants

As discussed in the previous chapter, the reflectivity of a multi-layered film depends on a variety of parameters: the incident angle, the layer thicknesses, the optical properties of the materials, and, with the latter two, on the wavelength. In general, it is therefore impossible to determine all of these parameters from a single measurement.

However, for certain substances, such as polymers or glassy substances with negligible absorption, the wavelength dependence of the refractive index can be described by the *Cauchy dispersion relation* [Bor99]

$$n(\lambda) = n_0 + \frac{n_1}{\lambda^2} + \frac{n_2}{\lambda^4} \quad (3.44)$$

$$k(\lambda) = 0.$$

In the case of non-resonant absorption, the model can be enhanced by an absorption term³

$$k = \frac{k_0}{\lambda} + \frac{k_1}{\lambda^3} + \frac{k_2}{\lambda^5}. \quad (3.45)$$

If the refractive index is properly described by a Cauchy model, it is often possible to determine both the layer thickness and the index of refraction of the substance with a variable angle measurement. The optical constants of the substrate must, of course, be known. The refractive index of the substrate itself can also be determined in this way. For the glass of the Merck ITO substrates we found

$$n_{glass} = 1.482 + \frac{147.8 \cdot 10^2 \text{ nm}^2}{\lambda^2} + \frac{68.7 \cdot 10^7 \text{ nm}^4}{\lambda^4}. \quad (3.46)$$

³In the literature one sometimes finds the coefficients k_i defined with the same wavelength dependency as n_i . In the software accompanying the ellipsometer the predefined Cauchy layers also follow this convention. Due to symmetry arguments, however, $n(\lambda)$ and $k(\lambda)$ need to be even and odd functions, respectively. We therefore chose an odd series in λ for the extinction coefficient.

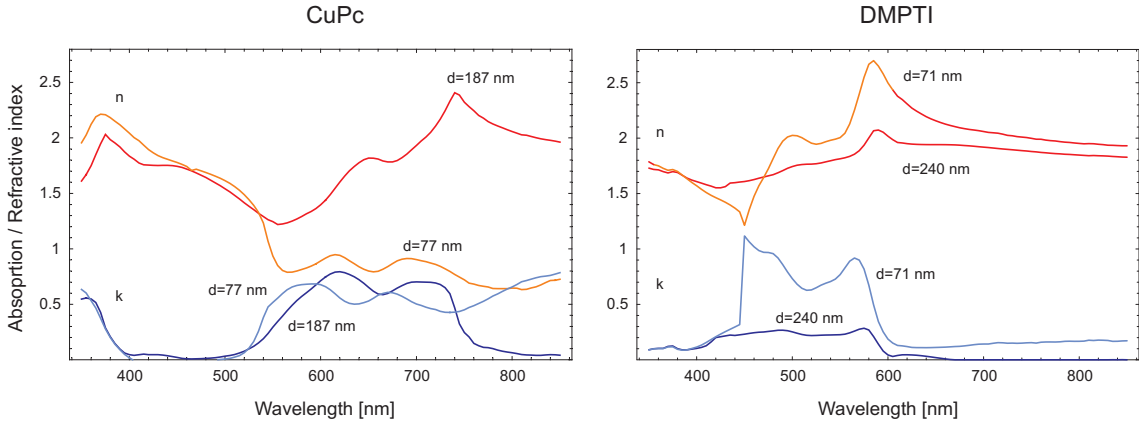


Figure 3.5: *Extinction coefficient and refractive indices of CuPc and DMPTI as obtained from a point-to-point fit on samples of different thickness (CuPc: 77 nm and 187 nm, DMPTI: 71 nm and 240 nm). The substrate was a silicon wafer with a natural oxide layer of 2.9 nm.*

which nearly coincides with the data for a *Schott BK7* glass. Similarly, Titanium dioxide was fitted with an extended Cauchy model

$$\begin{aligned}
 n_{TiO_2} &= 2.206 + \frac{-322.1 \cdot 10^2 \text{ nm}^2}{\lambda^2} + \frac{714.0 \cdot 10^7 \text{ nm}^4}{\lambda^4} \\
 k_{TiO_2} &= \frac{8.968 \cdot 10^2 \text{ nm}^2}{\lambda} + \frac{100.1 \cdot 10^7 \text{ nm}^4}{\lambda^3} + \frac{170.3 \cdot 10^7 \text{ nm}^4}{\lambda^5}
 \end{aligned} \tag{3.47}$$

The measurements of the glass substrates were carried out at spots where the ITO had been chemically etched away; to determine the optical constants of the layer materials, we used silicon substrates with a 2.9 nm thick oxide layer as these provide high reflectivity and thus a good signal-to-noise ratio.

For materials that exhibit resonant absorption within the spectroscopic range of the measurement, the Cauchy model will fail to properly describe the optical constants. Instead, one can use a point-to-point fitting algorithm that, at each wavelength, calculates the optimal solution for n and k . For this approach to work the layer thickness has to be determined by a different method and to be plugged into the model. We determined the layer thickness at the border of a scratch with a scanning force microscope *Dimension 3100* of *Veeco Digital Instruments*, typical statistical errors being in the order of ± 5 nm. This approach can produce smooth curves for n and k . Varying the film thickness in the order of the error of the AFM measurement is sometimes necessary. In doing this fitting procedure for films of different layer thickness, however, we found that the fits would only partially coincide in the short-wavelength range (Figure 3.5). The origin of this finding is twofold. One reason is that with such a complex parameter space, the algorithm may not find the physically correct minimum but instead follows a local optimum branch in the parameter space. This is the case for the high absorption in the long-wavelength range of CuPc and also for the discontinuity in the absorption curve of the 71 nm DMPTI sample. The high-absorption branch is obviously non-physical, as can be seen by comparison with

Material	CuPc	DMPTI
d_1	187 nm	108 nm
d_2	77 nm	72 nm
n ($\lambda = 405$ nm)	1.780	1.541
k ($\lambda = 405$ nm)	0.0434	0.124

Table 3.1: *Optical constants for DMPTI and CuPc determined for a wavelength of 405 nm from simultaneous fits on two samples of different thickness (d_1 and d_2). The wavelength has been chosen so that both materials show absorption but nevertheless differ in their optical properties.*

the absorption spectra 3.18 of thin films. We had hoped to circumvent this problem by including measurements of samples with different layer thickness in a single fit routine. For this purpose, we developed a Mathematica[®] program that can accomplish such a global fit. Unfortunately, the resulting fits did not seem sufficiently trustworthy over the whole spectral range.

This directs us to the second, more fundamental origin of the differences, the non-homogeneity of the layer materials. As both of the dye molecules employed possess planar symmetry and show a tendency towards crystallisation, assuming an optically isotropic material is justified only in the absence of any directional ordering of the molecules. The different optical properties observed for different films can therefore originate either from local inhomogeneities or from a surface-induced orientation. In the latter case, the substrate material and the layer thickness will enter as additional parameters as will preparation conditions such as evaporation rate and substrate temperature. As the spot of the ellipsometer is about 2 mm in size and as we see nearly identical Δ and Ψ curves at different locations of a sample, we can exclude large-scale inhomogeneities.

Systematically studying the molecular orientation as a function of the substrate material and film thickness would go beyond the scope of this work. Instead we decided to use a pragmatic approach.

To determine layer thicknesses, it is sufficient to know the optical properties at a single wavelength. We therefore picked a wavelength (405 nm) where the point-to-point fits of samples with different thicknesses nearly coincide and where the two materials significantly differ in their optical properties. The values of n and k presented in Table 3.1 are the results from simultaneous fits on two samples of different layer thickness. To determine the spectral dependence of the optical properties we used models to describe an *effective refractive index* and an *effective extinction coefficient* that would cover the influence of polycrystallinity or coexistence of different modifications. This approach will fail if there is a high optical anisotropy of the monocrystalline material together with a preferential ordering of the crystallites. It turns out that the substrate and thickness dependence in parts of the visible spectrum prevents us from using the results for thickness measurements. Nevertheless, the results can safely be used for the calculation of the optical field in multi-layer structures, since the absolute intensities are much less sensitive to changes in n and k than the relative intensities and phase shifts reflected by Ψ and Δ .

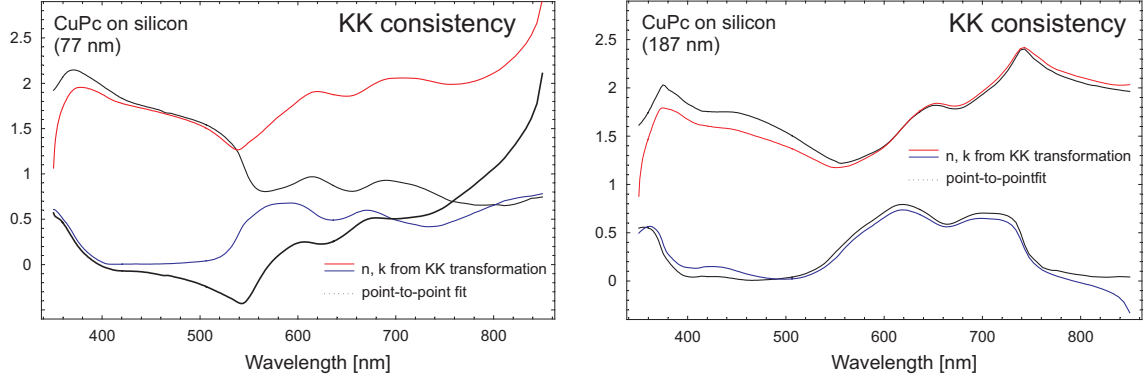


Figure 3.6: *Extinction coefficient and refractive indices of 77 nm and 187 nm CuPc films on silicon as obtained from a point-to-point fit together with the respective Kramers-Kronig transforms. In the case of the 77 nm film, the n - and k -spectra are not KK-consistent and the solution must be discarded.*

We have already described the mathematical problems of a point-to-point fitting algorithm. A very general relation between the extinction coefficient and the refractive index, the so-called *Kramers-Kronig relations* [Kra27, Kro26], can be of some help in this context

$$n = n_{\infty} + \frac{2}{\pi} \int_0^{\infty} \frac{k(\omega') \omega'}{\omega'^2 - \omega^2} d\omega' \quad (3.48)$$

$$k = -\frac{2\omega}{\pi} \int_0^{\infty} \frac{n(\omega') - n_{\infty}}{\omega'^2 - \omega^2} d\omega'. \quad (3.49)$$

In a discrete approximation, the above equations read

$$n(\omega_i) = n_{\infty} + \frac{2}{\pi} \sum_{j \neq i} \frac{k(\omega_j) \omega_j}{\omega_j^2 - \omega_i^2} \Delta\omega_j \quad (3.50)$$

$$k(\omega_i) = -\frac{2\omega_i}{\pi} \sum_{j \neq i} \frac{n(\omega_j) - n_{\infty}}{\omega_j^2 - \omega_i^2} \Delta\omega_j. \quad (3.51)$$

These relations intimately connect n and k and are not necessarily fulfilled by solutions of a point-to-point algorithm. Figure 3.6 impressively shows the strength of this relation. The point-to-point solution for the 77 nm CuPc must be discarded, whereas the point-to-point result for the 187 nm sample reasonably coincides with the respective KK transforms. The deviations at the interval borders are due to our neglecting higher and lower-lying transitions. They are inevitable if one is restricted to a certain wavelength range.

There are two general approaches to obtaining solutions that satisfy the Kramers-Kronig (KK) relations: global fitting routines that incorporate these complex relations on the one hand and fitting models for n and k that intrinsically satisfy the KK restrictions on the other. For the first to work, the reflectivity has to be known over a broad spectral range, which presents a serious drawback. The latter have been extensively studied for

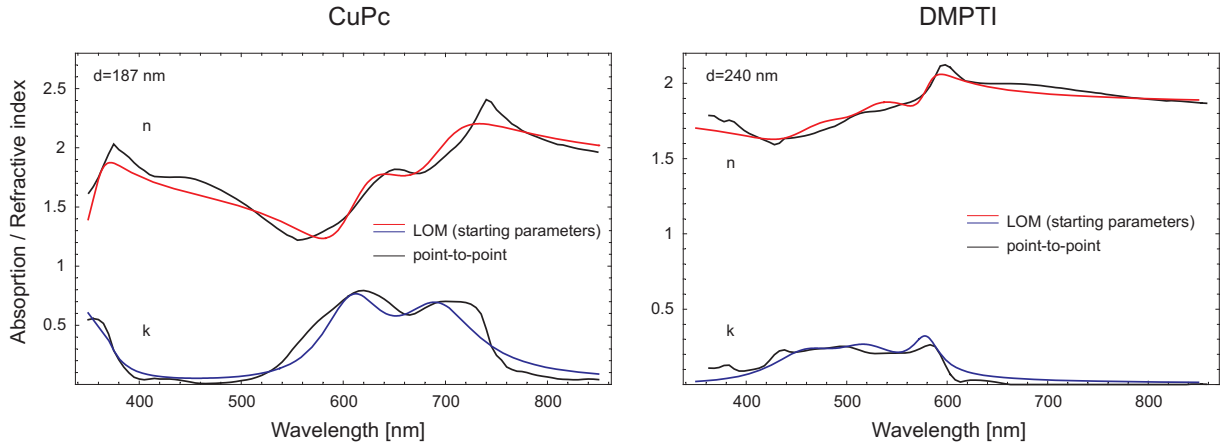


Figure 3.7: *Point-to-point fitting results and Lorentz-Oscillator Model (LOM) for n and k . The LOM parameters have been adjusted to best fit the point-to-point solution. These parameters serve as starting parameters for subsequent LOM fits.*

inorganic materials that exhibit band gaps and absorption edges. For organic materials, they have been investigated more intensively only in the recent past, as interest in organic optoelectronic devices has increased. The empiric *Lorentz-Oscillator Model* (LOM) is such a model and it is often applied for modelling the excitonic absorption of organic materials. The LOM treats the electrons of a material as the sum of resonating oscillators, leading to the following solution for the complex dielectric constant [Jel93]

$$\epsilon_{\text{LOM}}(\omega) = \epsilon_{\infty} + \sum_{j=1}^N \frac{f_j}{\omega_j^2 - \omega^2 - i\omega\Gamma_j}, \quad (3.52)$$

where ω is the frequency of the light and the ω_j are resonance frequencies. The parameters f_j and Γ_j are the respective oscillator strengths and the damping factors. To calculate the refractive index from this equation we recall that

$$n + ik = \sqrt{\mu\epsilon} \approx \sqrt{\epsilon} \quad (3.53)$$

The assumption $\mu \approx 1$ is valid for most organic substances at optical frequencies.

Although there are more sophisticated modifications of this model [Fra96, Dju00, Dju02] that take into account the non-Lorentzian shape of organic absorption lines originating from the vibronic structure, we decided to employ the simple LOM. In cases where the convergence did not seem sufficient, we used a piecewise LOM fit. For CuPc, ellipsometry studies of CuPc films on glass have shown that the LOM model can be reasonably applied to films deposited at room temperature [Dju02]. For DMPTI the situation is slightly different, as we will shortly see.

To find good starting points for a LOM fit, we chose resonance frequencies at the absorption peaks and fitted the LOM to the point-to-point fits of CuPc (187 nm) and DMPTI (240 nm). The results are depicted in Figure 3.7. In the following we will discuss the fitting efforts on CuPc and DMPTI separately.

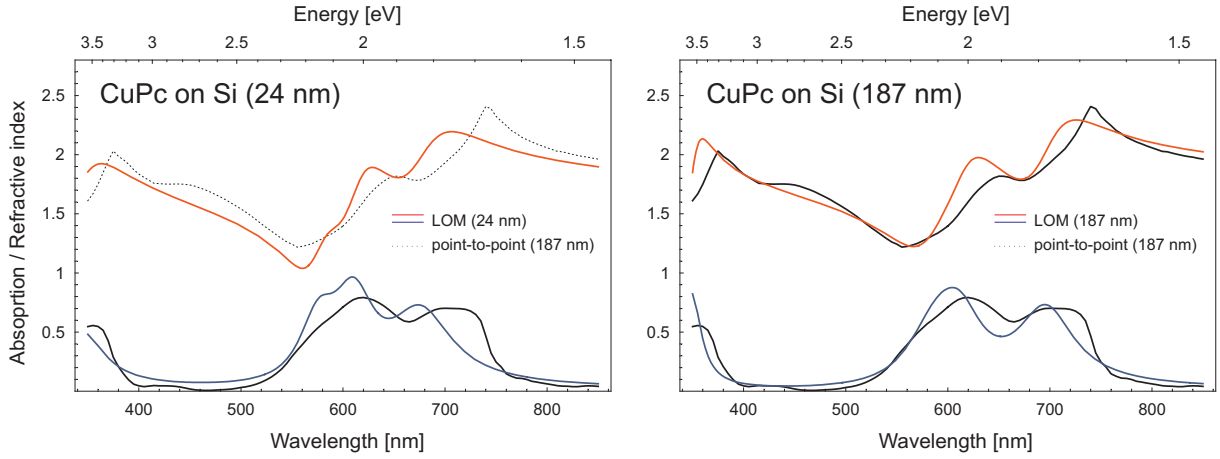


Figure 3.8: LOM fits to a 24 nm and to a 187 nm thick CuPc film on silicon. The changes in the spectra indicate that the morphology of the film and with it the effective optical properties depend on the film thickness.

Material	CuPc (24 nm)	CuPc (187 nm)
ϵ_∞	2.30	2.89
ω_1 [eV]	1.8216	1.7698
f_1 [eV ²]	0.8551	0.7567
Γ_1 [eV]	0.1897	0.1614
ω_2 [eV]	2.0175	2.0132
f_2 [eV ²]	0.7411	0.4940
Γ_2 [eV]	0.1494	0.1565
ω_3 [eV]	2.1378	2.0762
f_3 [eV ²]	0.3504	0.7311
Γ_3 [eV]	0.1466	0.2362
ω_4 [eV]	3.5750	3.5358
f_4 [eV ²]	3.1400	2.4112
Γ_4 [eV]	0.5162	0.2264
ω_5 [eV]	4.5326	5.1394
f_5 [eV ²]	15.720	18.668
Γ_5 [eV]	0.0908	0.0832

Table 3.2: Fitting parameters of a 5-Lorentz-oscillator model for two samples with different CuPc-layer thickness

Optical Constants of CuPc

Starting from the LOM solutions displayed in Figure 3.7 we have used the *Sentech* evaluation software for optimising the LOM parameters over the whole spectral range (350–850 nm). To investigate if there is any thickness dependence of the optical properties, we have fitted a 5-oscillator LOM to both a 24 nm and a 187 nm thick CuPc layer on silicon where the thickness was determined by AFM, as mentioned above. The resulting model

parameters are listed in Table 3.2 and the corresponding curves are shown in Figure 3.8. For comparison, we have in both cases added the point-to-point fit of the 187 nm sample. We see that the absorption peaks of the 24 nm film are slightly shifted to lower wavelengths or higher energy. Furthermore, the LOM model for the thinner film exhibits an additional absorption peak at 580 nm (2.14 eV). The importance of this peak is a little surprising and may be a fitting artefact. We note, however, that the peak position coincides with a weak peak in the UV/Vis absorption spectrum 3.18. To test the fitting results further, we take a closer look at Δ and Ψ . The upper four graphs (A,B) in Figure 3.9 show the data and model predictions of the 187 nm LOM fit; the lower four graphs (C, D) include the prediction of the 24 nm LOM fit. In both cases we first display the data the model was fitted to.

We find that for the 187 nm film the fitted curves follow the data reasonably closely (A). Some deviations arise between 400 nm and 600 nm for large incident angles. By fitting this model to the 24 nm sample by varying only the layer thickness, we obtain a good agreement with the measurement, the only questionable part being the region around 580 nm (B). A still better agreement is obtained by the 24 nm LOM fit for the 24 nm sample (C). However, the prediction of this model for the 187 nm sample is poor, particularly around 410 nm and 550 nm (D).

We conclude that there are small variations in the optical properties for films of different thickness, particularly around 580 nm, and we may speculate that they originate from a preferential orientation of the crystallites close to the surfaces. As CuPc possesses an α - and a β -modification, the difference could also arise from a different ratio of the two phases. Alternatively, we could imagine that the molecules form aggregates by stacking without forming true crystals, which could also lead to anisotropic optical properties. In any of these cases the macroscopic anisotropy is expected to be surface induced. Hence, the influence of such anisotropy should be less important for thicker films and the respective fitting results should therefore reflect the effective optical properties of an polycrystalline, but macroscopically isotropic phase. Since the shape of k is very similar to the absorption spectrum of the α -modification, we assume that the film mainly consists of polycrystalline α -CuPc.

We note that we had to use a Lorentz-oscillator model to be able to fit the thin layer samples, as the point-to-point algorithm would not converge towards a KK-consistent solution. The fit to the 24 nm sample may overemphasise the optical changes in the film, due to the nature of the Lorentz-oscillator model. We further note that for thin samples errors in the alignment or in the calibration of the instrument will more importantly influence the fitting results, as the shape of Δ and Ψ is much less pronounced. This consideration and the comparison of our results with the findings of other groups [Bar75, Deb92, Fra96, Dju02, Stü02] lead us to accept the 187 nm LOM model for further calculations. We have done so, although in the setup of the photovoltaic cell presented in chapters 3.7, 3.8, and 3.9 the films are only 20–40 nm thick. The reason is that we do not know whether there is any preferential orientation of CuPc on top of a DMPTI layer and whether the thin films will exhibit any variations in the optical properties.

We are thus led to the question of how much the optical properties are influenced by the substrate material. We therefore evaporated a 81 nm thick layer of CuPc simultaneously

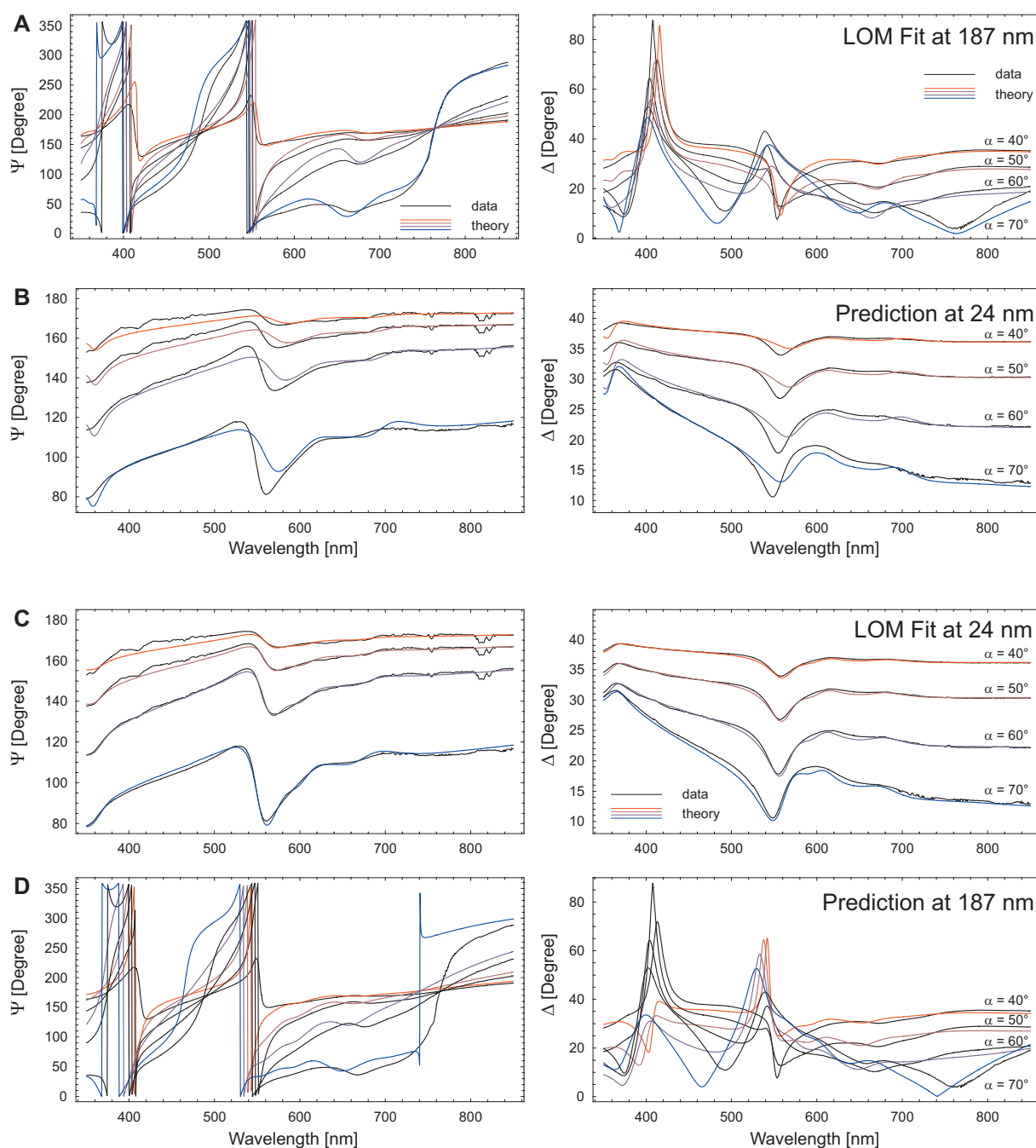


Figure 3.9: Δ and Ψ of a 24 nm and a 187 nm thick CuPc film on silicon as measured (black) and as predicted by the two Lorentz-Oscillator Models (red and blue). The 187 nm LOM fit reasonably coincides with the data of the 187 nm sample (A) and shows only slight deviations from the data of the 24 nm sample around 580 nm (B). The 24 nm LOM fit explains the Ψ and Δ - spectra of the 24 nm sample (C) almost perfectly, but fails to correctly predict the spectra of the 187 nm sample (D). These findings indicate slight morphological differences between the two films, which lead to differences in the optical properties around 580 nm. The 24 nm LOM fit possibly overemphasises this effect, due to the nature of the Lorentz-oscillator model.

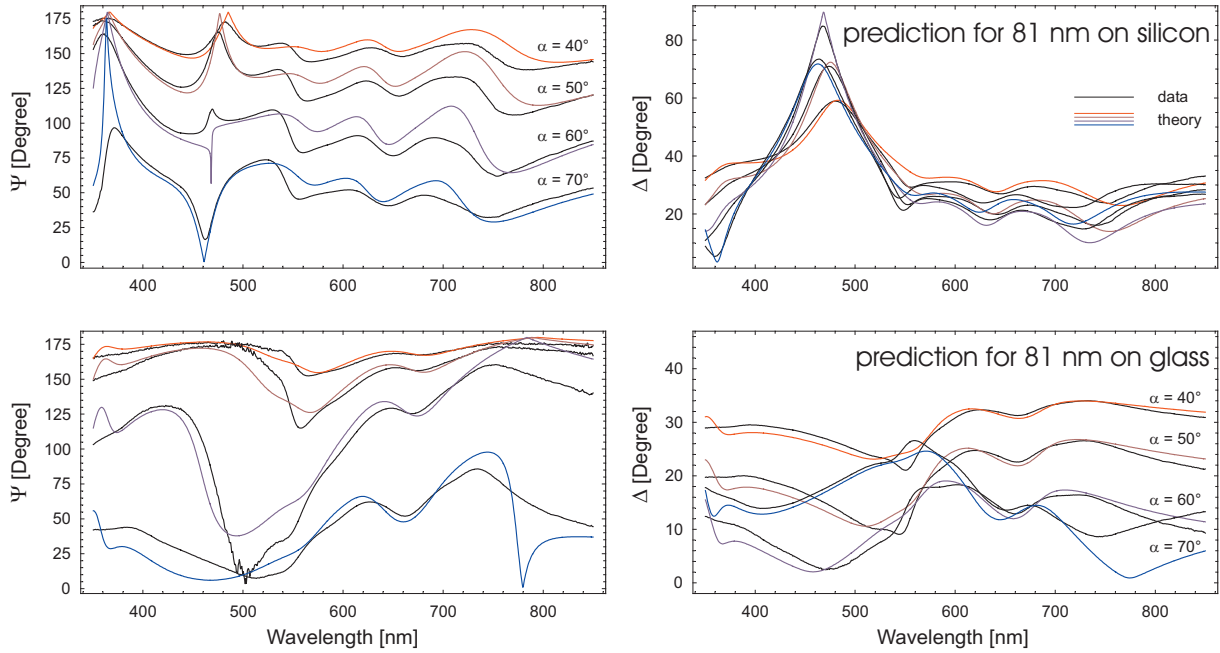


Figure 3.10: Δ and Ψ of a 81 nm thick CuPc film on silicon and on glass as measured (black) and as predicted by the 187 nm LOM fit (red and blue). The important deviations between data and theory in the case of the glass substrate indicate that CuPc adopts a different morphology on glass than on a silicon wafer.

onto a silicon and onto a glass substrate. In Figure 3.10 we present the data and model predictions of the 187 nm LOM fit for the two samples. We find that the shape of the data for silicon follows our prediction reasonably, but the height of the modulations is underestimated as it has been for the 24 nm sample in Figure 3.9. For the prediction on glass, we find deviations even in the shape of the curves around 520–590 nm. We may speculate that this finding and the additional peak in the 24 nm LOM fit (Figure 3.8) have the same origin, be it preferential ordering or the existence of a β -modification. The prediction for the glass substrate, however, shows strong deviations from the data in shape as well as in the modulation amplitude. Deviations exist not only around 550 nm, as expected, but also at the borders of the visible spectrum. The predicted feature around 370 nm is not present and at 780 nm we find no coincidence in the Ψ -values. For Δ we find a strong deviation for large incident angles. Fitting the LOM to the data on the glass substrate was not successful, not even when we tried to fit the data piecewise. In the long-wavelength range we would obtain the same strong absorption as in the point-to-point fit of the 77 nm sample which we had recognised as a fitting artefact.

At this point we have no definite explanation of this finding. One possible reason is a strong anisotropy in the optical properties, due to preferential alignment of the crystallites. This would explain why the deviations are stronger for large incident angles. Some of the deviations could also originate from calibration errors of the instrument or from measurement errors at low intensities due to the low reflectivity of the glass substrate. The spectra are reproducible and the same problems arise when fitting bilayer systems of DMPTI and CuPc on glass.

We conclude that the effective optical properties of CuPc vary with the film thickness as well as with the substrate material. Especially for glass substrates, the data could not be fitted with an isotropic single-layer model. This is at least one reason why determining absolute layer thicknesses of multi-layer systems on glass is unreliable. Also, the comparison of the extinction coefficient from ellipsometry with the UV/Vis absorption spectra (see Figure 3.18) reveals larger deviations. This is another hint that anisotropy is indeed existent. To confirm this we have estimated the refractive index by the KK relation from the absorption spectra and have tried to fit the ellipsometry spectra. But neither the measurements on glass nor the measurements on silicon could be nicely described with that kind of solution.

Optical Properties of DMPTI

For DMPTI, we have pursued a different approach. Since the point-to-point fitting results of the 67 nm sample and the 240 nm sample differ by a factor of 2 in the extinction coefficient, we accept that there must definitely be an influence of the layer thickness on the effective optical properties. There are further hints that this is not a fitting artefact: On the one hand, the BASF company has independently determined the optical properties of DMPTI by spectroscopic ellipsometry [BAS03]. The extinction coefficient is almost identical with the point-to-point fit of the 240 nm sample. On the other hand, there are spectroscopic investigations on the very similar molecule 3,4,9,10-perylene tetracarboxylic dianhydride (PTCDA), suggesting that the absorption of DMPTI is much larger [Bul96a, Dju00, Kra01, Alo02]. In these articles it is also shown that optical anisotropy and coexistence of α and β -modifications can occur for differently prepared samples. We have therefore chosen to concentrate on the optical properties of films that are comparable in thickness to the layers used in our photovoltaic cells.

The broad, plateau-shaped region of the DMPTI absorption spectrum is only badly described by a pure Lorentz-oscillator model, as can be seen from Figure 3.7. This problem has already been addressed for PTCDA; a modified LOM with an additional broadening parameter was applied to correct this deficiency [Dju00]. Here we have pursued an alternative approach. We have fitted the data piecewise with a conventional LOM in partially overlapping sections and concatenated the solutions by linear fading within the overlapping areas. As these solutions do not necessarily fulfil the KK relations we have performed a KK-consistency check, which turned out positive for both substrate layers. In the case of the glass substrate, we used 5 sections for the LOM fits; in the case of the silicon substrate, three intervals were sufficient. As the fitting parameters in this case do not necessarily correspond with absorption lines of the material, we will not give all the parameters here but instead simply mention the intervals of the piecewise fits. The overlapping area varied between 5 and 20 nm and is given in detail in the following table. Figure 3.11 shows the piecewise LOM fits for a 67 nm DMPTI layer on a silicon and on a glass substrate which were simultaneously prepared. Together with the fit, we display the point-to-point fit of the silicon-substrate sample for comparison. The respective fitting parameters are displayed in Table 3.3 We see nearly perfect agreement between the point-to-point fit and the piecewise LOM on silicon; the discontinuity around 450 nm has been smoothed. The piecewise LOM for DMPTI on glass is very similar in shape and

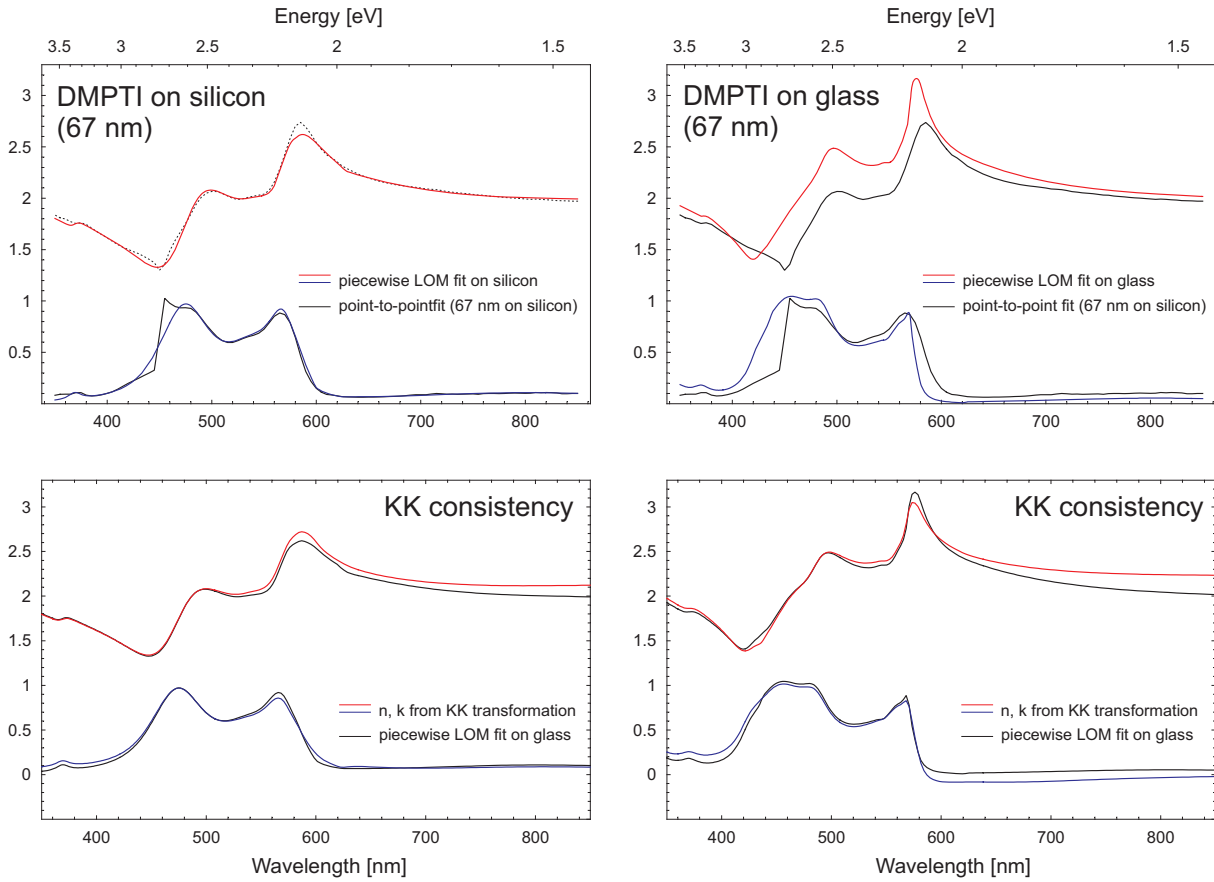


Figure 3.11: Absorption and refractive indices of DMPTI as obtained by a piecewise LOM fit on silicon (left) and on glass (right). For comparison, we have included the point-to-point fit on silicon.

amplitude but shows slight differences at the borders of the absorption feature: A new absorption peak emerges around 440 nm and broadens the left absorption peak, which reasonably coincides with the absorption feature of DMPTI films on glass. The absorption edge around 580 nm is much sharper than determined for the sample on the silicon substrate. The two lower graphs show the comparison between the original curves and the respective KK transforms, where we have allowed for an offset in $\text{KK}(n)$ and $\text{KK}(k)$ to account for transitions outside the visible range. The analysis proves that both solutions are KK-consistent.

To decide whether the different features in n and k are fitting artefacts and to check whether one of the solutions could possibly fit both sets of data, we present in Figure 3.12 the data and the model prediction for Δ and Ψ , as we have already done for CuPc. The upper two graphs show a nearly perfect coincidence between the data on glass and the respective piecewise LOM fit. The prediction for the data on silicon, however, shows strong deviations at wavelengths around 450 nm and 600 nm, which coincide with the regions where the optical properties differ significantly. Vice versa, the fit to the sample on glass shows excellent agreement in Ψ and Δ , but exhibits deficiencies in predicting the spectra for the sample on silicon, the feature in Δ around 400 nm being too narrow and the shape around 480 nm and 600 nm differing importantly in shape.

67 nm DMPTI on Silicon	67 nm DMPTI on glass
$350 \text{ nm} \leq \lambda < 600 \text{ nm}$	$350 \text{ nm} \leq \lambda < 440 \text{ nm}$
$580 \text{ nm} \leq \lambda < 630 \text{ nm}$	$435 \text{ nm} \leq \lambda < 550 \text{ nm}$
$620 \text{ nm} \leq \lambda < 850 \text{ nm}$	$540 \text{ nm} \leq \lambda < 580 \text{ nm}$
—	$570 \text{ nm} \leq \lambda < 625 \text{ nm}$
—	$620 \text{ nm} \leq \lambda < 850 \text{ nm}$

Table 3.3: *Wavelength regions where piecewise Lorentz-oscillator models were fitted. A 67 nm film of DMPTI was evaporated simultaneously on silicon and on glass. In case of the silicon substrate, a division into three sections was sufficient; in the case of the glass substrate, we had to fit in five different regions. Within the overlapping regions linear fading was applied to ensure a smooth transition between the two solutions.*

We conclude that, as for CuPc, we have characteristic variations in the optical properties as a function of the substrate layer. Additionally, the layer thickness plays an important role, which we have not further investigated, restricting ourselves to film thicknesses that are used in our photovoltaic cells. This finding is in accordance with what is reported by other groups on the similar molecule PTCDA. To directly determine the optical properties of the layer materials in working photovoltaic cells, it would be very useful to measure the spectrally resolved internal photon conversion efficiency (IPCE), as the analysis of ellipsometry measurements of bilayer structures on glass was not successful. We are currently developing a setup that will allow the combinatorial measurement of IPCE.

3.4.5 Determination of Film Thickness

Having shown that the effective optical properties of CuPc and DMPTI both depend on the layer thickness and on the substrate material and possibly also on the preparation conditions, it is clear that ellipsometry will not be suited to determining absolute film thicknesses to 1 nm precision, particularly not in a multi-layer system on a glass substrate where reflectivity is low. Ellipsometry is, however, very efficient for checking the homogeneity of the evaporation process or the slope of a gradient profile.

The arrangement of the evaporation cells in the evaporation chamber is of great importance for the production of homogeneous films. For small distances between the evaporation cell and the substrate, a homogeneous film cannot be obtained without special evaporation protocols. For a first test of the film homogeneity, we have evaporated films from the five different sources (three effusion cells and two crucibles) onto glass substrates and have measured the film thickness at 5×9 spots with a profilometer. The results and the geometric arrangement of the evaporation cells are shown in Figure 3.13. The substances (tris(2-phenylpyridine) iridium ($\text{Ir}(\text{ppy})_3$), aluminium and lithium fluoride) were chosen arbitrarily from the set of substances that are commonly used in the evaporation chamber. We see that none of the films are of constant height. Instead, they show a shape that can be fairly well approximated by a gradient. The direction of the gradients

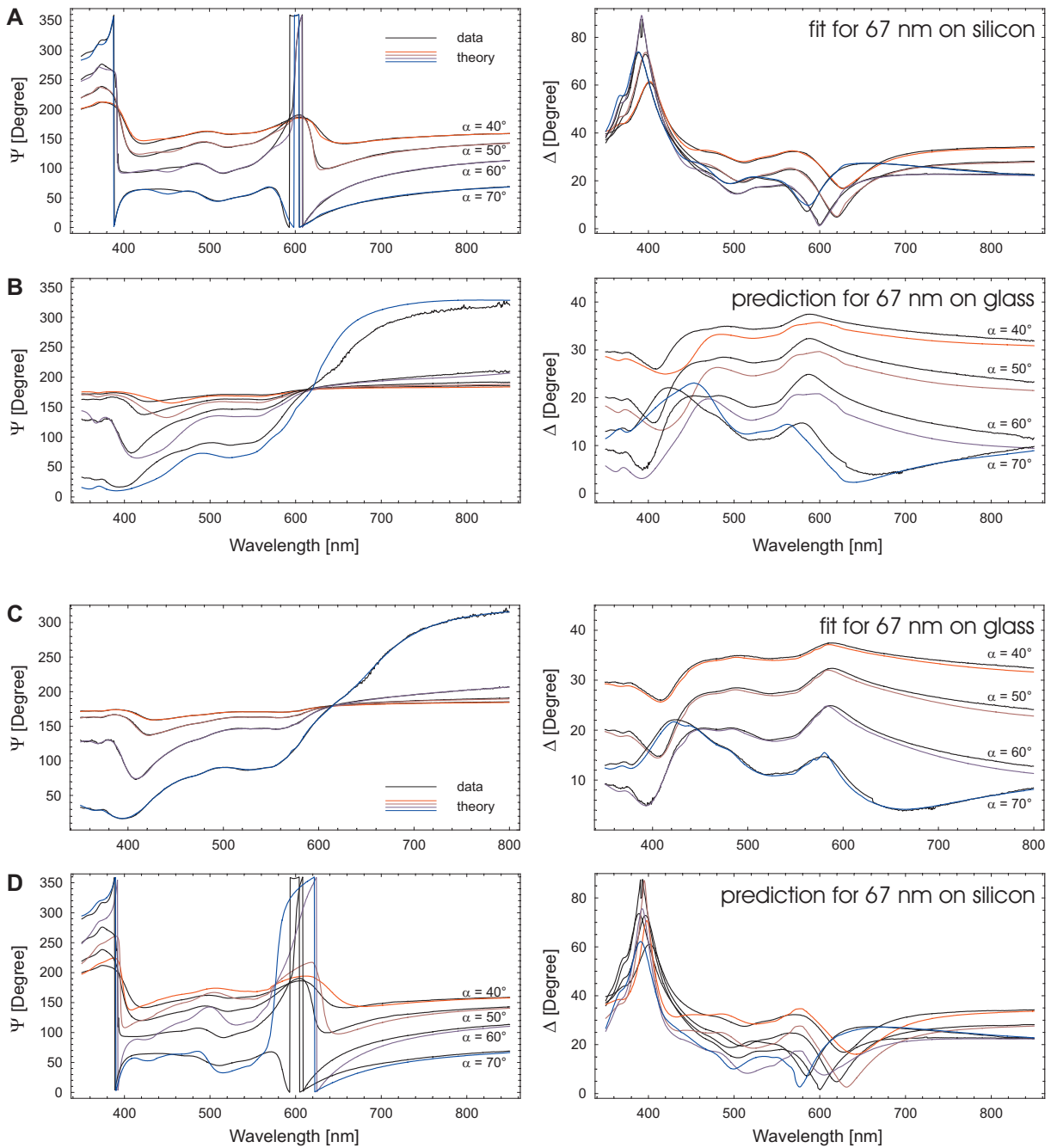


Figure 3.12: Δ and Ψ of a 67 nm thick DMPTI film on silicon and on glass as measured (black) and as predicted by piecewise LOM fits (red and blue). A and B show the predictions of the piecewise LOM fit on silicon for silicon and glass substrate, C and D show the predictions of the piecewise LOM fit on glass for glass and silicon substrate.

can be understood from the position of the evaporation sources. Secondly, we see from the scattering of the values that the accuracy of the profilometer results is in the order of 5–10 nm. To overcome this accuracy problem and to replace the tedious profilometer measurements we decided to check whether ellipsometry would be a useful tool for this task. Knowing the difficulties with glass substrates, we performed another evaporation

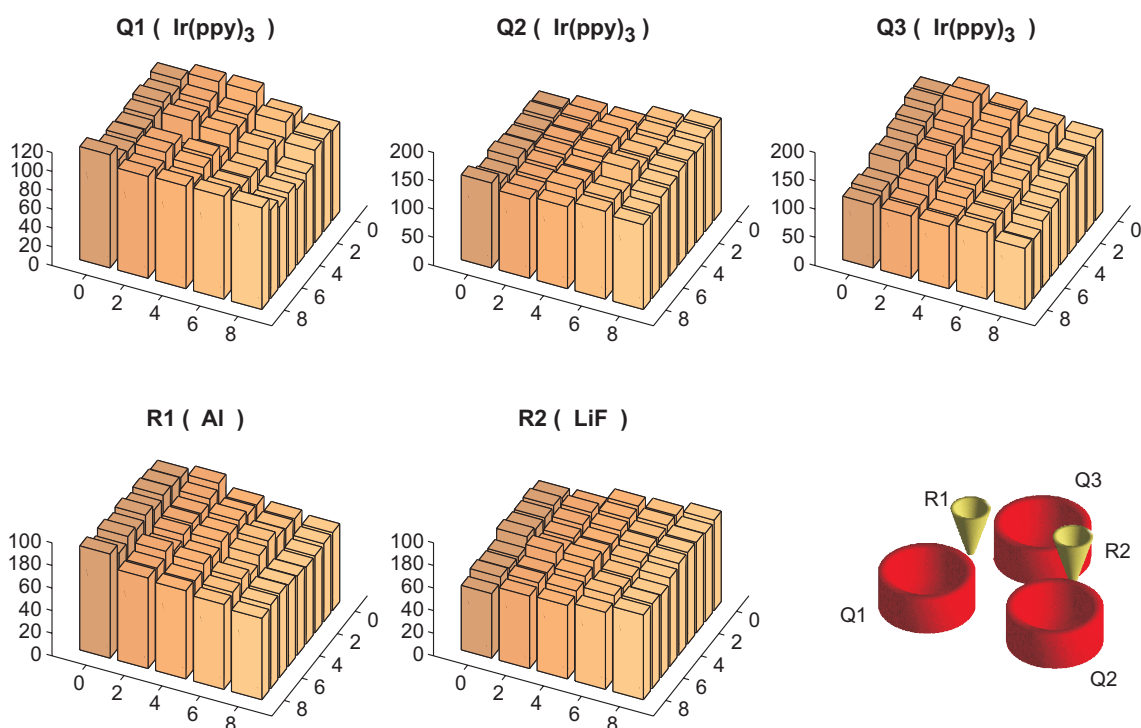


Figure 3.13: *Profilometer data of films evaporated from the 5 different evaporation sources. All films show a slight gradient due to the position of the evaporation source, the gradient of Q3 being the largest.*

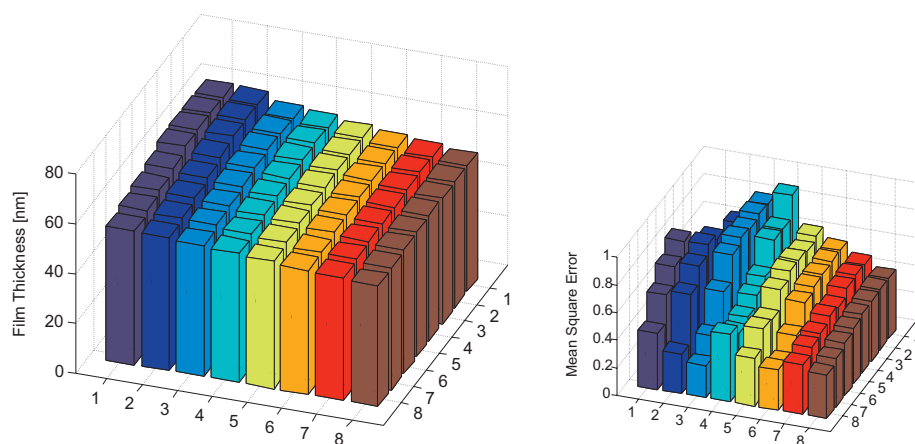


Figure 3.14: *Fit for the thickness of a homogeneously evaporated CuPc film onto a silicon substrate.*

experiment with CuPc on silicon, and automated the ellipsometer to measure the Δ and Ψ spectra on an array of 8×8 spots. A subsequent automated fit of the layer thickness with the optical constants taken from the results described in the previous section leads to a map of thickness values. This is displayed in Figure 3.14 together with the mean square error. Although we have said that we should not expect an absolute accuracy on the nm scale, the fitting results suggest that the relative accuracy is indeed as precise as that. We observe a continuous increase in the layer thickness along the diagonal of the

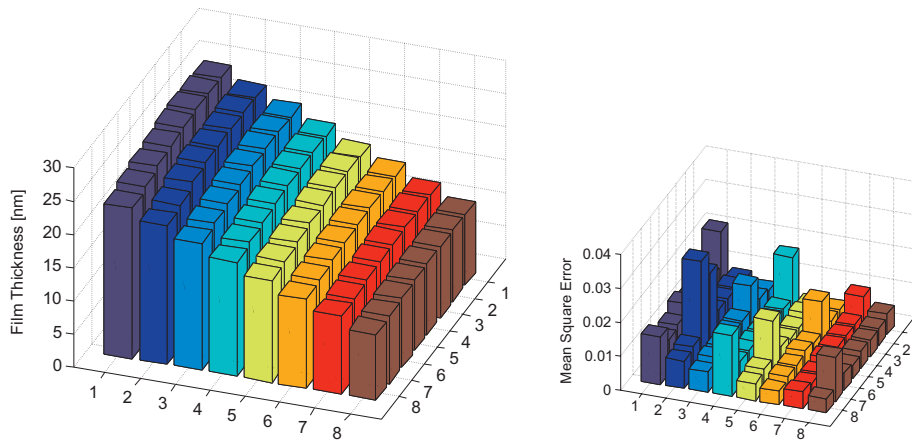


Figure 3.15: *Fit for the thickness of a CuPc film on a silicon substrate that has been evaporated with a continuous gradient.*

sample with values ranging from 40 nm to 60 nm, the mean value being 54.85 nm and the standard deviation being 1.92 nm. Realising that the profile is mainly a linear gradient, we have adapted our evaporation protocol in such a way that we rotate the sample around 180 degrees after the first half of the evaporation time. This procedure eliminates any linear component in the layer profile and leads to nearly flat films.

In the same way, we have investigated a CuPc layer that has been evaporated as a gradient onto a silicon wafer by a moving mask. Details about the evaporation process can be found in [Sch01]. Figure 3.15 shows the expected gradient, which is precisely mapped out by the fitting routine. A second glance reveals the influence of the sample position which leads to a slight gradient along the lines of nominally constant thickness. In this case, the variation is small compared with the intended gradient. Depending on whether the device properties are strongly correlated with the thickness, the second gradient may be neglected. In cases where the gradient is non-negligible, measurements like the one presented can be used to calibrate the layer thickness at each particular spot on the sample. The geometry of our current setup does not, unfortunately, allow us to correct for the unintended gradient by rotation of the sample, since the mask can only move in one direction, due to space limitations. Having been successful in determining the thickness of a CuPc layer on silicon, we tried to map out a bilayer system of a DMPTI gradient and a CuPc gradient on glass as it is used in our photovoltaic cells. For this purpose, we selected the wavelength of 405 nm and used the n and k values of CuPc and DMPTI determined by a global fit to two samples of different layer thickness (see Table 3.1). The fitting results give the correct direction of the gradient (Figure 3.16), but the accuracy is far less than for the single-layer measurements presented above and the starting parameters had to be chosen appropriately for the fitting algorithm to converge. We even achieved a reasonable convergence of a fit over the whole wavelength range by using two LOM models for CuPc and DMPTI (Figure 3.17), but again not without much fine-tuning in the fitting algorithm.

We conclude that ellipsometry is able, with some restrictions, to approximately determine layer thicknesses in a bilayer system of CuPc and DMPTI, but due to the large parameter space and due to the problems of anisotropy, reflectivity etc., which were discussed in the

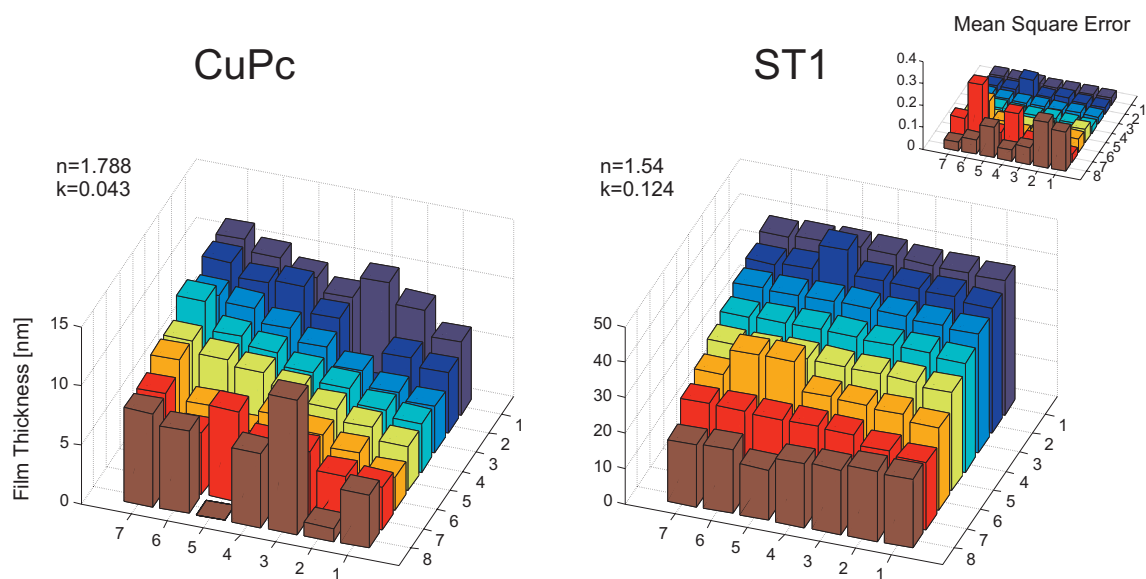


Figure 3.16: Fits for the layer thickness of DMPTI and CuPc that were evaporated onto a glass substrate with perpendicular gradients. The fits were performed at a wavelength of 450 nm with optical properties that were determined by simultaneously fitting two samples of different film thickness for each of the substances.

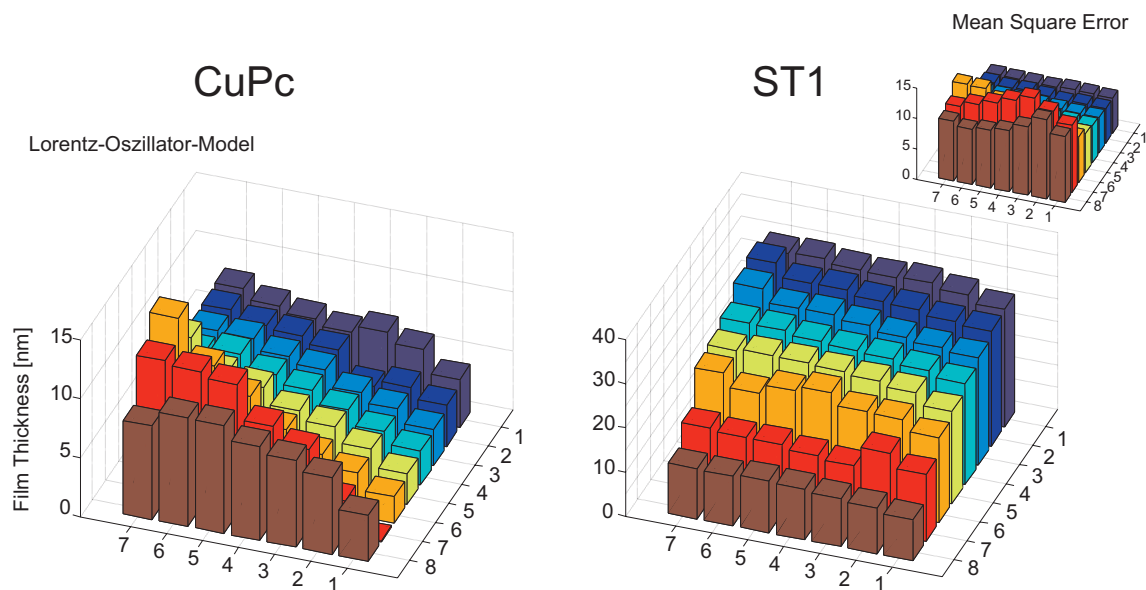


Figure 3.17: Fit for the layer thickness of DMPTI and CuPc on the basis of two Lorentz-oscillator models.

previous chapter, we should talk of verification rather than of determination. As in the near future the acquisition of a combinatorial flash lamp UV/Vis spectrometer will give us another method for layer thickness determination, we have not put any more effort into the optimisation of combinatorial ellipsometry. Preliminary results of the combinatorial UV/Vis method are discussed in the following section.

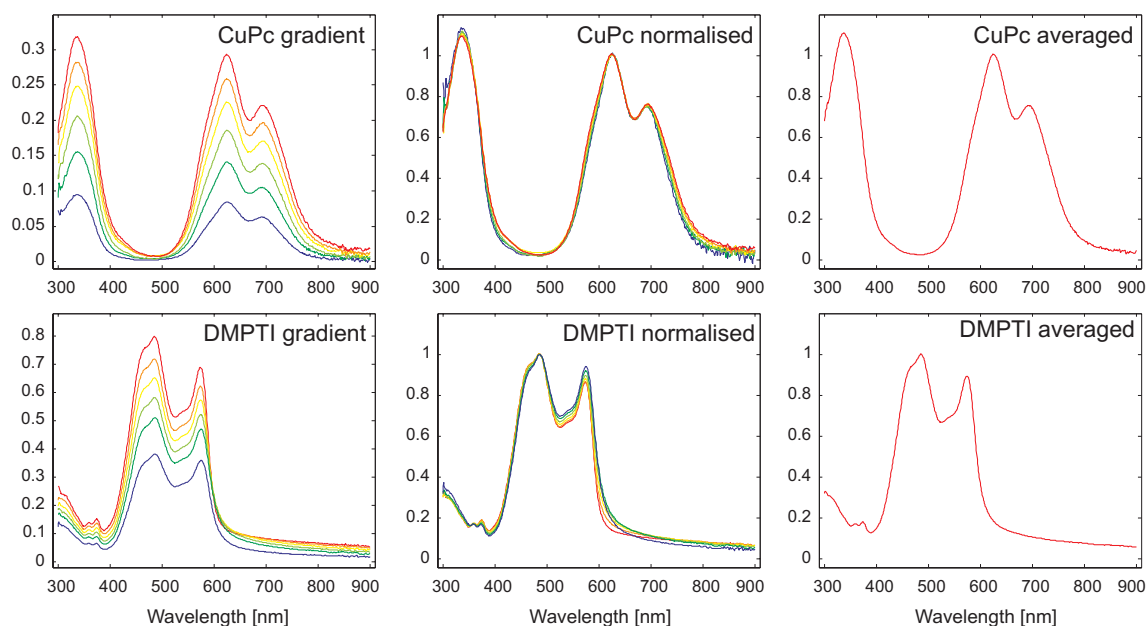


Figure 3.18: Absorption spectra of CuPc and DMPTI a combinatorial measurement on evaporated gradients of the respective materials on glass. The thickness of the samples had not been determined. The spectra are normalised to the absorption maximum and subsequently averaged to give an effective absorption spectrum.

3.5 UV/Vis Spectrometry

For transparent substrates UV/Vis spectrometry is an excellent tool for determining the total absorption of the device. As a first-order approximation, the thickness of a multi-layer structure can be determined by fitting the total absorption spectrum as the sum of the single spectra of the materials employed. This procedure is successful if the differences between the refractive indices of different materials are not too large (remember that the reflectivity goes as $\frac{n_1-n_2}{n_1+n_2}$ for normal incidence, see Equation 3.9). A more advanced approach would be to calculate the transmission according to Equation 3.15 if the spectrum is known and to fit the layer thickness in much the same way as for ellipsometry evaluation. The results from the first-order approximation mentioned above will then be excellent starting parameters, once the spectra are known and calibrated to the sample thickness.

In this section we present preliminary results of experiments that were carried out during a presentation of a FLASHScan[®] S12 spectrometer that our group is currently planning to purchase. As the results are definitely preliminary, we have restricted ourselves to the approximation described above. To obtain the single spectra of CuPc and DMPTI, we scanned two linear gradients of the two materials and normalised the spectra to the maximum of the absorption feature. Subsequent averaging leads to an *effective absorption spectrum* as shown in Figure 3.18. To test the method, we measured the absorption spectra of the solar cell array, the results of which are presented in 3.9. The spectra were taken at spots where no aluminium had been deposited. The absorption spectra were then fitted as the sum of the effective absorption spectra of CuPc and DMPTI, neglecting any

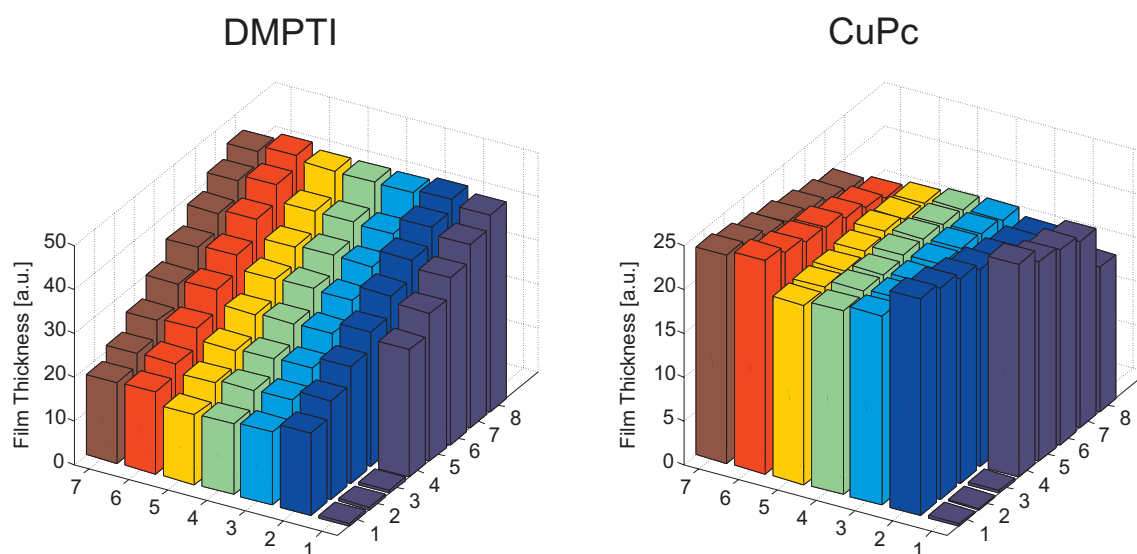


Figure 3.19: *Fit for the thicknesses of a DMPTI and CuPc from a combinatorial UV/Vis absorption measurement on the solar cell array presented in Section 3.9. The evaporated layers are a constant CuPc film of 30 nm on top of a DMPTI gradient from nominally 25 nm to 53 nm on glass. In the middle rows, an additional layer of 30 nm TiO_2 is evaporated.*

absorption of ITO and TiO_2 and neglecting any interference. Additionally, we allowed for an offset, as some of the measurement spots were partially covered with aluminium. The resulting coefficients of CuPc and DMPTI are plotted in Figure 3.19. The scales are in units of the normalised spectra; no calibration has yet been done. Positions (1,1) to (3,1) of the solar-cell array had been cleaned from all organic material by acetone in order to provide a reference measurement of the glass substrate. Hence, the zero thickness at these position is not a fitting error but a successful result. The graph shows a very homogeneous gradient for the DMPTI coefficients (0.22-0.55) and nearly constant coefficients for CuPc. While the fit for the middle part, where TiO_2 had been deposited, indicates a constant CuPc layer, the fits at spots without a TiO_2 layer would suggest a slight gradient in the CuPc film. This difference is definitely due to interference and will be subjected to closer investigation as soon as the UV/Vis instrument is available at our laboratory.

We conclude that combinatorial UV/Vis spectrometry is a very efficient tool that allows a precise analysis of the layered structure of the combinatorially fabricated devices. Particularly the thickness of gradient structures that defy easy calibration by a quartz oscillator can be mapped out by this technique. The measurement as well as the fitting routines (at least the one presented here) are much faster and more robust than those of ellipsometry. Whether more advanced fitting routines which include the refractive index of the materials employed will reliably converge has to be tested in the future. However, the convergence is very likely because of the continuous dependence of the absorption on the layer thickness. The Mathematica[®] program that was developed for the ellipsometry fitting routines and for the calculation of the optical field in the photovoltaic cells has all the necessary ingredients for this purpose. The refractive index could be estimated from the Kramers-Kronig relations. We finally note that at least in the small-thickness range

that has been investigated with UV/Vis spectrometry we do not see a strong dependence of the absorption on the layer thickness. A probable explanation is that light propagation in the UV/Vis setup is always normal to the surface. Therefore, it is only sensitive to the respective optical properties. Variable-angle ellipsometry, complementarily, involves different, non-perpendicular paths and is therefore sensitive to anisotropy. If we assume that the dye layer has a uniaxial symmetry, or, more precisely, that the optical properties differ for in-plane propagation and normal-to-the-plane propagation, the effect might only be visible by ellipsometry. Hence, ellipsometry will stay an important technique for the determination of optical constants and will be an indispensable tool for the understanding and optimisation of electro-optical devices. Combinatorial UV/Vis spectrometry can perfectly assist ellipsometry, particularly by providing reliable extinction coefficients.

3.6 Combinatorial Setup for Device Screening

In this chapter we present the setup that has been developed for the automated short- and long-term characterisation of 8×8 optoelectronic devices. Both light-emitting diodes and solar cells can be analysed under realistic conditions over a period of several hundred hours. For light-emitting devices comparable test conditions are achieved by a separate current control for each device. For solar cells homogeneous solar-like illumination is provided by a 2×2 array of Ultra-Vitalux[®] light bulbs. Characteristic values such as efficiency, short-circuit current or open-circuit voltage are taken from regularly measured I - V curves and local electroluminescence intensity measurements. Comfortable control and data evaluation software has been written in Labview[®], including the control and synchronisation of the multiplexer, the camera and the source-measure unit (SMU). The multiplexer and the corresponding electronic control unit has been developed in close collaboration with Franz Fischer, whose ideas and support were of invaluable help.

3.6.1 Mechanical Details

Since most organic devices show degradation upon contact with oxygen or water, a measuring setup needs to provide suitable protection. Such protection can be realised by either an inert gas system (e.g. a glove box) or by a vacuum chamber. Secondly, one has to decide whether optical access is provided within the measuring chamber or outside. As one of our goals is the characterisation of solar cells and as the required illumination involves non-negligible heat production, it is difficult to build an internal solution. We therefore set up a vacuum chamber in which optical access is accomplished by a rectangular glass window for either optical detection or bright illumination. Electrical addressing is provided by a 64-pin feedthrough as shown in Figure 3.20. This choice enables us to measure either in vacuum or, if necessary, in inert gas atmosphere. Typical pressures that were achieved in the measuring chamber are between 10^{-5} and 10^{-6} mbar.

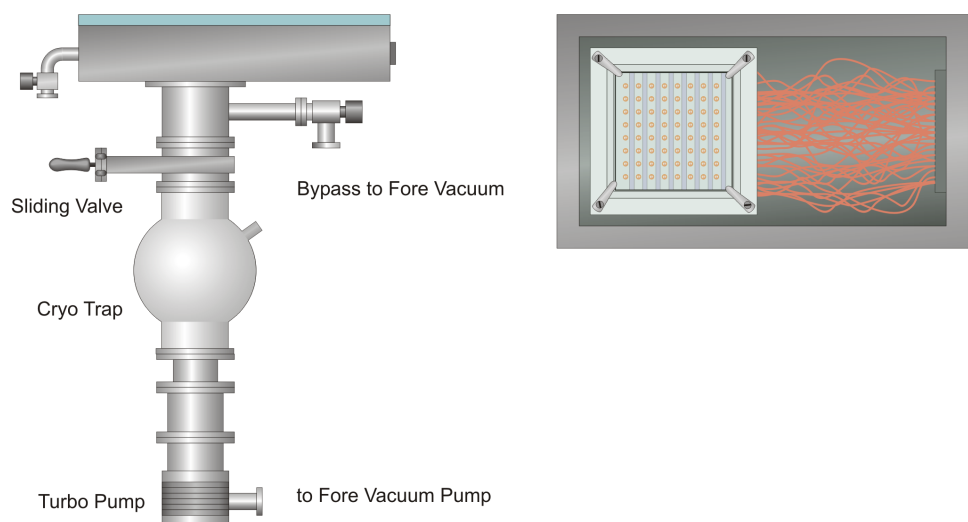


Figure 3.20: *Mechanical setup of the vacuum chamber.*

3.6.2 Electrical Details

For a combinatorial analysis of optoelectronic devices it is necessary to address each of the devices individually both optically and electrically.

For this purpose the ITO substrate is patterned into 8 rows by chemical etching with zinc powder and HCl solution [Sch01]. After the evaporation of the functional layers, an array of 8×8 electrodes is evaporated on top to form overlapping areas with the ITO of 0.12 cm^2 as schematically depicted in Figure 3.21. The aluminium electrodes are contacted with gold-coated spring contacts on locations where the ITO had been etched away in order to prevent short contacts through the evaporated layers. The ITO is contacted on each side of the patterned rows to prevent a voltage drop along the ITO layer. This is important for the simultaneous testing of OLEDs as the voltage drop would affect the I - V characteristics of an OLED if another OLED in the same row were simultaneously driven at high current. For the most recent measurements we have further optimised the setup with the help of pointed spring contacts that contact the ITO in the middle of the rows through the organic layers as indicated by the small circles.

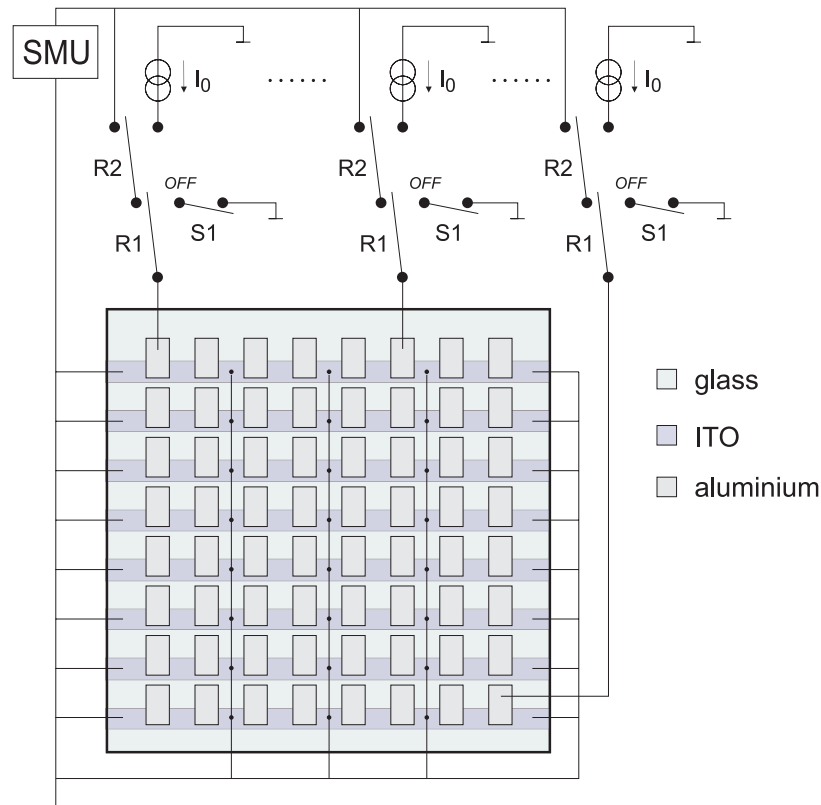


Figure 3.21: *Electrical setup. The ITO has been patterned on rows so that 8 devices share a common anode which is contacted at each side of the substrate. The aluminium cathodes are individually addressed by spring contacts at locations without an ITO layer. Each cathode can be switched to either the SMU, a current source or an off-position. The latter can be set by a dip switch to either short the device or to leave the cathode unconnected.*

To separate the devices electrically, we chose to characterise the devices serially by multiplexing them to a Source Measure Unit (SMU, Keithley 236), while the rest of the devices is operated under constant conditions. We did so for the following reasons: First, the multiplication of a reliable source measuring system to the number of devices would be very costly. Second, the simultaneous recording of electroluminescence curves is non-trivial, as the influence of scattered light from neighbouring devices can hardly be excluded. If conditions for the other devices are kept constant, scattered light can be corrected for by background subtraction. Third, the measuring of the optoelectronic characteristics does not present a bottleneck in the combinatorial analysis: for a short-term comparative analysis, the devices that are currently not under testing can be completely switched off or shorted. For a long-term study, particularly for OLEDs where a continuous current is supplied, it may be desirable not to operate the device before having taken the first I - V curve. We have therefore implemented the option to only switch a device to continuous operation after the first I - V measurement.

The multiplexing unit was realised by computer controlled reed relays that allow switching between the SMU, an ‘off’-position and a constant-current source. The latter possibility is designed for comparative long-term testing of OLEDs: since the shelf lifetime of OLEDs is much higher than their operational lifetime, the main part of the degradation must be induced by charge flow and by heat. Comparable testing conditions are therefore best achieved by ensuring identical current flow for all devices. For this purpose we have integrated 64 voltage-current converters that are controlled by a common control voltage. Applying an identical *voltage* to the diodes would instead lead to higher currents for thinner devices, which in consequence will degrade faster. In our prototype setup, where 20 TPD/Alq₃ devices with a linear thickness gradient were simultaneously tested (see [Zet00]), we were indeed able to observe this effect and we have adapted the final setup to overcome this problem. For the same reason it is not always desirable to use the same voltage range when taking I - V curves of different devices. We have therefore implemented different I - V measuring protocols: a) linear voltage steps, b) linear current steps, c) non-linear current steps

Additionally, each off-position can be set manually to either short the device or to interrupt the connection by a dip switch (S1 in Figure 3.21). This does not make a difference for OLEDs but is desirable for solar cells. As mentioned above, charge flow is one of the important degradation factors for OLEDs. In a short-circuited (grounded) device, there will be a short-circuit current (I_{SC}) flowing, whereas in a disconnected (floating) device no current flow occurs. Instead the device will produce the open-circuit voltage (V_{OC}) between its electrodes under illumination. If there is any current-induced degradation, we would expect different degradation curves for differently connected devices. In a first attempt we set the switches in a chessboard pattern (Figure 3.22A). It turned out, however, that the V_{OC} for floating devices was slightly lower than for grounded devices, even without the devices having been driven over a long period. So the effect must originate from the electrical setup rather than from the devices themselves. A possible explanation is cross-talk between the devices: the nearest neighbours of a floating device are all grounded and will lower the measured V_{OC} , whereas the nearest neighbours of a grounded device are all floating and hence leave the open-circuit voltage of the device under test unperturbed. In a similar way, the whole I - V curve will be influenced by the contact-

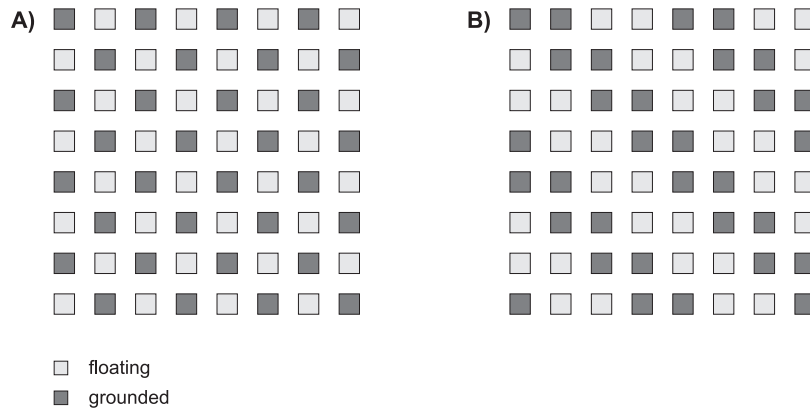


Figure 3.22: *Dip switch configurations. In the chessboard pattern (A), a grounded device has floating nearest neighbours and vice versa. In the diagonal pattern (B), both the grounded and the floating device have an identical environment up to their second nearest neighbours.*

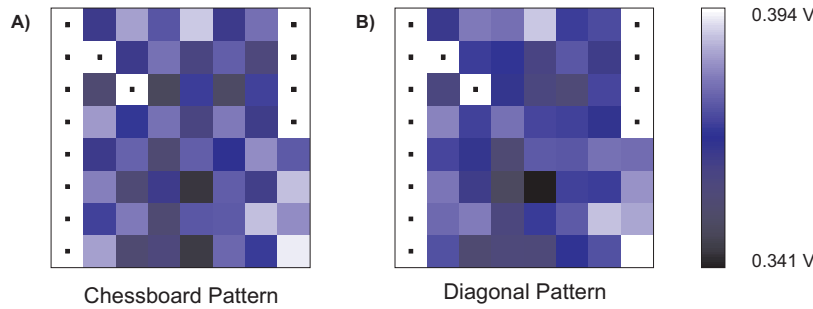


Figure 3.23: *Open-circuit voltage of a solar-cell array taken with the chessboard (A) and the diagonal switch configuration (B). A clear correlation between the configuration pattern and the V_{OC} can be only be seen for the chessboard pattern.*

ing of the neighbouring devices. To reduce such influence, we chose a configuration that provides a neighbourhood as similar as possible for both grounded and floating devices: a diagonal pattern as shown in Figure 3.22B leads to an identical number of floating and grounded devices as nearest and second nearest neighbours. We have documented the influence of the neighbourhood by changing the contacting pattern between two successive measurement cycles of a solar-cell array from the chessboard pattern to the diagonal pattern (Figure 3.23, the layout of the solar-cell array is given in section 3.9). While we can easily recognise a chessboard pattern in the V_{OC} in the left-hand image, there is no such clear correlation between the contacting pattern and the V_{OC} in the right-hand image, which is a first success. To quantify the improvement further, we calculated the mean values of the grounded and floating devices (Table 3.4) and found a decrease in the mean difference of V_{OC} by a factor of 4. This result shows that the cross-talk interpretation is correct and that the influence of neighbouring solar cells can be reasonably minimised by an appropriate choice of the contacting pattern while retaining the possibility of having half the devices grounded and the other half floating.

Pattern	$\langle V_{OC} \rangle_{\text{grounded}}$	$\langle V_{OC} \rangle_{\text{floating}}$	$\langle V_{OC} \rangle_{\text{grounded}} - \langle V_{OC} \rangle_{\text{floating}}$
Chessboard	0.3783 V	0.3615 V	0.0168 V
Diagonal	0.3724 V	0.3676 V	0.0048 V

Table 3.4: Mean values of V_{OC} for grounded and floating devices and their difference for different connection patterns of switched-off devices. The difference in the mean values is 4 times less with the diagonal pattern than with the chessboard pattern.

3.6.3 Optical Details

The combinatorial long-term testing of optoelectronic devices not only requires electrical and electronic but also optical addressing of the devices. In the case of OLEDs this means a locally resolved detection of the electroluminescence, in the case of solar cells it means a homogeneous white-light illumination over an area of $8 \times 8 \text{ cm}^2$ and over a period of several hundred hours per experiment.

Detection of Electroluminescence

To resolve the electroluminescence (EL) of each device locally, we installed a black/white CCD camera (SENSICAM, PCO) at variable distance over the glass window of the vacuum chamber (Figure 3.20). The detection of the full spectra would require moving parts, which we wanted to exclude at this point. The detection of the electroluminescence is synchronised via a hardware trigger between the SMU and the camera. The detection area for each diode is set from within the software program. The intensity is summed within the region of the diode under test to give the raw electroluminescence signal (Figure 3.26). A background subtraction is performed by the evaluation software to eliminate contributions

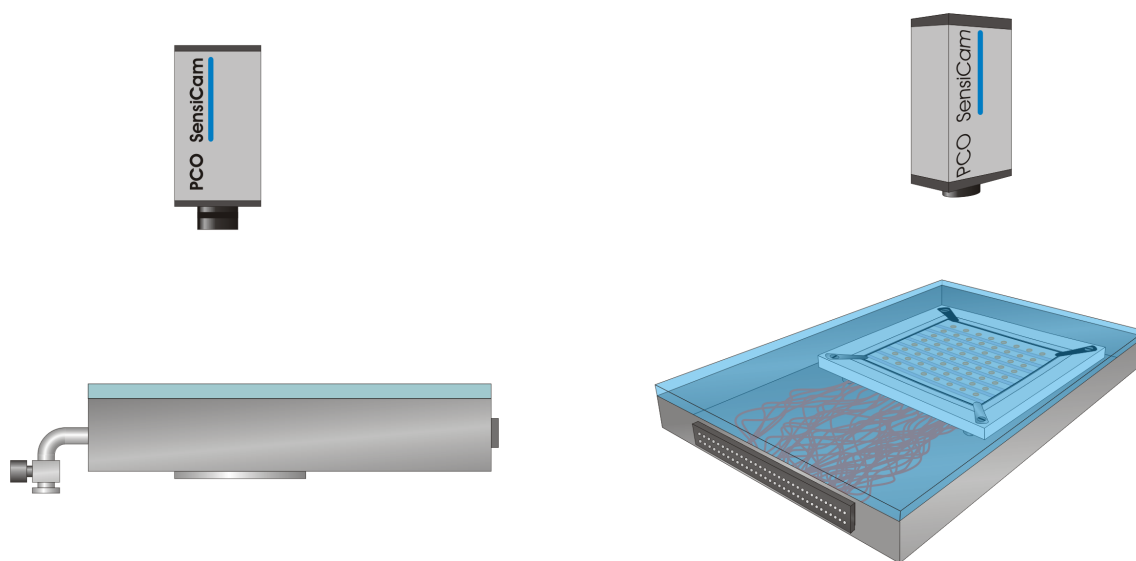


Figure 3.24: The locally resolved detection of the electroluminescence is realised through the glass windows by a black/white CCD camera.



Figure 3.25: *Photograph of the OLED analysis setup: In the foreground the measuring chamber with an OLED device installed, in the background the multiplexer electronic, a power supply and the SMU together with the controller PC.*

from the scattered light of the diodes operated at constant current. Daylight is held off by a black cloth that covers the camera and the device array, as shown in Figure 3.25. At the end of each measuring cycle all diodes are switched back to continuous operation mode and an image of all diodes at constant current is saved. This images sequence can be played as a video to visualise the degradation process.

Illumination

Since typical lifetimes of commercial solar simulator lamps are of the order of the duration of a single experiment and since such lamps are very expensive, we had to search for a more cost-effective solution to provide homogeneous solar-like illumination. We have chosen the OSRAM Ultra-Vitalux[®] (300 W) light bulb as light source, whose spectrum is, apart from the inert gas lines, nearly flat in the visible range. To protect the devices from the heat of the lamps, we placed a water filter with cycling water at a temperature of $\approx 15^\circ\text{C}$ in front of the vacuum chamber. With this filter applied, typical temperatures during long-term experiments are about 50°C ; without protection they reach 80°C and above. The UV/Vis transmission curves of the water filter, the vacuum window and the combination of both are given in Figure 3.27 together with the lamp spectrum. It turns out that the effective illumination spectrum given by the product of the total transmission and the lamp spectrum nicely coincides with the shape of the Air Mass 1.5 standard solar

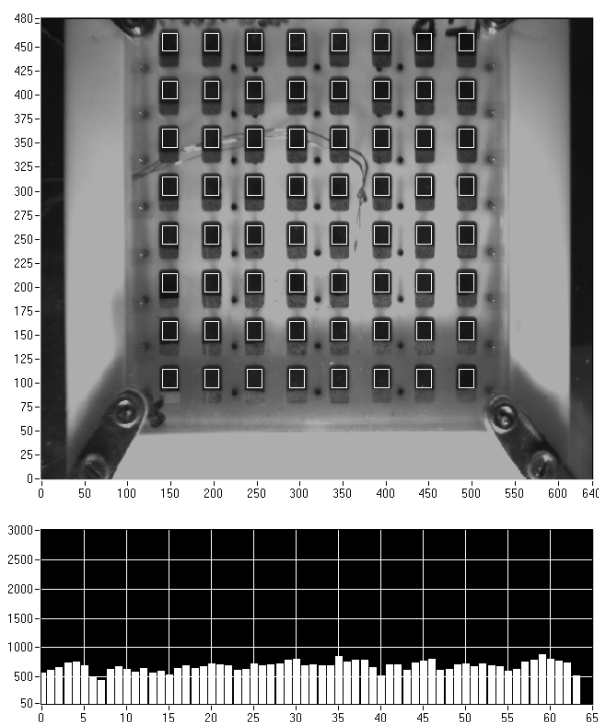


Figure 3.26: *Setting the areas of interest for the OLED measurement: Clipping from the control program where the detection area of each device can be set. The upper part displays the CCD image with the detection regions. The temperature sensor can be seen in the middle of the image. The lower part shows the resulting intensity for each device in arbitrary units.*

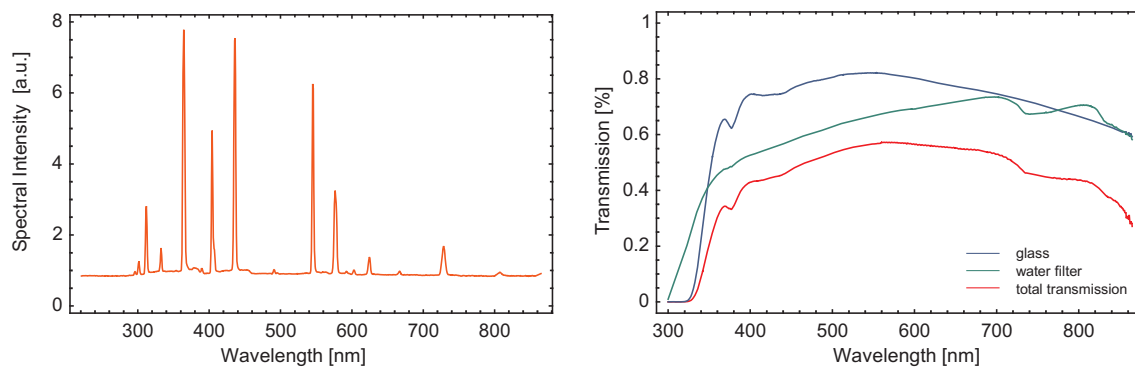


Figure 3.27: *Lamp spectrum of the OSRAM Ultra-Vitalux[®] (300 W) light bulb and transmission curves of the water filter and the vacuum window.*

spectrum (AM 1.5), as shown in Figure 3.28. No additional filters are needed.

To achieve the required spatial homogeneity, we arranged four lamps in a quadratic array above the glass window of the vacuum chamber, as shown in Figure 3.29. To optimise this configuration, we determined the intensity profile of a single light bulb for different lamp distances z_i . For this measurement, the detector was kept in the object plane. We first tried to model the profile obtained by a point-source field, but the resulting distances were far too high and could not be reasonably connected to the measured distances. This

is not surprising as the diameter of the light bulbs is of the same order of magnitude as the distance from the sample. Fitting the intensity profiles empirically with a Lorentzian shape was far more successful, resulting in individual parameters $I_0(z_i)$ and $w(z_i)$ for the maximum intensity and for the width of the profile (Figure 3.30). The width depends linearly on the distance which corresponds to a geometrical broadening. The $I_0(z_i)$ show a nearly inverse quadratic dependence, reflecting the energy conservation. When we fit

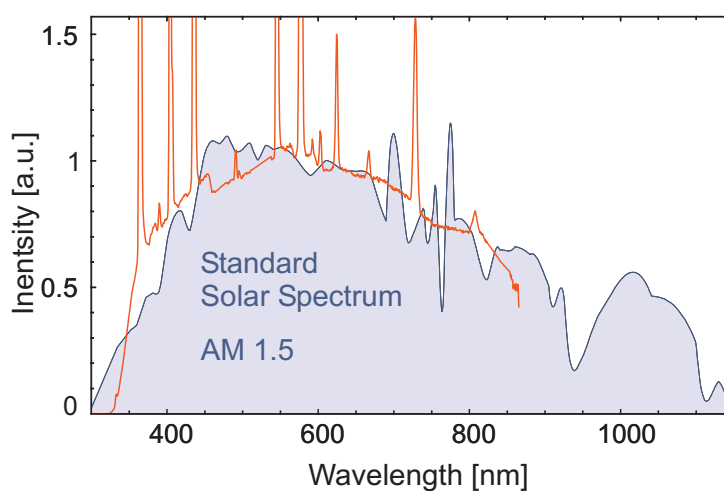


Figure 3.28: *Illumination spectrum at the position of the devices (red) in comparison with the standard solar spectrum Air Mass 1.5 (AM 1.5). The AM 1.5 spectrum has been scaled to best match the lamp spectrum.*

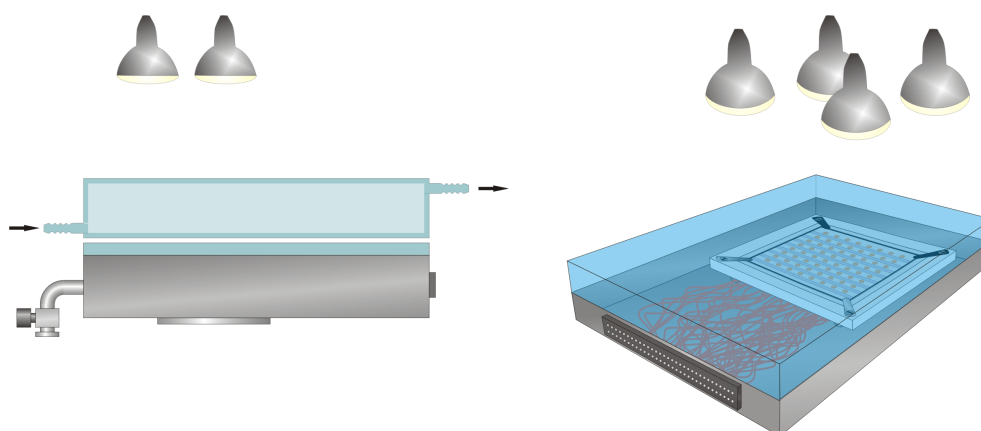


Figure 3.29: *The illumination of the sample was accomplished by a 2×2 array of light bulbs, which was optimised for homogeneous intensity at the device surface.*

these dependencies we arrive at the following parametrisation:

$$I(x) = \frac{I_0(z)}{1 + \left(\frac{x}{w(z)}\right)^2}$$

$$w(z) = 0.269z + 0.959 \text{ cm} \quad (3.54)$$

$$I_0(z) = 13741z^{-1.86} \text{ mW/cm}^2,$$

where x is the detector position in the object plane and z the distance of the lamp from the device surface. With this parametrisation we calculated the intensity profile of a quadratic lamp array with a lamp-to-lamp distance Δx_{Lamp} of 14 cm. It is clear that at distances lower than Δx_{Lamp} the profiles of the lamps can be clearly separated, whereas the profiles will add to a broad peak at distances much larger than Δx_{Lamp} . The most homogeneous intensity is achieved at a distance of around 30 cm, as shown in Figure 3.31: both the horizontal and the diagonal cross section show a flat maximum. To quantify the homogeneity, we calculated the relative mean square deviation $\sigma_I/\langle I \rangle$ in an area of 8×8 cm. Figure 3.32 shows that this quantity is minimised at $z_{min} = 29.6$ cm with a minimum value of 0.12 %, which is even below the intensity fluctuation of the lamps. This shows that it is possible to obtain a very homogenous illumination without any extra diffusor which would decrease the intensity. Together with the mean deviation we plotted the mean intensity, which necessarily decreases with increasing distance. Taking into account that the filter absorbs about 50 % of the intensity, we built a lamp array with a distance of 23.5 cm, which is a compromise between the optimum distance and a reasonably strong intensity. The measurement at an 8×8 grid with a distance of 2 cm reveals a mean intensity of 39.8 mW/cm^2 and a relative mean deviation of 2.8 %, which even exceeds the specification of some commercially available solar generators.

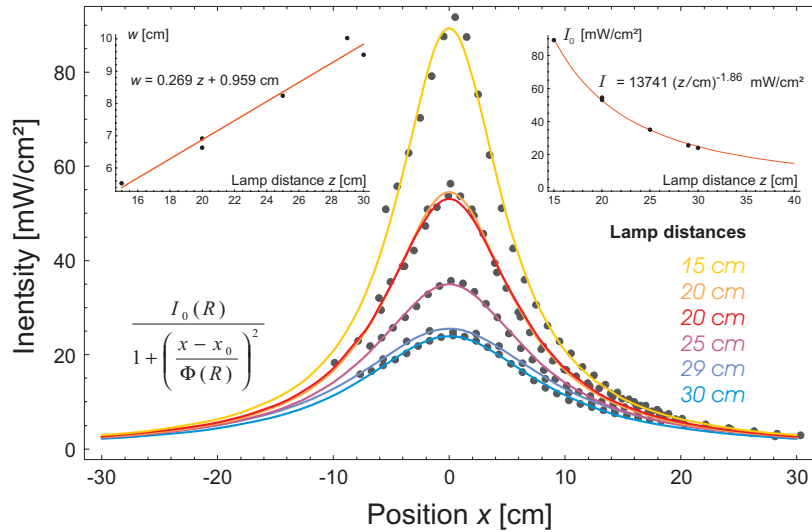


Figure 3.30: *Parametrisation of the intensity profile of the OSRAM Ultravitalux (300 W) light bulb. The parameters $w(z_i)$ and $I_0(z_i)$ from Lorentzian fits are themselves fitted by a linear and by a potential dependence on z respectively.*

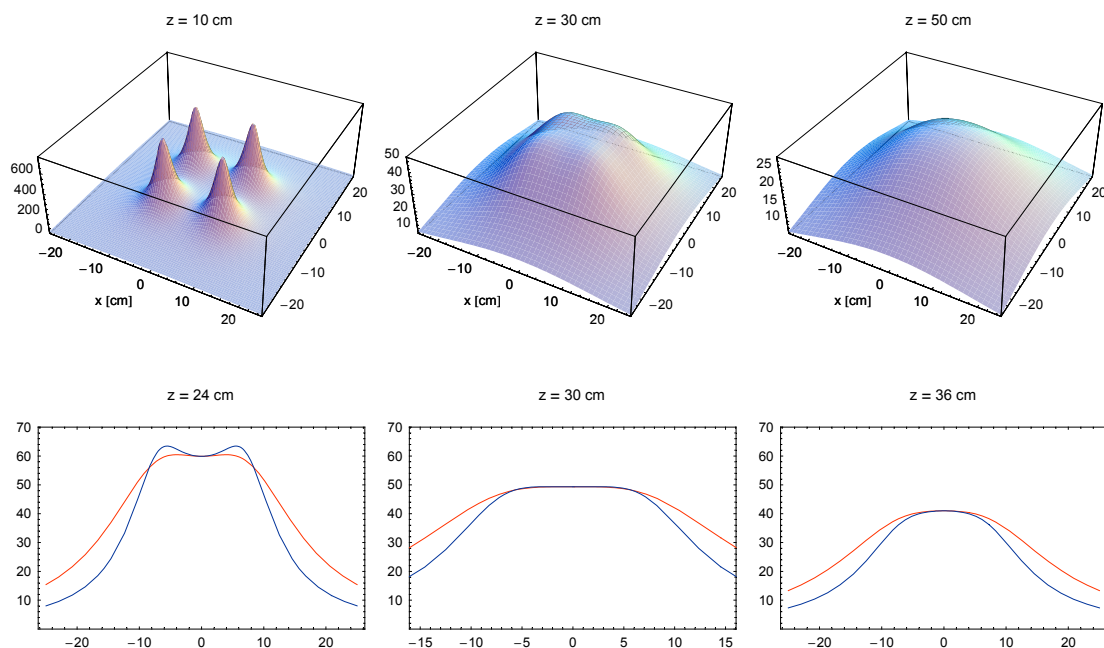


Figure 3.31: Calculated intensity profile of a four-bulb array at distances $R=10, 30,$ and 50 cm. The lower part displays the horizontal (red) and the diagonal (blue) cross sections

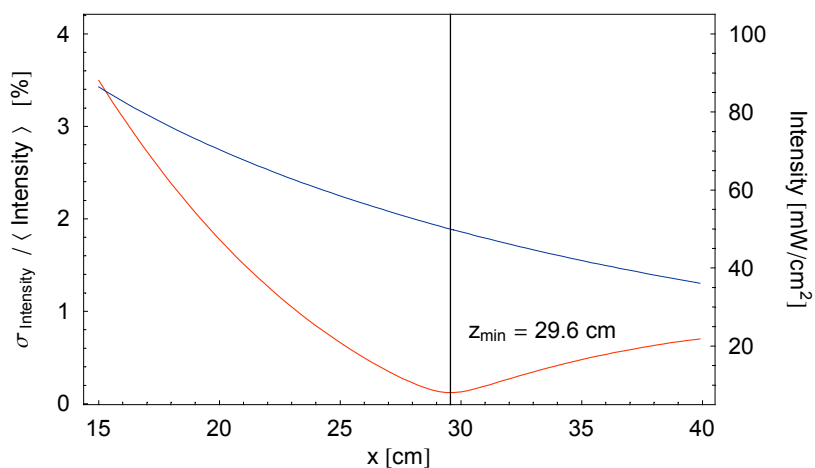


Figure 3.32: Distance dependence of the mean intensity (blue) and the relative mean deviation (red). The latter shows a clear minimum at 29.6 cm with a minimum value of 0.12 %

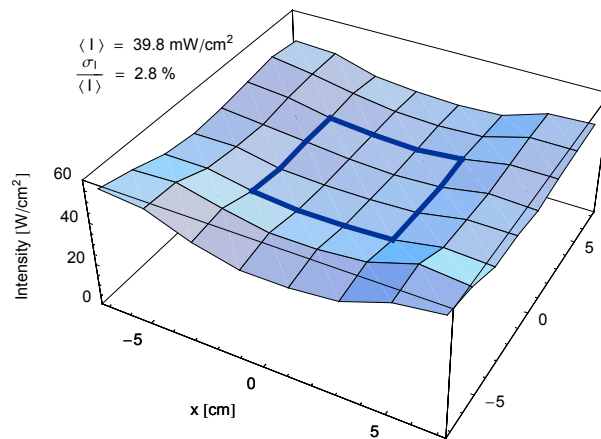


Figure 3.33: Intensity measured at a grid of 8×8 points with a spacing of 2 cm. Within the marked area, a mean intensity of 39.8 mW/cm^2 and a relative mean deviation of 2.8 % is obtained.

3.7 Solar Cell Performance and Long-Term Stability I: Materials Library

3.7.1 Abstract

We present a newly developed setup that allows the combinatorial study of organic multi-layer devices for durability and degradation mechanisms. Arrays of 8×8 thin-film organic devices are prepared by vacuum deposition and investigated under vacuum conditions. Measurements of 9 types of organic solar cells are presented. Continuous solar-like illumination at 80 mW/cm^2 and a temperature of 80°C provide realistic testing conditions. The degradation of solar cells was investigated as a function of layer combination and layer thickness over a period of 800 hours. Different timescales of degradation were identified and attributed to the layer structure of the devices⁴.

3.7.2 Introduction

Since the first report of organic electro-optical devices by Tang *et al.* [Tan86, Tan87] many efforts have been made to optimise the device parameters (film thicknesses, layer materials, etc.). The wealth of possible parameter combinations makes combinatorial methods a necessary tool for device development. Combinatorial device preparation has already been shown to be a very efficient tool [Sch99a, Sch99b], thus creating the demand for an equivalent testing procedure. Especially issues of degradation and lifetime can only be reasonably addressed with a combinatorial measurement setup. This may be one reason why only very few studies of the long-term behaviour have been carried out yet [Pet01, Hin01].

In this section we report the development of a combinatorial setup designed to study the degradation process of various organic thin-film devices in parallel. We present the simultaneous measurement of the electro-optical behaviour of 64 solar cells of nine different types over a period of more than 800 hours. We are able to distinguish two degradation mechanisms with different time scales.

3.7.3 Experimental

A two-dimensional array of 64 organic multi-layer solar cells was prepared by an evaporation process starting with a 35 nm thick copper phthalocyanine (CuPc) layer as hole conductor onto an Indium Tin Oxide (ITO) coated glass substrate ($76 \times 76 \text{ mm}$). The ITO (Merck, 80 nm) was treated with an oxygen plasma before evaporation. On top of the CuPc layer, 25 nm of different perylene dyes (dimethyl perylene tetracarboxydiimide (DMPTI: 2,9-Dimethyl-anthra[2,1,9-def:6,5,10-d'e'f']diisoquinoline-1,3,8,10-tetraone) and bisbenzimidazole perylene (BBIP: Bisbenzimidazo[2,1-a:1',2'-b']anthra[2,1,9-def:6,5,10-d'e'f']diisoquinoline-6,11-dione (mixture with cis-isomer))) were evaporated as sensitizers in two different rows; one row was left empty. As a third functional layer, three columns

⁴The results of this chapter are published in [Hän02]

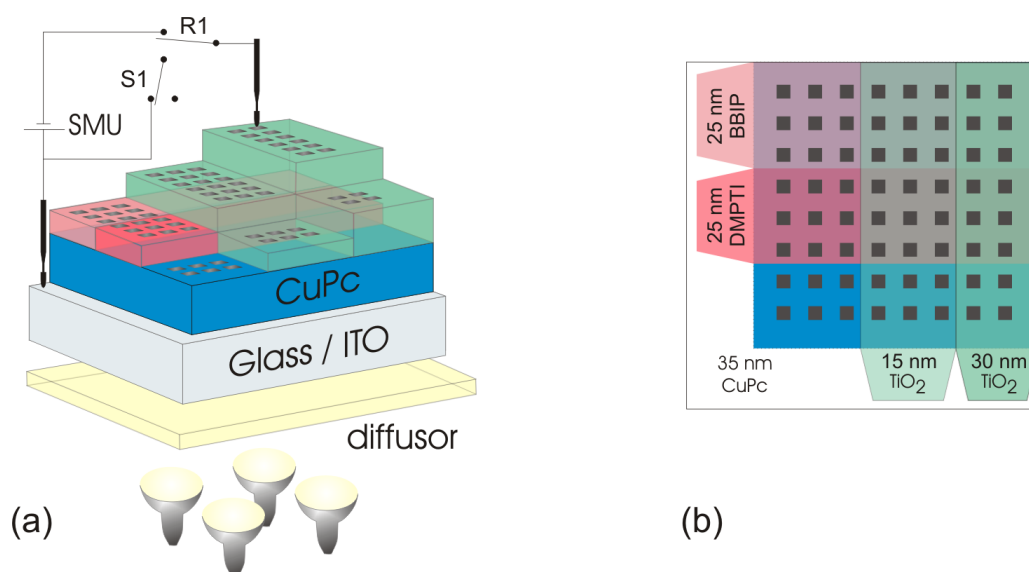


Figure 3.34: *Experimental setup: (a) Perspective view of the layered structure with electrodes. Illumination by a four lamp array and the electrical circuit of a single device are plotted schematically. (b) Top view of the 3×3 organic solar cell library and the 64 aluminium electrodes.*

of 0, 15 and 30 nm of TiO_2 were evaporated on top. This was done by heating Ti_3O_5 at an oxygen partial pressure of 2.5×10^{-5} mbar, the subliming TiO reacting with the oxygen and forming a predominantly anatase crystal phase on the substrate. As the top layer an array of 8×8 aluminium electrodes was evaporated; this results in 9 device types with at least four devices per type (see Figure 3.34), each 0.12 cm^2 in size.

For simultaneous investigation of the 64 devices, the substrate was placed in a vacuum chamber at 5×10^{-5} mbar. Electrical contacts to the electrodes as well as to the ITO were provided by gold-coated spring contacts. Electrical shorts were prevented by etching away the ITO in the contact area before evaporation. Four light bulbs, type OSRAM Ultra – Vitalux[®] (300 W), provided homogeneous solar-like illumination with an irradiation intensity of 80 mW/cm^2 . (On a quasi-white background, there are emission peaks at 363, 404, 435, 545, 576, 624 and 728 nm).

The glass window of the vacuum chamber has a cutoff wavelength of 320 nm; no further optical filtering was done. The temperature inside the vacuum chamber reached about 80°C . This corresponds to conditions found for inorganic solar cells in power generating setups. Every three hours, all devices were characterised by sequentially taking I – V curves from -0.2 to 0.6 V in steps of 0.02 V per second with a *Keithley SMU 236*. Switching between the devices was done by a home-built relay-multiplexer. During idle time, half the devices were short-circuited, while the other half were left open-circuited. The experiment was stopped after about 800 hours. During the measurement, 8 devices exhibited a short from the beginning on or showed strange behaviour in the I – V characteristic. They were excluded from the data evaluation and their values were replaced by the mean values of the corresponding group. Except for Figure 3.35a, which nicely shows the homogeneity of the devices in a single group, all data presented is averaged over identical devices.

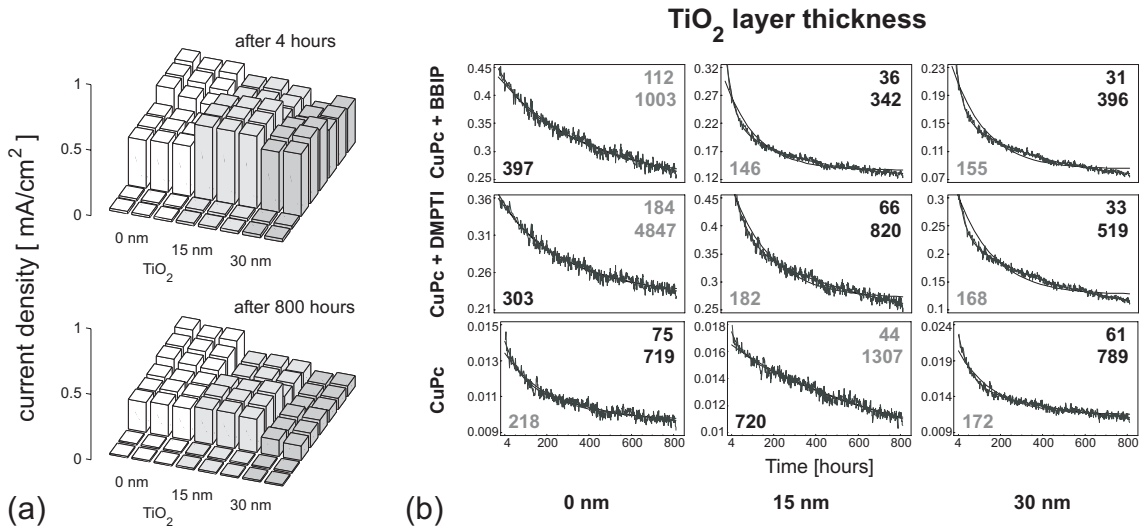


Figure 3.35: (a) Current density I_{SC} of all 64 devices after 4 and 800 hours of illumination. The homogeneity of devices of the same type is clearly visible. The sensitising layer enhances I_{SC} by one order of magnitude. The additional TiO₂ layer does not increase the long-term device performance. (b) Time behaviour of I_{SC} for the 9 device types. The data within respective groups has been averaged. Together with the data a single and a double exponential fit is shown. The decay times (in hours) are displayed in the bottom left-hand and the top right-hand corners respectively. Values of the less appropriate model are shaded grey.

3.7.4 Results and Discussion

Figure 3.35a compares the short-circuit current (I_{SC}) of all devices determined within the first measuring cycle and after 800 hours of illumination. For experimental reasons, the first measurement cycle was taken after 4 hours of illumination. We can see clearly that the initial performance of the solar cells is significantly improved by the sensitiser layers. The effect of the additional TiO₂ layer as an electron injection layer is less pronounced and different in sign for the two dyes. For the devices with DMPTI we find an increase in I_{SC} which does not depend much on the layer thickness of TiO₂. The contrary effect is observed for the BBIP layer, where I_{SC} is slightly decreased. After 800 hours, the advantage of the TiO₂ layer has nearly vanished in cells containing DMPTI. At the same time, the negative effect of TiO₂ found in the BBIP devices has increased. Details regarding the initial effect of the TiO₂ layer and on the evaporation technique are discussed in [The02]. The data presented in [The02] show an increase in efficiency even for BBIP, which at first glance seems to contradict our findings. We anticipate that the following discussion will identify a fast degradation process involving the TiO₂ layer, so that the value of I_{SC} taken after 4 hours of illumination will be smaller than the initial value taken independently on a different device without preceding thermal and optical stress.

We now turn to the discussion of the long-term stability of the multi-layer devices. Figure 3.35b shows the evolution of the short-circuit current I_{SC} . We present I_{SC} rather than the power conversion efficiency, as the former mainly reflects the exciton generation and charge separation probabilities whereas the latter additionally involves changes in the

chemistry of the electrodes. We find a strong decrease in I_{SC} for all nine device types, but the curves show a difference in shape. In order to analyse this decrease qualitatively, we fitted both a single and a double exponential to the sets of data. The statistical f-test with a 5% threshold was used to judge whether the more complicated model, i. e. the double exponential, is necessary to describe the data properly. Both fit curves are plotted together with the data. The decay times of the models in hours are given in the bottom left-hand and the top right-hand corners of the plots. We see that the devices without a sensitiser layer exhibit enhanced initial I_{SC} values with increasing TiO_2 thickness. After 800 hours, however, they show nearly the same I_{SC} value. The decay times do not show a clear tendency with varying TiO_2 thickness. The devices with a sensitiser layer but without a TiO_2 layer exhibit a single exponential decay of three to four hundred hours. In the presence of a TiO_2 layer we find an additional, shorter, decay time of around 30 hours. The TiO_2 layer thickness does not strongly influence the decay times. We note that for the double-exponential fits, fixing one decay time at the value of the device without TiO_2 also results in consistent fits. The existence of more than one timescale is nevertheless evident.

The open-circuit voltage (V_{OC}) is a second important parameter for the stability of the solar cells. Its behaviour with operation time is displayed in Figure 3.36. It reflects changes in the HOMO and LUMO energy levels. Remarkably, we see two opposite tendencies at different timescales: Over a period of a few days, V_{OC} increases for devices with no TiO_2 layer. This period is shortened or vanishes completely in the presence of TiO_2 . All devices show a slight decrease in V_{OC} on a timescale of several hundred hours. After 800 hours nearly all devices with TiO_2 show a lower V_{OC} than the corresponding devices without a TiO_2 layer. Devices with both a TiO_2 layer and a sensitiser layer show the strongest decay of V_{OC} .

3.7.5 Conclusion

In summary, we find a long-term degradation process for all devices with a timescale of several hundred hours. Photo-bleaching may be anticipated as a possible reason, which would eventually lead to a lower exciton generation probability. Additionally, chemical changes of the electrode or injection layers may occur, which in turn lead to a decrease in electrical conductivity. Such changes are indicated by the long-term behaviour of V_{OC} and are most probably the result of the high temperature. The introduction of a TiO_2 layer in thin-film organic solar cells can lead to initial enhancement of the performance. For CuPc/sensitizer cells the TiO_2 layer introduces a new degradation mechanism and does not necessarily lead to an improvement in long-term performance. Our measurements suggest that the interface between the sensitiser and the TiO_2 plays a key role in this process. Bearing in mind that the preparation of the TiO_2 layer requires the reaction of the unstable TiO species with oxygen, this reaction may not have been complete and/or metastable crystals may have formed. Reordering or further oxidation of TiO may be involved. An oxidation of aluminium at the interface to TiO_2 could also play a role. A depth-profile analysis of the chemical composition could possibly help us achieve a deeper understanding of the degradation mechanism [Xin01] and is planned for future investigations.

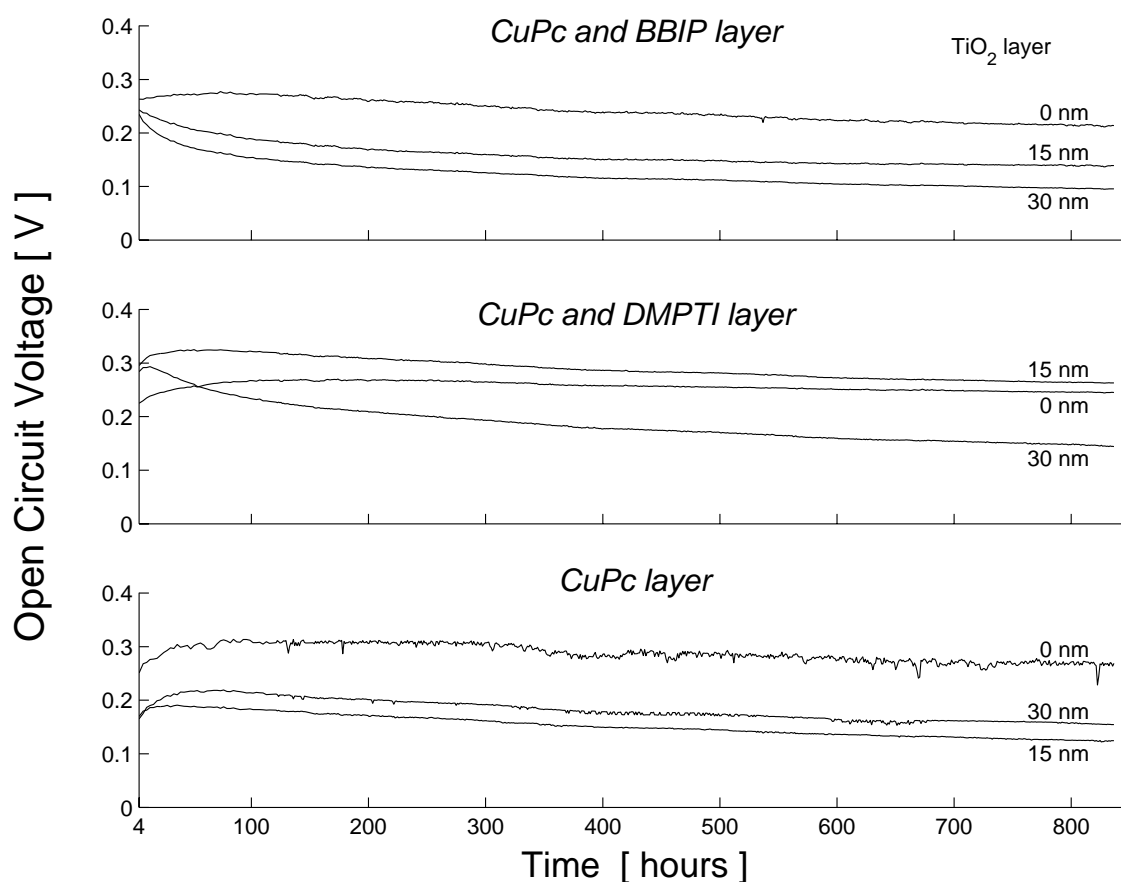


Figure 3.36: *Open-circuit voltage vs. time: Devices with sensitiser and TiO₂ layer show a decrease in V_{OC} . Devices without this layer combination exhibit an initial increase and only a slight decrease for longer times if any. Together with the I_{SC} data this leads to the assumption that the interface between TiO₂ and the sensitiser layer is involved in the degradation mechanism.*

We conclude that our setup is well suited to combinatorially characterise thin-film organic solar cells over a long period under realistic conditions. This is important for the understanding of the degradation processes in thin-film devices and thus for optimising layer structure and layer thicknesses. Our results demonstrate that the initial performance, which is commonly reported for a new layer or material combination, is not sufficient to determine the suitability of a device. No differences were found between devices that were shorted and devices without current flow.

In future experiments we will study the influence of the illumination spectrum. A water filter has recently been built which is designed to cut out the infra-red spectrum and to allow temperature control. Further wavelength ranges can be cut out by the adding of dyes to the water. This should permit us to gain further insight into the degradation mechanism.

We finally note that the setup was originally developed for the long-term characterisation of organic light-emitting diodes. Electroluminescence can be detected via a CCD camera and each device can be driven at constant current. Preliminary results have been obtained

for a single gradient device and work is in progress for combinatorial devices, as presented in [Sch99b, Bei02].

3.8 Solar Cell Performance and Long-Term Stability II: Thickness Library

3.8.1 Abstract

From the experiments described in the previous chapter and in [The02] we have learned that CuPc/DMPTI photovoltaic cells show superior performance over CuPc/BBIP cells. In this section we therefore take a closer look at ITO/CuPc/DMPTI/TiO₂/Al devices by varying the DMPTI layer thickness in a three-step gradient, thus producing a library of 3 device types with 16 or 24 representatives each. The initial characteristic values of the I - V curves are presented and the averaged I - V curve for each device type is discussed. While the short-circuit current decreases with increasing layer thickness, the open-circuit voltage and the fill factor of all devices is nearly identical. Consistently, the efficiency at the maximum power point decreases with increasing layer thickness. The time-evolution of the I - V curves differs from the behaviour observed in previous experiments: with forward bias all devices exhibit a rapidly increasing serial resistance with time. The origin of this effect has not been understood. The time dependence of the short-circuit current is fitted by a double exponential decay. In this experiment, both decay times and amplitudes are very similar for all devices. Long-term degradation is slightly slower for thicker devices. The effect of a temperature increase on the I - V curves is briefly described.

3.8.2 Experimental

ITO/CuPc/DMPTI/TiO₂/Al photovoltaic cells were prepared by evaporation onto an ITO substrate. The thickness of the DMPTI layer is varied in a three-step gradient as shown in Figure 3.37. The nominal layer thickness, i. e. the thickness estimated from the evaporation protocol, was 20, 25 and 30 nm. Later UV/Vis measurements, described in Section 3.5, indicate that the thickness varies between 20 and 50 nm. Such problems can arise if the evaporation rate changes during the preparation procedure. In the following discussion we use the corrected layer thickness and we will refer to 20 nm, 35 nm, and 50 nm devices in order to distinguish the three groups of devices. The experimental conditions for the long-term study were kept as in the experiment described in the previous section, except for the insertion of a water filter to reduce the temperature in the vacuum chamber and to imitate the solar spectrum more closely (see 3.6). With the filter inserted, the light intensity at the device surface is 39 mW/cm² and the average temperature in the vacuum chamber is around 49 °C. The interruption of the water cooling during the experiment led to a temperature increase to 68 °C for about 18 hours. Five devices did not work properly or were shorted. Their values have been replaced by the mean value of the respective device type.

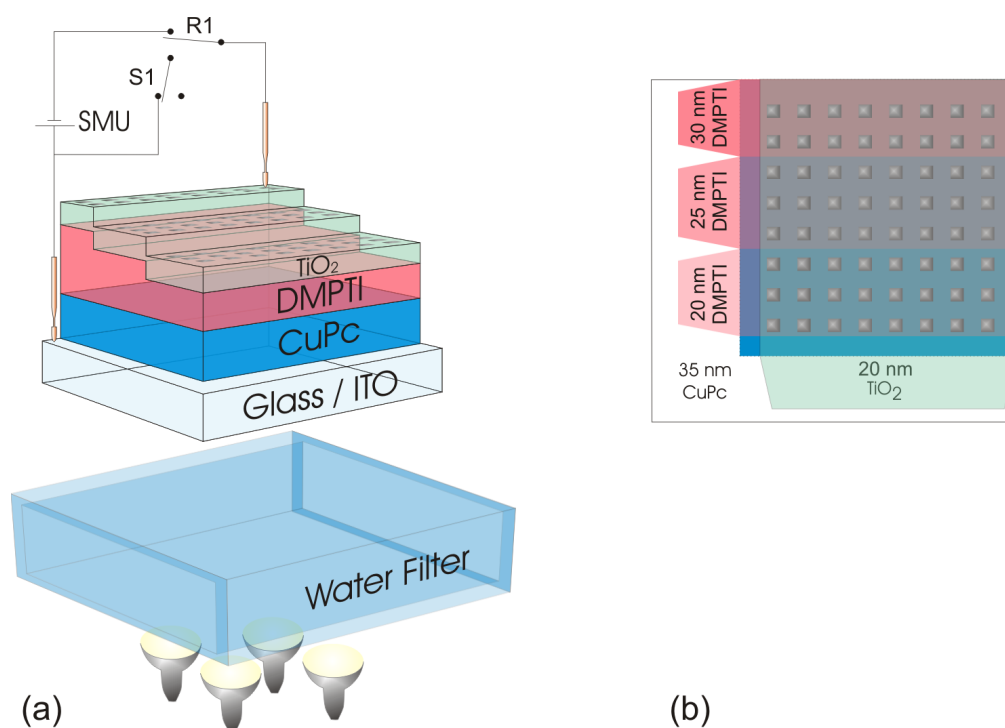


Figure 3.37: *Experimental setup: (a) perspective view of the layered structure with a step gradient of DMPTI. Illumination by a four-lamp array. (b) top view of the organic solar-cell library and the 64 aluminium electrodes.*

3.8.3 Results

Graph (a) in Figure 3.38 displays the DMPTI layer thickness as estimated from the combinatorial UV/Vis spectrometry; graph (b) shows the same results from a different viewpoint. The values clearly show the three-step structure. In addition, we observe a slight gradient within each step. This will most probably have resulted from the movement of the shadowing mask between the three steps, as the main shutter was not closed during the mask movement to guarantee an interruption-free layer deposition for all layers. So we can state here that combinatorial UV/Vis spectrometry is an ideal tool, not only to verify whether the evaporation procedure was successful but also to explicitly measure the layer thickness once the optoelectronic experiment is over. In this way we are able to correct for deviations from the expected device structure. One could even think of establishing the UV/Vis scanner in the glove box and characterising the device array before the optoelectronic measurement.

The graphs (c) and (d) in Figure 3.38 display the initial values of the short-circuit current (I_{SC}), the open-circuit voltage (V_{OC}), the fill factor (FF) and the power-conversion efficiency (η_{PC}) at the maximum power point (MPP). All the plots are oriented the same as graph (a). The layer thickness is clearly reflected in the characteristic values and devices within one row perform nearly identically. Small deviations in I_{SC} can be observed only at the borders where the ITO electrodes are contacted. This shows that both the preparation and the illumination of the devices reach the reliability required for a combinatorial analysis.

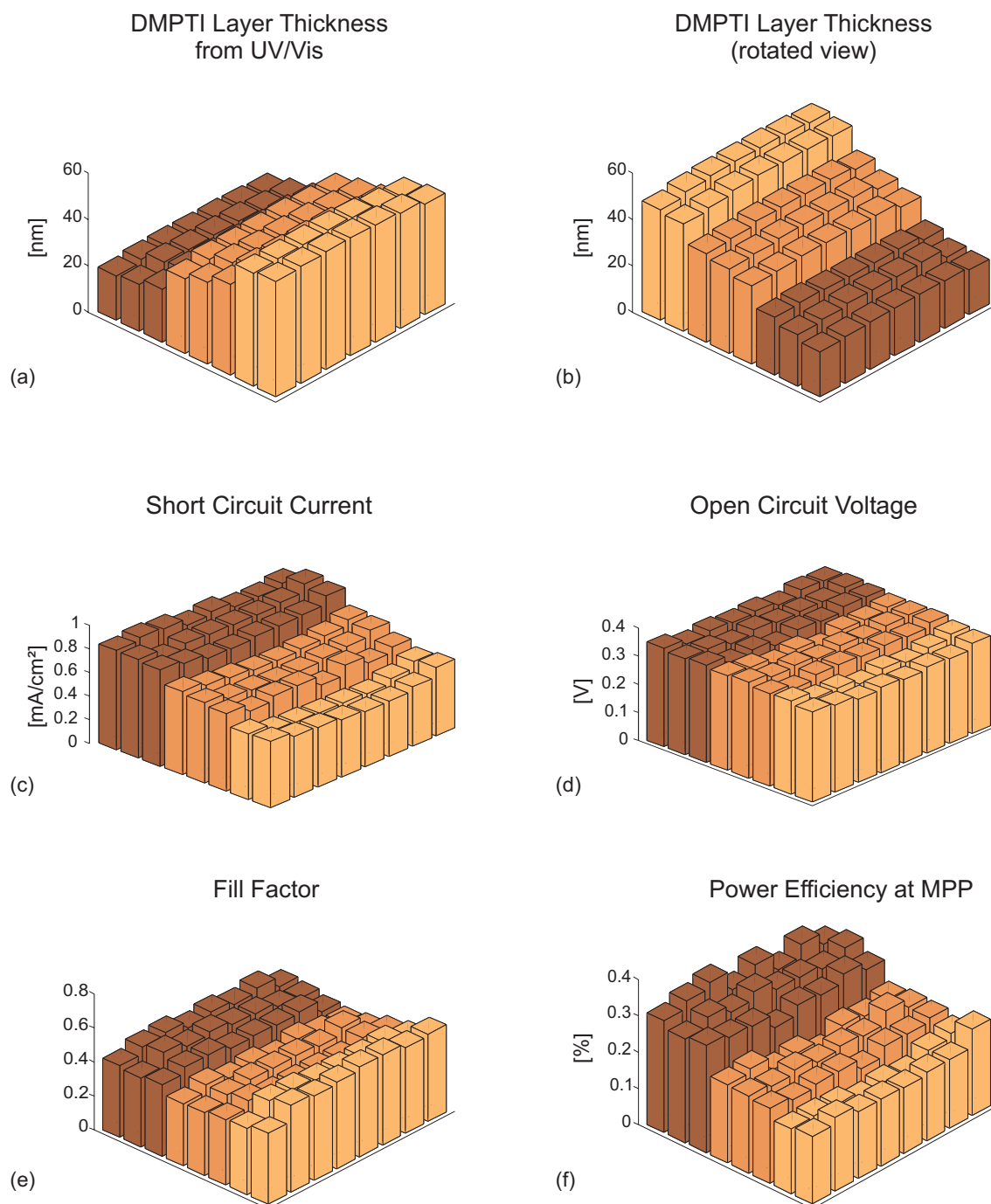


Figure 3.38: Characteristic values of $(ITO/CuPc/DMPTI/TiO_2/Al)$ devices with a DMPTI layer thickness varying between 20 and 50 nm at $t=0$ h. The thickness as estimated from UV/Vis spectrometry is displayed in (a) and (b), (a) being the reference orientation for all graphs except (b). I_{SC} decreases importantly with increasing layer thickness, V_{OC} decreases only slightly; the fill factors go through a minimum and η_{PC} decreases. Devices in one row perform nearly identically, which proves the accuracy of both the preparation and the illumination.

I_{SC} decreases from 0.8 mW/cm² down to 0.5 mW/cm² with increasing DMPTI layer thick-

ness. This dependence might seem counterintuitive at first glance. However, taking into account reflection at the aluminium electrode, interference and exciton diffusion, this behaviour can be well described. The necessary theory has been developed in Chapter 3.3 and a detailed discussion on the topic is given in the subsequent section (3.9). Here we concentrate on the degradation issues, as it seems that these devices show a different degradation than has been observed in other experiments. The reason for this deviation is, however, unknown. V_{OC} decreases slightly for thicker films, the mean values of the different types being 0.335 V, 0.325 V, and 0.306 V. The fill factors of the best devices are larger than 50 %. However, the values do not show a clear dependency on layer thickness. We find that the thickest devices exhibit slightly larger values (48 %) than the rest of the devices (42 %). We do not have an explanation for this fact and further experiments on a wider thickness range will have to be done to clarify this effect. The external power conversion efficiency is lower for thicker films, which is to be expected if I_{SC} decreases at constant V_{OC} .

We now turn to the degradation of the devices in vacuum. For this purpose we have plotted in Figure 3.39 the temporal evolution of the previously described characteristic values of each working device. The curves are coloured according to the dye layer thickness: red = 20 nm, green = 35 nm, and blue = 50 nm. Each plot in Figure 3.39 has an inset which shows the evolution of the average value of the respective device type. Devices with the same DMPTI layer thickness show a very similar time dependence with respect to each of the characteristic values. This indicates once more the homogeneity of experimental conditions.

Before we take a look at the shape of the curves, we shall briefly discuss the meaning of the characteristic values. As I_{SC} is proportional to the photon conversion efficiency, the time behaviour of I_{SC} reflects changes in all the processes involved, namely exciton generation, exciton diffusion, charge transfer, and charge collection (compare Equation 3.41). Considering that we did not see any relevant differences in the ellipsometric spectra before and after illumination (not shown here), we conclude that the electro-optical bulk properties of the materials did not significantly change. Hence, we do not expect any changes in η_{EG} and η_{ED} . Variations in I_{SC} should rather result from changes in the charge transfer and charge collection processes. V_{OC} in bulk heterojunction organic solar cells is mainly determined by the difference between the HOMO level of the electron donor species and the LUMO level of the acceptor material. The work functions of the electrodes play only a minor role, which can be explained by Fermi-Level pinning at the electrode/donor and at the electrode/acceptor interface [Bra01]. In consequence V_{OC} is temperature-dependent due to the shifting of the energy levels. Furthermore, V_{OC} will be sensitive to structural changes at the interface, as these will influence the Fermi-Level pinning. The fill factor is a measure of the shape of the I - V curve and is influenced by many parameters. Changes in the serial or in the shunt resistivity are the main influences on this characteristic value. Finally, the efficiency is a measure of the total performance of the device. Physical changes can hardly be deduced from this value as all of the previous parameters enter.

I_{SC} shows an important decrease with time. The first impression is that all curves are nearly parallel. To qualify the curve shape further, we fitted a double-exponential decay for each of the devices and plotted the result together with the data in Figure 3.39a. The parameters of the fit are discussed below. We observe that during the period of increased

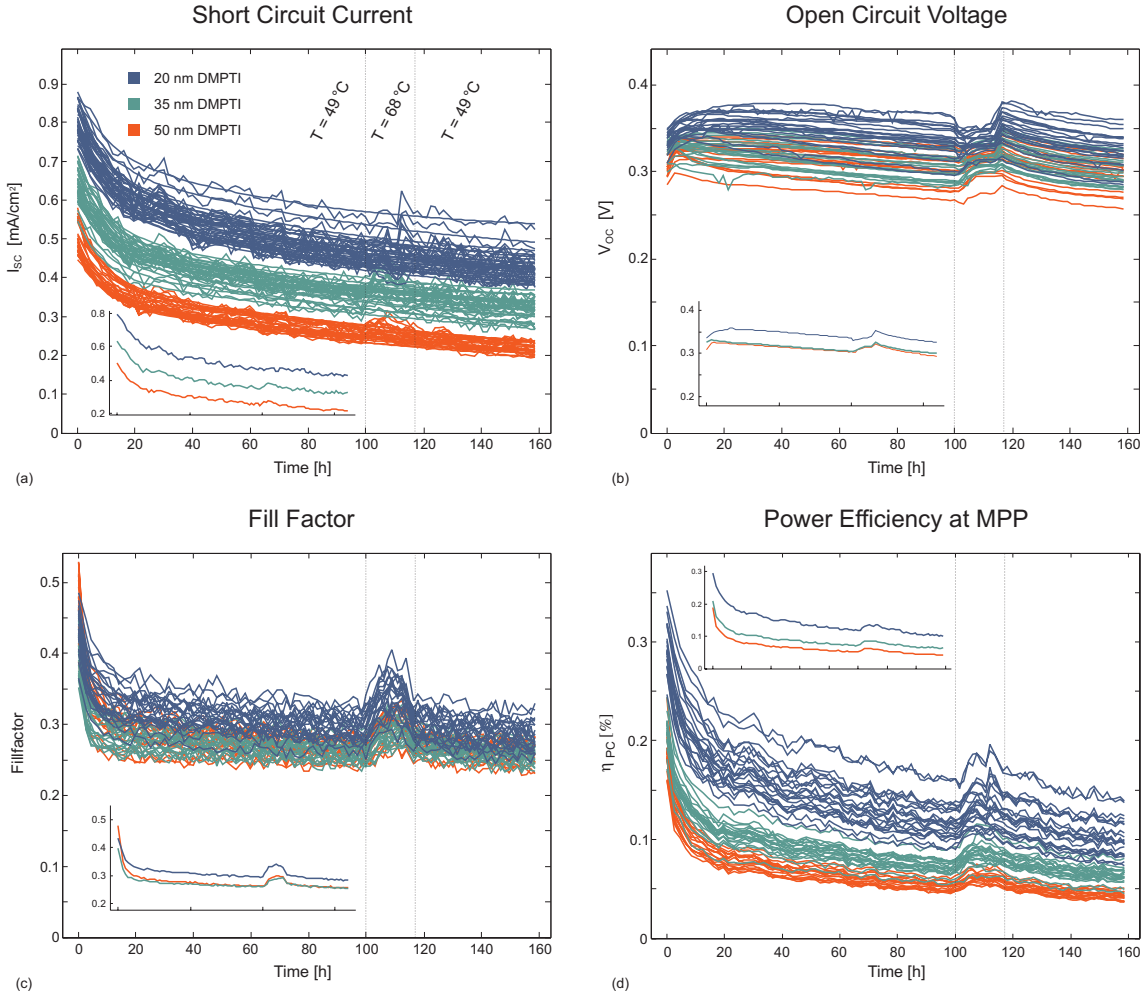


Figure 3.39: Time evolution of the characteristic values: (a) short-circuit current (I_{SC}), (b) open-circuit voltage (V_{OC}), (c) fill factor, and (d) power conversion efficiency at the maximum power point (η_{PC}). The curves are coloured according to the dye layer thickness: red = 20 nm, green = 35 nm, and blue = 50 nm. The insets of each graph show the respective mean values of a device type. For I_{SC} , we have plotted a double exponential fit together with the data.

temperature around $t = 100$ h I_{SC} rises slightly. In principle, temperature can affect all of the above-mentioned processes: exciton generation, exciton diffusion, charge transfer, and charge collection. As thermally separated excitons make up only a small fraction of the totally generated charge, η_{EG} should increase only very slightly if at all. Similarly, as thermal energies are small compared with the exciton binding energy, only little influence on η_{CT} is expected. Concerning η_{ED} and η_{CC} , both the exciton and the charge mobilities increase with temperature. As the life times of free electrons or holes is large compared with the travelling time through the device, the charge mobility is not a limiting factor. Therefore, we attribute the slight increase in I_{SC} mainly to the larger exciton mobility. The behaviour of V_{OC} is very different. All devices show an initial increase in V_{OC} and a subsequent slow decay. For thicker devices, the initial increase is faster, the slow process does not show a thickness dependence. Interestingly, the mean values of the 35 nm and

the 50 nm devices nearly coincide. At increased temperature, the 20 nm devices show a decrease in V_{OC} whereas the thicker devices show the opposite behaviour. Upon cooling down to the previous operating temperature, all devices show an increase in V_{OC} and a subsequent decay with a slightly higher time constant than the slow process observed before. At present we cannot interpret this finding. Temporally correlated with the initial increase in V_{OC} , we find a decrease in the fill factor, which then settles at an almost constant value. At an elevated temperature, the fill factor shows a significant increase but returns to the previous value on cooling down to the previous temperature. The efficiency at the maximum power point decays with time, which is not surprising since I_{SC} decreases at almost constant V_{OC} .

In order to compare the time development of I_{SC} qualitatively, we show in Figure 3.40 the fit parameters of a double-exponential model to each of the I_{SC} - t curves

$$I_{SC}(t) = a_0 + a_1 e^{-t/\tau_1} + a_2 e^{-t/\tau_2}, \quad (3.55)$$

with a_0 the offset, a_1 and a_2 the decay amplitudes, and τ_1 and τ_2 the respective time constants. As the time constants for the fast degradation process were all very close, we have chosen to fix this parameter at a value $\tau_1 = 10$ h for all devices. The fits well describe the time behaviour and thus suggest that at least two different processes contribute to the degradation. Our attempt to fit a single-exponential decay to the fill factor curves in order to separate the processes directly was not successful. Nevertheless, all I_{SC} curves converge towards an offset which shows the same thickness dependence as the initial I_{SC} values: the thicker the device, the lower the offset. The time constant τ_2 does not show a clear correlation with the dye layer thickness. The thickest devices exhibit larger time constants than the rest of the devices. Astonishingly, we find that both the fast and the slow decay amplitudes are nearly thickness-independent. For similar degradation processes one might have expected a constant ratio $a_i/I_{SC}(t=0)$. At present, we do not have an explanation for this finding.

To complete the degradation analysis we finally present the time development of the I - V curves. For this, we have calculated an average I - V curve for each group of devices and display the different curves in a rainbow colour scheme from red ($t = 0$ h) to blue ($t = 159$ h) for the 50 nm, 35 nm, and 20 nm devices (Figure 3.41). The insets show the curves with the full y-axis range. Already with the second measurement cycle all device types exhibit a significantly altered I - V characteristic: the slope around V_{OC} has diminished and the curve shape in the current-delivering quadrant has flattened. This flattening is then reflected in the fill factor, as described above. With increasing time, the curve takes on a more and more sigmoid shape. This finding cannot be explained solely by an increased serial resistivity. It is rather a sign of reduced hole injection from the ITO layer or reduced electron injection from the TiO_2/Al electrode. Charge *extraction*, however, seems less affected. Again, we cannot, at present, give any explanation for this finding. We are not going to speculate about its origin, particularly as in different experiments this behaviour has not reoccurred in this distinctness. For different experiments only a slight sigmoid shape was observed at very late stages of degradation (compare Figure 3.54).

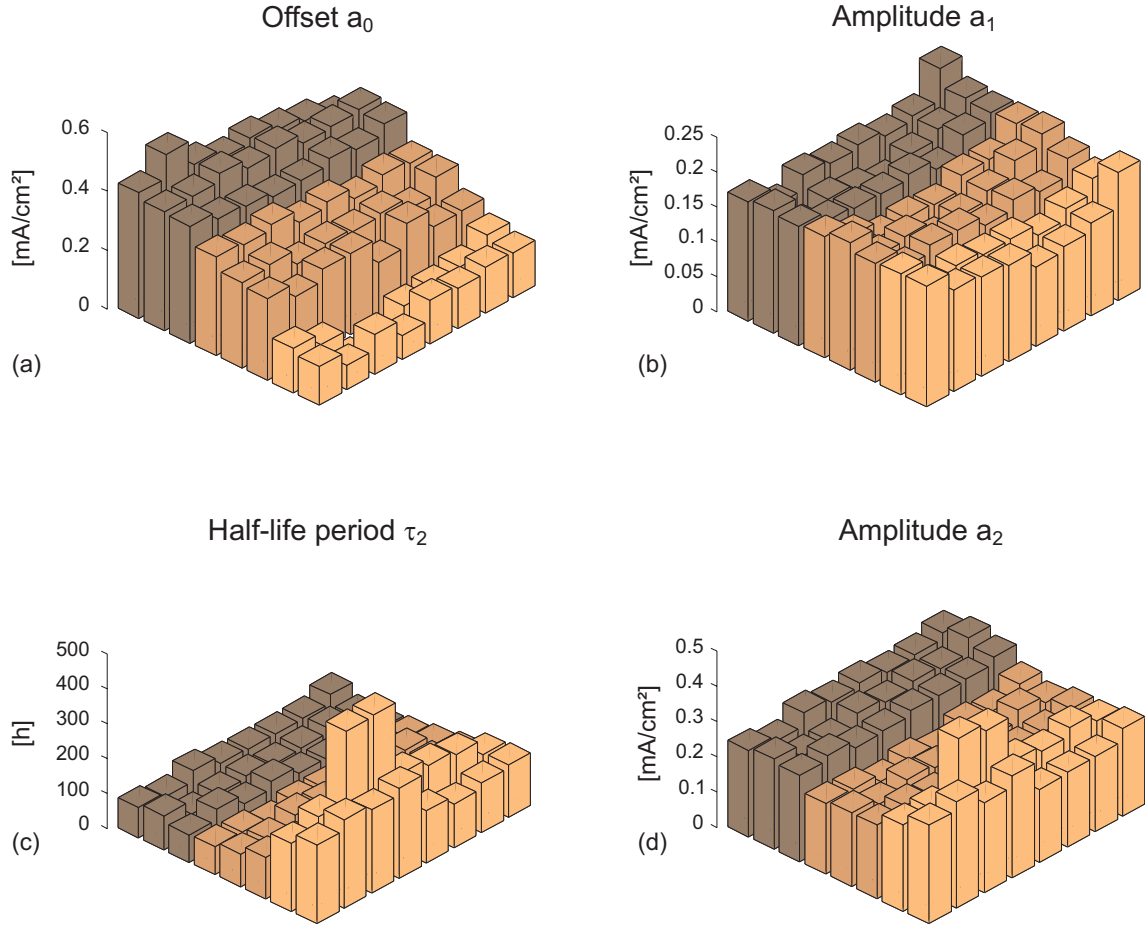


Figure 3.40: Model parameters for the double exponential fits to the $I_{SC}-t$ curves with a fixed value of $\tau_1=10$ h for all devices. All curves converge towards an offset which decreases with increasing dye layer thickness. The thickest devices show an increased time constant τ_2 which means that they degrade a little more slowly. The amplitudes a_1 and a_2 do not vary significantly.

3.8.4 Conclusion

We conclude that a step-gradient library of devices is very useful for checking the homogeneity of device production and testing. Once the homogeneity has been confirmed, a step-gradient library is well suited to distinguishing systematic from statistical variations. We have learnt from the experiment that more care has to be taken with the shutter movements in order to provide flat layers throughout a step. We have shown that for the given device structure, the short-circuit current does not necessarily grow with the thickness of the absorption layer. On the contrary, we find a strong decrease in I_{SC} with increasing layer thickness. This finding is investigated more closely in the following section. The changes in I_{SC} , V_{OC} , fill factor and η_{PC} have been observed for a period of 160 hours under constant conditions. The degradation has been quantitatively described for I_{SC} and found to follow a double-exponential law, in accordance with the results reported in the previous section. The $I-V$ curves were found to develop a sigmoid shape with increasing time. The influence of a temporary increase in temperature has been described.

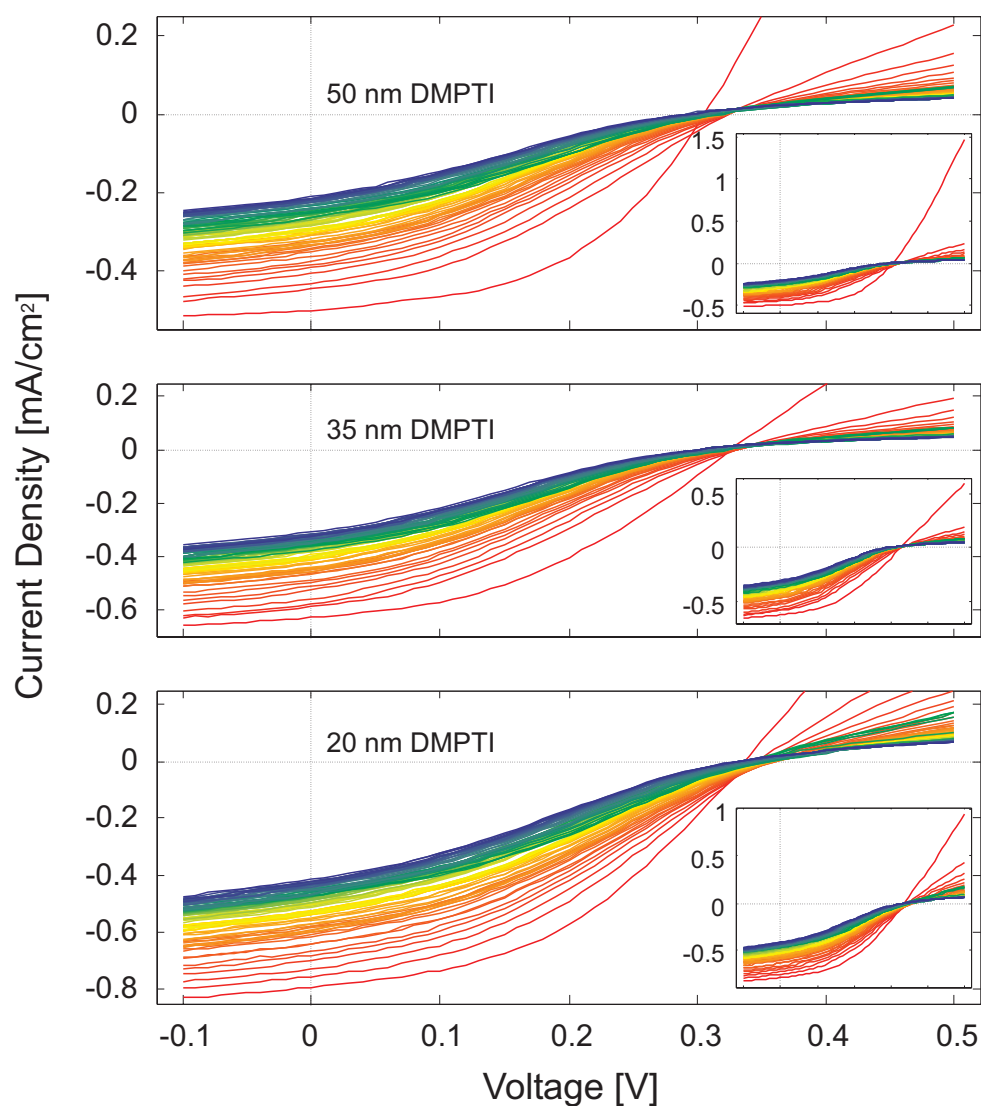


Figure 3.41: Time evolution of $I-V$ curves. The $I-V$ curves are averaged over devices of the same type: (a) 20 nm, (b) 35 nm (c) 50 nm DMPTI layer thickness. The curves are coloured in a rainbow colour scheme from red ($t=0h$) to blue ($t=159h$). The axes have been chosen so that the curve shape in the current-delivering regime is clearly visible. The full current range is displayed in the insets of each graph. With increasing time all devices develop a sigmoid shape, indicating a lower charge injection capability; charge extraction is less affected. The most significant change is observed from the first to the second measurement cycle.

3.9 Optical and Electronic Contributions in Organic Thin-Film Solar Cells

3.9.1 Abstract

Combinatorial studies of organic thin-film photovoltaic cells can separate the optical and the electronic contributions to the photocurrent. Applying the theory developed in 3.3, we can explain the counterintuitive thickness dependence of the photocurrent found in 3.8. Moreover, we find that the optical effect of TiO_2 alone cannot explain the augmentation of the short-circuit current observed in previous experiments ([The02] and 3.7). The assumption of a second charge transfer zone at the DMPTI/ TiO_2 interface can explain the measurements and leads to an estimate of the ratio of the exciton diffusion lengths in CuPc and DMPTI of $\approx 8/5$ ⁵.

3.9.2 Introduction

Different studies have shown that the introduction of additional functional layers in donor/acceptor organic solar cells can enhance their performance significantly [Hir92, Tak00, Bre01, Peu00, Peu01]. TiO_2 has been proved to serve as an exciton dissociation surface [Bre01], poly(3,4-ethylene dioxothiophene):poly(styrene sulfonate) (PEDOT:PSS) has been found to facilitate hole injection and to increase the built-in potential [Peu01, Loi03]; in organic light-emitting diodes (OLEDs) it has also been shown to hinder oxygen-induced aging at the ITO electrode [Sco97, Bro99]. LiF is used as an electron injector in combination with an aluminium cathode, and bathocuproine (BCP) has been shown to be an efficient exciton-blocking layer in both photovoltaic cells [Peu00, Peu01] and OLEDs [O'B99]. In our own experiments [The02, Hän02], an additional TiO_2 layer resulted in higher efficiencies of single heterojunction organic solar cells. Until now, the function of this layer has not been understood quantitatively. Both, an electronic and an optical effect were proposed as possible explanations; however, it was not possible to determine their relative importance. For polymer/ C_{60} and CuPc/ C_{60} heterojunction cells, it has been shown by layer thickness variation that the light intensity at the heterojunction determines the photocurrent and that interference with the light reflected from the electrode has to be taken into account [Pet99, Stü01]. A comparison of the experimental data with predictions from a standing-wave argument led to good agreement in the periodicity of the photocurrent. Electronically, the interface morphology, exciton diffusion, charge carrier mobility [Bre01], and charge transfer efficiency [Hir92, Tak00] have been discussed in this context. Especially the latter is expected to play an important role when the strong electron acceptor titanium dioxide (TiO_2) is used.

In this work, we investigate the photocurrent of a (ITO/copper phthalocyanine/perylene dye/Al) cell and a (ITO/copper phthalocyanine/perylene dye/titanium dioxide/Al) cell as a function of the perylene dye layer thickness. In addition to the experimental data, we present a model that describes the short-circuit current of these cells. The charge

⁵The results of this chapter are published in [Hän03b]

generation probability is estimated from the intensity profile that is calculated via a matrix transfer algorithm, taking into account the full illumination spectrum. Careful comparison of data and theory reveals that the introduction of an additional titanium dioxide layer modifies the short-circuit current by two effects: optically, by shifting the charge transfer interface with respect to the light intensity profile, and electronically, by introducing a second heterojunction where additional charge transfer can occur. Thickness-dependent studies can clearly separate these two effects and can yield an estimate of the ratio of the exciton diffusion lengths in the absorbing media. The high accuracy in thickness variation that is necessary for such a study is achieved by the combinatorial fabrication and testing of the devices. We can furthermore show that the introduction of the titanium dioxide layer leads to a second degradation process.

3.9.3 Experimental Setup

A two dimensional array of 64 organic multi-layer solar cells is prepared by successive evaporation of 30 nm copper phthalocyanine (CuPc), a perylene dye (DMPTI, see *Experimental*) gradient (27–57 nm), and 30 nm titanium dioxide onto an Indium Tin Oxide (ITO)-coated glass substrate. The outer columns are shadowed by a mask during TiO₂ evaporation. The top layer consists of an array of 8×8 aluminum electrodes, resulting in two device types with varying perylene thickness with at least two devices per type and layer thickness, each 0.12 cm² in size (Figure 3.42). The photocurrent is measured under white light illumination in vacuum (5×10^{-5} mbar) and the devices are prevented from heating up by a water filter. The optical constants of the layer materials necessary for the theory were obtained by spectroscopic ellipsometry and are displayed in Figure 3.43. A map of the short-circuit current densities (I_{SC}) of all devices directly after preparation is provided in Figure 3.44A. Devices that did not work properly are marked with a filled box. As for some devices the electrode was misaligned with respect to the TiO₂ layer, Figure 3.44B shows the same map with the values for these devices suppressed. From this map we see that identically prepared devices show very similar performance.

3.9.4 Theory

Based on the refractive indices of the different materials, we have used a transfer matrix algorithm (see 3.3.1 and [Hea65]) to calculate the $|E|^2$ profile within the organic layers for normal incidence. As the longitudinal coherence length of the light is shorter than the thickness of the glass substrate (1 mm), we assume coherent superposition within the organic layers and incoherent superposition when the glass layer is involved.

For exciton diffusion lengths lower than the film thickness and much lower than the wavelength of the light, the optical field near the charge transfer zone determines the photocurrent [Stü01]. In our model, we additionally incorporate exciton diffusion by assuming that all excitons generated within a range x_D from the interface contribute to the photocurrent. Considering that the local exciton generation probability is proportional to $k n |E|^2$, where k is the extinction coefficient and n the refractive index of the material, we calculate the number of separated excitons at the interface by integrating this quantity

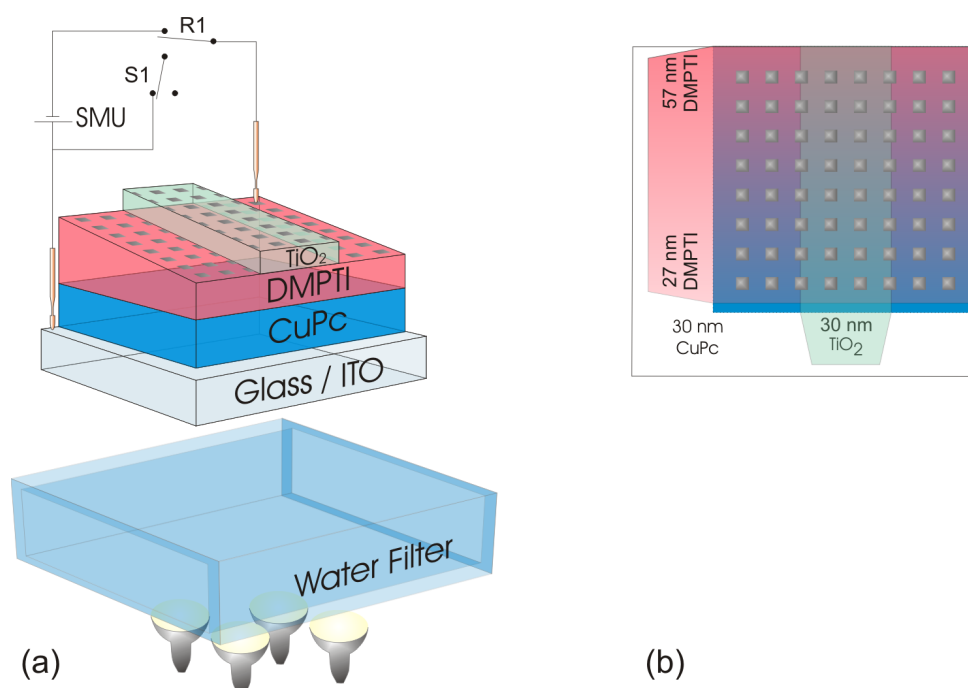


Figure 3.42: *Experimental setup: (a) perspective view of the layered structure with a linear gradient of DMPTI, partly covered with TiO_2 . Illumination is provided by a four lamp array through a water filter. (b) top view of the organic solar cell library and the 64 aluminium electrodes.*

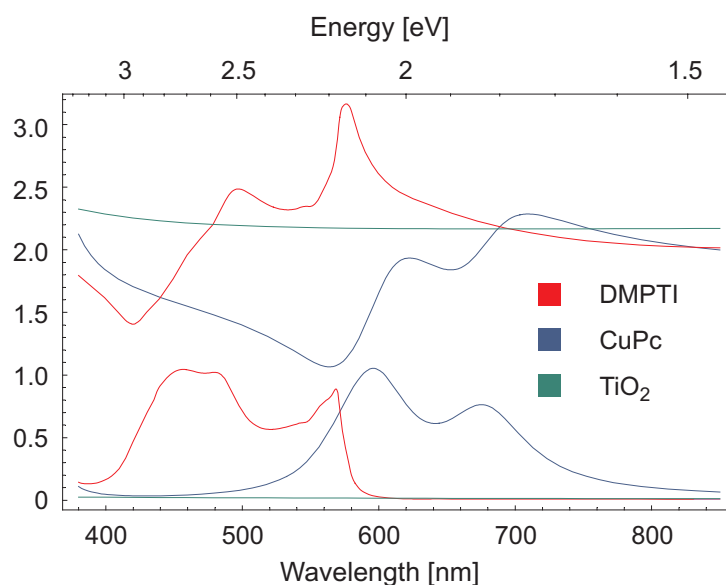


Figure 3.43: *Extinction coefficient and refractive index of the layer materials as obtained by variable angle spectroscopic ellipsometry.*

over the range x_D . x_D should be of the order of the exciton diffusion length and was chosen to be 8 nm for CuPc and 5 nm for DMPTI. Summing up the contributions of all absorbing layers at all interfaces provides a measure for the photocurrent. As we use white light, we have to integrate the photocurrent over all wavelengths weighed with the

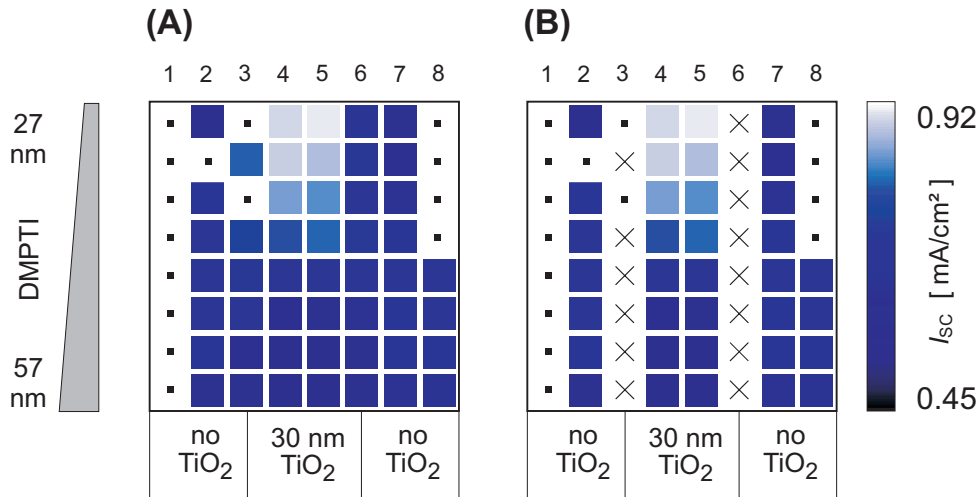


Figure 3.44: *Short-circuit current density for the devices of interest. Devices that exhibited a short are marked with a filled box. (A) shows all working devices, while in (B) the values of some devices are suppressed and marked with a cross, since the aluminium contacts were accidentally placed on the border of the TiO₂ layer. The values are displayed to show the homogeneity of the device array.*

spectral intensity of our light source. Possible losses due to recombination and charge carrier extraction efficiency are accounted for by an overall scaling factor.

3.9.5 Results and Discussion

Short-Circuit Current

Figure 3.45A displays the $|E|^2$ profile within the devices with and without TiO₂ layer, calculated for a wavelength of 550 nm. The different curves show the calculation for different DMPTI layer thickness, ranging from 27 (red) to 57 nm (blue). The zero position is chosen to be at the CuPc/DMPTI interface. We recognise that without a TiO₂ layer, the varying DMPTI layer thickness leads to only a small variation in the intensity at the CuPc/DMPTI interface. An additional TiO₂ layer acts as an optical spacer and shifts the intensity maximum into the DMPTI layer, thus leading to a strong decrease in $|E|^2$ with increasing DMPTI layer thickness. The resulting contributions to the photocurrent from the different absorbing media are shown in Figure 3.45B. Obviously the behaviour of $|E|^2$, discussed above, is reflected in the photocurrent. We note that the contribution to the photocurrent from the DMPTI/TiO₂ interface shows a decreasing tendency with increasing layer thickness, due to the absorption in the preceding layer.

Finally, we calculate the total short-circuit current and compare it with the data measured (Figure 3.46A). We have adjusted the calculated photocurrent with an overall scaling factor to the data of the single heterojunction devices. As a second fit parameter we have scaled the nominal DMPTI layer thickness (25–53 nm) with a constant factor, to account for a possible inaccuracy of the quartz crystal calibration. Allowing for a correction factor of 1.08, we find excellent agreement between the measured and the predicted photocurrent.

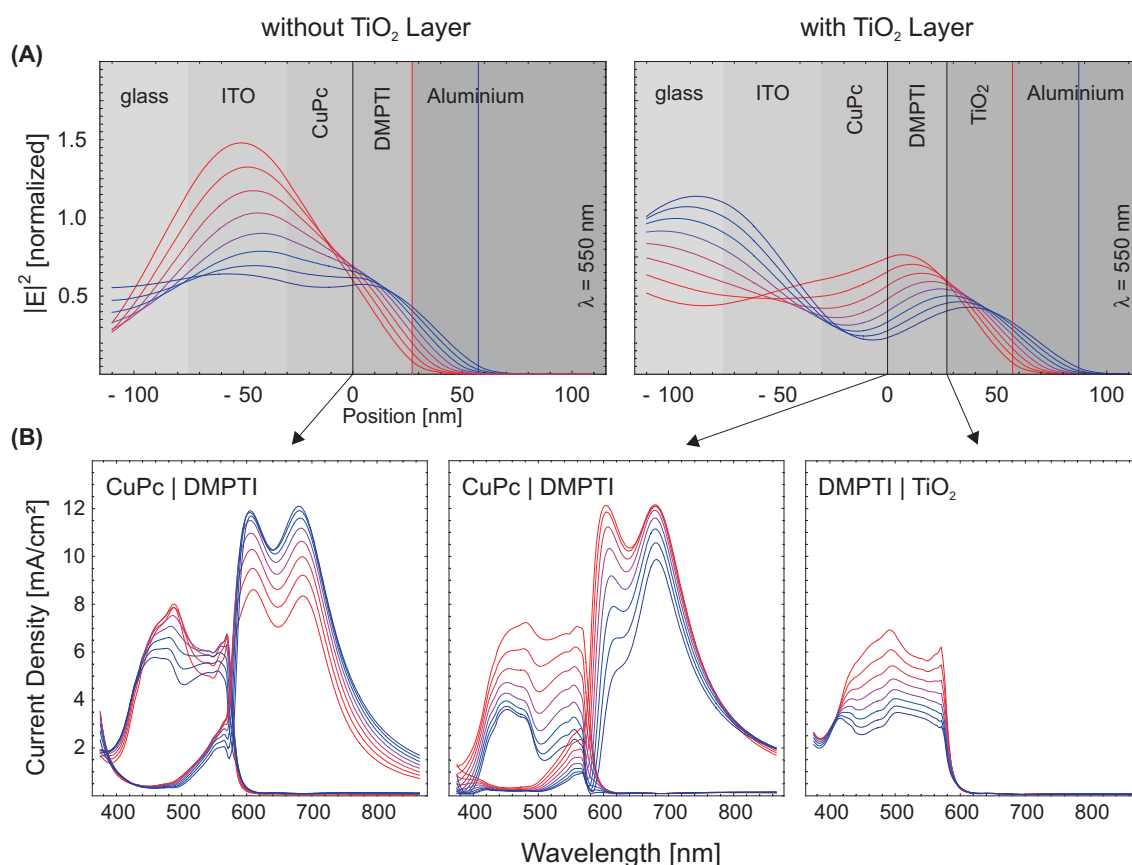


Figure 3.45: (A) $|E|^2$ profile in the solar cells for a wavelength of 550 nm. It is calculated by the matrix transfer algorithm assuming coherence within the organic layers and loss of coherence within the glass substrate. (B) Contribution to the photocurrent at the interfaces of CuPc/DMPTI and DMPTI/TiO₂ as a function of the wavelength. The colours from red to blue indicate the order of the curves with increasing DMPTI layer thickness (27–57 nm). The photocurrent is calculated from $|E|^2$ weighed with the extinction coefficient and the refractive index and integrated over a range of 8 nm in CuPc and 5 nm in DMPTI in order to take into account the diffusion of excitons in the respective materials.

Once these two parameters have been fixed, our model is able to predict the short-circuit current for the double-heterojunction devices. The solid and the dotted line display the prediction with and without charge transfer at the DMPTI/TiO₂ interface being taking into account.

We can see clearly that the optical effect of TiO₂ alone cannot explain the data measured. Instead the data shows a significant offset. We suggest that this results from additional free carriers that are generated from excitons at the DMPTI/TiO₂ interface that otherwise would have been quenched by the cathode. Hence, the TiO₂ layer not only acts as a blocking layer but also builds a charge transfer interface together with the DMPTI layer. Figure 3.47 shows the corresponding energy level diagrams with the possible charge transfer processes sketched. If we assume that the major part of the free carriers in the DMPTI layer does not recombine, the photocurrents generated at the two interfaces add; this is different from the situation in multi-stack devices, where electrodes are placed

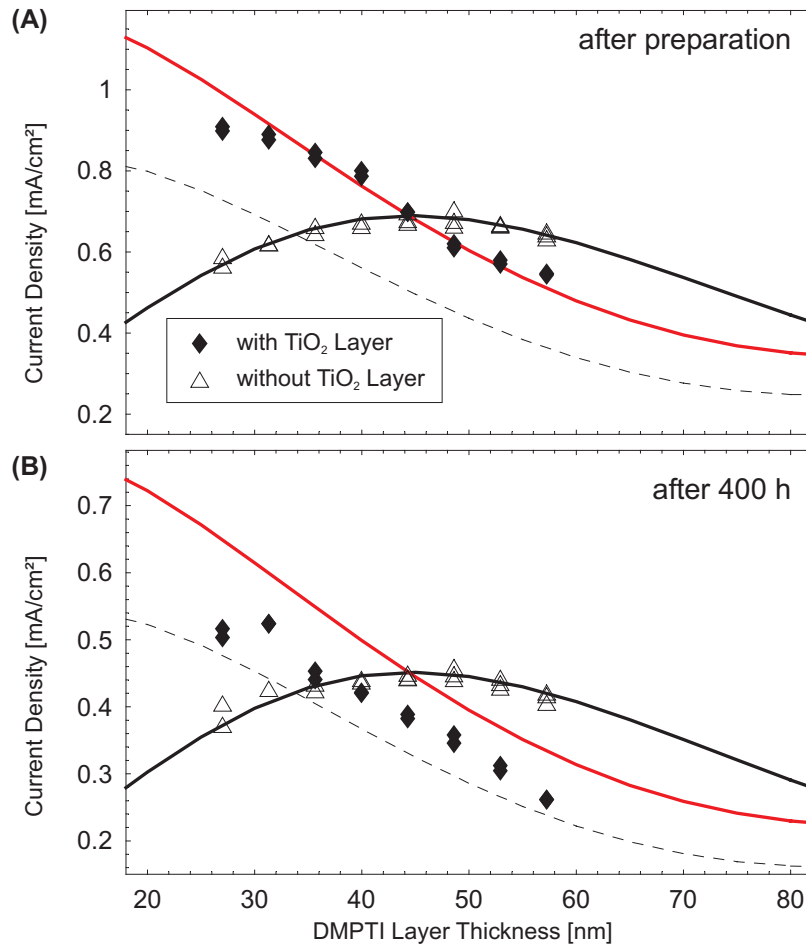


Figure 3.46: Short-circuit current density as a function of the DMPTI layer thickness after preparation (A) and after 400 h of illumination (B). The diamonds and triangles show the data for layers with and without TiO₂. The theoretical curves are calculated assuming charge separation in the vicinity of the two heterojunctions (red). The dotted line shows the calculation when we assume that there is no charge separation at the DMPTI/TiO₂ interface. The adjusted parameters are an overall scaling factor, a correction factor for the DMPTI layer thickness and the exciton diffusion length in DMPTI.

between consecutive photovoltaic cells and where the open-circuit voltages add. If we choose an exciton diffusion length of 5 nm in DMPTI the theory (solid line) can nicely fit the data observed (diamonds). Alternatively, a higher charge extraction efficiency for the double-heterojunction devices could explain the higher short-circuit current observed. In order to exclude this effect playing a major role, we have studied the shape of the I - V curves. Figure 3.48 shows the I - V curves of single and double-heterojunction devices with identical DMPTI layer thickness (44 nm). We have selected these two devices because for this thickness the optical and electronic effect cancel and both devices exhibit nearly the same initial short-circuit current. A better charge extraction efficiency should result in a higher slope at $V > V_{OC}$ or a lower slope at $V = 0$ Volt, both resulting in a higher fill factor [Ker00]. Neither of the two effects is observed. On the contrary, the slope at $V > V_{OC}$ is lower for devices with an additional TiO₂ layer, indicating that the layer leads

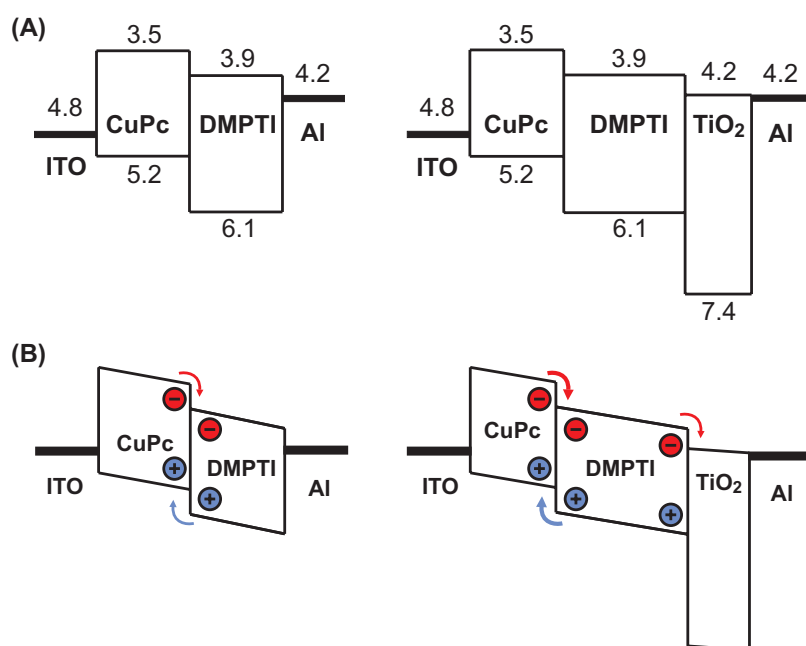


Figure 3.47: Energy-level diagram and charge transfer processes. (A) Flat-band diagram with the energies given in eV. (The HOMO and LUMO energies for CuPc are taken from [Hil99], the values for DMPTI are estimated from [Ito00]). (B) Sketch of the charge transfer processes at the interfaces for a short-circuited device under illumination.

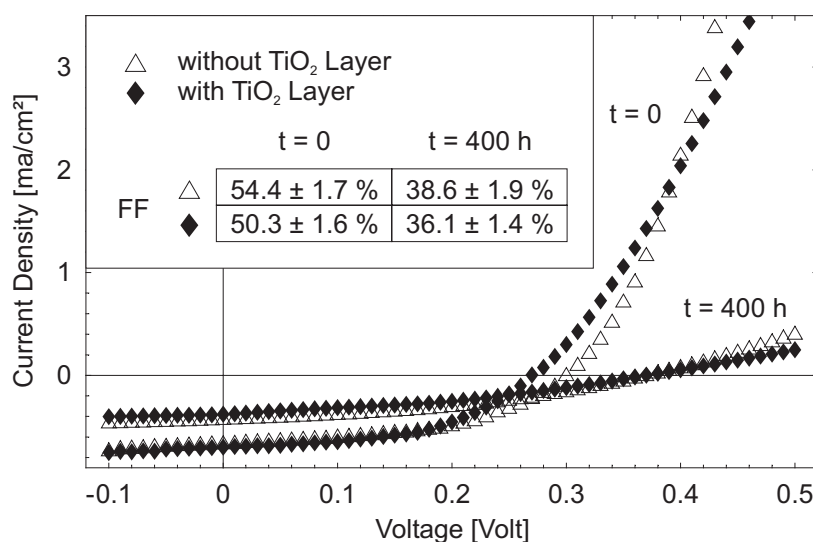


Figure 3.48: I - V curves of a single and a double-heterojunction device with a DMPTI layer thickness of 44 nm at $t=0$ h and $t=400$ h. The thickness is chosen so that at $t=0$ h the devices with and without TiO_2 exhibit the same I_{SC} . At $t=400$ h, the degradation is clearly visible in the shape of the I - V curves and consequently in the fill factors (FF). At $t=0$ h the fill factors differ by 4 %, an indication that either charge extraction or charge transport is less effective in TiO_2 devices.

to a higher serial resistivity, resulting in a 4 % lower fill factor: the fill factors are nearly constant for a device type, the average fill factor being $54.4 \pm 1.7 \%$ and $50.3 \pm 1.6 \%$ for

the single and double-heterojunction devices respectively. From this we conclude that the increased serial resistivity is not due to increased film thickness. We rather assume that partial recombination of free carriers within the DMPTI layer is responsible for this effect. Hence, we conclude that we do have a relevant contribution to the photocurrent from charges separated at the DMPTI/TiO₂ interface.

We now take a closer look at the exciton diffusion range. The choice of $x_D(\text{CuPc}) = 8 \text{ nm}$ is somewhat arbitrary and inspired by the values of 10 nm for CuPc and 3 nm for PTCBI (3,4,9,10-perylenetetracarboxylic bis-benzimidazole) found by Peumans *et al.* [Peu03]. Larger values of x_D are compatible with the data as well, if we adjust the overall scaling factor accordingly. We can, however, define an upper bound of 20 nm to $x_D(\text{DMPTI})$ because otherwise the short-circuit current is predicted to increase with increasing DMPTI layer thickness, which is not observed. The shape starts to deviate significantly from the measurements for values of $x_D > 20 \text{ nm}$. This seems to corroborate the finding of Peumans *et al.* that the exciton diffusion range in CuPc and perylene derivatives is smaller than could be expected from earlier work by other groups [Bul96b, Cho96, Cho97, Ker00]. Turning once more to Figure 3.46A, we have seen that the optical effect of the TiO₂ layer alone shifts the I_{SC} curve to the left and that including a second charge transfer zone in the model can explain the observed offset of the data measured. This offset is determined by the number of charge carriers that are separated at the second interface. As our model assumes that the charge carrier extraction probability at both interfaces is identical, the only parameter that controls the height of the offset is $x_D(\text{DMPTI})$. We have therefore varied this parameter and find that $x_D(\text{CuPc}) / x_D(\text{DMPTI}) \approx 8/5$ if we accept that the observed offset results from the second charge transfer zone alone. A value of 5 nm for $x_D(\text{DMPTI})$ accords quite well with the value of 3 nm for the similar substance PTCBI. In order to more deeply investigate this effect we are currently setting up a combinatorial photocurrent spectrometer that should allow us to distinguish the charge transfer processes at the two interfaces.

Finally, we have studied the degradation of the devices over a period of 400 hours. Within this period, the short-circuit current dropped to nearly half of its initial value (Figure 3.46B, note the different scales for A and B). Accounting for the degradation with an overall decrease in efficiency, we have once more fitted our model to the bilayer devices. The prediction for the double-heterojunction devices, though, is not met by the data, meaning that some additional degradation involving the TiO₂ layer must have taken place. At this point we are not able to decide whether this is due to a lower charge extraction efficiency or whether the charge transfer at the DMPTI/TiO₂ interface has become less effective. Both explanations can be reasonably fitted with our model. With the planned setup we will be able to answer this question. We can, however, already exclude current-induced degradation: during the illumination period, half the devices were open-circuited, while the other half were short-circuited and no significant difference in any characteristic value could be seen.

Remaining Characteristic Values

As discussed above, the additional TiO₂ layer leads to faster degradation. From the experiment presented in Section 3.8 we have hints that there might be a thickness dependence

of the degradation, but the results were not conclusive.

In this section we take a closer look at the characteristic values of the photovoltaic cells and their degradation behaviour. All devices show a double-exponential decay of I_{SC} . Both V_{OC} and the fill factor follow single-exponential laws with time constants of the same order as found in the double-exponential law for I_{SC} . This suggests that there are two degradation mechanisms that affect V_{OC} and FF separately. Final conclusions about the origin of the degradation cannot be drawn yet.

Figure 3.49 displays the characteristic values for the devices at $t = 0$ h. The graphs (a) and (b) show the DMPTI layer thickness as estimated from UV/Vis spectrometry from different viewpoints (see 3.5), graph (a) being the reference orientation for all other 3D graphs presented in this section. The devices where the electrodes have been misplaced are suppressed from the evaluation, values of shorted devices have been replaced by the mean value of the working devices of the respective device type. As all devices of the first column (all without TiO_2) were shorted, this column displays the average of devices without TiO_2 . The fact that these values coincide with the values of the neighbouring column shows the reliability of the data.

The short-circuit current has been discussed above and is repeated here to present all the characteristic values coherently in a single figure. V_{OC} does not show a relevant dependence on the layer thickness and only a slightly lower value for devices with TiO_2 ($\langle V_{OC} \rangle_{wo. TiO_2} = 0.299$ V and $\langle V_{OC} \rangle_{w. TiO_2} = 0.283$ V). Also from theory a large change in V_{OC} is not expected, as firstly the LUMO of TiO_2 and the work function of aluminium are identical and secondly the Fermi-Level of the cathode only slightly influences V_{OC} , as discussed in [Bra01] and mentioned in 3.8. The values of V_{OC} are lower than found in previous experiments (Section 3.8 and [The02]) but will reach comparable values after ≈ 20 h, as discussed later in this section. The systematic variation of V_{OC} in the form of a chess board pattern, clearly visible in the middle columns, results from the contacting of the devices, as explained in 3.6.2. The fill factor also varies only slightly: the additional TiO_2 layer reduces the FF from 54.4% to 50.3%. V_{OC} and the FF being nearly constant, the power efficiency η_{PC} mainly reflects the variation of I_{SC} .

We now turn to the time dependence of the characteristic values. Figure 3.50 displays I_{SC} , V_{OC} , FF and η_{PC} for a duration of 400 h of the experiment. After that time the water cycle was stopped, which led to an increase in temperature from ≈ 49 °C to ≈ 68 °C (The temperature was not recorded but we were able to estimate it from earlier measurements.) Then the illumination was turned off and the measurement was interrupted for a period of 440 h. The devices were kept in vacuum. After that time the measurement was continued under normal conditions for three cycles.

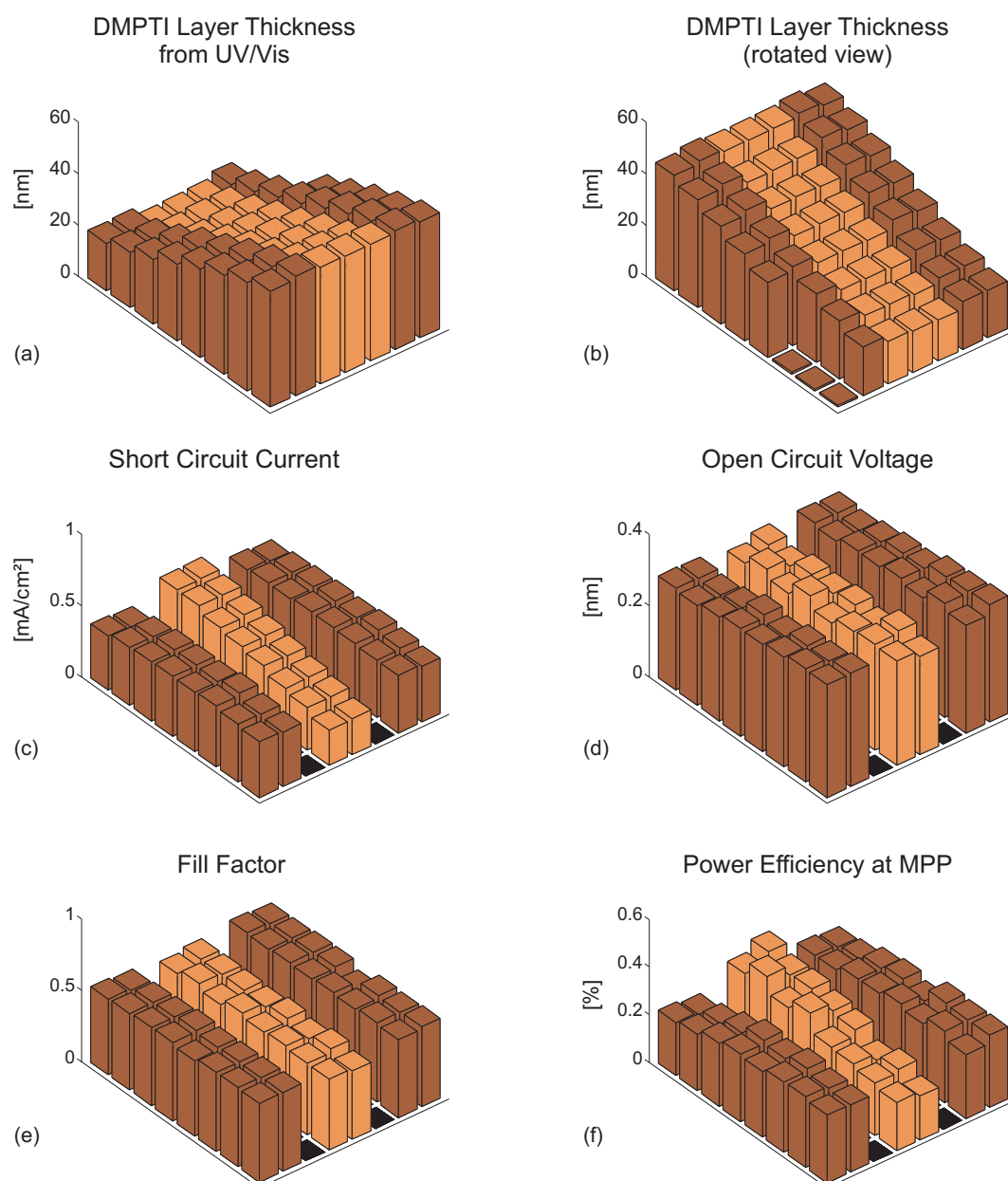


Figure 3.49: Characteristic values of $(ITO/CuPc/DMPTI/Al)$ devices (dark) and $(ITO/CuPc/DMPTI/TiO_2/Al)$ devices (light) with a DMPTI layer thickness varying between 20 and 50 nm at $t=0$ h. (a) and (b) Thickness as estimated from UV/Vis spectroscopy, (a) is the reference orientation for all other graphs. In one corner of the substrate all organic layers were removed after the long-term test in order to determine the ITO thickness with ellipsometry. These spots show a zero-thickness in graph (b). The behaviour of I_{SC} has been discussed earlier in this chapter. V_{OC} is independent of the layer thickness, but is slightly reduced from $\langle V_{OC} \rangle = 0.299$ V to $\langle V_{OC} \rangle = 0.283$ V by the TiO_2 layer. Similarly, the fill factors are slightly reduced from $\langle FF \rangle = 54.4 \pm 1.6$ % to $\langle FF \rangle = 50.3 \pm 1.6$ % by the device structure. V_{OC} and FF being nearly constant, η_{PC} reflects the behaviour of I_{SC} .

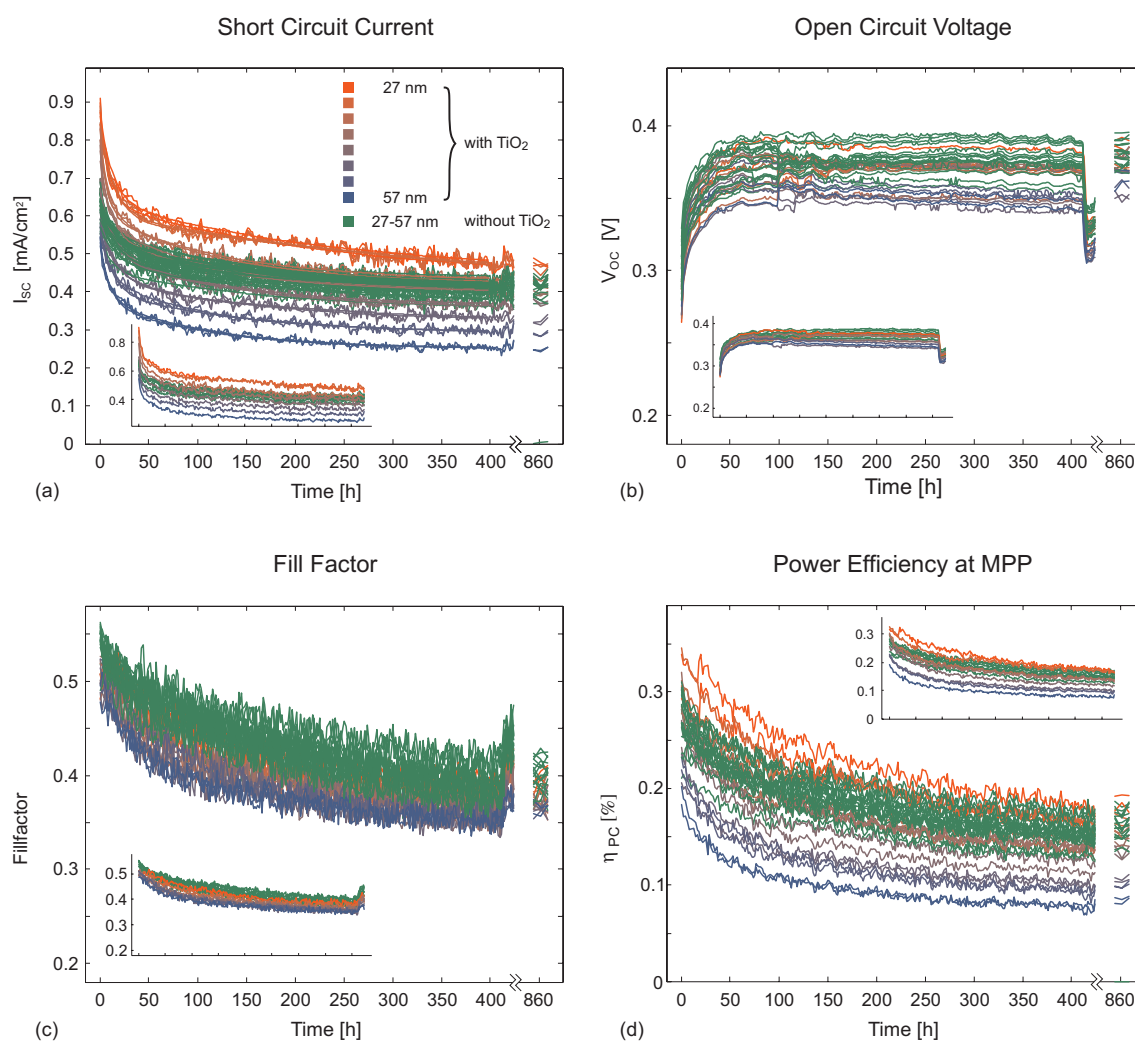


Figure 3.50: Time evolution of the characteristic values: (a) short-circuit current (I_{SC}), (b) open-circuit voltage (V_{OC}), (c) fill factor, and (d) power conversion efficiency at the maximum power point (η_{PC}). The curves of devices with TiO_2 are coloured according to the dye layer thickness from red (27 nm) to blue (57 nm). The curves of devices without TiO_2 are all coloured green, as their values are very similar. The insets of each graph show the respective mean values of a device type. For I_{SC} , we have plotted a double exponential fit together with the data.

All devices show a fast and a slow decay in I_{SC} that can be fitted by a double-exponential law. The fits are displayed together with the data; the resulting parameters are given in Figure 3.52. This finding is in contrast to the results of Section 3.7 and published in [Hän02], where single heterojunction devices followed a single exponential model. We note, however, that the conditions of the two experiments are different: the previous experiments were performed without a water filter. Consequently the intensity as well as the temperature were much higher ($I = 80 \text{ mW/cm}^2$, $T = 80 \text{ }^\circ\text{C}$). Moreover, the ITO layer was thicker (80 nm) and, for experimental reasons, we had not recorded I - V curves during the first 4 h. The fast degradation may have occurred during this period, since both higher temperature and higher intensity can accelerate the degradation.

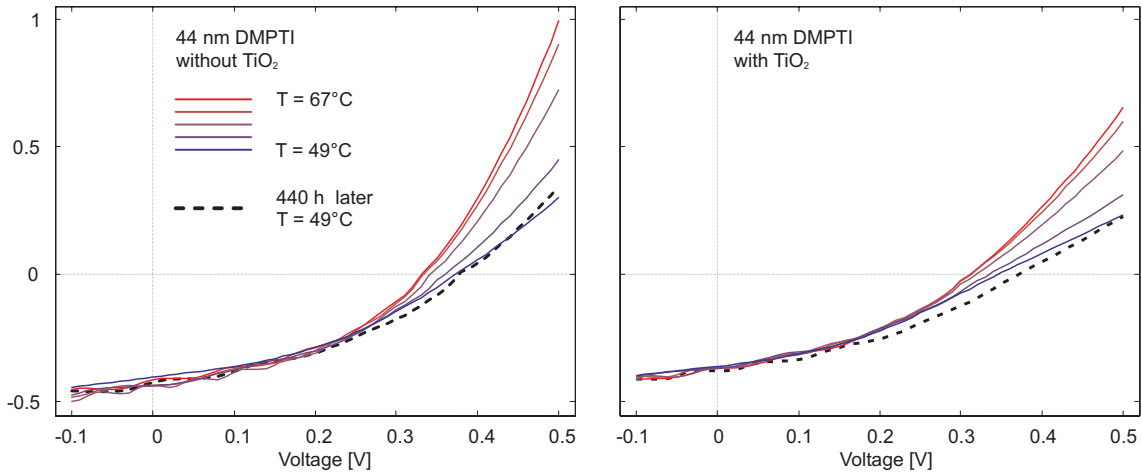


Figure 3.51: Influence of temperature and influence of storage on the I – V curves. The curves are coloured from blue ($T \approx 49^\circ\text{C}$) to red ($T \approx 68^\circ\text{C}$). The dotted curve has been recorded after a storage time in vacuum of 440 h.

V_{OC} exhibits comparatively low values at the beginning and increases to values found in earlier experiments (see Section 3.8 and [The02]) within the first 50 h. This increase can be fitted reasonably well by a single-exponential behaviour with time constants of the same order as the fast decay in I_{SC} . The fill factors show a weak time dependency, which also can be fitted by a single-exponential decay; this is different from what has been found in the previously discussed experiment (Section 3.8), where we observed a strong initial decrease in FF. Together with the I – V curves presented below (Figure 3.54) this finding strengthens the assumption that the degradation observed in Section 3.8 was atypical.

The temporary temperature increase at the end of the measurement affects the characteristic values similarly to what has been described in Section 3.8. I_{SC} increases slightly, V_{OC} decreases—this time for all devices—and reaches the previous values after the period of elevated temperature. The fill factor increases, as observed before. Interestingly, the efficiency is hardly time-dependent, as the influence of V_{OC} and the FF cancel. Figure 3.51 shows the I – V curves of two selected devices during the temperature increase. The dotted line is the I – V curve measured after the storage period of 440 h without illumination in vacuum. For both devices the slope of the I – V curves increases, which is expected due to higher charge carrier mobilities. The effect is more pronounced for the single heterojunction devices. In both cases, the I – V curves recorded after the storage period coincide reasonably well with the I – V curves measured directly before the temperature increase. In other words, without illumination no further degradation is observed.

Figure 3.52 displays the fit parameters for the double-exponential decay of I_{SC} , using the same notation as before (Equation 3.55):

$$I_{\text{SC}}(t) = a_0 + a_1 e^{-t/\tau_1} + a_2 e^{-t/\tau_2}.$$

The offset a_0 clearly shows the same trend as $I_{\text{SC}}(t=0\text{ h})$. More interestingly, also the decay amplitudes of both the faster and the slower decay, a_1 and a_2 , are proportional to the initial short-circuit current, but devices with TiO_2 exhibit higher decay amplitudes than devices without TiO_2 . This is in contrast to the results reported in 3.8, but more

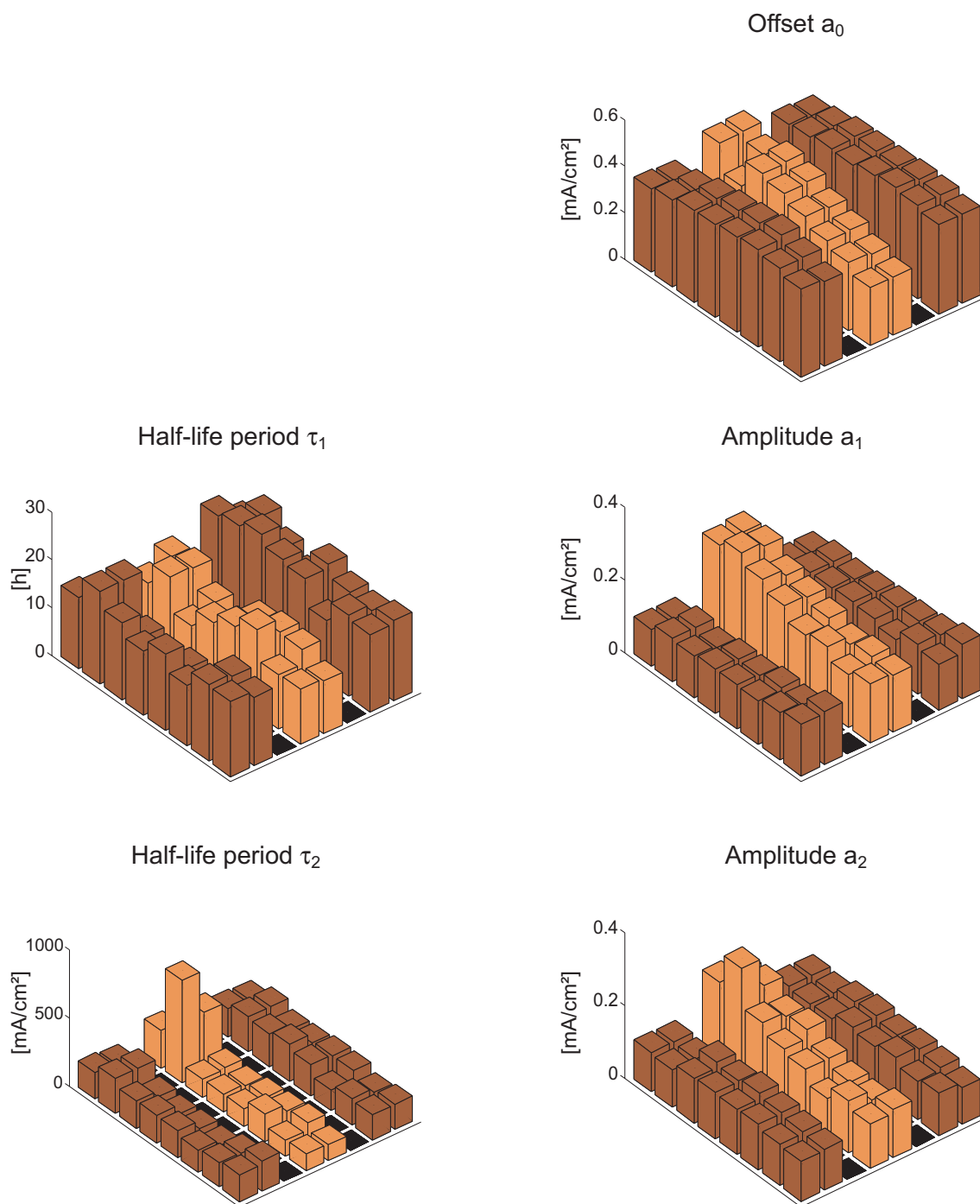


Figure 3.52: Model parameters for the double exponential fits to the $I_{SC}-t$ curves. The decay amplitudes a_1 and a_2 scale with the initial value of I_{SC} , but with different factors for each device type. The relative amplitudes for TiO_2 devices are higher. The decay times are very similar for all devices. Averaging over all devices in one group clearly reveals lower time constants for TiO_2 devices for both fast and slow decay.

intuitive: a degradation process affecting any of the efficiencies involved, i.e. exciton generation (η_{EG}), charge transfer (η_{CT}) or charge collection (η_{CC}), is expected to linearly influence I_{SC} for single heterojunction devices. A degradation affecting the charge transfer

at only one of the charge-separating interfaces could, however, lead to a decay amplitude that is not proportional to $I_{SC}(t = 0)$. We dare not deduce, however, that this is the only effect that leads to the constant amplitude decrease in 3.8. Concerning the life time we see that TiO_2 negatively influences not only the decay amplitudes but also the speed of degradation: the average of the shorter time constant decreases from 15 h for devices without TiO_2 to 12 h for devices with TiO_2 the larger time constant is reduced from 190 h to 140 h (130 h if the two largest values of τ_2 (see Figure 3.52) are omitted). A clear thickness dependence cannot be seen within one device type. The extremely high time constant for the thinnest TiO_2 seems to be a fitting artefact: for these devices we perceive a temporary increase in I_{SC} between $t = 150$ h and $t = 250$ h; the origin of the increase, however, is not clear.

As already described above, both V_{OC} and FF can be fitted with a simple exponential model, revealing a fast and a slow timescale that coincide with the two time constants found for I_{SC} . This is clearly seen in Figure 3.53, where we display the time constants with the same scaling. Also for V_{OC} and FF, the TiO_2 layer leads to a reduction in the time constants, which is, however, more pronounced in the latter case. Additionally, thinner devices with TiO_2 show larger time constants so that a proportionality to $I_{SC}(t = 0)$ can be established in the same manner as for the decay amplitudes. The coincidence of the two timescales leads us to speculate that there might be a common process leading to the time behaviour observed. For the slower time constant this appears reasonable. A decrease in charge collection or extraction efficiency due to an increased injection or extraction barrier at one of the electrodes would decrease both I_{SC} and FF. However, concerning the shorter process, a common process can hardly be identified: in all experiments, we have always observed a strong initial decrease in I_{SC} , but we did not find such an important change in V_{OC} in all of them. It is quite possible that there are different processes involved but that these processes share a common origin, for example heat. Morphological changes at the different interfaces are then possible candidates for such heat-induced changes. The observed timescale of ≈ 15 h seems reasonable for the temperatures involved. Finally, we want to draw attention to an odd finding: all devices in row no. 5 exhibit a lower time constant for V_{OC} . As these devices all share the same ITO layer, we think that the ITO layer plays an important role for the time behaviour of V_{OC} . At present two origins can be imagined: (a) the ITO cleaning procedure, particularly at the borders of the substrate, where the contacting is accomplished, (b) the contacting of the ITO itself. To further check this hypothesis we have increased the number of the contacting points of the ITO layer and the influence of this will be tested in future experiments. This could also clarify whether the two fast processes are intrinsically connected.

Finally, we present in Figure 3.54 the evolution of the I - V curves of a TiO_2 and a non- TiO_2 device. (We have chosen the same devices whose initial and final I - V curves have already been shown above.) Figure 3.54 displays the I - V curves from $t = 0$ h (red) to $t = 400$ h (blue), where all devices were constantly illuminated. The insets show the same curves with the full data range.

Both devices exhibit a very similar degradation behaviour. An initially steep slope continually decreases to finally end up in a sigmoid shape. For the devices with TiO_2 this kink around V_{OC} is more pronounced, indicating a slightly higher charge injection barrier for this device type. A qualitative difference between the different device types cannot be

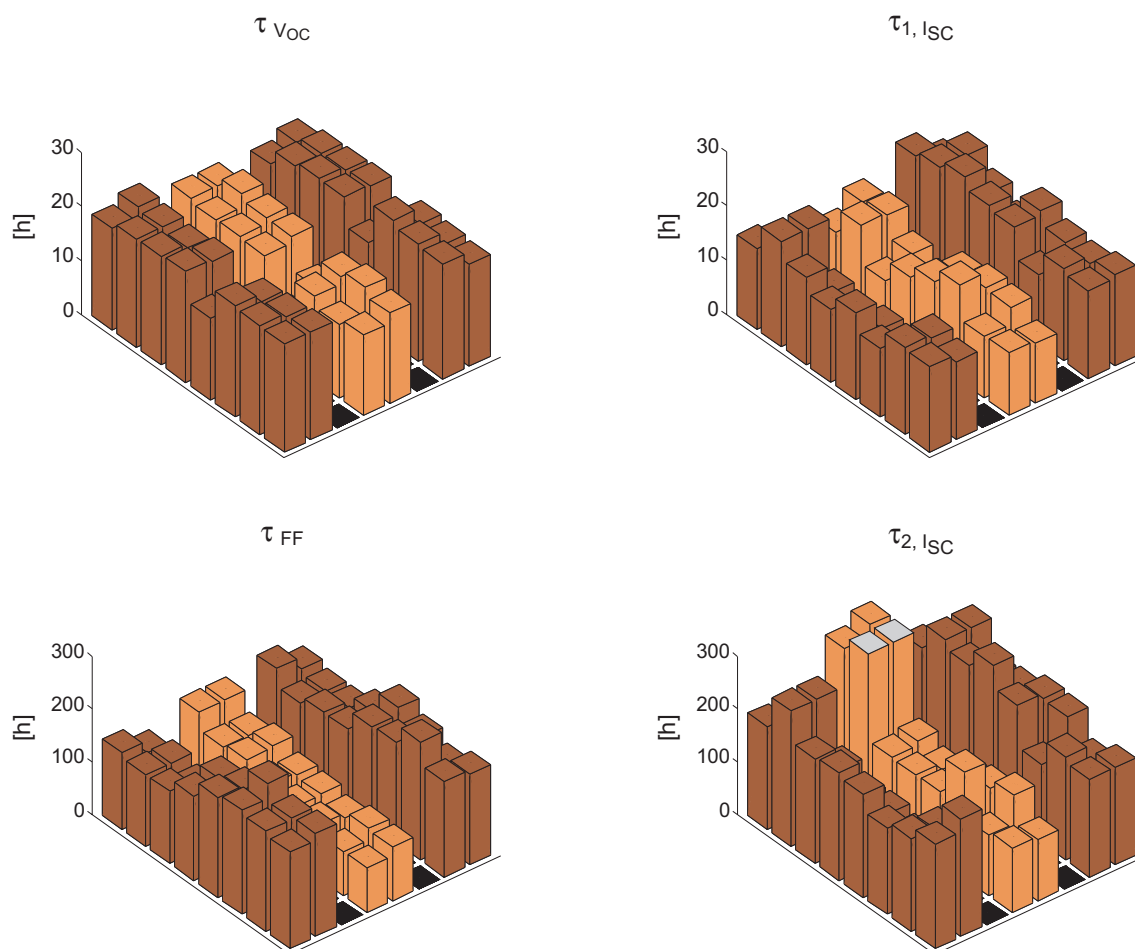


Figure 3.53: Comparison of different time constants. The values of τ_{VOC} and $\tau_{1,ISC}$ nearly coincide as well as τ_{FF} and $\tau_{2,ISC}$. This suggests a common underlying process, e. g. an increased charge injection barrier, or a common origin, e. g. heat, for different underlying processes.

found.

3.9.6 Summary and Conclusion

We have shown that by combinatorially varying device structure and film thickness together with careful modelling, we can gain a better understanding of the optical and electrical effects in multi-layer thin-film solar cells. We have demonstrated that the positioning of the charge transfer zone is a key issue in device optimisation and we were able to prove that it is possible to introduce a second charge transfer zone, where the hole and electron current from neighbouring heterojunctions do not cancel by recombination, as is the case for stacked multi-layer solar cells. Furthermore, we were able to estimate the ratio of the exciton diffusion lengths of CuPc and DMPTI to be $\approx 8/5$. We have shown that the degradation of the cells during 400 h of illumination is not induced by the charge flow through the device. As all materials employed are photostable in the visible range

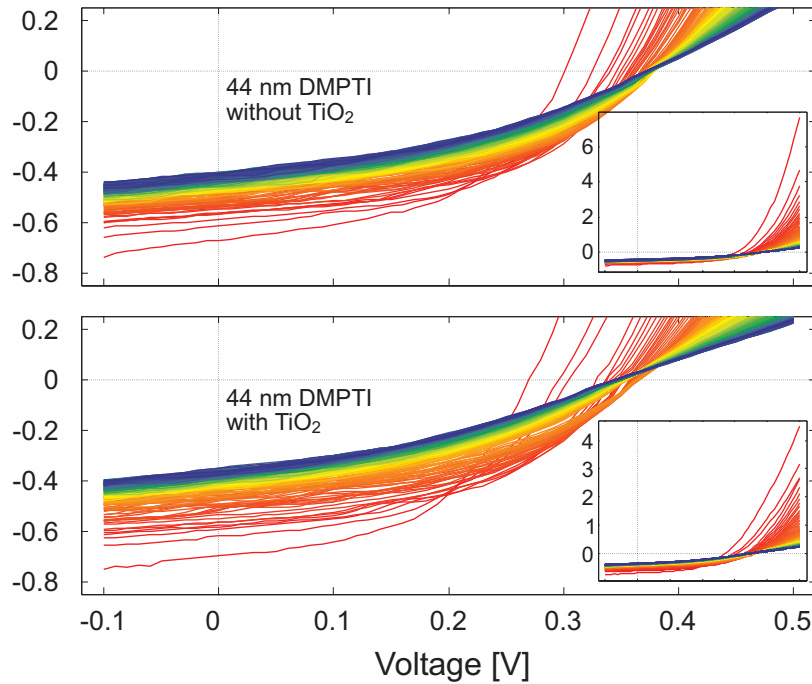


Figure 3.54: Time evolution of I - V curves of two different device types: $ITO/CuPc(30\text{ nm})/DMPTI(44\text{ nm})/aluminium$ and $ITO/CuPc(30\text{ nm})/DMPTI(44\text{ nm})/TiO_2(30\text{ nm})/aluminium$. The curves are coloured in a rainbow colour scheme from red ($t=0\text{ h}$) to blue ($t=400\text{ h}$). The axes have been chosen so that the curve shape in the current-delivering regime is clearly visible. The full current range is displayed in the insets of each graph. The I - V curves of both device types show strong degradation in I_{SC} and later develop a slightly sigmoid shape, which indicates a lower charge injection capability while charge extraction is less affected. The sigmoid shape is, however, much less pronounced than in the measurements presented in Figure 3.41 and occurs much later. A qualitative difference in the I - V curves between the different device types cannot be found.

and as we do not see any relevant changes in the ellipsometry spectra before and after illumination (not shown here), we conclude that the degradation is mainly due to chemical, photochemical or thermally induced changes at the interfaces of the device. This view is further corroborated by the fact that a storage period has only little influence on the I - V curves. Furthermore, the time behaviour of I_{SC} can be characterised by a double exponential decay, suggesting that there are at least two different degradation mechanisms present in all devices. The comparison of devices with and without TiO_2 layer yields that the degradation of the former is faster and stronger. Correlations between the time constants of I_{SC} and the fill factor suggest a common origin for their time behaviour.

In a recent review article by Peumans *et al.* [Peu03] a very similar model for I_{SC} and similar experiments with an exciton-blocking layer are presented. One of their conclusions is that the optimal thickness for the absorbing layers is approximately the exciton diffusion length. In our setup, the relative position of the energy bands of TiO_2 together with the strong electron-accepting character not only allows the blocking of the excitons, but it also creates an additional charge transfer interface. Hence, we suggest that the optimal

film thickness for the middle absorption layer is *twice* the exciton diffusion length and that with such a device setup the efficiency of solar cells can be further improved.

3.9.7 Experimental Details

The ITO (Merck, 45 nm) was treated by an oxygen plasma before evaporation. The perylene dye DMPTI (also known as Me-PTCDI or DiMe-PTCDI, see 3.12) was purchased from SynTec GmbH. TiO₂ is evaporated by heating Ti₃O₅ at an oxygen partial pressure of 2.5×10^{-5} mbar, the subliming TiO reacting with the oxygen and forming a predominantly anatase crystal phase on the substrate. The illumination is provided by four light bulbs, type OSRAM Ultra-Vitalux[®] (300 W), that simulate the solar spectrum. The total intensity at the device surface is 38 mW/cm² with a lateral homogeneity of 2.8%. The devices were illuminated for a period of over 400 h and I - V characteristics were taken periodically. More details about the setup can be found in the literature [Hän02] and will be published elsewhere. The optical constants of the layer materials were obtained from angle-dependent ellipsometry measurements on silicon or glass (DMPTI) with a Sentech 850 spectroscopic ellipsometer. The layer thickness was independently determined by atomic force microscopy (Dimension 3100, Veeco Digital Instruments). The data were fitted using a Cauchy model (TiO₂), a Lorentz-oscillator model (CuPc) and a piecewise Lorentz-oscillator model (DMPTI). The ITO coefficients were provided by the manufacturer of the ITO glass (Merck) and the data for aluminium were taken from the Palik handbook of optical constants [Pal85]. In our setup, we have some light contribution at non-zero incident angles with respect to the surface normal. Thus, we have tentatively calculated the fields for angles up to 10° and find only slight changes in shape. As the angle distribution is not known exactly, we have restricted our calculation to normal incidence. Finally, we would like to mention a minor detail of the experimental setup. If we compare the time behaviour of different devices, we realise that there are fluctuations in the time curves that affect all devices simultaneously. This can be seen for each characteristic value, for instance in Figure 3.50. Particularly in V_{OC} , a periodicity of 24 h is clearly visible. In I_{SC} we see a common fluctuation rather than a periodical shape. However, smoothing the data over 3 measurements (Figure 3.55), we can recognise a 24 h rhythm here too. The change in V_{OC} suggests that temperature is one of the origins of the fluctuations. The influence on I_{SC} is probably due to an interplay of temperature and scattered light, as the room could not be darkened completely. Also, the room temperature might slightly affect the efficiency of the lamp array.

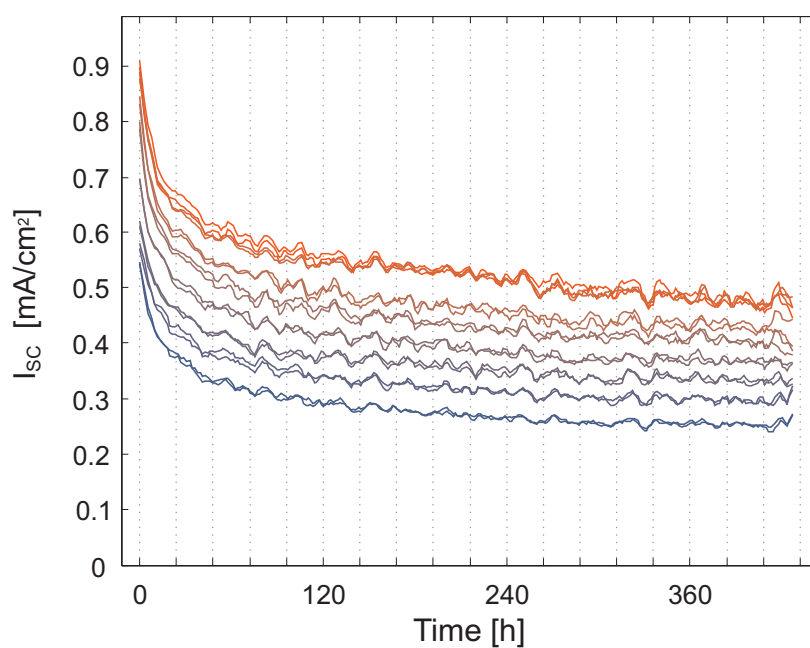


Figure 3.55: I_{sc} - t curves of the devices with TiO_2 layer smoothed by a moving average over 3 neighbouring data points. The smoothed curve shows that there are periodic fluctuations with a periodicity of 24 h. The fact that the curves of all devices fluctuate identically although the devices are measured sequentially reveals that the fluctuations are not of an electronic but of an environmental nature, such as scattered daylight and temperature.

3.10 Influence of inert gas on the Degradation of Organic Light-Emitting Devices

3.10.1 Abstract

We show that the presence of inert gas can be essential for the functioning of organic light-emitting devices. Particularly the first operation has to be carried out in gas atmosphere rather than in vacuum to prevent early failure of the devices. At present, we assume that the reason can be found in the combination of two processes: non-radiative current anomalies during the first operation and low heat-transport capability in vacuum. Furthermore we have evidence of the existence of a self-repair mechanism where the inert gas atmosphere plays an essential role. Device failure in vacuum is found to differ from scenarios in air or in inert gas. We attribute this behaviour to the heat transport of the gas molecules and to heat-induced morphology changes. In the same experiment we show that devices with the two hole-transport-layer materials H1T (2,3,6,7,10,11-hexamethoxy-triphenylene) and α -NPD (N,N'-bis(1-naphthyl)-N,N'-diphenyl-(1,1'-biphenyl)-4,4'-diamine) differ in their efficiency as well as in their degradation behaviour. Finally, the effect of the thickness of the emitter layer is discussed.

3.10.2 Introduction

Testing of organic light-emitting devices (OLEDs) is most often performed in an inert gas atmosphere, since oxygen and humidity lead to the formation of non-emissive regions, also called *dark spots* ([Sat94, Bur94, McE96, Fuj96, Do97, Azi98a, Azi98b, Lie00, Kol01] and Section 2.3 above). For technical applications of OLEDs, many efforts are therefore made to encapsulate the devices. For mechanical reasons, these encapsulations all enclose a small volume of inert gas. Our findings indicate that the inert gas prevents degradation not only chemically but also physically by its heat transport capability.

Our first combinatorial degradation studies of small molecule OLEDs involved a linear thickness gradient of the emitter molecule [Zet00] and were carried out under a constant flow of nitrogen. These experiments have served as a prototype for the setup described in Chapter 3.6. In order to exclude any oxygen or humidity more efficiently, the current setup is placed in a vacuum chamber. It turns out, however, that the devices degrade much faster in vacuum than any devices we had tested with the prototype setup, lifetimes being in the range of minutes or less. When the same type of device is operated in nitrogen atmosphere, however, the fast degradation vanishes.

In this chapter we investigate more closely the influence of the gas atmosphere on the degradation of OLEDs. We assume that lacking heat transport is the origin of the failure of devices in vacuum. Particularly, the non-luminescent current anomaly during the first measure cycle is proposed to be the source of the destructive heat. Furthermore, a characteristic failure of devices in vacuum is found to be an increased conductivity together with a complete loss of electroluminescence. This is in contrast to the dark-spot failure, where the affected regions exhibit lower conductivity or complete delamination of the cathode

layer, e.g. [McE96, Do97]. Moreover, we show that this kind of defect can heal under operation in nitrogen atmosphere. Finally, we take a comparative look at the efficiency of the two device types and the influence of the emitter layer thickness.

3.10.3 Experimental

An array of 64 OLEDs of two different hole transport materials was produced by vapour deposition. On top of an ITO substrate (Merck, 45 nm, treated with ozone plasma) a 40 nm layer of H1T or α -NPD was evaporated as hole transport material. The emitter layer was evaporated as a step gradient of Alq₃ ranging from 30 to 50 nm, followed by a 1 nm electron injection layer of LiF. The top layer consists of 64 Al electrodes as shown in Figure 3.56. I - V curves were taken regularly by a source/measure unit with both increasing and decreasing voltage. The respective I - V curves are denoted ‘forward’ and ‘backward’. Electroluminescence was synchronously detected by a CCD camera. No voltage or current was applied to devices currently not under test. More details about the setup are given in 3.6.

After initial evacuation the chamber was flooded with nitrogen and kept slightly above atmospheric pressure to prevent oxygen and water from diffusing into the chamber. The first measure cycles were performed in nitrogen atmosphere, the voltage ranging from 0 to 4 V. Then, vacuum was reapplied and I - V curves of a single device were taken in a voltage range from 0 to 4 V and from 0 to 8 V. The chamber was refilled with nitrogen and I - V curves of all devices were taken in a voltage range between 0 and 8 V. The measurement was repeated every 3.6 h over a period of 330 h.

3.10.4 Results and Discussion

It is a common finding that OLEDs can exhibit a current anomaly when operated for the first time. The typical signature of such an anomaly is a sudden increase in the current density well below the onset voltage without any luminescence. If the voltage is further increased the current decreases and the devices show a regular behaviour. Subsequent lowering of the voltage leads to the expected monotonous decrease in the current density. Figure 3.57 displays the forward and backward I - V curves of the first and second measure cycle performed in nitrogen atmosphere. The colour ranges from red to blue according to the emitter layer thickness (red=30 nm, blue=50 nm). We see that the devices show a strong current anomaly with two maxima in the forward curves of the first measure cycle. The anomaly is more pronounced for devices with H1T as hole-transport layer and decreases with the thickness of the emitter layer for a given device type. The backward curves show regular diode characteristics. Subsequently taken I - V characteristics resemble the backward curves of the first measurement cycle and show only a slight hysteresis, which is probably due to space charges that accumulate during the measurement.

After ten measure cycles, the chamber is evacuated and a single NPD device is measured in vacuum. The device runs stably between 0 and 4 V and the I - V curve coincides with the one measured in nitrogen atmosphere. During the measurement of an I - V curve between 0 and 8 V the current increases by three orders of magnitude and the EL vanishes completely

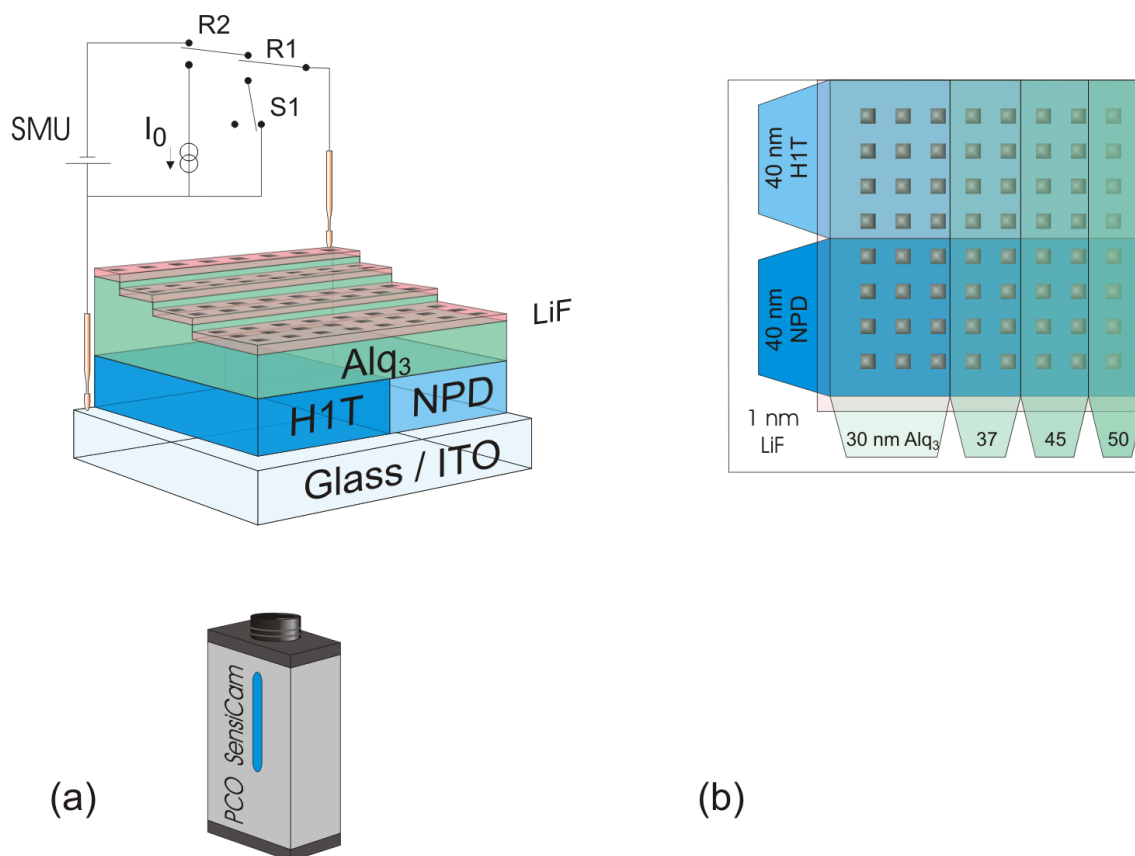


Figure 3.56: *Experimental setup: (a) perspective view of the layered structure with electrodes: two different hole-transport layers (NPD and H1T, 40 nm) with an Alq₃ emitter layer of varying thickness (30–50 nm) and an electron injection layer of LiF. The detection of the electroluminescence and the electrical circuit of a single device are plotted schematically. (b) top view of the 2×4 OLED library.*

during the backward measurement. Subsequent measurements reproduce the increased conductivity and the loss of EL. The chamber is then refilled with nitrogen and data of all devices are taken in the range between 0 and 8 V. Nearly all devices work properly under these conditions and their degradation is monitored over a period of 330 h. Device failure of the type found in vacuum is not observed; on the contrary, the defective device returns to proper operation and continues to work until the end of the measurement.

Figure 3.58 shows the described behaviour of the device by displaying I – V and EL curves before, during and after evacuation. The upper graphs document the initial current anomaly and the subsequent stable operation for ten measure cycles in nitrogen atmosphere. The onset of the EL is around 3.2 V. The colour of the curves changes from red to blue with increasing time. For comparison, we have also plotted the first curve from 0–8 V recorded in vacuum. We realise that up to this point only little degradation has taken place. The middle graphs shows three consecutive forward measurements between 0 and 8 V. The device failure for measurements 2 and 3 is obvious. The dotted curves show the device characteristics after the device has returned to proper operation in nitrogen atmosphere. Although the shape of the dotted line resembles the initial curve in vacuum,

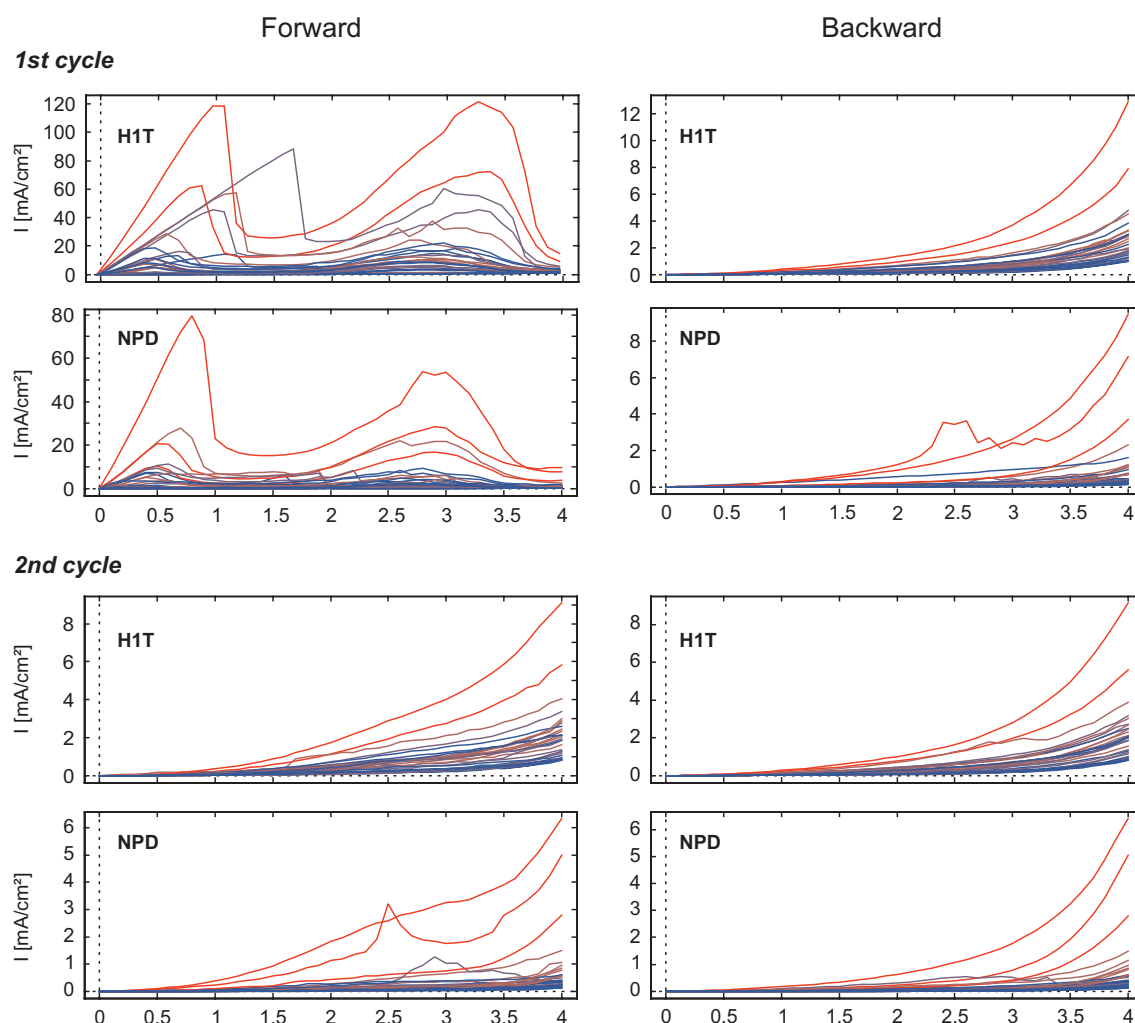


Figure 3.57: *Anomaly in the I - V characteristics. In each measurement cycle, two I - V curves are taken for each device, one with increasing ('forward') and one with decreasing voltage ('backward'). The devices with a common hole-transport layer (HTL) are displayed in one graph and coloured according to their Alq_3 layer thickness from red (30 nm) to blue (50 nm). All devices exhibit a very strong anomaly in the first forward measure cycle with two maxima at voltages between 0 and 4 V. With the second measure cycle, the current anomaly has reduced to a weak hysteresis in the I - V curve. The anomalous current increase is stronger for devices with NPD than with HTL and decreases with increasing thickness of the emitter layer.*

an important degradation can be seen between the respective curves: the conductivity has decreased and the onset voltage has shifted by 0.5 V. Finally the lower graphs present the development of the device characteristic in nitrogen atmosphere during 330 h. The observed degradation is due to the repetitive measuring of the I - V curves up to 8 V. The degradation manifests itself by a further decrease in conductivity and a shift of the onset voltage to approximately 6 V.

At this point, we conclude that the observed fast degradation of OLEDs in vacuum is caused by an overheating of the devices. The non-emissive current anomaly during the

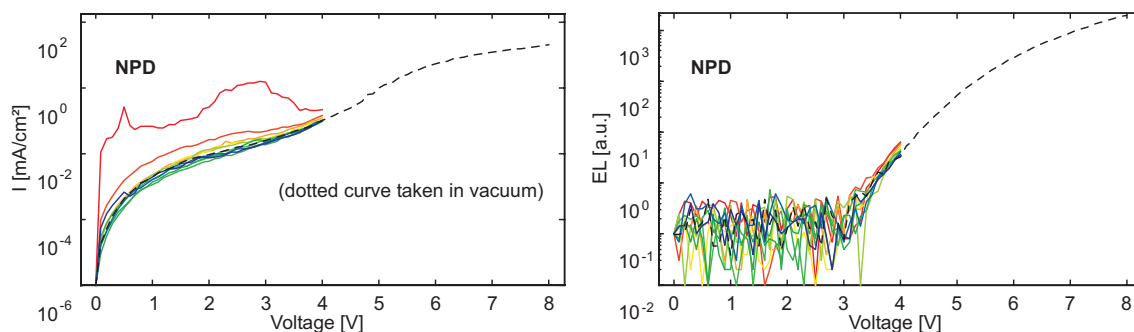
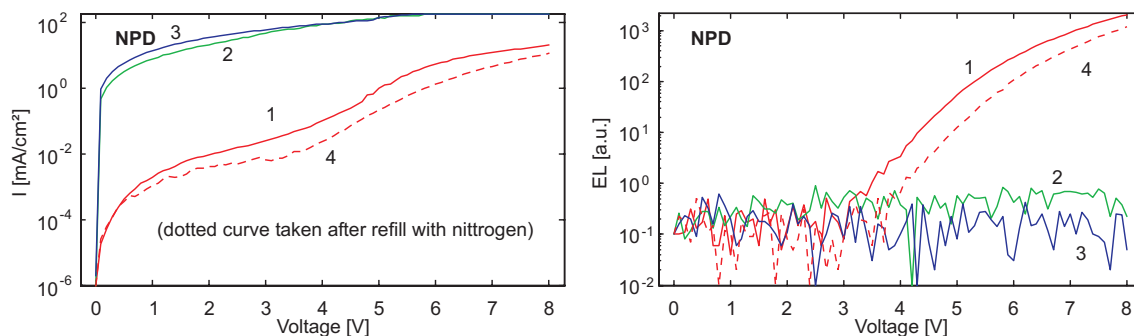
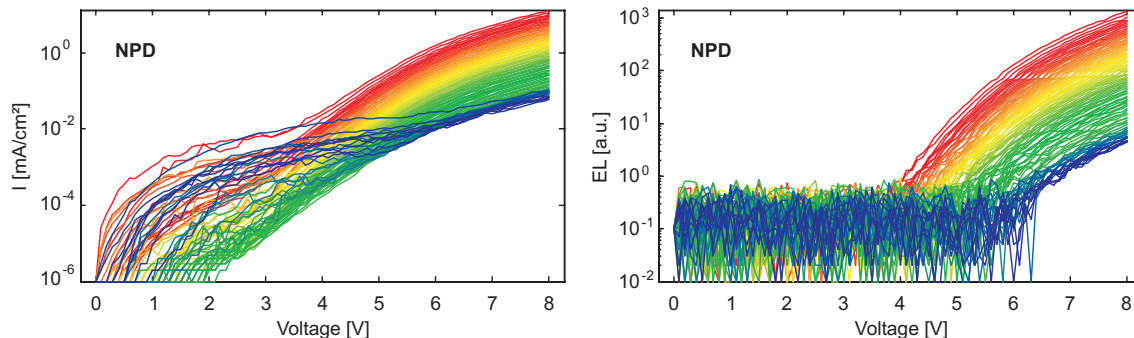
Current anomaly in nitrogen atmosphere**Failure and self-repair****Long-term stability in nitrogen atmosphere**

Figure 3.58: *Failure in vacuum and self-repair in nitrogen atmosphere of a particular OLED (D46): I-V and EL curves of a particular OLED document the three stages of operation. The curves are coloured in a rainbow colour scheme from t_{first} (red) to t_{last} (blue). Top: Current anomaly and initial performance in nitrogen, the dotted line is taken from a subsequent measurement in vacuum. Middle: After one successful measurement in vacuum (curve 1), the device shows strongly increased conductivity and loss of EL (curves 2,3). After a refill with nitrogen the device returns to proper operation (curve 4, dotted line). Bottom: Degradation after a refill with nitrogen. The current density decreases with time and the onset voltage of EL shifts from 3.3 V to 6 V. For later times, the current increases at low voltages. The EL is not affected.*

first operation is probably the fundamental origin of the Joule heat that cannot be transported away and that in consequence leads to the early failure of the device. The underlying microscopic process is not yet understood. We might speculate, however, that local

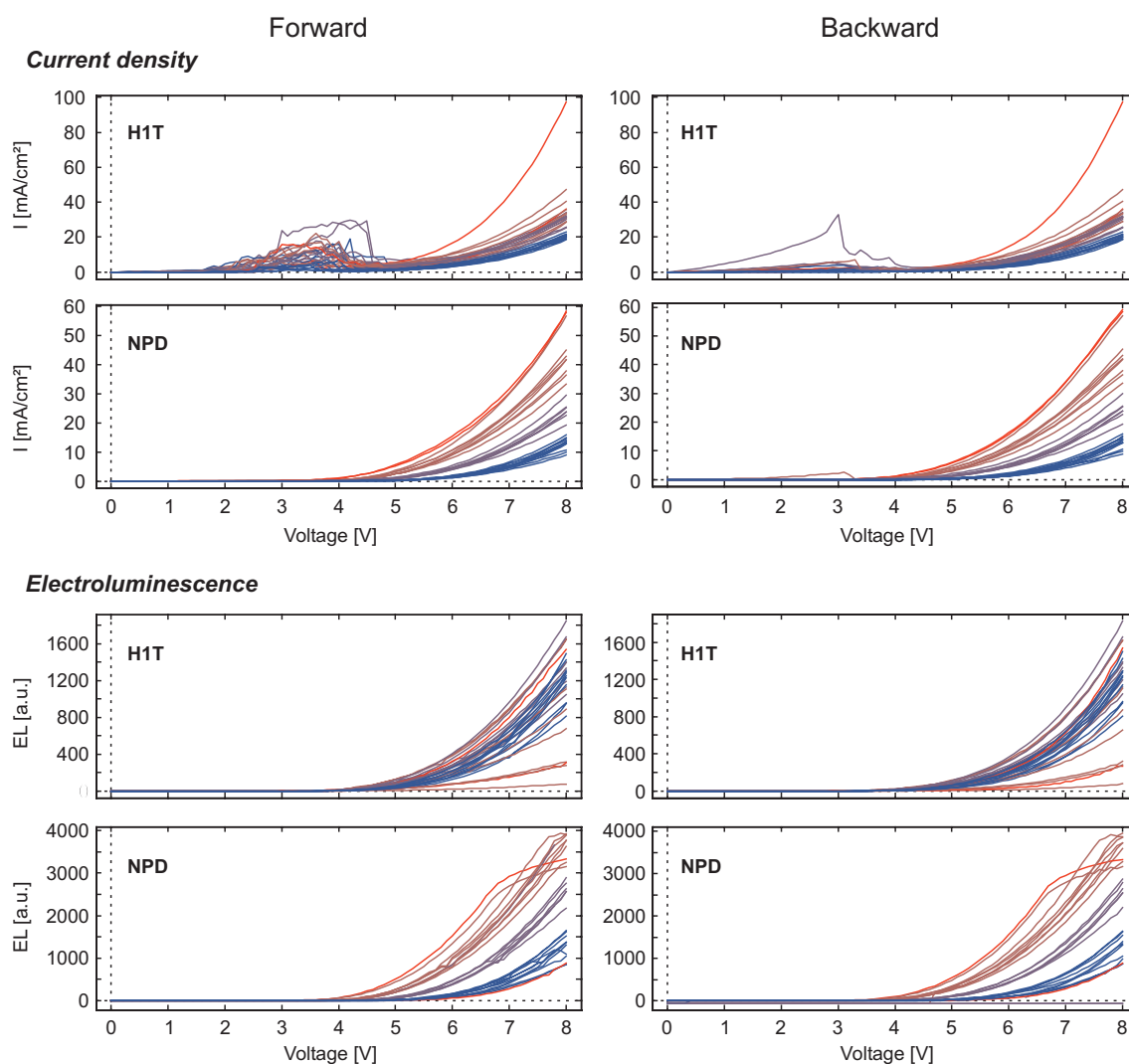


Figure 3.59: I - V and EL characteristics of all devices after evacuation and a refill with nitrogen. Curves have been taken with increasing ('forward') and with decreasing voltage ('backward'). Devices with H1T as HTL show an anomaly in the forward measure cycle at voltages between 3 and 4 V. This anomaly developed after the first I - V cycle from 0 to 8 V (the previous I - V curves were taken between 0 and 4 V). As for the previous curves, the current anomaly is reduced remarkably when measured in the backward direction. The corresponding EL curves show that the anomaly is completely non-radiative. Devices with NPD as HTL do not show this anomaly.

oxidation processes with residual oxygen lead to the formation of dark spots. Lower residual oxygen or moisture concentrations or higher temperature might influence the growth process so that short circuits are formed rather than the reported self-insulating spots [Bur94, McE96, Azi98a, Azi98b, Lie00, Lim01, Kol01]. This would also explain why upon operation in nitrogen atmosphere the defect is repaired: the passing high currents would lead to the classical growth of dark spots and the eventually delaminating electrodes would insulate the defective area.

We now turn to the comparative analysis of the devices operated in nitrogen atmosphere

only. Figure 3.59 shows the I - V and EL characteristics of all devices grouped by the hole transport material and coloured according to the respective thickness of the emitter layer from red 30 nm to blue 50 nm. We see that thinner devices exhibit higher conductivities than expected. However, the thickness dependence is less pronounced for devices with H1T as hole transport material. What is remarkable is the existence of a non-emissive current anomaly for the H1T devices. In contrast to the initially observed anomaly, this anomaly has formed after the first operation to 8 V and does not vanish for later measurements. In backward mode, the anomaly is still present, but it is much less pronounced. The anomaly grows with time (not shown here) and is most probably connected to the faster degradation of this device type (see Figure 3.61). The NPD devices do not show such an anomaly. As already mentioned, the anomaly does not show up in the EL characteristics. Again, the thickness of the emitter layer is clearly reflected in the EL curves of the NPD devices.

To visualise the relative performance of the devices, we show in Figure 3.60 the current density, EL and efficiency of all devices at 4 V and at 6 V. The 4 V values are taken from the very first measurement; the 8 V values are taken after the evacuation and refill with inert gas. We see that at 4 V, the H1T devices exhibit higher currents and higher EL than the NPD devices. The correlation between current or EL and Alq₃ layer thickness is weak. The efficiency of the NPD devices is clearly superior (note the rotated view of the efficiency graph). At 6 V, we find a very similar situation. The influence of the emitter layer thickness is now clearly visible for both device types; only the thinner H1T devices exhibit very poor luminescence. Again, the luminance efficiency of the H1T devices is inferior to that of the NPD devices and decreases with decreasing emitter layer thickness. The efficiency of the NPD devices is nearly thickness-independent.

Finally, we will briefly discuss the degradation of the devices. Figure 3.58 displays the development of the current density, EL and luminance efficiency at a voltage of 7 V with time. Again, the emitter-layer thickness is coded by the colour. Both device types show a continuous degradation in current density, which seems to slow down around 250 h. The plateau values of H1T devices are slightly greater. By contrast, the behaviour of the EL is fundamentally different for the two device types: first, the degradation of the NPD devices is slower; second, thinner NPD devices are more stable than thicker devices, whereas thinner H1T devices degrade the fastest. This difference is also reflected in the efficiency: H1T devices show a continuous decrease and thinner devices lose their efficiency the quickest. The efficiency of the NPD devices is less affected; some devices even gain in efficiency. At present, we have no definite explanation for these findings. The low performance of the H1T devices could be a purity issue, as this material was synthesised by a new chemical route and was tested for the first time for OLED application. This might also explain why thinner devices are less stable, as thinner emitter layers are naturally more sensitive to impurities.

3.10.5 Conclusion

We have investigated the influence of inert gas on the degradation of small-molecule OLEDs. We have shown the heat transport capability of the gas to be essential for the

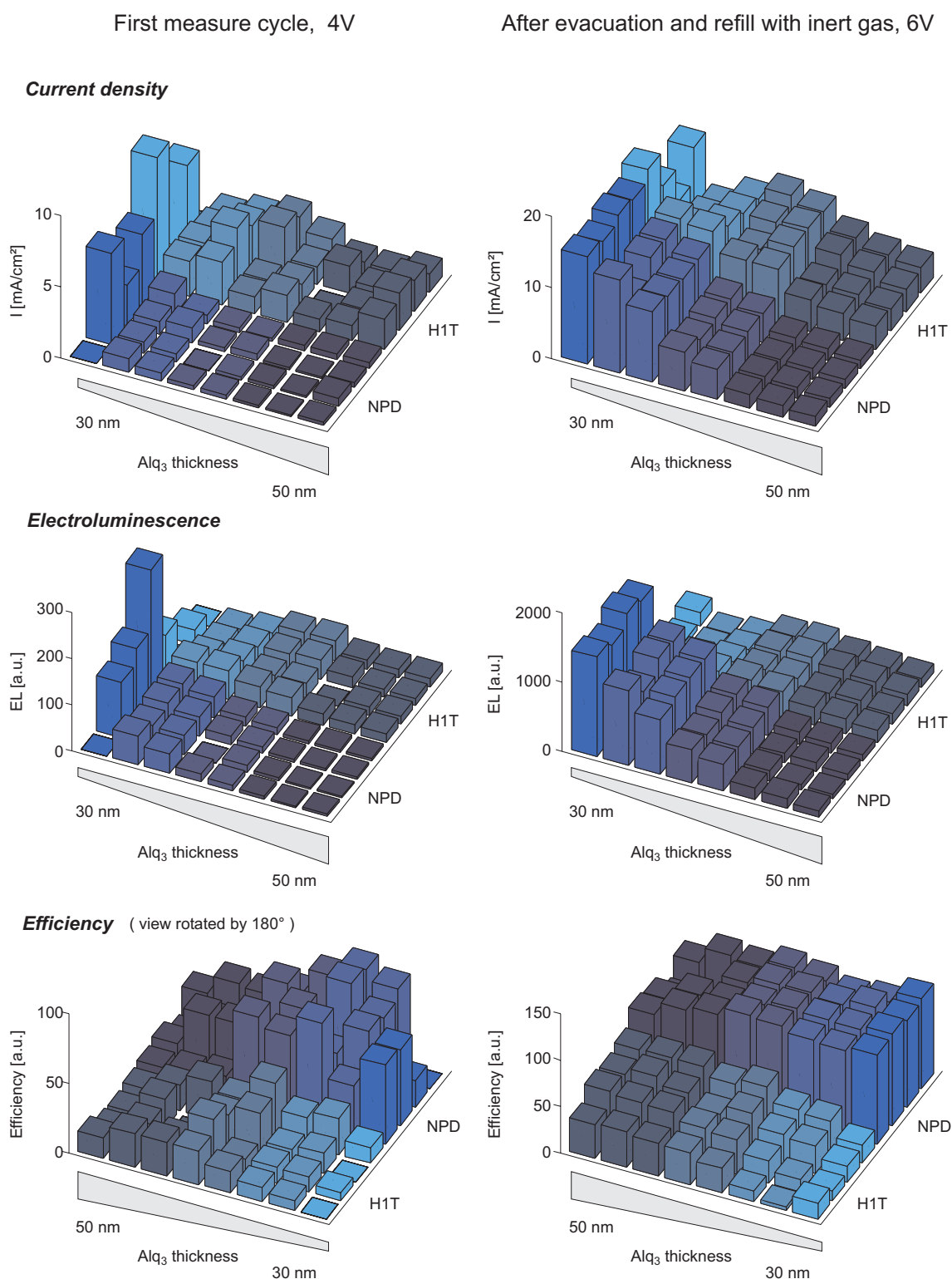


Figure 3.60: *Current density, EL, and efficiency (rotated view) at 4 V (before evacuation) and 8 V (after refill with nitrogen). The efficiency of H1T devices is inferior to that of NPD devices and decreases with decreasing Alq₃ layer thickness. The efficiency of the NPD devices is thickness-independent.*

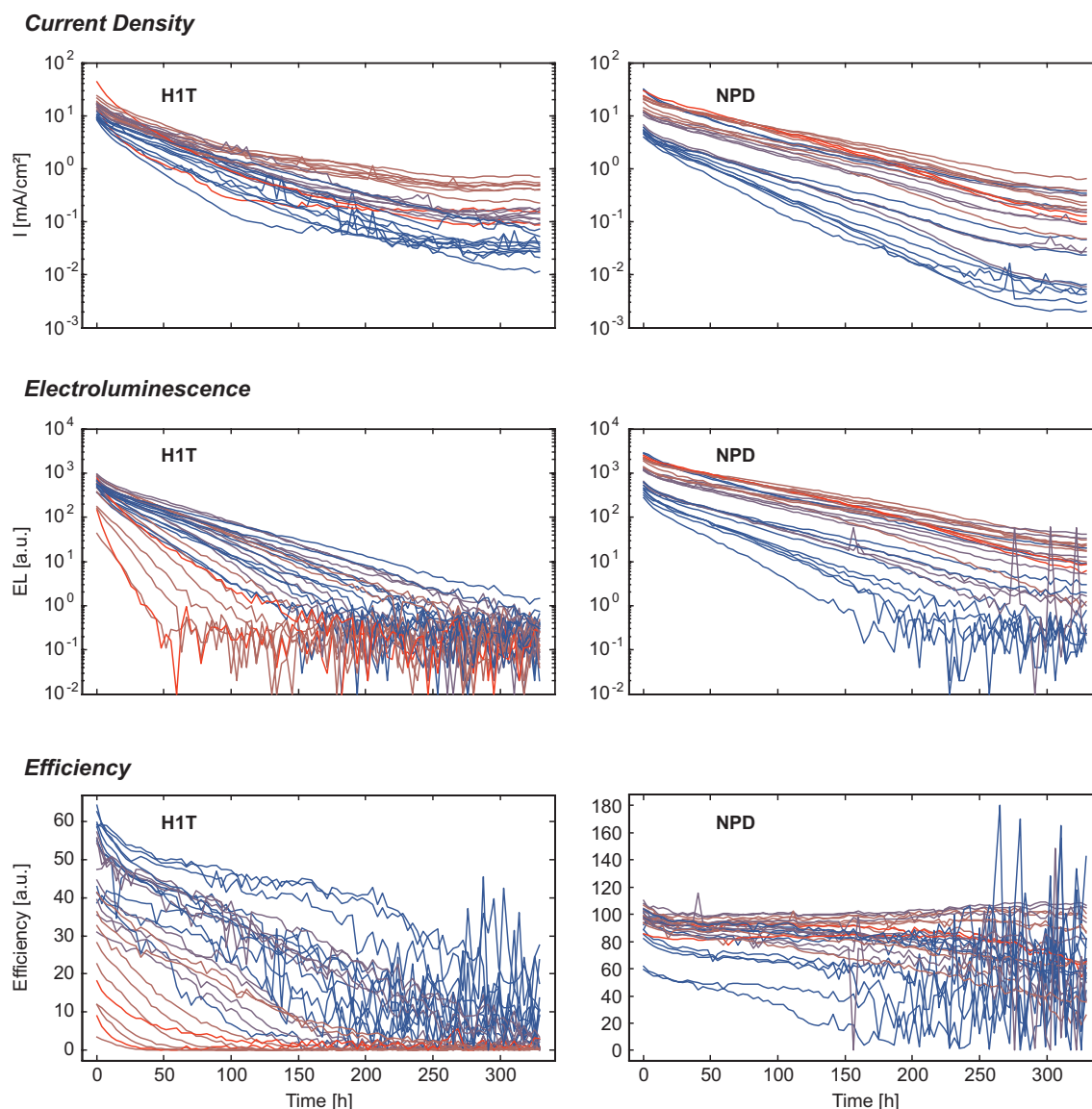


Figure 3.61: *Temporal evolution of current density, EL, and efficiency of the devices at a voltage of 7 V. The change in current density of the two device types is similar; the currents of H1T devices seem to settle at slightly higher values. Their EL behaviour, however, is very different. The EL of thinner H1T devices decays the fastest, whereas thinner NPD decay the slowest. In total, NPD devices are more stable. This is also reflected in the efficiency: H1T devices quickly lose efficiency, whereas some of the NPD devices even gain in efficiency.*

stability of the devices and we have identified the non-emissive current anomaly during the first operation as the fundamental origin of the destructive Joule heat. The self-repairing of a previously defective device in inert gas atmosphere has been observed and it has been attributed to the classical growth of dark spots in the presence of inert gas which was previously suppressed in vacuum. We have furthermore studied the degradation behaviour of two device types with different hole transport materials (H1T and α -NPD) as a function of the emitter layer thickness. The NPD devices are found to be more stable

and their luminance efficiency is largely independent of the emitter layer thickness in the range observed. This makes the thinnest NPD devices the best choice out of the devices investigated.

3.11 Phosphorescent Emitter OLEDs: Thickness Gradient vs. Concentration Gradient

3.11.1 Introduction

In recent times the efficiency of OLEDs has been greatly improved by the use of heavy-metal complexes as phosphorescent emitters [Bal98, O'B99, Bal99, Ada00, Bal00a, Bal00b, Bur00, Lee00, Ada01a, Ada01b, Ada01c, D'A01, Ika01, For03, Kwo03]. Due to their increased stability they are already used in active-matrix displays [Lee03]. The success of the phosphorescent emitters is based on the fact that both singlet and triplet excitons of the host material can be transferred to the organic metal complexes. The strong spin-orbit coupling in heavy metals allows not only for the radiative decay of triplet states into singlet states but also for the transition of singlet excitons to triplet excitons, thus creating the possibility of phosphorescence generation by singlet excitons. For the phosphorescent emitters to be efficient in collecting triplet excitons, they are doped into the emitter layer of a "classical" OLED, typical concentrations varying between 5 and 10 %wt. The stability of such devices has been reported to be extremely high due to the removal of the potentially reactive triplet states [Bur00].

Since our evaporation chamber has recently been extended to incorporate more complex masks and to allow the co-evaporation of organic materials, we here present first results on the performance and degradation of phosphorescent OLEDs. We have used the option for continuous operation of the devices and have documented the degradation by means of a time-lapse video. We want to emphasise that the results presented are preliminary for three reasons: The mask alignment with respect to the electrode structure was not exact. The current drivers for continuous testing of the devices were operated at their lower limit and thus did not necessarily supply identical currents to the devices. We used nitrogen without a further drying stage. Therefore, this section is kept descriptive to a large extent and further experiments have to be made before definite conclusions can be drawn.

3.11.2 Experimental

A library of five-layer phosphorescent OLEDs is prepared by evaporation, starting with a 40 nm layer of α -NPD as hole-transport layer. Half of the substrate is then covered with a step gradient of CBP:Ir(ppy)₃ ranging from 30 to 50 nm; the doping concentration of Ir(ppy)₃ was 6 %wt and was achieved by co-evaporation. The second half of the substrate is covered with a 40 nm thick layer of CBP with a doping concentration of Ir(ppy)₃ varying between 20 and 3 %wt. A 6 nm hole-blocking layer of BCP, a 20 nm Alq₃ layer as electron-transport layer and an LiF injection layer of 1 nm are then evaporated successively onto

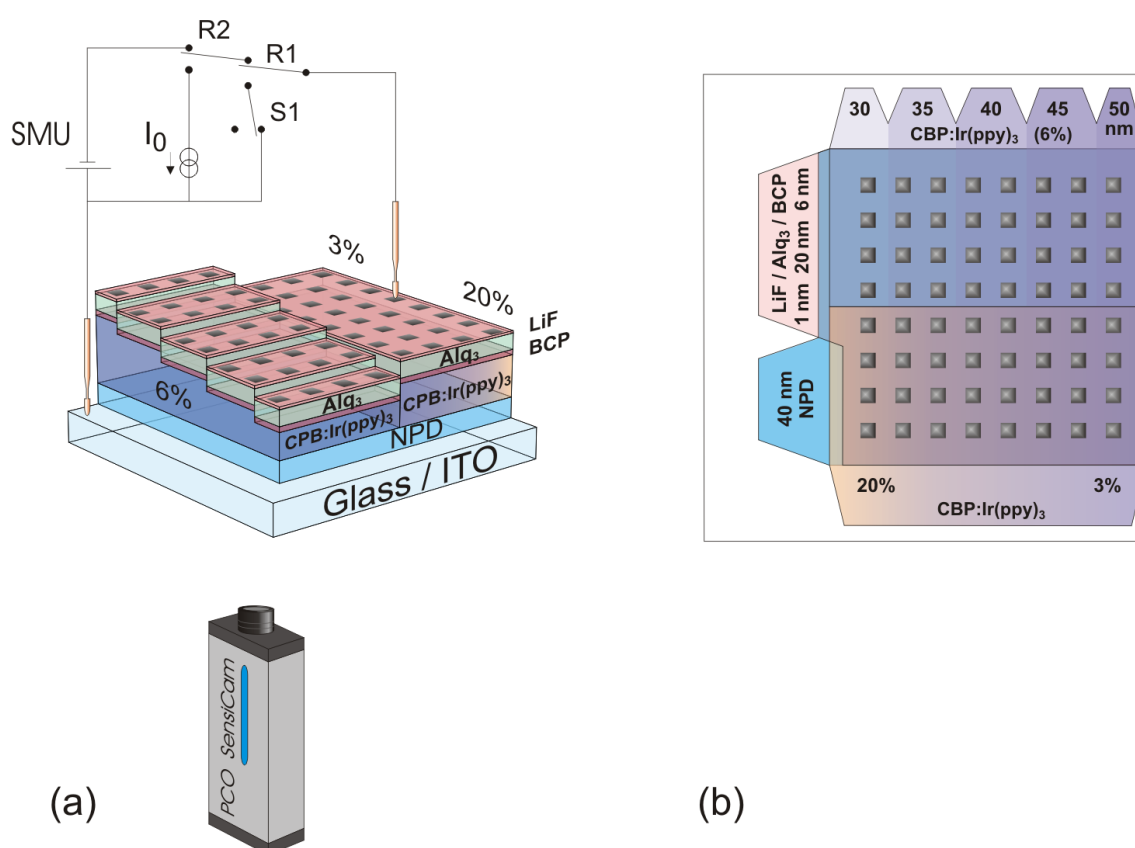


Figure 3.62: *Experimental setup: (a) perspective view of the layered structure: a step gradient of CBP:Ir(ppy)_3 (6 %wt) from 30–50 nm and a 40 nm layer of CBP:Ir(ppy)_3 with the concentration of Ir(ppy)_3 varying between 3 and 20 %wt (b) top view of the OLED library.*

the whole substrate. Finally, the Al electrodes are evaporated to form the library of 64 devices as shown in Figure 3.62. The testing of the devices is performed in nitrogen atmosphere, similar to the procedure described in 3.10. For the long-term testing, we applied a constant current of 1.77 mA/cm^2 to each device. I – V characteristics were taken by imposing the current rather than the voltage to achieve better comparability of curves with different onset voltages or different conductivities.

3.11.3 Results and Discussion

Before any long-term testing I – V and EL curves are taken between 0 and 5 V. Among all device types, there are some that exhibit current anomalies similar to the ones found for the H1T devices shown in Figure 3.59. As in H1T, the anomalies are not restricted to a single I – V curve. At present, we do not have any explanation for the instability observed.

Figure 3.63 presents the initial current density, EL, and efficiency for a voltage of 5 V. We see a largely homogeneous current density for all devices, regardless of the doping concentration or the emitter layer thickness. In contrast to this finding, the EL does show

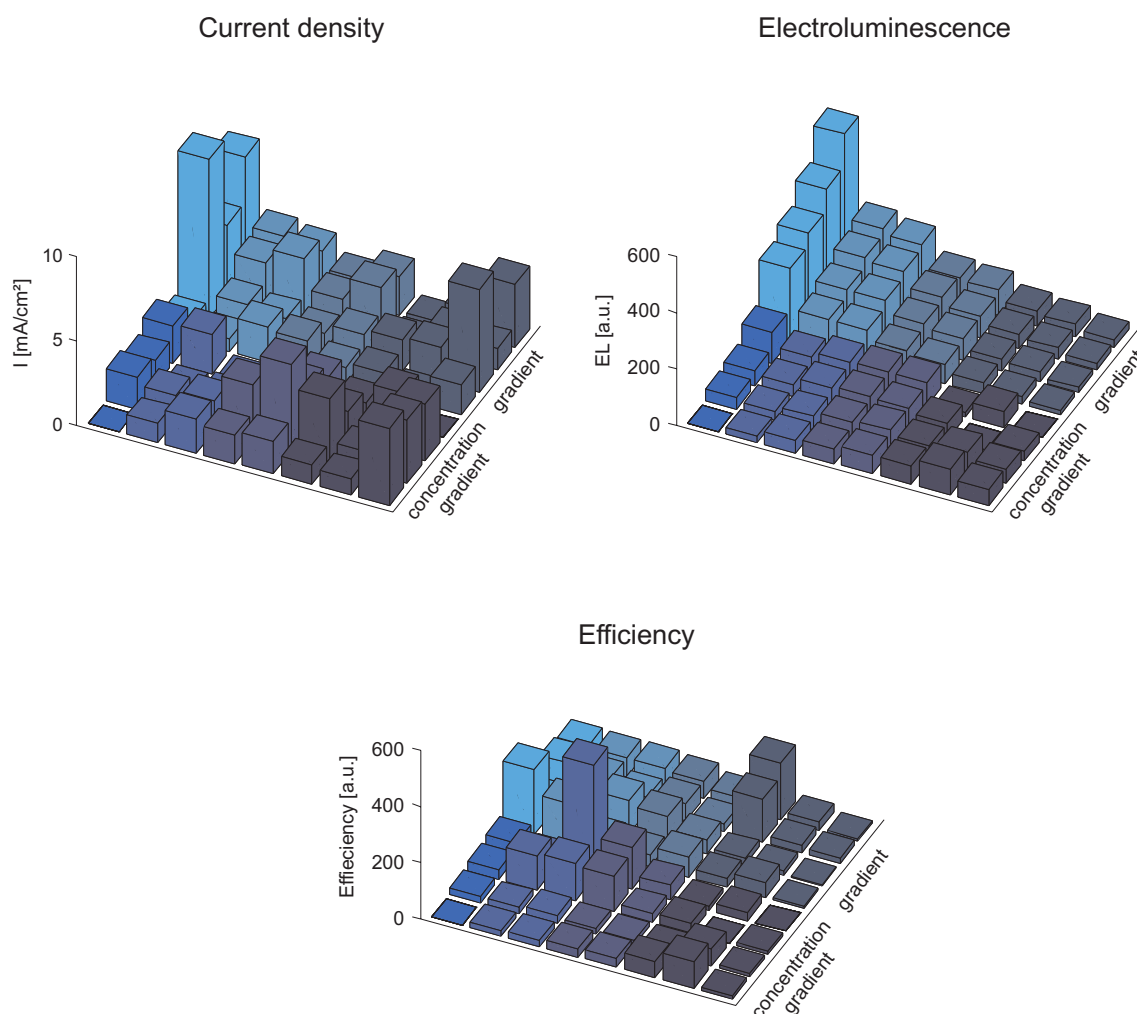


Figure 3.63: Current density, EL, and efficiency at a constant voltage of 5 V. The current density is largely homogeneous; no clear correlation between emitter layer thickness or doping concentration and current density is observed. The EL decreases both with increasing emitter layer thickness and with increasing doping concentration and so does the efficiency, if we disregard the five peak values in the concentration gradient group.

a dependence on both the emitter layer thickness at constant doping concentration and on doping concentration at constant thickness. Devices with a thinner emitter layer exhibit higher EL, as do devices with a lower doping concentration. The latter dependency is, however, very weak. This finding translates directly to the efficiency, where we see higher values for thinner emitter layers and lower doping concentrations, if we disregard the peak values exhibited by some of the devices in the concentration gradient group. This is in agreement with Baldo *et al.*'s finding that devices with a doping concentration of 6% are brighter and more efficient than devices with a doping concentration of 20% [Bal98].

After the initial characterisation of the devices we changed the operational mode to investigate the life-time of the devices. For this purpose, all devices were driven at a continuous current density of 1.77 mA/cm². *I-V* curves were taken regularly by imposing the current rather than the voltage, as commonly done. This is done to protect thinner devices from

the high currents that would occur during a measurement with fixed voltage range. After a period of 190 h, we stopped the flow of nitrogen to allow oxygen and humidity to diffuse into the chamber. Once all devices have failed, the chamber was again flooded with nitrogen to see if any self-repair would occur. The measurement was stopped after 350 h of operation.

Figure 3.64 shows the temporal evolution of the current density, EL, and efficiency at a driving current of 2.2 mA/cm^2 . The curves are coloured according to the emitter layer thickness or doping layer concentration from red (30 nm or 20 %wt) to blue (50 nm or 3 %wt), respectively. The current density is found to be fairly stable for all devices, for some devices even an increase in current density is observed. In the presence of oxygen the current decreases drastically and increases again to comparable values after the refill with nitrogen. The EL behaves differently: All devices show a continuous decrease in EL. Devices in the thickness-gradient group, i. e. devices with an identical doping concentration, are very similar in shape; devices in the concentration-gradient group differ in shape: higher doping concentrations apparently lead to faster degradation. Upon exposure to air, the EL vanishes completely for all devices. After a refill with nitrogen, most of the devices recover partially. However, most of them degrade very fast afterwards. Only a group of seven devices was operated stably for some time. The scenario described is also reflected in the efficiency: devices with high doping concentrations lose their efficiency during operation in nitrogen; all other devices show only little variation in their efficiency. The EL breaks down at the presence of air and recovers completely only for some devices.

To visualise the degradation of the EL, we have taken an image of the whole substrate at the end of each measure cycle, when all devices are operated at constant current. The sequence of images has been arranged so as to give a time-lapse video of the degradation. To cover a wider range of intensities, the brightness is scaled logarithmically. Figures 3.65 and 3.66 show every 10th image of this video with a fixed and an adaptive colour scale. The fixed colour scale is used to visualise the development of the absolute luminance; the adaptive scale is useful for comparing the relative degradation between devices of different type.

We realise, that except for the devices in the leftmost column, the brightness among the devices is fairly homogeneous. A slight overall decrease in EL intensity can be seen for the first ten pictures. The devices in the bottom left-hand corner, which have the highest doping concentrations, show a particularly fast degradation. At the beginning of oxygen diffusion into the chamber, these devices exhibit an increase in brightness (picture 11) before they finally fail. After a refill with nitrogen, a small fraction of devices again show remarkable EL. However, these devices quickly develop dark spots that fragment the luminescing surface and finally lead to the failure of the devices.

3.11.4 Conclusion

We have compared five-layer phosphorescent OLEDs that differ in emitter layer thickness and in concentration of the phosphorescent complex $\text{Ir}(\text{ppy})_3$. We have found that at constant voltage the efficiency of devices decreases with increasing emitter layer thickness and with increasing doping concentration. Strong degradation in nitrogen is observed

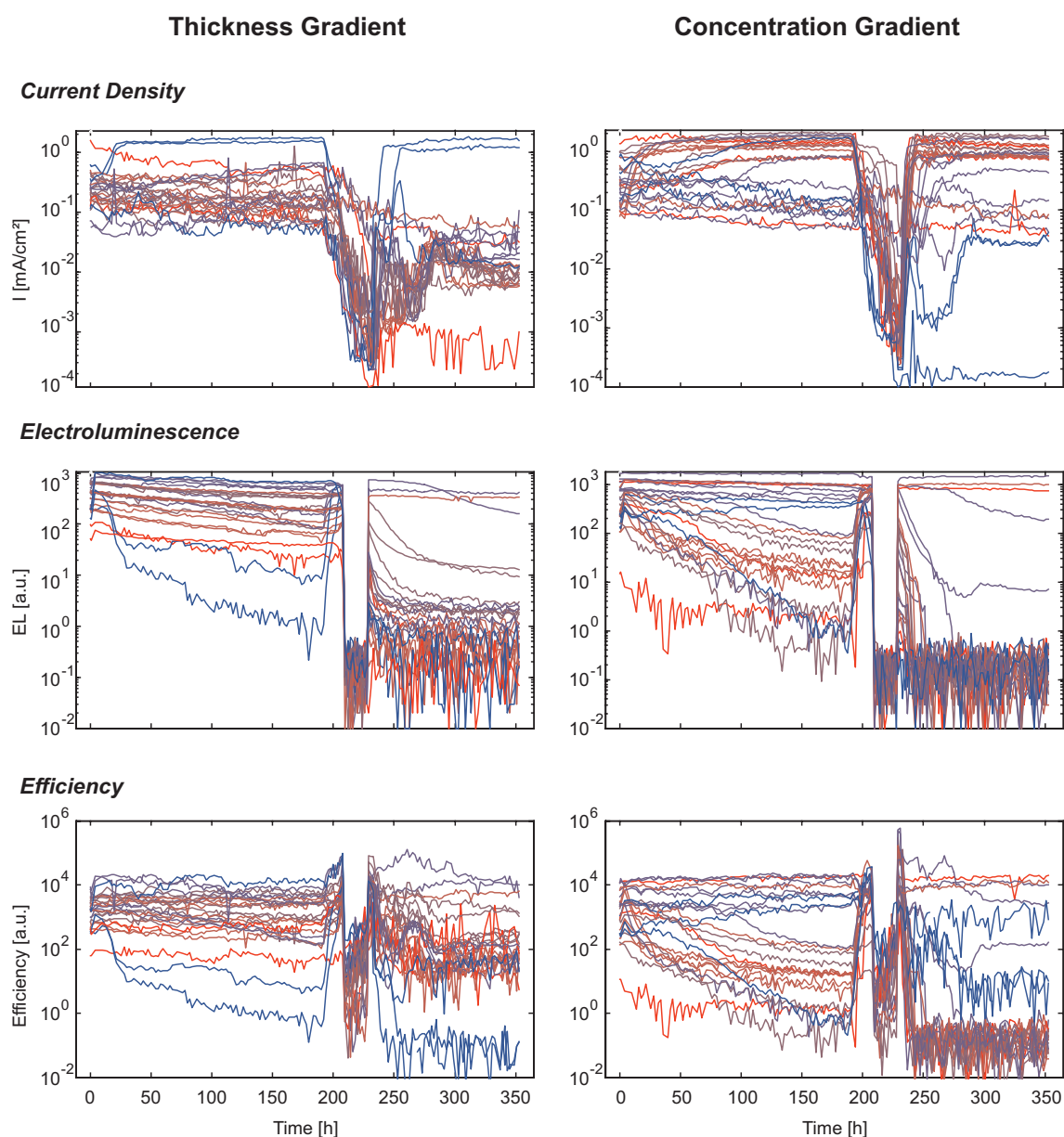


Figure 3.64: Temporal evolution of current density, EL and efficiency at a current density of $I=1.77\text{ mA/cm}^2$. The experiment is performed in nitrogen atmosphere, with an intermediate exposure to air from $t = 190 - 220\text{ h}$. The current densities of all devices are fairly stable; the EL shows a slight degradation for most devices. A strong degradation is observed for devices with high doping concentration. The same holds for the efficiency. Upon the influence of air, the current density decreases significantly and the EL vanishes after a short increase. After a refill with nitrogen, most devices show an increase in the current density, but only a few of them exhibit stable EL.

for devices with high doping concentrations. This suggests that devices should be made as thin as possible and with very low doping concentrations. Obviously, there has to be an optimal thickness and an optimal doping concentration, which will be subject of future systematic studies. Failure upon exposure to air is partially recoverable through

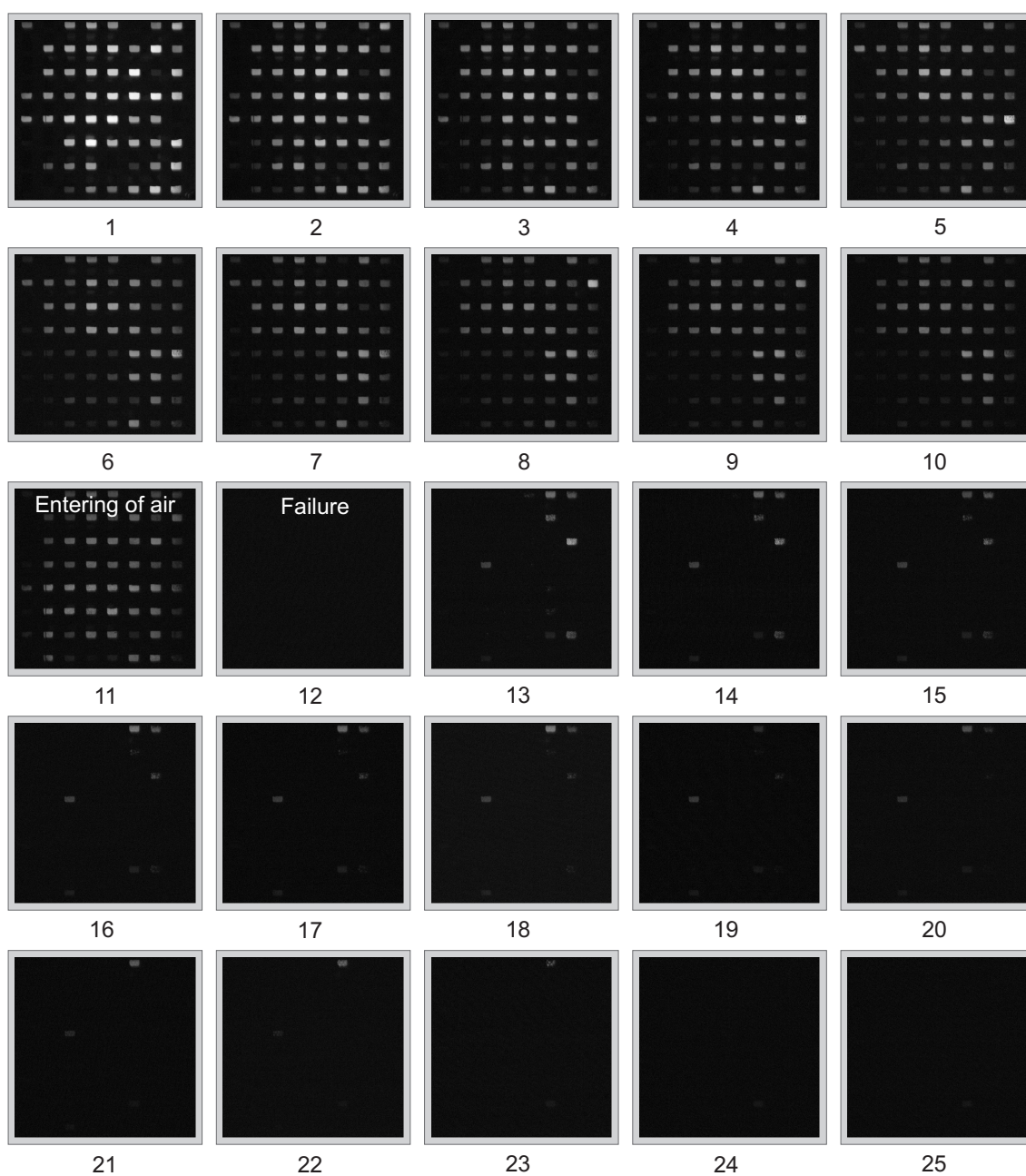


Figure 3.65: *Time-lapse photographs of the degradation at a current density of $1.77\text{mA}/\text{cm}^2$. Every 10th picture of the series is plotted. The EL intensity is scaled logarithmically and the colour scale is identical for all pictures.*

subsequent operation in nitrogen atmosphere. The final failure of the devices seems to originate from the growth of dark spots that might have come into existence as a result of exposure to air. Finally, we have shown that time-lapse photography of the EL at constant current is able to reveal both the absolute and the relative degradation of the device library.

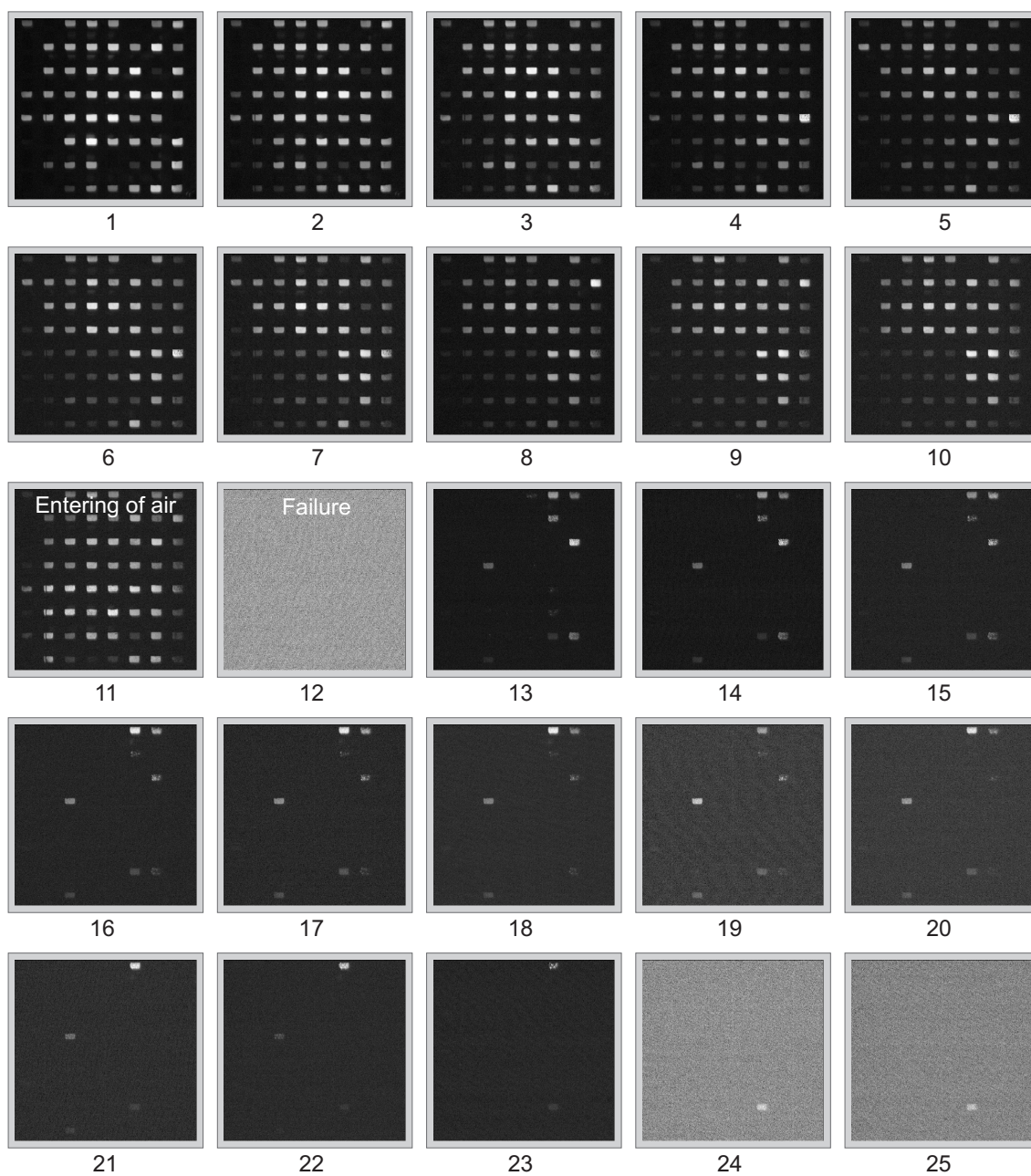


Figure 3.66: *Time-lapse photographs of the degradation at a current density of 1.77 mA/cm^2 . Every 10th picture of the series is plotted. The EL intensity is scaled logarithmically and the colour scale of each picture is adapted to its maximum intensity.*

3.12 Materials

Here we give a summary of all organic materials used in the combinatorial solar-cell and OLED experiments. The structure formulae of the organic compounds are given in Figures 3.67 and 3.68.

- CuPc: *Copper Phthalocyanine*
- DMPTI: *Dimethyl Perylene Tetracarboxydiimide* (also Me-PTCDI or DiMe-PTCDI)
2,9-Dimethyl-anthra[2,1,9-def:6,5,10-d'e'f']diisoquinoline-1,3,8,10-tetraone
- BBIP: *bisbenzimidazole perylene*
Bisbenzimidazo[2,1-a:1',2'-b']anthra[2,1,9-def:6,5,10-d'e'f']diisoquinoline-6,11-dione (mixture with cis-isomer)
- Alq₃: *Aluminium Quinolate*
Tris-(8-hydroxyquinolate)-aluminium
- α -NPD: *Naphthyl Phenyl Diamine* (also NPB)
N,N'-bis(1-naphthyl)-N,N'-diphenyl-(1,1'-biphenyl)-4,4'-diamine
- BCP: *Bathocuproine*
2,9-Dimethyl-4,7-diphenyl-[1,10]phenanthroline
- CBP: *Carbazol Biphenyl*
4,4'-Bis(carbazol-9-yl)biphenyl
- H1T: *Hexamethoxy Triphenylene*
2,3,6,7,10,11-Hexamethoxy-triphenylene
- Ir(ppy)₃: *Iridium Phenyl Pyridine*
fac-tris(2-phenylpyridine) iridium

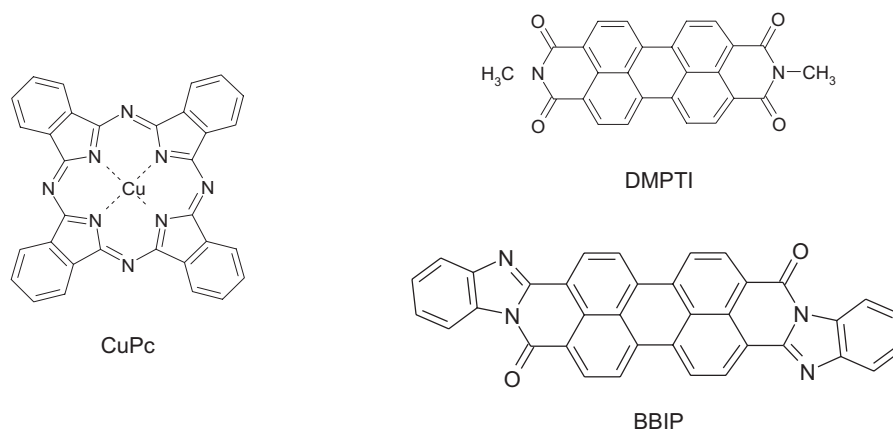


Figure 3.67: *Organic compounds used in the combinatorial solar-cell experiments.*

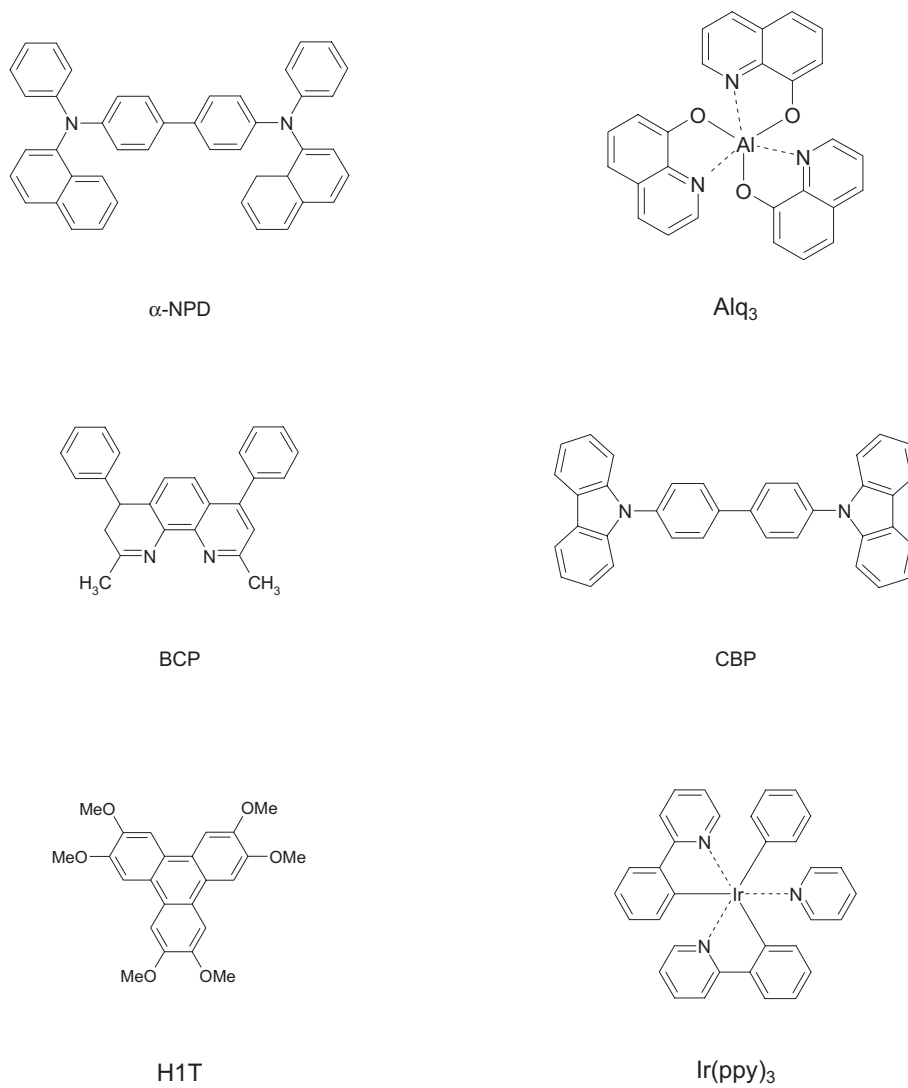


Figure 3.68: *Organic compounds used in the combinatorial OLED experiments.*

Summary

We have developed new techniques for the investigation of organic thin-film devices and have focussed on properties on the molecular scale as well as on macroscopic properties of organic devices.

Scanning probe techniques were used to obtain spatially resolved information on morphology and electro-optical properties. Structural changes in composite-based devices were found to have an important influence on device performance. Furthermore, two modes of electroluminescence detection have been developed. Local luminescence detection in the optical near-field by a scanning near-field optical microscope allowed us to monitor the light emission around a dark spot with a resolution better than 134 nm and to observe the electrode ablation. Finally, we have established a new scanning probe technique, named SELM, “Scanning Electroluminescence Microscop”. The simultaneous detection of a PtIr-tip-induced electroluminescence and shear force allows us to distinguish between topography and conductivity. This technique has revealed a strong spatial variation in the electro-optical properties of Alq₃ films on ITO substrates.

The existing combinatorial preparation method has been supplemented by a variable testing setup that permits the simultaneous investigation of 64 devices under nearly identical conditions. Both OLEDs and photovoltaic cells have successfully been tested over more than 300 hours of continuous operation so that it was possible to study the influence of material combinations and layer thicknesses on the performance and on the degradation of the devices. Variable-angle spectroscopic ellipsometry has been used for the optical characterisation of materials and an automation has been provided for the analysis of combinatorially prepared device arrays. Furthermore, a Mathematica[®] program has been developed for the theoretical description of the short-circuit current in photovoltaic cells. By this means it was possible to explain in detail the observed performance enhancement in heterojunction solar cells, induced by an additional TiO₂ layer. The optical and electronic contribution could only be identified by the variation of both layer thickness *and* device type. The strength of the setup presented is its ability to produce and to test devices under nearly identical conditions and to yield reliable data, which in turn can be used to test physical models. Finally, we have addressed the degradation process of OLEDs. The experiments have shown that inert gas plays an essential role in protecting against degradation, not only by the exclusion of reactive species but also by its heat-transport capabilities. These investigations are only just beginning and further combinatorial studies paired with AFM measurements are currently being developed.

Zusammenfassung

Im Rahmen dieser Arbeit wurden verschiedene Techniken zur Untersuchung von organischen Dünnschichtbauelementen entwickelt und weiterentwickelt. Der Fokus lag dabei einerseits auf lokalen Sondentechniken zur Untersuchung von Eigenschaften auf molekularer Skala, andererseits auf makroskopischen Eigenschaften von Bauelementen.

Mit Rastersondentechniken haben wir die Morphologie und die elektrooptischen Eigenschaften auf Submikrometerskala detektieren können. Strukturveränderungen in Kompositfilmen konnten beobachtet und mit der Effizienz von Bauelementen verknüpft werden. Ferner haben wir zwei Modi zur Elektrolumineszenzdetektion im Nahfeld entwickelt. Die lokale Detektion der Elektrolumineszenz hat es uns ermöglicht einen "dark spot"-Defekt mit einer Auflösung unterhalb von 134 nm während seiner Entstehung zu beobachten. Schließlich haben wir eine neue Methode entwickelt, die wir SELM, "Scanning Electroluminescence Microscopy", getauft haben. Durch die simultane Detektion von Scherkraft und lokal induzierter Elektrolumineszenz konnten wir zwischen der Topographie und lokaler Leitfähigkeit unterscheiden, was bei klassischen STM-Techniken nicht möglich ist. Mithilfe dieser neuen Methode haben wir gezeigt, dass die elektrooptischen Eigenschaften von Alq₃Filmen auf ITO Substraten stark variieren.

Im zweiten Teil der Arbeit wurde die am Lehrstuhl vorhandene kombinatorische Präparationsmethode durch ein sehr variables Testsystem erweitert, das die simultane Analyse von 64 Bauelementen auf einem Substrat erlaubt. Sowohl organische Leuchtdioden als auch organische Solarzellen wurden erfolgreich über eine Zeit von über 300 Stunden betrieben, so dass Material- und Schichtdickenabhängigkeit der Degradation studiert werden konnten. Mit winkelabhängiger spektroskopischer Ellipsometrie haben wir den komplexen Brechungsindex der verwendeten organischen Materialien bestimmt und das Ellipsometer automatisiert für die kombinatorische Schichtdickenanalyse der aufgedampften Bauelemente. Ferner wurde ein Mathematica[®] Programm entwickelt, das den Kurzschlussstrom in Solarzellen modelliert. Damit war es möglich, optische und elektrische Anteile im Kurzschlussstrom zu unterscheiden. Die Stärke des vorgestellten Aufbaus liegt darin, einheitlich hergestellte Bauelemente einem einheitlichen Testverfahren zu unterziehen, so dass parasitäre Einflüsse minimiert werden. Auf diese Weise haben wir zuverlässige Daten erhalten, die später mit physikalischen Modellen verglichen werden konnten. Zuletzt haben wir die Degradation von Leuchtdioden genauer untersucht. Unsere Experimente haben gezeigt, dass die Anwesenheit von Schutzgas nicht nur chemisch vor Degradation schützt sondern auch physikalisch durch Wärmetransport. Die Degradationsmechanismen in Vakuum und in Schutzgas unterscheiden sich deutlich und sind zum Teil reversibel. Derzeit sind weitere Messungen in Kombination mit AFM-Untersuchungen in Planung.

List of Publications

A. Böker, H. Elbs, H. Hänsel, A. Knoll, S. Ludwigs, H. Zettl, V. Urban, V. Abetz, A. H. E. Müller, and G. Krausch

“Microscopic mechanisms of electric-field-induced alignment of block copolymer microdomains”

Phys. Rev. Lett., **89** (13), 135502 (2002).

A. Böker, H. Elbs, H. Hänsel, A. Knoll, S. Ludwigs, H. Zettl, A. V. Zvelindovsky, G. J. A. Sevink, V. Urban, V. Abetz, A. H. E. Müller, and G. Krausch

“Electric field induced alignment of concentrated block copolymer solutions”

Macromol. Symp., **36** (21), 8078–8087 (2003).

H. Hänsel, H. Zettl, G. Krausch, C. Schmitz, R. Kisselev, M. Thelakkat, and H. W. Schmidt

“Combinatorial study of the long-term stability of organic thin-film solar cells”

Appl. Phys. Lett., **81** (11), 2106–2108 (2002).

H. Hänsel, D. C. Müller, M. Gross, K. Meerholz, and G. Krausch

“Morphological changes in composite-based organic light-emitting diodes”

Macromol. Symp., **36** (13), 4932–4936 (2003).

H. Hänsel, H. Zettl, G. Krausch, R. Kisselev, M. Thelakkat, and H. W. Schmidt

“Optical and Electronic Contributions in Double-Heterojunction Organic Thin-Film Solar Cells”

Adv. Mater., **15** (24), 2056–2060 (2003).

A. Knoll, H. Hänsel, N. Rehse, R. Magerle, and G. Krausch. “TappingMode atomic force microscopy on polymers: Where is the true sample surface?”

Abstr. Pap. Am. Chem. Soc., **221**, U341–U341 (2001).

G. Krausch, A. Böker, H. Elbs, H. Hänsel, A. Knoll, S. Ludwigs, H. Zettl, V. Urban, V. Abetz, and A. H. E. Müller

“Macroscopic alignment of concentrated block copolymer solutions in electric fields.”

Abstr. Pap. Am. Chem. Soc., **224**, U366–U366 (2002).

Bibliography

- [Ada97] C. Adachi, S. Hibino, T. Koyama, and Y. Taniguchi. “Submicrometer-sized organic light emitting diodes with a triphenylamine-containing polycarbonate as a guest molecule in a polymer blend”. *Jpn. J. Appl. Phys. Pt. 2*, **36** (6B), L827–L830 (1997)
- [Ada00] C. Adachi, M. A. Baldo, S. R. Forrest, and M. E. Thompson. “High-efficiency organic electrophosphorescent devices with tris(2-phenylpyridine)iridium doped into electron-transporting materials”. *Appl. Phys. Lett.*, **77** (6), 904–906 (2000)
- [Ada01a] C. Adachi, M. A. Baldo, S. R. Forrest, S. Lamansky, M. E. Thompson, and R. C. Kwong. “High-efficiency red electrophosphorescence devices”. *Appl. Phys. Lett.*, **78** (11), 1622–1624 (2001)
- [Ada01b] C. Adachi, M. A. Baldo, M. E. Thompson, and S. R. Forrest. “Nearly 100% internal phosphorescence efficiency in an organic light-emitting device”. *J. Appl. Phys.*, **90** (10), 5048–5051 (2001)
- [Ada01c] C. Adachi, R. C. Kwong, P. Djurovich, V. Adamovich, M. A. Baldo, M. E. Thompson, and S. R. Forrest. “Endothermic energy transfer: A mechanism for generating very efficient high-energy phosphorescent emission in organic materials”. *Appl. Phys. Lett.*, **79** (13), 2082–2084 (2001)
- [Ade99] H. Ade, D. A. Winesett, A. P. Smith, S. Qu, S. Ge, J. Sokolov, and M. Raifailovich. “Phase segregation in polymer thin films: Elucidations by X-ray and scanning force microscopy”. *Europhys. Lett.*, **45** (4), 526–532 (1999)
- [Alo02] M. I. Alonso, M. Garriga, N. Karl, J. O. Osso, and F. Schreiber. “Anisotropic optical properties of single crystalline PTCDA studied by spectroscopic ellipsometry”. *Org. Electron.*, **3** (1), 23–31 (2002)
- [Alv97] S. F. Alvarado, W. Riess, P. F. Seidler, and P. Strohriegel. “STM-induced luminescence study of poly(p-phenylenevinylene) by conversion under ultraclean conditions”. *Phys. Rev. B*, **56** (3), 1269–1278 (1997)
- [Alv98] S. F. Alvarado, P. F. Seidler, D. G. Lidzey, and D. D. C. Bradley. “Direct determination of the exciton binding energy of conjugated polymers using a scanning tunneling microscope”. *Phys. Rev. Lett.*, **81** (5), 1082–1085 (1998)
- [Ami02] E. J. Amis, X. D. Xiang, and J. C. Zhao. “Combinatorial materials science: What’s new since Edison?” *MRS Bull.*, **27** (4), 295–297 (2002)
- [Ari01] A. C. Arias, J. D. MacKenzie, R. Stevenson, J. J. M. Halls, M. Inbasekaran, E. P. Woo, D. Richards, and R. H. Friend. “Photovoltaic performance and morphology of polyfluorene blends: A combined microscopic and photovoltaic investigation”. *Macromol. Symp.*, **34** (17), 6005–6013 (2001)

- [Ari02] A. C. Arias, N. Corcoran, M. Banach, R. H. Friend, J. D. MacKenzie, and W. T. S. Huck. “Vertically segregated polymer-blend photovoltaic thin-film structures through surface-mediated solution processing”. *Appl. Phys. Lett.*, **80** (10), 1695–1697 (2002)
- [Azi98a] H. Aziz, Z. Popovic, C. P. Tripp, N. X. Hu, A. M. Hor, and G. Xu. “Degradation processes at the cathode/organic interface in organic light emitting devices with Mg : Ag cathodes”. *Appl. Phys. Lett.*, **72** (21), 2642–2644 (1998)
- [Azi98b] H. Aziz, Z. Popovic, S. Xie, A. M. Hor, N. X. Hu, C. Tripp, and G. Xu. “Humidity-induced crystallization of tris (8-hydroxyquinoline) aluminum layers in organic light-emitting devices”. *Appl. Phys. Lett.*, **72** (7), 756–758 (1998)
- [Bal98] M. A. Baldo, D. F. O’Brien, Y. You, A. Shoustikov, S. Sibley, M. E. Thompson, and S. R. Forrest. “Highly efficient phosphorescent emission from organic electroluminescent devices”. *Nature*, **395** (6698), 151–154 (1998)
- [Bal99] M. A. Baldo, S. Lamansky, P. E. Burrows, M. E. Thompson, and S. R. Forrest. “Very high-efficiency green organic light-emitting devices based on electrophosphorescence”. *Appl. Phys. Lett.*, **75** (1), 4–6 (1999)
- [Bal00a] M. A. Baldo, C. Adachi, and S. R. Forrest. “Transient analysis of organic electrophosphorescence. II. Transient analysis of triplet-triplet annihilation”. *Phys. Rev. B*, **62** (16), 10967–10977 (2000)
- [Bal00b] M. A. Baldo and S. R. Forrest. “Transient analysis of organic electrophosphorescence: I. Transient analysis of triplet energy transfer”. *Phys. Rev. B*, **62** (16), 10958–10966 (2000)
- [Bar75] M. A. Barrett, Z. Borkowska, M. W. Humphreys, and R. Parsons. “Ellipsometry of thin films of copper phthalocyanine”. *Thin Solid Films*, **28** (2), 289–302 (1975)
- [BAS03] BASF. “Optical Constants of DMPTI” (personal communication 2003)
- [Bei02] T. A. Beierlein, H.-P. Ott, H. Hofmann, H. Riel, B. Ruhstaller, B. Crone, S. Karg, and W. Riess. “Combinatorial Device Fabrication and Optimization of Multilayer Organic LEDs”. *Proc. SPIE*, **4464**, 178–186 (2002)
- [Ben97] C. Benecke, T. Grüner, A. Kerber, R. Laue, and T. Wieland. “MOLEcular structure GENeration with MOLGEN, new features and future developments”. *Fresen. J. Anal. Chem.*, **359** (1), 23–32 (1997)
- [Bin99] K. Binder. “Phase transitions of polymer blends and block copolymer melts in thin films”. *Adv. Polym. Sci.*, **138**, 1–89 (1999)
- [Blo98] J. Blochwitz, M. Pfeiffer, T. Fritz, and K. Leo. “Low voltage organic light emitting diodes featuring doped phthalocyanine as hole transport material”. *Appl. Phys. Lett.*, **73** (6), 729–731 (1998)

- [Bor99] M. Born and E. Wolf. *Principles of optics : electromagnetic theory of propagation, interference and diffraction of light* (Cambridge University Press, Cambridge, 1999), 7th (expanded) edition
- [Bra01] C. J. Brabec, A. Cravino, D. Meissner, N. S. Sariciftci, T. Fromherz, M. T. Rispens, L. Sanchez, and J. C. Hummelen. “Origin of the open circuit voltage of plastic solar cells”. *Adv. Funct. Mater.*, **11** (5), 374–380 (2001)
- [Bre01] A. J. Breeze, Z. Schlesinger, S. A. Carter, and P. J. Brock. “Charge transport in TiO₂/MEH-PPV polymer photovoltaics”. *Phys. Rev. B*, **64** (12), 125205 (2001)
- [Bro99] T. M. Brown, J. S. Kim, R. H. Friend, F. Cacialli, R. Daik, and W. J. Feast. “Built-in field electroabsorption spectroscopy of polymer light-emitting diodes incorporating a doped poly(3,4-ethylene dioxythiophene) hole injection layer”. *Appl. Phys. Lett.*, **75** (12), 1679–1681 (1999)
- [Bru92] F. Bruder and R. Brenn. “Spinodal Decomposition in Thin-Films of a Polymer Blend”. *Phys. Rev. Lett.*, **69** (4), 624–627 (1992)
- [Bud99] A. Budkowski. “Interfacial phenomena in thin polymer films: Phase coexistence and segregation”. *Adv. Polym. Sci.*, **148**, 1–111 (1999)
- [Bul96a] V. Bulovic, P. E. Burrows, S. R. Forrest, J. A. Cronin, and M. E. Thompson. “Study of localized and extended excitons in 3,4,9,10-perylenetetracarboxylic dianhydride (PTCDA) .1. Spectroscopic properties of thin films and solutions”. *Chem. Phys.*, **210** (1-2), 1–12 (1996)
- [Bul96b] V. Bulovic and S. R. Forrest. “Study of localized and extended excitons in 3,4,9,10-perylenetetracarboxylic dianhydride (PTCDA) .2. Photocurrent response at low electric fields”. *Chem. Phys.*, **210** (1-2), 13–25 (1996)
- [Bur94] P. E. Burrows, V. Bulovic, S. R. Forrest, L. S. Sapochak, D. M. McCarty, and M. E. Thompson. “Reliability and Degradation of Organic Light-Emitting Devices”. *Appl. Phys. Lett.*, **65** (23), 2922–2924 (1994)
- [Bur00] P. E. Burrows, S. R. Forrest, T. X. Zhou, and L. Michalski. “Operating lifetime of phosphorescent organic light emitting devices”. *Appl. Phys. Lett.*, **76** (18), 2493–2495 (2000)
- [Car97] S. A. Carter, J. C. Scott, and P. J. Brock. “Enhanced luminance in polymer composite light emitting devices”. *Appl. Phys. Lett.*, **71** (9), 1145–1147 (1997)
- [Cho96] V. Choong, Y. Park, Y. Gao, T. Wehrmeister, K. Müllen, B. R. Hsieh, and C. W. Tang. “Dramatic photoluminescence quenching of phenylene vinylene oligomer thin films upon submonolayer Ca deposition”. *Appl. Phys. Lett.*, **69** (10), 1492–1494 (1996)
- [Cho97] V. E. Choong, Y. Park, Y. Gao, T. Wehrmeister, K. Müllen, B. R. Hsieh, and C. W. Tang. “Effects of Al, Ag, and Ca on luminescence of organic materials”. *J. Vac. Sci. Technol. A*, **15** (3), 1745–1749 (1997)

- [D'A01] B. W. D'Andrade, M. A. Baldo, C. Adachi, J. Brooks, M. E. Thompson, and S. R. Forrest. "High-efficiency yellow double-doped organic light-emitting devices based on phosphor-sensitized fluorescence". *Appl. Phys. Lett.*, **79** (7), 1045–1047 (2001)
- [Deb92] M. K. Debe. "Variable Angle Spectroscopic Ellipsometry Studies of Oriented Phthalocyanine Films .2. Copper Phthalocyanine". *J. Vac. Sci. Technol. A*, **10** (4), 2816–2821 (1992)
- [Dju00] A. B. Djuriscic, T. Fritz, and K. Leo. "Modeling the optical constants of organic thin films: application to 3,4,9,10-perylenetetracarboxylic dianhydride (PTCDA)". *Opt. Commun.*, **183** (1-4), 123–132 (2000)
- [Dju02] A. B. Djuriscic, Y. Chan, and E. H. Li. "Progress in the room-temperature optical functions of semiconductors". *Mat. Sci. Eng. R*, **38** (6), 237–293 (2002)
- [Do96] L. M. Do, M. Oyamada, A. Koike, E. M. Han, N. Yamamoto, and M. Fujihira. "Morphological change in the degradation of Al electrode surfaces of electroluminescent devices by fluorescence microscopy and AFM". *Thin Solid Films*, **273** (1-2), 209–213 (1996)
- [Do97] L. M. Do, K. J. Kim, T. Zyung, H. K. Shim, and J. J. Kim. "In situ investigation of degradation in polymeric electroluminescent devices using time-resolved confocal laser scanning microscope". *Appl. Phys. Lett.*, **70** (25), 3470–3472 (1997)
- [For03] S. R. Forrest. "The road to high efficiency organic light emitting devices". *Org. Electron.*, **4** (2-3), 45–48 (2003)
- [Fra96] A. Franke, A. Stendal, O. Stenzel, and C. v. Borczyskowski. "Gaussian quadrature approach to the calculation of the optical constants in the vicinity of inhomogeneously broadened absorption lines". *Pure Appl. Opt.*, **5** (6), 845 (1996)
- [Fri99] R. H. Friend, R. W. Gymer, A. B. Holmes, J. H. Burroughes, R. N. Marks, C. Taliani, D. D. C. Bradley, D. A. Dos Santos, J. L. Bredas, M. Logdlund, and W. R. Salaneck. "Electroluminescence in conjugated polymers". *Nature*, **397** (6715), 121–128 (1999)
- [Fuj96] M. Fujihira, L. M. Do, A. Koike, and E. M. Han. "Growth of dark spots by interdiffusion across organic layers in organic electroluminescent devices". *Appl. Phys. Lett.*, **68** (13), 1787–1789 (1996)
- [Gre99a] G. Greczynski, T. Kugler, and W. R. Salaneck. "Characterization of the PEDOT-PSS system by means of X-ray and ultraviolet photoelectron spectroscopy". *Thin Solid Films*, **354** (1-2), 129–135 (1999)
- [Gre99b] M. Grell, W. Knoll, D. Lupo, A. Meisel, T. Miteva, D. Neher, H. G. Nothofer, U. Scherf, and A. Yasuda. "Blue polarized electroluminescence from a liquid crystalline polyfluorene". *Adv. Mater.*, **11** (8), 671–675 (1999)

- [Hea65] O. S. Heavens. *Optical properties of thin solid films* (Dover Publications, New York, 1965)
- [Hee98] A. J. Heeger. “Light emission from semiconducting polymers: Light-emitting diodes, light-emitting electrochemical cells, lasers and white light for the future”. *Solid State Commun.*, **107** (11), 673–679 (1998)
- [Hel65] W. Helfrich and G. Schneider. “Recombination radiation in anthracene crystals”. *Phys. Rev. Lett.*, **14**, 229–231 (1965)
- [Hil99] I. G. Hill and A. Kahn. “Organic semiconductor heterointerfaces containing bathocuproine”. *J. Appl. Phys.*, **86** (8), 4515–4519 (1999)
- [Hin01] A. Hinsch, J. M. Kroon, R. Kem, I. Uhlendorf, J. Holzbock, A. Meyer, and J. Ferber. “Long-term stability of dye-sensitised solar cells”. *Prog. Photovolt., Res. Appl.*, **9** (6), 425–438 (2001)
- [Hir92] M. Hiramoto, H. Fukusumi, and M. Yokoyama. “Organic Solar-Cell Based on Multistep Charge Separation System”. *Appl. Phys. Lett.*, **61** (21), 2580–2582 (1992)
- [Hän02] H. Hänsel, H. Zettl, G. Krausch, C. Schmitz, R. Kisselev, M. Thelakkat, and H. W. Schmidt. “Combinatorial study of the long-term stability of organic thin-film solar cells”. *Appl. Phys. Lett.*, **81** (11), 2106–2108 (2002)
- [Hän03a] H. Hänsel, D. C. Müller, M. Gross, K. Meerholz, and G. Krausch. “Morphological changes in composite-based organic light-emitting diodes”. *Macromol. Symp.*, **36** (13), 4932–4936 (2003)
- [Hän03b] H. Hänsel, H. Zettl, G. Krausch, R. Kisselev, M. Thelakkat, and H. W. Schmidt. “Optical and electronic contributions in double-heterojunction organic thin-film solar cells”. *Adv. Mater.*, **15** (24), 2056–2060 (2003)
- [Ika01] M. Ikai, S. Tokito, Y. Sakamoto, T. Suzuki, and Y. Taga. “Highly efficient phosphorescence from organic light-emitting devices with an exciton-block layer”. *Appl. Phys. Lett.*, **79** (2), 156–158 (2001)
- [Ito00] E. Itoh, M. Iwamoto, M. Burghard, and S. Roth. “Ultraviolet photoelectron spectroscopy and surface potential of pi-conjugated Langmuir-Blodgett films on gold metal electrode”. *Jpn. J. Appl. Phys. Pt. 1*, **39** (7A), 5146–5150 (2000)
- [Jac75] J. D. Jackson. *Classical electrodynamics* (Wiley, New York, 1975), 2nd edition
- [Jel93] G. E. Jellison, M. F. Chisholm, and S. M. Gorbatkin. “Optical Functions of Chemical-Vapor-Deposited Thin-Film Silicon Determined by Spectroscopic Ellipsometry”. *Appl. Phys. Lett.*, **62** (25), 3348–3350 (1993)
- [Jon91] R. A. L. Jones, L. J. Norton, E. J. Kramer, F. S. Bates, and P. Wiltzius. “Surface-Directed Spinodal Decomposition”. *Phys. Rev. Lett.*, **66** (10), 1326–1329 (1991)

- [Kar98] A. Karim, T. M. Slawecki, S. K. Kumar, J. F. Douglas, S. K. Satija, C. C. Han, T. P. Russell, Y. Liu, R. Overney, O. Sokolov, and M. H. Rafailovich. “Phase-separation-induced surface patterns in thin polymer blend films”. *Macromol. Symp.*, **31** (3), 857–862 (1998)
- [Ke01] L. Ke, S. F. Lim, and S. J. Chua. “Organic light-emitting device dark spot growth behavior analysis by diffusion reaction theory”. *J. Pol. Sci. B*, **39** (14), 1697–1703 (2001)
- [Ke02] L. Ke, S. J. Chua, K. R. Zhang, and P. Chen. “Bubble formation due to electrical stress in organic light emitting devices”. *Appl. Phys. Lett.*, **80** (2), 171–173 (2002)
- [Ker00] H. R. Kerp and E. E. van Faassen. “Effects of oxygen on exciton transport in zinc phthalocyanine layers”. *Chem. Phys. Lett.*, **332** (1-2), 5–12 (2000)
- [Kno01] A. Knoll, H. Hänsel, N. Rehse, R. Magerle, and G. Krausch. “Tappingmode atomic force microscopy on polymers: Where is the true sample surface?” *Abstr. Pap. Am. Chem. Soc.*, **221**, U341–U341 (2001)
- [Kol01] D. Kolosov, D. S. English, V. Bulovic, P. F. Barbara, S. R. Forrest, and M. E. Thompson. “Direct observation of structural changes in organic light emitting devices during degradation”. *J. Appl. Phys.*, **90** (7), 3242–3247 (2001)
- [Kra27] H. Kramers. “La Diffusion de la Lumière par les Atomes”. *Atti Congr. Intern. Fis. Como*, **2**, 545 (1927)
- [Kra95] G. Krausch, S. Wegscheider, A. Kirsch, H. Bielefeldt, J. C. Meiners, and J. Mlynek. “Near-Field Microscopy and Lithography with Uncoated Fiber Tips - a Comparison”. *Opt. Commun.*, **119** (3-4), 283–288 (1995)
- [Kra01] B. Krause, A. C. Durr, K. A. Ritley, F. Schreiber, H. Dosch, and D. Smilgies. “On the coexistence of different polymorphs in organic epitaxy: alpha and beta phase of PTCDA on Ag(111)”. *Appl. Surf. Sci.*, **175**, 332–336 (2001)
- [Kro26] R. d. L. Kronig. “On The Theory of Dispersion of X-Rays”. *J. Opt. Soc. Am.*, **12**, 547–557 (1926)
- [Kwo03] R. C. Kwong, M. S. Weaver, M. H. M. Lu, Y. J. Tung, A. B. Chwang, T. X. Zhou, M. Hack, and J. J. Brown. “Current status of electrophosphorescent device stability”. *Org. Electron.*, **4** (2-3), 155–164 (2003)
- [Lee00] C. L. Lee, K. B. Lee, and J. J. Kim. “Polymer phosphorescent light-emitting devices doped with tris(2-phenylpyridine) iridium as a triplet emitter”. *Appl. Phys. Lett.*, **77** (15), 2280–2282 (2000)
- [Lee03] J. Y. Lee, J. H. Kwon, and H. K. Chung. “High efficiency and low power consumption in active matrix organic light emitting diodes”. *Org. Electron.*, **4** (2-3), 143–148 (2003)

- [Lid97] D. G. Lidzey, S. F. Alvarado, P. F. Seidler, S. F. Bleyer, and D. D. C. Bradley. “Electroluminescence from a soluble poly(p-phenylenevinylene) derivative generated using a scanning tunneling microscope”. *Appl. Phys. Lett.*, **71** (14), 2008–2010 (1997)
- [Lie00] Y. F. Liew, H. Aziz, N. X. Hu, H. S. O. Chan, G. Xu, and Z. Popovic. “Investigation of the sites of dark spots in organic light-emitting devices”. *Appl. Phys. Lett.*, **77** (17), 2650–2652 (2000)
- [Lim01] S. F. Lim, W. Wang, and S. J. Chua. “Degradation of organic light-emitting devices due to formation and growth of dark spots”. *Mat. Sci. Eng. B*, **85** (2-3), 154–159 (2001)
- [Loi03] M. A. Loi, P. Denk, H. Hoppe, H. Neugebauer, C. Winder, D. Meissner, C. Brabec, N. S. Sariciftci, A. Gouloumis, P. Vazquez, and T. Torres. “Long-lived photoinduced charge separation for solar cell applications in phthalocyanine-fulleropyrrolidine dyad thin films”. *J. Mater. Chem.*, **13** (4), 700–704 (2003)
- [McE96] J. McElvain, H. Antoniadis, M. R. Hueschen, J. N. Miller, D. M. Roitman, J. R. Sheats, and R. L. Moon. “Formation and growth of black spots in organic light-emitting diodes”. *J. Appl. Phys.*, **80** (10), 6002–6007 (1996)
- [Mei02] A. Meisel, T. Miteva, G. Glaser, V. Scheumann, and D. Neher. “Influence of the dopant concentration on the morphology of hole-transporting alignment layers based on a polyimide matrix”. *Polymer*, **43** (19), 5235–5242 (2002)
- [Mit01] T. Miteva, A. Meisel, W. Knoll, H. G. Nothofer, U. Scherf, D. C. Müller, K. Meerholz, A. Yasuda, and D. Neher. “Improving the performance of polyfluorene-based organic light-emitting diodes via end-capping”. *Adv. Mater.*, **13** (8), 565–570 (2001)
- [Mül01] M. Müller, K. Binder, and E. V. Albano. “Phase equilibria in thin polymer films”. *Int. J. Mod. Phys. B*, **15** (13), 1867–1903 (2001)
- [Mor01] J. Morgado, E. Moons, R. H. Friend, and F. Cacialli. “De-mixing of polyfluorene-based blends by contact with acetone: Electro- and photo-luminescence probes”. *Adv. Mater.*, **13** (11), 810–814 (2001)
- [Ney98] K. A. Neyts. “Simulation of light emission from thin-film microcavities”. *J. Opt. Soc. Am. A*, **15** (4), 962–971 (1998)
- [Ney00] K. Neyts, P. De Visschere, D. K. Fork, and G. B. Anderson. “Semitransparent metal or distributed Bragg reflector for wide-viewing-angle organic light-emitting-diode microcavities”. *J. Opt. Soc. Am. B*, **17** (1), 114–119 (2000)
- [O’B99] D. F. O’Brien, M. A. Baldo, M. E. Thompson, and S. R. Forrest. “Improved energy transfer in electrophosphorescent devices”. *Appl. Phys. Lett.*, **74** (3), 442–444 (1999)

- [Pal85] E. D. Palik. *Handbook of optical constants of solids* (Academic Press, Orlando, 1985)
- [Par94] I. D. Parker, Q. Pei, and M. Marrocco. “Efficient Blue Electroluminescence from a Fluorinated Polyquinoline”. *Appl. Phys. Lett.*, **65** (10), 1272–1274 (1994)
- [Pet99] L. A. A. Pettersson, L. S. Roman, and O. Inganäs. “Modeling photocurrent action spectra of photovoltaic devices based on organic thin films”. *J. Appl. Phys.*, **86** (1), 487–496 (1999)
- [Pet01] H. Pettersson and T. Gruszecki. “Long-term stability of low-power dye-sensitised solar cells prepared by industrial methods”. *Sol. Energy Mater. Sol. Cells*, **70** (2), 203–212 (2001)
- [Peu00] P. Peumans, V. Bulovic, and S. R. Forrest. “Efficient photon harvesting at high optical intensities in ultrathin organic double-heterostructure photovoltaic diodes”. *Appl. Phys. Lett.*, **76** (19), 2650–2652 (2000)
- [Peu01] P. Peumans and S. R. Forrest. “Very-high-efficiency double-heterostructure copper phthalocyanine/C-60 photovoltaic cells”. *Appl. Phys. Lett.*, **79** (1), 126–128 (2001)
- [Peu03] P. Peumans, A. Yakimov, and S. R. Forrest. “Small molecular weight organic thin-film photodetectors and solar cells”. *J. Appl. Phys.*, **93** (7), 3693–3723 (2003)
- [Pur97] S. Puri and H. L. Frisch. “Surface-directed spinodal decomposition: Modelling and numerical simulations”. *J. Phys.: Condens. Matter*, **9** (10), 2109–2133 (1997)
- [Ren91] P. Renaud and S. F. Alvarado. “Mapping Quantum-Well Energy Profiles of III-V-Heterostructures by Scanning-Tunneling-Microscope-Excited Luminescence”. *Phys. Rev. B*, **44** (12), 6340–6343 (1991)
- [Rie03] H. Riel, S. Karg, T. Beierlein, W. Riess, and K. Neyts. “Tuning the emission characteristics of top-emitting organic light-emitting devices by means of a dielectric capping layer: An experimental and theoretical study”. *J. Appl. Phys.*, **94** (8), 5290–5296 (2003)
- [Sai00] D. Sainova, T. Miteva, H. G. Nothofer, U. Scherf, I. Glowacki, J. Ulanski, H. Fujikawa, and D. Neher. “Control of color and efficiency of light-emitting diodes based on polyfluorenes blended with hole-transporting molecules”. *Appl. Phys. Lett.*, **76** (14), 1810–1812 (2000)
- [Sat94] Y. Sato and H. Kanai. “Stability of Organic Electroluminescent Diodes”. *Mol. Cryst. Liq. Cryst.*, **252**, 435–442 (1994)
- [Sch99a] C. Schmitz, P. Posch, M. Thelakkat, and H. W. Schmidt. “Efficient screening of electron transport material in multi-layer organic light emitting diodes by combinatorial methods”. *Phys. Chem. Chem. Phys.*, **1** (8), 1777–1781 (1999)

- [Sch99b] C. Schmitz, M. Thelakkat, and H.-W. Schmidt. “A Combinatorial Study of the Dependence of Organic LED Characteristics on Layer Thickness”. *Adv. Mater.*, **11** (10), 821–826 (1999)
- [Sch00] C. Schmitz, P. Posch, M. Thelakkat, and H. W. Schmidt. “Efficient screening of materials and fast optimization of vapor deposited OLED characteristics”. *Macromol. Symp.*, **154**, 209–221 (2000)
- [Sch01] C. Schmitz. *Investigation of Opto-Electronic Thin-Layer Devices Using a Combinatorial Approach*. Ph.D. thesis, University of Bayreuth (2001)
- [Sco97] J. C. Scott, S. A. Carter, S. Karg, and M. Angelopoulos. “Polymeric anodes for organic light-emitting diodes”. *Synthet. Metal.*, **85** (1-3), 1197–1200 (1997)
- [Shi77] H. Shirakawa, E. ELouis, M. A., and A. Chiang, C. Heeger. “Synthesis of electrically conducting organic polymers: Halogen derivatives of polyacetylene (CH)_n”. *Journal of the Chemical Society: Chemical Communications*, p. 579 (1977)
- [Stü01] T. Stübinger and W. Brütting. “Exciton diffusion and optical interference in organic donor-acceptor photovoltaic cells”. *J. Appl. Phys.*, **90** (7), 3632–3641 (2001)
- [Stü02] T. Stübinger. “Ellipsometry on thin films of copper phthalocyanine” (personal communication 2002)
- [Str98] R. Strohmaier, J. Petersen, B. Gompf, and W. Eisenmenger. “A systematic STM study of planar aromatic molecules on inorganic substrates - I. Submolecular image contrast”. *Surf. Sci.*, **418** (1), 91–104 (1998)
- [Tak00] K. Takahashi, N. Kuraya, T. Yamaguchi, T. Komura, and K. Murata. “Three-layer organic solar cell with high-power conversion efficiency of 3.5%”. *Sol. Energy Mater. Sol. Cells*, **61** (4), 403–416 (2000)
- [Tan86] C. W. Tang. “Two-layer organic photovoltaic cell”. *Appl. Phys. Lett.*, **48** (2), 183–185 (1986)
- [Tan87] C. W. Tang and S. A. VanSlyke. “Organic electroluminescent diodes”. *Appl. Phys. Lett.*, **51** (12), 913–915 (1987)
- [The02] M. Thelakkat, C. Schmitz, and H.-W. Schmidt. “Fully-vapor deposited thin-layer Titanium dioxide solar cells”. *Adv. Mater.*, **14** (8), 577–581 (2002)
- [Vin82] P. Vincett, W. Barlow, R. Hamm, and C. Roberts. “Electrical conduction and low voltage blue electroluminescence in vacuum-deposited organic films”. *Polymer*, **24**, 733–762 (1982)
- [Wie96] T. Wieland. “The use of structure generators in predictive pharmacology and toxicology”. *Arzneimittel-Forsch*, **46** (2), 223–227 (1996)

- [Wu97] C. C. Wu, J. C. Sturm, R. A. Register, J. Tian, E. P. Dana, and M. E. Thompson. “Efficient organic electroluminescent devices using single-layer doped polymer thin films with bipolar carrier transport abilities”. *IEEE Trans. Electron Devices*, **44** (8), 1269–1281 (1997)
- [Xin01] X.-K. Xin and G.-C. Cao. “A thermal failure model of solar cells and its experimental studies”. *Sol. Energy Mater. Sol. Cells*, **69** (1), 79–84 (2001)
- [Yam01] N. Yamamoto, H. Muramatsu, L. M. Do, E. M. Han, T. Kato, and M. Fujihira. “Study of energy transfer from excited TPD to Alq in organic electroluminescent devices by time-resolved fluorescence spectroscopy using a scanning near-field optical atomic force microscope”. *J. Microsc.*, **202**, 395–400 (2001)
- [Zet00] H. Zettl. *Neue Methoden zur Charakterisierung von Organischen Leuchtdioden*. Diploma thesis, Universität Bayreuth (2000)

Danksagung

An erster Stelle möchte ich Prof. Georg Krausch danken, der mir die Möglichkeit gegeben hat, an seinem Lehrstuhl über organische Bauelemente zu promovieren, und der mich besonders in den schwierigen Zeiten dieser Promotion motiviert und in jeglicher Hinsicht unterstützt hat.

Mein weiterer Dank gilt den vielen Kollaborationspartnern, durch die diese Arbeit erst ermöglicht worden ist:

Prof. Christoph Bräuchle und seinen Mitarbeitern Klaus Meerholz, David Müller und Markus Gross, unter deren Händen die PMMA/TPD Leuchtdioden entstanden sind.

Hagen Göttlich für die Hilfe beim SNOM-Eigenbau in München.

Prof. Markus Schwoerer und den Mitgliedern des Lehrstuhls EP11, insbesondere Stefan Berlepp, Anton Mückl, die die Alq₃ Leuchtdioden mit semitransparenten Elektroden zu Wege gebracht haben. Mein besonderer Dank geht an Thomas Stübinger, der mir ein offener und hilfreicher Diskussionspartner bei Fragen zu Ellipsometrie und Solarzellen gewesen ist.

Prof. Hans-Werner Schmidt und seinem Lehrstuhl danke ich für die intensive Zusammenarbeit bei den kombinatorischen Experimenten. Besonders danken möchte ich Christoph Schmitz, Roman Kisselev, Christian Neuber und Markus Bäte für das Aufdampfen komplexer Schichtsysteme. Ohne ihre Geduld wären die vorgestellten Ergebnisse nicht zustande gekommen. Mein herzlicher Dank gilt auch Mukundan Thelakkat, der mir mit vielen wissenschaftlichen, aber auch nichtwissenschaftlichen Diskussionen zur Seite gestanden hat.

Heiko Zettl, der sich getraut hat, bei mir eine Diplomarbeit anzufangen, danke ich für viele Tage und Nächte im Labor, für fruchtbare und Streitbare Diskussionen, für Anregungen und Hilfe bei dieser Arbeit, für eine großartige Zusammenarbeit und für eine tiefe Freundschaft.

Desweiteren sind mir die Mitarbeiter unseres Lehrstuhls auf verschiedenste Weise eine Hilfe auf dem Weg zur Erlangung des Doktorgrades gewesen:

Christina Cecco, Hubert Elbs und Kevin Phelan als Männer – und Frau – der ersten Stunde. Kevin danke ich besonders für seine linguistischen Delikatessen.

Armin Knoll, die Labview-Online-Hilfe, aber auch ein Diskussionspartner für tiefgehende mathematische und physikalische Diskussionen, offen für skifahrerische Experimente.

Das “Läster²”, ohne das die Messzeit am ESRF nur halb so unterhaltsam gewesen wäre.

Nicolaus Rehse, verantwortlich für LAN- und andere Parties und Stellvertretung für seinen phonetischen Namensvetter.

Frank Schubert, äußerst würdiger Nachfolger im Amt des Administrators: “Steht doch im Kopka!”

Kristin Schmidt, Nothelferin bei chemischen Formeln.

Wolfgang Häfner, stets bereit zu ausschweifenden Diskussionen über Übungsaufgaben, die schwerer waren als gedacht. Eine große Hilfe waren auch seine Lektionen im *Unixschen* und im *Fränggischen*.

Markus Hund, “Des iss schwierig!” ... ging dann aber doch.

Carmen Kunert, Kunstausstatterin des Lehrstuhls.

Frau Zimmermann, die mit allen erdenklichen Mitteln das Leben am Lehrstuhl noch lebenswerter gemacht hat.

Schließlich danke ich allen Mitarbeitern der mechanischen Werkstatt unter der Meisterschaft von Herrn Krejtschi, die die großen und kleinen mechanischen Herausforderungen willig angenommen und bewältigt haben. Ebenfalls danken möchte ich der Glasbläser-Werkstatt, die den Wasserfilter nach jeder Beschädigung geduldig wieder instand gesetzt hat.

Unabdingbare Voraussetzung für das Gelingen dieser Arbeit war auch der Einsatz unseres Hauselektronikers Franz Fischer, der die Entwicklung des Multiplexers und manch anderen Schaltkreises unter seine Fittiche genommen hat.

Meiner Freundin Rasa danke ich für ihre Engelsgeduld, besonders in der letzten Phase meiner Arbeit, und für die letzten Korrekturen vor dem Druck.

Schließlich gilt mein großer Dank meinen Eltern, die mich während der gesamten Studienzzeit unterstützt haben, meinen beiden Brüdern, die mir in schwierigen Situationen mit Rat zur Seite standen, Wolfgang ganz besonders für die Diskussionen, in denen mal wieder richtig fundamentale QM betrieben werden durfte.

Ferner danke ich

den Firmen Carl-Zeiss-Jena und Digital Instruments für die Zurverfügungstellung des Prototyp SNOM und für das Vertrauen, das sie in uns als Betatester gesetzt haben,

dem Fonds der Chemischen Industrie,

dem Staat Bayern (Langfristprogramm Neue Werkstoffe),

und der Deutschen Forschungsgemeinschaft, die die Arbeit im Rahmen des SFB 481 finanziert hat.

Erklärung

Die vorliegende Arbeit wurde von mir selbstständig verfasst, und ich habe dabei keine anderen als die angegebenen Quellen und Hilfsmittel benutzt.

Ferner habe ich nicht versucht, anderweitig mit oder ohne Erfolg eine Dissertation einzureichen oder mich der Doktorprüfung zu unterziehen.

Bayreuth, den 26.01.2004

Helmut Hänsel